

Germanium nanospheres as high precision optical tweezers probes

DISSERTATION

der Mathematisch-Naturwissenschaftlichen Fakultät
der Eberhard Karls Universität Tübingen
zur Erlangung des Grades eines
Doktors der Naturwissenschaften
(Dr. rer. nat.)

vorgelegt von
Swathi Sudhakar
aus Indien

Tübingen
2020

Gedruckt mit Genehmigung der Mathematisch-Naturwissenschaftlichen Fakultät der
Eberhard Karls Universität Tübingen.

Tag der mündlichen Qualifikation: 20.01.2021

Stellvertreter Dekan:	Prof. Dr. József Fortágh
1. Berichterstatter:	Prof. Dr. Erik Schäffer
2. Berichterstatter:	Prof. Dr. Klaus Harter

Contents

Summary	5
Zusammenfassung	7
1 Introduction	9
1.1 Visualization and quantification of single biomolecules to study their mechanism	9
1.2 Surface passivation techniques to perform single molecule fluorescence assays	10
1.2.1 Supported lipid bilayers as an alternative surface platform to existing techniques	10
1.3 Cytoskeleton and motor proteins play a major role in various cell functions	12
1.3.1 Microtubules are important structures in cells	12
1.3.2 Molecular motors	12
1.3.3 Kinesins are microtubule based motor proteins	12
1.4 DNA mechanics	15
1.5 Optical tweezers are a position and force transducer	16
1.5.1 Principles of optical tweezers	16
1.5.2 Geometric/ray optics	17
1.5.3 Rayleigh scattering	17
1.5.4 Mie theory	18
1.5.5 Calibration of optical tweezers	18
1.6 Novel probes for optical tweezers	18
1.6.1 Metallic nanoparticles as an optical tweezers probe with their usage limited by heating and denaturation of biomolecules	19
1.6.2 High refractive index nanoprobe for high precision optical tweezers measurements	20
1.6.3 Germanium nanospheres	20
1.6.4 Optical trapping of antireflective microspheres for force measurements in the nanonewton range	21
2 Objectives of this work	23
3 List of publications included in the thesis	25
3.1 Published papers	25
3.2 Submitted papers not included in the thesis	25

3.3	Manuscripts in preparation	26
4	Personal contribution to publications done in team work	27
5	Results	31
5.1	Supported solid lipid bilayers as a platform for kinesin stepping assays . .	31
5.1.1	Development of a supported solid lipid bilayer platform	31
5.1.2	Kinesin stepping assay	31
5.1.3	Platform for studying single DNA molecules	32
5.2	Germanium nano- and microspheres	33
5.2.1	Size-controlled synthesis of water stable germanium nanospheres .	33
5.2.2	Characterization of germanium nanospheres using different techniques	33
5.2.3	X-ray diffraction shows cubic phase of germanium nanospheres . .	34
5.2.4	Germanium nanospheres enable ultraprecise spatiotemporal measurements	35
5.2.5	Antireflective germanium microparticles for high force measurements	36
5.3	Kinesin stepping	38
5.3.1	Membrane-coated germanium nanospheres for kinesin transport .	38
5.3.2	Kinesin takes 4-nm steps	39
5.3.3	Kinesin detachment and rescue	39
6	Discussion	41
6.1	Supported solid lipid bilayers as an excellent platform for single molecule fluorescence and force measurements	41
6.2	Germanium nano- and microspheres for optical tweezers measurement . .	42
6.2.1	Germanium nanosphere synthesis and functionalization	42
6.2.2	Antireflection coated germanium microspheres for high force measurements	43
6.3	Stepping mechanism of kinesin-1	44
7	Conclusion and outlook	47
	Abbreviations	49
	Acknowledgement	51
	Appendix	71

Summary

Single-molecule methods are promising to provide deep insight into all biological problems. Methods include among others single-molecule fluorescence and force measurements. Such measurements are limited by Brownian motion that puts bounds to the spatiotemporal resolution and by nonspecific interactions of the molecules of interest to probes and surfaces that are involved in the measurement. To reduce nonspecific interactions and improve the spatiotemporal resolution of single-molecule assays, I have developed several novel methods in this thesis. First, I have developed a highly reproducible supported solid lipid bilayer platform for such assays. This platform provides specific and load bearing attachments with less nonspecific interactions of biomolecules and probes to the surface. Thus, the lipid bilayer platform enabled fluorescence and force measurements to study the mechanics of single DNA molecules and molecular motors. One such molecular motor is kinesin that transports vesicles along microtubules. Kinesin motor proteins walk in a rotary hand-over-hand mechanism associated with a center-of-mass displacement of 8 nm during the hydrolysis cycle. Early reports indicated that kinesin takes substeps. However, despite constant research over the last three decades, load-bearing substeps could not be confirmed and the stepping mechanism of kinesin remains unclear. An ideal tool, to study the mechanics of kinesin are optical tweezers. Optical tweezers use microspheres as handles for measuring piconewton forces generated by kinesin. However, micron-sized probes with a low refractive index limit the spatiotemporal resolution. To overcome this limit, I have synthesized high refractive index germanium nanospheres and antireflection coated, core-shell germanium microspheres. High-refractive index particles beyond a certain size limit cannot be trapped by a laser in optical tweezers unless they are photonicly structured to reduce the scattering force. To reduce scattering and to increase the trap force, I added an antireflection coating to germanium microspheres. With these probes, we can, in the future, increase the optical force generated by the optical tweezers beyond a nanonewton or achieve a very fast response time below a microsecond. The germanium nanospheres already enabled me to perform high spatiotemporal optical tweezers measurements. I found that, instead of 8-nm steps, kinesin-1 motors take 4-nm center-of-mass steps with alternating step durations depending on force and ATP. At high loads, motors switched to a weakly bound state, but did not detach. Instead, motors slipped on microtubules in 8 nm steps on a microsecond time scale. Surprisingly, rescue of directed motion after such a slip event happened in about 80% of events. Such rescue events indicated that the run lengths of individual motors are concatenations and rescues need to be accounted for to understand long-range transport. By these measurements, I have resolved a long

standing controversy bringing together the kinesin stepping and detachment behavior. In sum, this thesis provides mechanistic insights into how kinesin-1 walks and detaches from microtubules, thus helps to understand the big picture of how kinesin motors work in a team to transport vesicles. In the long-term, employment of novel probes that enable an ultrahigh resolution opens up new avenues for detailed investigations and new discoveries of conformational changes that are key for the biological function of many other molecular machines.

Zusammenfassung

Einzelmolekülmethoden sind vielversprechend, um tiefe Einblicke in alle biologischen Probleme zu gewinnen. Zu den Methoden gehören unter anderem Einzelmolekül-Fluoreszenz- und Kraftmessungen. Solche Messungen sind einerseits begrenzt durch die Brownsche Bewegung, die der raum-zeitlichen Auflösung Grenzen setzt und andererseits durch unspezifische Wechselwirkungen der zu untersuchenden Moleküle mit Sonden und Oberflächen, die an der Messung beteiligt sind. Um unspezifische Wechselwirkungen zu reduzieren und die räumlich-zeitliche Auflösung von Einzelmolekül-Assays zu verbessern, habe ich in dieser Arbeit mehrere neue Methoden entwickelt. Erstens habe ich eine hochgradig reproduzierbare, Oberflächen-gestützte feste Lipid-Doppelschicht-Plattform für solche Assays entwickelt. Diese Plattform bietet eine stabile und spezifische Befestigungsmöglichkeit für Biomoleküle und Sonden mit gleichzeitig minimierten unspezifischen Wechselwirkungen dieser mit der Oberfläche. Auf diese Weise ermöglichte die Lipid-Doppelschicht-Plattform Fluoreszenz- und Kraftmessungen zur Untersuchung der Mechanik einzelner DNA-Moleküle und molekularer Motoren. Ein solcher molekularer Motor ist das Kinesin, das Vesikel entlang von Mikrotubuli transportiert. Kinesin-Motorproteine laufen in einem rotierenden Hand-über-Hand-Mechanismus, der mit einer Massenschwerpunktverschiebung von 8 nm während des Hydrolysezyklus verbunden ist. Frühe Berichte deuteten darauf hin, dass das Kinesin zusätzliche Zwischenschritte macht. Trotz ständiger Forschung während der letzten drei Jahrzehnte konnten diese lasttragenden Zwischenschritte jedoch nicht eindeutig bestätigt werden, und der Schrittmechanismus des Kinesins bleibt unklar. Ein ideales Werkzeug, um die Mechanik des Kinesins zu untersuchen, ist eine optische Pinzette. Optische Pinzetten verwenden Mikrokugeln als Proben zur Messung der vom Kinesin erzeugten Piconewton-Kräfte. Allerdings begrenzen mikrometergroße Sonden mit einem niedrigen Brechungsindex die räumlich-zeitliche Auflösung. Um diese Grenze zu überwinden, habe ich Germanium-Nanokugeln mit hohem Brechungsindex und antireflexbeschichtete, Kern-Schale-Germanium-Mikrokugeln synthetisiert. Teilchen mit hohem Brechungsindex, die eine bestimmte Größengrenze überschreiten, können von einem Laser in optischen Pinzetten nicht mehr gefangen werden, es sei denn, sie werden photonisch strukturiert, um die Streukraft zu verringern. Um die Streuung zu verringern und die Einfangkraft zu erhöhen, habe ich den Germanium-Mikrokugeln eine Antireflexbeschichtung hinzugefügt. Mit diesen Sonden können wir in Zukunft die von der optischen Pinzette erzeugte optische Kraft über ein Nanonewton hinaus erhöhen oder eine sehr schnelle Reaktionszeit unter einer Mikrosekunde erreichen. Die Germanium-Nanosphären ermöglichten es mir bereits, mit der optischen Pinzette Messungen mit hoher raum-zeitlicher Auflösung durchzuführen. Ich fand heraus,

dass Kinesin-1-Motoren anstelle von 8-nm-Schritten 4-nm-Massenmittelpunkt-Schritte mit wechselnden Schrittdauern in Abhängigkeit von Kraft und ATP ausführen. Bei hohen Lasten schalteten die Motoren in einen schwach gebundenen Zustand, lösten sich aber nicht ab. Stattdessen rutschten die Motoren auf Mikrotubuli in 8-nm-Schritten auf einer Zeitskala von Mikrosekunden. Überraschenderweise geschah die Rettung einer gerichteten Bewegung nach einem solchen Rutschereignis in etwa 80% der Fälle. Solche Rettungsereignisse deuteten darauf hin, dass es sich bei den Lauflängen der einzelnen Motoren um Verkettungen handelt und dass Rettungen berücksichtigt werden müssen, um den Langstreckentransport zu verstehen. Durch diese Messungen habe ich eine seit langem bestehende Kontroverse gelöst, die das Kinesin-Schritt- und Ablöseverhalten zusammenbringt. Zusammenfassend lässt sich sagen, dass diese Arbeit mechanistische Einblicke in die Art und Weise liefert, wie Kinesin-1 läuft und sich von den Mikrotubuli ablöst, und somit zum Verständnis des Gesamtbildes beiträgt, wie Kinesin-Motoren in einem Team arbeiten, um Vesikel zu transportieren. Langfristig eröffnet der Einsatz neuartiger Sonden, die eine ultrahohe Auflösung ermöglichen, neue Wege für detaillierte Untersuchungen und neue Entdeckungen von Konformationsänderungen, die für die biologische Funktion vieler anderer molekularer Maschinen von entscheidender Bedeutung sind.

1 Introduction

1.1 Visualization and quantification of single biomolecules to study their mechanism

Almost all aspects of life are engineered at the molecular level, and without understanding single molecules we can only have a very sketchy understanding of life itself - Francis Crick

Everything in the world around and within us is made up of molecules. We humans are complex organisms with 30 trillion cells, countless single molecules, hardwired to survey [4]. Each and every single molecules acts together to create functional cells. The question which hit my mind every time is why should we explore single molecules in a biological system? What are the advantages of looking at one molecule at a time? These questions led me to realize that the studies on single molecules will render us to ask and answer questions that were impossible to address before.

All classical biophysical and chemical methods picture the behavior of enormous ensembles of molecules, averaging the measured parameters over the total molecular population. But, how the individual molecules behave, their conformation, properties and evolution over time, can be revealed only by performing single molecule imaging or force measurements [5, 6].

There are various techniques to explore single molecules. Fluorescence based methods like fluorescence resonance energy transfer, [7, 8] confocal, total internal reflection fluorescence microscopy (TIRF) techniques are used since many years to study single molecules [9, 10]. Atomic force microscopy techniques have opened up new avenues in both imaging and force measurements in understanding inter and intra molecular interaction forces exerted in or by molecules [11, 12]. Optical tweezers and magnetic tweezers are another force manipulation technique [13–16]. With these single molecule techniques we can resolve the mechanisms involving multienzyme and macromolecular complexes that remain challenging in biomolecular systems. Single molecule techniques help us to see and touch the molecules with novel probes. For many experiments, we need a surface platform to study complex and subtle biological processes of single molecules, which is discussed in next section.

1.2 Surface passivation techniques to perform single molecule fluorescence assays

When performing a single-molecule fluorescence protein study, it is vital to attain a great quality of surface passivation to prevent surface-induced protein malfunction or denaturation. Another methodological challenge is the nonspecific attachment of biomolecules to the imaging surface which causes problems during analysis of the target molecules.

Often, a glass surface is treated with surfactants like bovine serum albumin (BSA) and this surface was used for single-molecule nucleic acid studies and the proteins. As an alternative passivation technique to study the proteins, the glass surface was coated with a polymer (polyethylene glycol, PEG) [17–28]. The problem with this method was a non-uniform distribution of the PEG film, which resulted in defects [29, 30].

There are also studies of passivation of surfaces with polysiloxane and Tween-20 in addition to PEGylation [16, 30]. But these surfaces may destruct cells or active biomolecules, makes it inappropriate for cellular functional studies.

One more alternative surface passivation technique is to attach the biomolecule of interest to the nanoparticles or nanodots and arranging them in array like matrix [31–33]. But this method suffers from a problem of nonspecific adsorption of protein, which resulted in high background fluorescence.

There are also some studies that use pluronic F127 as a blocking agent to passivate hydrophobic surfaces [34–37]. But in this approach, harsh chemicals are involved with limited shelf life or sensitivity to humidity which is potentially harmful, more hazardous and ecohostile. Moreover, this procedure includes time consuming steps. Thus, a multifaceted method is required to improve surface passivation, especially for performing single-molecule fluorescence measurements.

1.2.1 Supported lipid bilayers as an alternative surface platform to existing techniques

Supported lipid membranes on solids are of scientific interest for several reasons. Lipid bilayers are a great alternative approach for single-molecule studies as they provide an environment more similar to the circumstance that the macromolecules face inside a living cell [38]. Therefore, lipid bilayers are suitable for many different proteins and nucleic acids. In addition, they also prevent many non specific interactions with the surface. Moreover, lipid bilayers can be easily modified through the incorporation of different functional lipids such as biotin, PEG or carboxyl in their head group.

There is a wide range of lipid-based model systems like Langmuir-Blodgett, Langmuir-Schaefer deposition, vesicle fusion, solvent assisted lipid bilayer and lipid/detergent mixed micelles methods [18, 39]. One of the easiest and widely used technique to form phospholipid bilayer is via vesicle deposition and fusion on a glass substrate [40] as described in Fig. 1.1. Phospholipids are rehydrated, vortexed and sonicated to form small

uni-lamellar vesicles. Flattening and rupture of vesicles resulted in a continuous planar lipid bilayer.

Lipid bilayers gained attention for their potential usage to form cell-cell interfaces [27], to study ligand-receptor-mediated interaction of vesicles, virus-like particle interaction with lipids, membrane-enveloped virions and lipid nanoparticles covered with lipid membranes [41–43].

Cytoskeletal motor proteins can also be attached to a fluid lipid bilayer surface [26]. However, because the membrane is fluid, forces cause motion of the attachment anchors in the membrane. However, a simple membrane based platforms for force experiments is missing. Supported solid lipid bilayer provides specific attachments of biomolecules and enable us to perform force measurements [44]. By using the solid supported lipid bilayer platform, we can explore the mechanism of cytoskeletal motor proteins and DNA, which is discussed in next section.

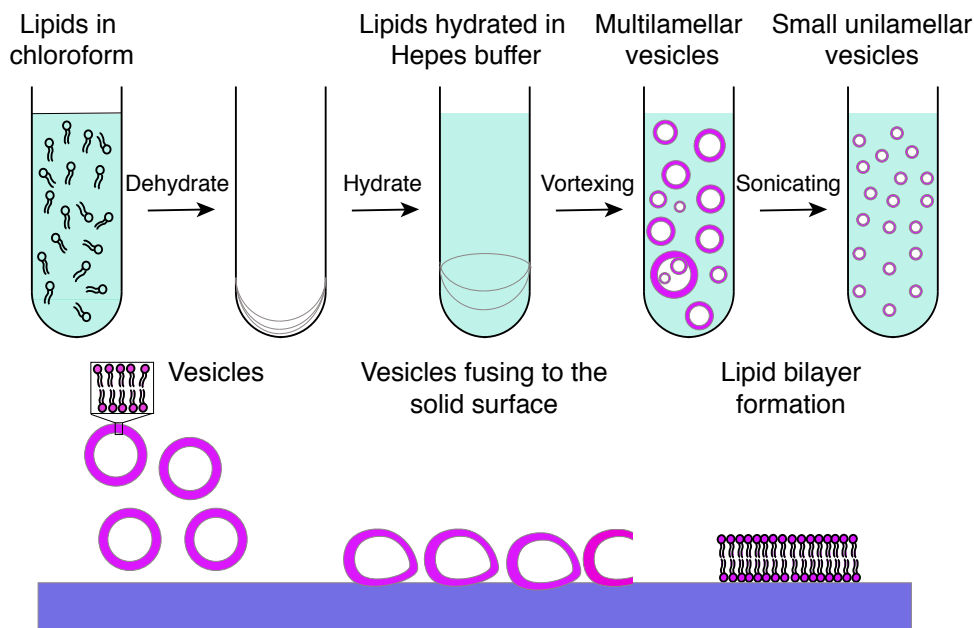


Figure 1.1: Schematic representing supported lipid bilayer formation using the vesicle fusion method. In the first step lipids are dissolved in chloroform. Then the solvent is evaporated. Next step, lipids are rehydrated in the supported lipid bilayer buffer. They are vortexed and sonicated to create multilamellar and small unilamellar vesicles. The calcium chloride helps in the fusion of vesicles to the surface forming lipid bilayer.

1.3 Cytoskeleton and motor proteins play a major role in various cell functions

In eukaryotic cells, motor proteins and the cytoskeleton are present in the cytoplasm. Cytoskeletal motor proteins move along a hierarchically arranged polymer tracks. Motors are sub divided into three superfamilies: kinesin, dynein and myosin [54–57]. They are responsible for the transport and movement of cargo within cells and for the shape and mobility of the cells [45–47]. The cytoskeleton is made up of three different types of protein filaments. microtubules, actin and intermediate filaments. Though actin and intermediate filaments play a vital role, this thesis is only concerned with microtubules.

1.3.1 Microtubules are important structures in cells

Microtubules are composed of tubulins. Alpha and beta tubulin (roughly 4 nm in size) form heterodimers that polymerize to form protofilaments. The lateral connection of thirteen protofilaments generates hollow cylindrical stiff microtubules [48]. The peripheral diameter of the microtubules is around 25 nm. The GTP bound alpha tubulin is stable while GTP attached to the beta tubulin can be easily hydrolyzed. The GTP tubulin exists at the end of the microtubules, thus preventing it from depolymerization and preserving the microtubule stability [49, 50]. But when GDP bound tubulin is present at the tip of microtubules, rapid shrinking occurs, known as catastrophe. This fascinating microtubule process to assemble and disassemble themselves is termed dynamic instability [51].

1.3.2 Molecular motors

For me, the most interesting scenario in living cells is to investigate motor proteins associated with the cytoskeleton. Billions of motor proteins work in a collaborative way in eukaryotic cells. Microtubule motors like kinesin and dynein progress along microtubules [54–56]. Myosin, moves along actin microfilaments. All these motor proteins utilize chemical energy to drive themselves along a straight track, with the sliding or moving direction dependent on the polarity of the path. The motor domain or “head” determines the identity of the path and the direction of movement along it while the type of cargo that motor proteins interact with or bind to is regulated by the tail of the motor protein [57, 58].

1.3.3 Kinesins are microtubule based motor proteins

Kinesins are involved in major cellular functions including meiosis, mitosis and in transporting cellular cargo from one place to another within the cell. Most kinesins are plus end directed thus transporting the membrane enclosed organelles or cargo from the center to the periphery of the cell, maintaining anterograde transport [59].

Kinesins have been sub classified into 14 classes according to their directionality towards plus or minus end of the microtubules, their peptide chain composition either they are homo or hetero dimers and also based on their motor head position placed at the C-terminus, internal or N-terminus [60, 61].

Among the kinesins, the most studied one is conventional kinesin. It belongs to the class of kinesin-1. The motor domain that generates motion is at the N-terminal heavy chain region with conserved 350 amino acids. The catalytic core in combination with the neck linker of 40 conserved amino acids build up the motor domain region. The catalytic core binds ATP and microtubules while the neck linker helps as a lever for the movement. The coiled coil region behind the motor domain is called stalk. The tail is at the C-terminal end and associated with transport of cargo [62, 63]. The whole kinesin-1 domain organization is shown in Fig. 1.2.

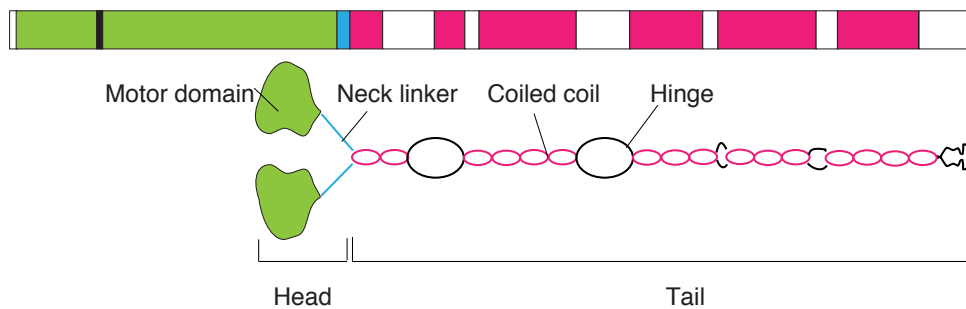


Figure 1.2: **Kinesin-1 domain organization (top)**. Motor domain or head region (green) binds to ATP and microtubules. Neck linker (blue) as a bridge between head and tail region. The pink and white regions corresponds to coiled coils and unstructured hinges.

How does kinesin operate in teams and transports organelles and macromolecules? What is the step size of kinesin while it is walking? How much load can they bear? Single-molecule techniques like optical tweezers helped to reveal part of the kinesin stepping mechanism but still there are a lot of unresolved questions. Optical tweezers and fluorescence microscopy studies clearly showed that kinesin walks along single protofilaments on the microtubules in a hand-over-hand mechanism with the step size of 8 nm and with an average speed about 800 nm/s [13, 64, 65]. In a hand-over-hand mechanism, each step of the motor is expected to rotate by 180-degree where the torque is transferred from the motor head to the motor bound cargo through the stalk. Ramaiya et al [64] found uni-directional rotation of kinesin motors implying that, the motor head is not free to rotate during stepping. Here, the one head of kinesin is strongly bound while the other head is weakly bound which diffuse along the microtubule. Next, how does kinesin take these steps and what is the mechanochemistry behind it? Slowly, there is a consensus model developing [13, 66].

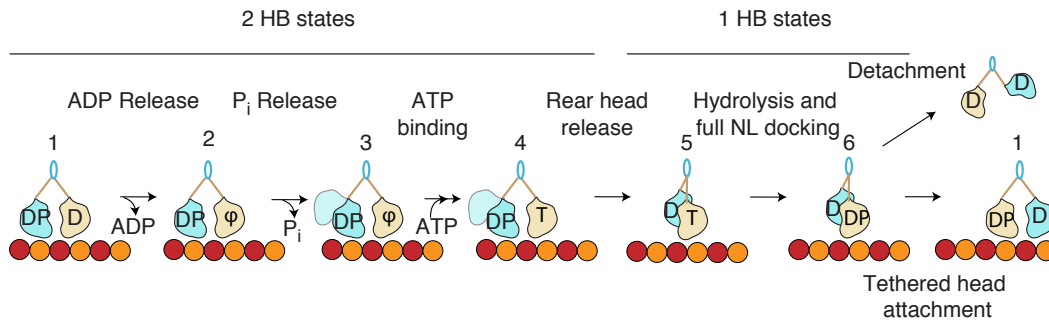


Figure 1.3: **Binding of kinesin to microtubules in a two head bound state. With the release of ADP and P_i from rear head, ATP binds to the front head. This provokes a conformation change that allows the detachment of rear head with displacement of 8 nm. In a next step, the ATP hydrolysis occurs in the front head. From this point either the kinesin can complete the cycle or they can detach from the microtubule lattice. Adapted from [66].**

The consensus model for the kinesin-1 chemomechanical cycle depicted in Fig. 1.3 helps us to figure out how kinesin walks against loads [67]. The model is divided into two parts with equal distribution of total cycle time between one head and two head bound states at saturated ATP. The cycle begins with the binding of both heads to the microtubule. In next step the adenosine diphosphate (ADP) is released rapidly. The rapid ADP release was confirmed by performing stop flow measurements [67]. Followed by the ADP release step, the phosphate (P_i) may be liberated, thus converting the rear head to a weakly bound state. Transition from the two head bound state to the one head bound state includes ATP binding at a fast rate followed by the detachment of the trailing head. Note that the one-head bound state has been refined by Ramaiya et al [64] to one head strongly bound and the other head being weakly bound. Thus in the former called one head bound state, both heads still remain in contact with the microtubule. With ATP binding to the front one and with rear head detachment, the cycle is completed.

There are lots of open questions in the above explained consensus model. The big argument in the literature is whether the trailing head detachment precedes ATP binding to the front head, or not. There are few single molecule fluorescence reports which show that the strain between a head in a two head bound state accelerates the rear head detachment followed by ATP binding to front head [68, 69]. But in contrast, tracking molecules with probes attached to one head proposes that ATP binds in a two head bound state. The mechanism here is like a power stroke, in which the conformational change in the front head triggers the rear head detachment [67].

The next controversial story concerns the step size. Do kinesins take 8 nm steps or not? There are studies which reported that kinesin takes steps that are smaller than 8 nm. Coppin et al. [2] reported that the 8 nm steps are subdivided into 5 and 3 nm steps. Nishiyama et al. [1] used smaller sized polystyrene beads and detected 4 nm steps of kinesin with optical tweezers. But both studies are criticized [3]. For example in Coppin et al. the starting and ending data points in the step were selected entirely 'by eye' and traces were filtered with a 15 ms median filter. Under these criteria, no statistically meaningful plateaus can exist. In Nishiyama et al [1], the problem is associated with the data sampling by selection and a failure to assess the effects of instrument bandwidth. Because of the presence of noise, individual records of steps showed no clear evidence of substeps. Carter and Cross argued that there is no substep at all [70]. But the response time which they acquire with large sized polystyrene (500 and 800 nm) microspheres was large and it is unclear how large instrument noise was. The Hancock group [67] tracked the position of gold nanoparticles coupled to individual kinesin motor domains in processively stepping dimers using interferometric scattering microscopy and detected intermediate steps. Isojima et al. [71] also visualized the intermediate steps in kinesin by employing high-temporal resolution dark-field microscopy. As there are lots of unanswered questions in the kinesin mechanism, I tried to find a solution to these problems, which is discussed in later parts of the introduction.

1.4 DNA mechanics

One of the foremost studied single molecule is DNA. DNA is the inherent hereditary material which affords a blue print for cell growth, replication and death [72]. DNA stores information in the cells. DNA is comprised of nucleic acids which in turn are made of deoxyribonucleotides. Deoxyribose, a phosphate group, and a nitrogenous base, a nitrogen-containing ring structure is responsible for the complementary base pairing between nucleic acid strands [73].

During DNA condensation, DNA is tightly packed within cells [72]. A particular region (gene) in DNA influences the characteristic behavior of the organism. Genes can be transcribed, translated and replicated according to the needs of the cells [74]. There are also lots of proteins which binds and interacts with DNA to modify chromatin structure [75, 76]. For these processes, the mechanical properties of DNA are important. Thus, single molecule techniques were employed to study the mechanical properties of DNA. Among others [7, 9, 11, 12, 15, 16] optical tweezers have been employed for trapping and for measuring the forces exerted by molecular motors or the mechanical properties of DNA. Let us have a detailed look on optical tweezers.

1.5 Optical tweezers are a position and force transducer

Force holds everything together, especially, small forces in the range of 1-100 pN regulate the structure and dynamics of single biomolecules. Now-a-days, optical tweezers have become a fantastic tool to probe the forces and dynamics associated with single-molecules with extraordinary resolution.

Optical tweezers utilize the laser light momentum to optically trap microscopic objects in the range from nano to micrometers. Optical tweezers were first developed by Arthur Ashkin and applied in biology [77]. The forces were applied to single molecules to detect their responses in the form of distance changes. The ultra high-resolution optical tweezers have a resolution range in measuring the distance, force and time in the range of 0.1 nm-50 μm , 0.02-250 pN, 0.1 ms-3,000 s [78].

Generally, biomolecules function depends on their thermal fluctuations, with an energy change of 4.1 pN nm at room temperature or $k_B T$ (k_B is the Boltzmann constant and T is the room temperature). If a single molecule goes through a conformational change of 1 nm, against a force of about 4.1 pN, then the mechanical work corresponds roughly to the thermal energy. This guesstimate suggests that the force exerted by bio-molecules is in the pico newton range. In particular for cases like the mechanical unfolding of macromolecules, the exerted forces are larger than the above estimated force. Otherwise molecules would not be stable against thermal fluctuations. Thus, optical tweezers are excellent tools to study the kinetics and thermodynamics of bio macromolecules [79].

1.5.1 Principles of optical tweezers

To understand the principle of how optical tweezers work, we need to know how the particles are trapped in a focussed laser beam and how we can measure the forces acting on the particles. When light interacts with a particle, some rays are absorbed while others are scattered with the effect of momentum transfer. In a simplified way we can say that force from the light is divided into two parts, gradient and scattering force where the gradient force (F_{grad}) acts in the direction of the light gradient facing the focus, and the scattering force (F_{scat}) in the direction of the light propagation. The laser holds the microscopic objects when the F_{grad} is larger than the F_{scat} and thermal fluctuation of the particles (Fig. 1.4). When F_{scat} is higher, then particles are shot or pushed away from the laser beam [80]. If the particle size is smaller than the wavelength of the laser, then optical forces are based on Rayleigh scattering [81]. When the particle size is much larger than the wavelength then ray optics [82] can be used.

1.5.2 Geometric/ray optics

Geometric optics are used when the radius of the particles is larger than the wavelength of the laser. Here the incident light is refracted twice by the microspheres which is according to the Snell's law. If the refractive index of the particles differs from the surrounding medium, light momentum changes and this change in momentum is transferred to the particles [80]. If the microsphere has a refractive index higher than the surrounding medium, then a gradient force acts towards the highest intensity area. The scattering force results from the rays that are reflected at the interface of the particle and the medium.

1.5.3 Rayleigh scattering

The conditions for Rayleigh scattering are satisfied when the particles are much smaller than the wavelength of the incident laser beam. The forces are calculated by considering a particle as an induced dipole point that elastically scatters light. The particle senses the gradient force called Lorentz force, if the induced dipole is in an intensity gradient. The scattering force is associated with the diameter d of the particle ($F_{scat} \propto d^6$). The gradient force increases with $F_{grad} \propto d^3$. Therefore, the trap is less stable for large sized particles in the Rayleigh regime [83].

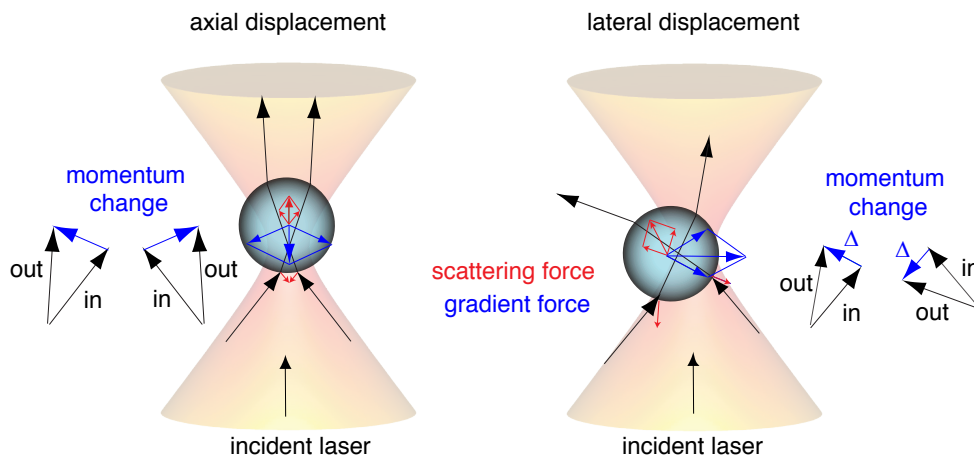


Figure 1.4: Schematic representing the microsphere trapped by the focused laser beam with portrayed gradient and scattering force. Adapted from [84].

1.5.4 Mie theory

When the microsphere dimension is comparable to the laser wavelength, we cannot apply either the ray optics or the Rayleigh scattering theory. For spherical particles in an optically trapped laser beam, this scattering regime can be explained mathematically by Mie theory [85, 86]. This theory solves Helmholtz wave equations to calculate the electric and magnetic field. The correlation between the incident, scattered, and internal fields calculated with boundary conditions provides us Mie expansion coefficients. From this, the trapping force can be determined. A focused laser beam with a Gaussian profile is used to trap a spherical particle, which complicates the application of the theory [87, 88]. To overcome this problem, we can use an optical tweezers computational tool box to calculate the forces and torques acting on a spherical particle [89, 90].

1.5.5 Calibration of optical tweezers

Next we will see how we can calibrate the optically trapped probe to precisely measure force and the displacement. Brownian motion (equipartition theorem), a drag coefficient measurement (Stoke's drag) and a sinusoidal calibration method are used to calibrate the tweezers [35, 91, 92]. For fast detection, the back focal plane interferometry was employed with the quadrupole photodiode detector (QPD) imaging the back focal plane to monitor the reflected or scattered light from the trapped microsphere [93]. The displacement of the microsphere from the trap center and the forces acting on the microsphere is determined from the detector signal.

The trapping force of a microsphere in a harmonic trap potential is described by Hook's law $F = \kappa\Delta x$. From the known displacement, x , from the laser focus and the trap stiffness, the force exerted on the microsphere can be calculated. But the displacement measured from the QPD will be in volts and we need to know the displacement sensitivity, a proportionality factor to convert the units from volts to nanometers.

1.6 Novel probes for optical tweezers

If we want to perform high spatiotemporal resolution measurements to unravel how a single molecule works, then the optical trap needs to be improved. The trap stiffness can be increased, by either modifying the laser beam or by improving the probe. Overfilling the back aperture by the laser beam with a TEM₀₀ mode or using laser beam with TEM₀₁ mode (donut shape) can improve the trap [80]. By optimizing the diameter d and the refractive index n of the particles, the probe trap stiffness can be improved.

Mostly, microspheres composed of polystyrene or silica were used as probe [10] for studying molecular mechanisms of motor proteins or mechanical properties of DNA. If we want to study more details of motor proteins, for example, in my case how they walk, what their step size is and how they detach from microtubules on microsecond time scales, I need some probes with a high spatiotemporal resolution. The ultimate precision

of the experiment is limited by the drag coefficient, i.e. the size of the microsphere. Thus, ideally, probes should be as small as possible.

The problem in optical trapping of polystyrene or silica beads that are smaller than 300 nm is that it is difficult. The trap stiffness and the forces exerted by such small particles are significantly smaller [80, 94]. Another problem faced by these beads, are they do not produce clear signals on the detector and so their signal-to-noise ratio for nanometry is low. To overcome this problem, metallic nanoparticles can be used as an alternative probe, which is discussed in the next section.

1.6.1 Metallic nanoparticles as an optical tweezers probe with their usage limited by heating and denaturation of biomolecules

Optical trapping of mesoscopic microparticles has promoted a wide range of innovative science and applications. Noble metal nanoparticles have gained special attention in recent years due to resonant collective oscillations of free electrons excited by light [95, 96]. The gold's large polarizability resulted in strong optical gradient forces resulting in a high trap stiffness even for small sized particles [97, 98].

Successive studies using gold nanoparticles showed that their surface plasmon resonance effect leads to strong trapping behavior. Recently, many groups explored optical trapping of gold nanoparticles in air and in water and studied how much force was exerted on these particles [99–101].

The Block lab introduced three dimensional trapping of gold nanoparticles in the size range below 100 nm [102]. They have also observed that 36 nm gold nanoparticles exhibited a seven times larger trapping force than a polystyrene sphere of similar size [102]. Hansen et al. [101] reported that they stably trapped gold nanoparticles three dimensionally, for the size range from 18 to 254 nm. They have also reported that forces up to tens of pico-newtons were exerted on these gold nanoparticles.

Silver nanoparticles have gained enormous interest, because they have more intense and sharper features in the visible light range in comparison with other plasmonic metallic nanoparticles like gold or copper [103, 104]. There are also studies on trapping other metallic nanoparticles composed, for example, of silver [105, 106].

But the main problem in trapping metallic nanoparticles is the significant heating of these particles caused by the absorption of light. Dramatic heating of these metallic nanoparticles at high laser power and causes damage to biomolecules. Seol et al. [99] reported that the gold nanospheres are not good handles to apply forces on biological molecules. They measured the internal heat produced by the metallic nanoparticles inside the trap and found that the measured heat is 20 folds higher than the heating of water under trapping. Thus, we need some nanoprobe with less heating, but at the same time, the probes should exert a high force to perform biomolecule force measurement with high spatiotemporal resolution. One solution is the use of high refractive index

nanoprobes which is discussed below.

1.6.2 High refractive index nanoprobes for high precision optical tweezers measurements

As the optical forces are associated and scale with the particle volume, for piconewton force measurements we need micron-sized optical probes practically limiting the spatiotemporal resolution [79, 80, 107, 108]. For high optical forces a high trap stiffness is necessary. This trap stiffness depends on the refractive index, particles size and volume of the particles. The higher the refractive index, the greater the trap stiffness. The smaller the size, the smaller the trap stiffness, however the better the resolution. This is the reason why we need high refractive nanoprobes.

According to Mie theory, germanium ($n = 4.4 \pm 0.11i$) and silicon ($n = 3.97 \pm 0.03i$) have a high refractive index at a trapping wavelength of 1064 nm and possibly a high trap stiffness. Moreover, these semiconductor materials have received an increasing attention in the field of nanophotonics [109–111]. These high refractive dielectric materials have geometric scattering resonances close to plasmonic materials, without the association of a large absorption coefficient resulting in less heating and negligible intrinsic optical loss. Especially, silicon improves the polarizability which enhances the trapping at the nanoscale range. Arroyo et al. [112] investigated the possibility of using commercially available silicon nanoparticles for trapping experiments. These particles were produced by grinding of silicon wafers. They have also shown that trapping was achieved for sizes up to 200 nm in diameter and the trap stiffness is comparable to the metallic nanoparticles with less heating. But there are a lot of difficulties associated with the synthesis of silicon nanoparticles in a spherical, crystalline and monodisperse manner and to functionalize these particles with biomolecules of interest. Germanium nanospheres are an alternative.

1.6.3 Germanium nanospheres

There are several methods reported in the literature to synthesize germanium nanoparticles [113–120]. Some chemical synthesis methods include metathesis reactions using Zintl salts [121], organogermane precursors decomposition using high boiling solvents [122], germanium halides reduction with mild-strong reducing agents [123, 124], germanium oxide (GeO_2) powder reduction in an aqueous media [119, 120, 125], thermal reductions of sol-gel polymers and copolymers with germanium and destruction of germanium chloride (GeCl_4) in a plasma reactor [114, 126].

But there are a lot of problems associated with the synthesis of germanium nanospheres in the above discussed methods. Many of these reports use toxic precursors, high temperatures and required specialized equipment. In addition to that the water soluble wet chemical reduction method did not result in monodisperse particles or in good crystallinity required for many applications. Also, particles often were not spherical. Other

synthesis methods have issues related to the use of pyrophoric reducing agents, synthesis of germanium containing complexes or preparation of time-consuming germanium precursors. A notable problem is that, if the reaction solution is not clean, polydisperse particles with different morphologies will be produced.

1.6.4 Optical trapping of antireflective microspheres for force measurements in the nanonewton range

So far, we had a look on the forces that we can exert on the probes from femto- to pico newtons using optical tweezers. This range is sufficient to study the mechanics of individual, biological molecular motor proteins or machines. But for the mechanical characterization of cellular processes like mitosis, cell adhesion and contraction, the beating of cilia, or to study of amyloid fibrils, it requires larger forces [127]. There is constant interest in developing probes, to extend and exert an optical force in the nano newton range. The high force can be achieved with the help of a strong trap, but it requires high laser power which heat the probe and affects the biological interactions. The majority of attempts to measure forces in the nanonewton range involves beam shaping techniques and set-up improvements [128]. But with these techniques, it was harder to achieve a laser momentum transfer. Using high refractive index materials, we can achieve a high trap stiffness, but only with certain sizes of the probe. After a certain size limit, the scattering force becomes larger than the gradient force, thus we cannot trap particles any more. One approach to significantly reduce the scattering force acting on a bead is to introduce an anti-reflective layer around the bead.

Thus, in our lab, we have designed and characterized antireflection coated microspheres. We have used high refractive index particles, untrappable until they are coated with low refractive index materials, which reduced the scattering forces and accompanies stronger trapping. Jannasch et al. [129] reported that trap stiffness increased by 40% when they coat polystyrene beads with silica in comparison to silica or polystyrene alone. Subsequently, our lab improved the idea further based on antireflection coated, high refractive index titania microspheres [129]. Silica coated nanodiamonds were also employed for performing high resolution experiments [130]. The silica shell around the nanodiamonds made them to be stable in water and allows us to couple the target proteins to the particle surface.

Still there are lots of problems associated with the above explained coated particles. Reproducibility and sphericity of the particles are main issues. Not only did the reaction result in secondary nucleation of the coating material, but the microspheres also tended to aggregate into large amorphous complexes. In addition, some shrinking of the particles could be observed after the coating, which might have been due to aqueous or thermal instability of the particles during the used coating protocol.

Taken together, germanium is a promising material to improve optical trapping probes ranging in size from tens of nanometers to a micrometer.

2 Objectives of this work

Mechanical processes are essential for cells. Cytoskeletal motor proteins like kinesin carry out various essential cellular processes. Kinesin motors progress by taking steps on microtubules in a rotational hand-over-hand fashion. Despite their biological importance and decades of work, many fundamental components of the mechanochemical cycle in kinesin motor remain disputed. For example, one of the most controversial topics is whether intermediate steps exist and whether they can support load in the hydrolysis cycle. One important aspect is how the transport distance is affected by loads due to opposing and unsynchronized motors. This force generation and distance depends on motor detachment. How kinesins detach from microtubules is not known.

Single molecular machines producing forces in the piconewton range can be studied with optical tweezers. There are fundamental limits to achieve a high spatiotemporal resolution because of Brownian motion of both molecular motors and probes. A high spatiotemporal resolution can only be achieved by the use of nanometer-sized optical trapping probes. However, such nanoprobe for force measurements in the piconewton range do not exist.

This thesis is an investigation towards exploring the kinesin stepping mechanism using ultraresolution single-molecule force assays. Thus, the first goal was to develop a promising solid supported lipid bilayer surface platform to carry out in vitro kinesin stepping assays in a more reproducible manner with less nonspecific interactions. The second goal was to synthesize and characterize high refractive index germanium nanoprobe and antireflective coated germanium microspheres for high resolution, high force and fast response time experiments. The third goal was to covalently couple the motor protein kinesin-1 to the germanium nanospheres to find out whether substeps exist and how motors detach from microtubules. Confocal, interference reflection and total internal reflection fluorescence microscopy and optical tweezers were employed to achieve the third goal. The ultimate intent of this project was to push the limits in resolution of optical tweezers to allow the measurement of so far hidden conformational changes of proteins.

3 List of publications included in the thesis

3.1 Published papers

1. **Swathi Sudhakar***, Tobias Jörg Jachowski*, Michael Kittelberger, Ammara Maqbool, Gero Lutz Hermsdorf, Mohammad Kazem Abdosamadi, and Erik Schäffer. Supported Solid Lipid Bilayers as a Platform for Single-Molecule Force Measurements. *Nano Letters*. 19, 8877–8886, 2019. doi: 10.1021/acs.nanolett.9b03761

* Authors contributed equally

2. **Swathi Sudhakar**, Mohammad Kazem Abdosamadi, Tobias Jörg Jachowski, Michael Bugiel, Anita Jannasch, Erik Schäffer. Germanium nanospheres for ultra-resolution picotensiometry of kinesin motors¹. *Science* 2020. In print (manuscript number: abd9944). *BioRxiv* doi: 10.1101/2020.06.18.159640.
3. Viktoria Wedler, Fabian Strauß, Swathi Sudhakar, Gero Lutz Hermsdorf, York-Dieter Stierhof and Erik Schäffer. Polycationic gold nanorods as multipurpose in vitro microtubule markers. *Nanoscale Advances*. 2, 4003, 2020.

3.2 Submitted papers not included in the thesis

4. Alexandra Ciorîta, Michael Bugiel, **Swathi Sudhakar**, Erik Schäffer, and Anita Jannasch. Single transport and depolymerizing kinesin stabilize microtubules. Submitted to the *Biophysical Journal*.
BioRxiv doi.org/10.1101/2020.10.05.326330

¹This manuscript has been accepted for publication in *Science*. This version has not undergone final editing. Please refer to the complete version of record at <http://www.sciencemag.org/>. The manuscript may not be reproduced or used in any manner that does not fall within the fair use provisions of the Copyright Act without the prior, written permission of AAAS

5. Akanksha Dohare*, **Swathi Sudhakar*** Björn Brodbeck, Ashutosh Mukherjee, Marc Brecht, Andreas Kandelbauer, Erik Schäffer, and Hermann A. Mayer, Simultaneous Delivery of Curcumin and Quercetin with Anisotropic Mesoporous Core-Shell Silica Microparticles. Submitted to Scientific Reports.

* Authors contributed equally

3.3 Manuscripts in preparation

6. **Swathi Sudhakar**, Mohammad Kazem Abdosamadi, Viktoria Wedler, Pasupathi Rajendran, York-Dieter Stierhof and Erik Schäffer. Germanium nanospheres as high precision optical tweezer probes.

4 Personal contribution to publications done in team work

1. **Swathi Sudhakar***, Tobias Jörg Jachowski*, Michael Kittelberger, Ammara Maqbool, Gero Lutz Hermsdorf, Mohammad Kazem Abdosamadi, and Erik Schäffer. Supported solid lipid bilayers as a platform for single-molecule force measurements. *Nano Letters*. 19, 8877–8886, 2019.

As a shared first author of this publication, T.J.J. and S.S. designed and executed the study under the supervision of E.S. To perform, single molecule fluorescent assays, we need a surface with less unspecific binding of molecules. For this I optimized and developed, a solid supported lipid bilayer platform for exploring the kinesin mechanism behavior by performing stepping assays with the help of TIRF and force spectroscopic studies with optical tweezers. All experiments and data analysis were carried out by T.J.J., E.S. and S.S., M.K. and A.M. helped to develop the assay. G.L.H. built the heating laser setup to carry out heating laser experiments. M.K.A. helped in data analysis. E.S, T.J.J. and S.S. altogether wrote the manuscript.

2. **Swathi Sudhakar**, Mohammad Kazem Abdosamadi, Tobias Jörg Jachowski, Michael Bugiel, Anita Jannasch, Erik Schäffer. Germanium nanospheres for ultra-resolution picotensiometry of kinesin motors ¹. *Science* 2020. In print (manuscript number: abd9944). *BioRxiv* doi: 10.1101/2020.06.18.159640

In this publication, I am the first author. E.S. and S.S. designed the experiments and contributed to the development of novel nanoprobe for motor protein experiments. Here I synthesized and characterized the germanium nanospheres and provided evidence that these high refractive index germanium nanoprobe have a high trap efficiency. I performed all force spectroscopic studies in a custom built ultrastable optical tweezer setup and analysed data. M.K.A, A.J. and E.S. helped

¹This manuscript has been accepted for publication in *Science*. This version has not undergone final editing. Please refer to the complete version of record at <http://www.sciencemag.org/>. The manuscript may not be reproduced or used in any manner that does not fall within the fair use provisions of the Copyright Act without the prior, written permission of AAAS

in analysing the data; M.K.A and T.J.J. provided data analysis software; T.J.J. developed the python package stepfinder; M.B. and A.J. developed protocols and provided advice; S.S. and E.S. wrote the paper.

3. Viktoria Wedler, Fabian Strauß, **Swathi Sudhakar**, Gero Lutz Hermsdorf, York-Dieter Stierhof and Erik Schäffer. Polycationic gold nanorods as multipurpose in vitro microtubule markers. *Nanoscale Advances*.2, 4003, 2020.

In this publication, I am the third author. V.W and E.S designed the experiments. V.W developed gold nanorod as biomarker for biosensor applications. I established the technique to synthesize gold nanorods in the lab and helped V.W in synthesizing different sized gold nanorods with different aspect ratios. F.S. helped with experiments. G.H. built the TIRF setup. V.W. and E.S. wrote the manuscript.

4. Alexandra Ciorîta, Michael Bugiel, **Swathi Sudhakar**, Erik Schäffer, and Anita Jannasch. Single transport and depolymerizing kinesins stabilize microtubules. *BioRxiv* doi: 10.1101/2020.10.05.326330

As a third author of this publication, I developed the supported lipid bilayer platform and taught A.C to construct this lipid bilayer platform to perform the single molecule Kip3 stepping and gliding assays. I also performed control experiments with kinesin-1 to study the stabilization effect of kinesin-1 on intrinsic microtubule depolymerisation. E.S. and A.J. designed the research; A.C., A.J., and S.S. performed measurements and analyzed the data. M.B. performed simulation studies. M.B., E.S., and A.J. wrote the manuscript together.

5. Akanksha Dohare*, **Swathi Sudhakar*** Björn Brodbeck, Ashutosh Mukherjee, Marc Brecht, Andreas Kandelbauer, Erik Schäffer, and Hermann A. Mayer, Simultaneous Delivery of Curcumin and Quercetin with Anisotropic Mesoporous Core-Shell Silica Microparticles. Submitted in *Scientific Reports*.

In this publication, I am a shared first author. S.S, A.D. and H.A.M. designed the project. Here, I studied the drug loading and drug delivery activity of the core shell dumbbell silica microparticles. I also performed cell viability assays in detecting anticancer activity of the novel dual drug loaded silica microparticles. I had also performed confocal microscopy imaging studies. A.D. and B.B synthesized dumbbell shaped silica microparticles. A.M., and A.K. performed Raman spectroscopic studies. E.S, M.B.,and H.A.M. supervised the project. S.S., A.D. and H.A.M. wrote the manuscript.

-
6. **Swathi Sudhakar**, Mohammad Kazem Abdosamadi, Viktoria Wedler, Pasupathi Rajendran, York-Dieter Stierhof and Erik Schäffer. Germanium nanospheres as high precision optical tweezer probes.

As a first author of this publication, I synthesized and characterized novel high refractive index semiconductor germanium nanospheres. Y.D.S and S.S performed transmission electron microscopic imaging. S.S performed X-ray diffraction, dynamic light scattering studies to characterize the size and shape behaviour of the nanospheres. I have also done force spectroscopic studies with the help of optical tweezers. M.K.A helped in analysing the data. V.W performed XRD data analysis. P.J helped S.S to develop protocol. S.S. and E.S. designed the project and wrote the manuscript. The manuscript was assembled and finalised for submission.

5 Results

This chapter summarizes the results of my PhD work. All results are included in the publications listed in the appendix. For detailed information, please refer to the original manuscript in the appendix as indicated in the text.

5.1 Supported solid lipid bilayers as a platform for kinesin stepping assays

5.1.1 Development of a supported solid lipid bilayer platform

For high contrast fluorescence or high precision force measurements, we need a platform for specific attachment with minimal nonspecific interactions. In single molecule, kinesin stepping assays, microtubules are often immobilized on a silanized surface for TIRF microscopy [37]. As a platform that can sustain loads and has minimal non specific interactions, we used a solid supported lipid bilayer (SSLB) platform was constructed with a lipid mixture of 15:0 phosphatidyl-choline (PC) and 1,2-distearoyl-sn-glycero-3-phosphoethanolamine-N-[carboxy(polyethylene glycol)-2000] (DSPE-COOH) with a molar ratio of 4:1. The vesicle fusion method was used to construct the lipid bilayer on the surface [18, 24, 132, 133]. After solid lipid bilayer formation tubulin antibodies and amino-PEG molecules were covalently coupled to the carboxyl groups of the membrane. Thus, this method allows specific and rigid attachment of microtubules to the solid lipid bilayer surface, if the melting temperature of the lipids is higher than room temperature. Moreover, the lipid bilayer surface also prevented the nonspecific interactions of the kinesin motors with the remaining surface (Fig. 5.1 and Fig. 1 in Appendix 1).

5.1.2 Kinesin stepping assay

The blocking capacity, i.e the amount of nonspecific binding was quantified by measuring the average green fluorescence protein (GFP) intensity in the presence of a high motor concentration of kinesin in small regions of interests. In comparison to controls of a supported *fluid* lipid bilayer and a standard F127 assay[34-37], the SSLB had the least amount of nonspecific interactions. The results confirmed that our PEGylated SSLB platform showed better blocking capacity. The co-localization of the kinesin motors on microtubules confirms the specific interaction.

To test whether the solid lipid bilayer affected the kinesin functionality, we measured the motility parameters of motors under single molecule conditions (Fig. 1 in Appendix 1). The run length and velocity of the kinesin were consistent with literature values [56, 134]. To answer the question whether SSLB can sustain loads, I used the optical tweezers to measure the force-dependent stepping behaviour of kinesin-1. (Fig. 2 in Appendix 1). The truncated GFP-tagged kinesin motors were attached to polystyrene microspheres with PEGs via a GFP nanobody [65, 135]. These microspheres were trapped and calibrated with the help of high-precision optical tweezers [35, 92, 136]. The kinesin bound microspheres were then placed on microtubules. Single kinesin motors walked along the microtubule with the step size of 8 nm and generated a maximum force of about 5.5 pN. This force is consistent with previous studies [64, 65, 80]. These results ensure that the lipid bilayer conserved the functionality of the motors and that the SSLBs can sustain loads. Moreover, there was no nonspecific interactions of microspheres with the PEGylated lipid bilayer platform. Thus, SSLBs act as an excellent platform for motor protein measurements.

5.1.3 Platform for studying single DNA molecules

To check whether the SSLBs can be used as a platform for other biomolecules like DNA and whether it can sustain higher loads, we unzipped and overstretched single DNA molecules tethered between the SSLB and optically trapped microspheres. Here, the lipid bilayer contained biotinylated lipids. Hence the SSLB was covered with Neutravidin to attach one end of DNA. The SSLBs with additional blocking agents reduced the non-specific interactions, more than tenfold. To test specific binding, DNA having a biotin at one end and digoxigenin tag at the other end was tethered between microspheres with a digoxigenin-antibody and the SSLB (Fig. 3.b in Appendix 1). All microspheres showed tethered particle motion indicative for specific attachment of the microsphere to the lipid bilayer via the DNA. Taken together, the SSLBs resulted in highly specific binding of DNA tethered microspheres with non-specific interactions.

Next, we unzipped and overstretched the DNA with a closed hairpin (Fig. 5.1 and Fig. 4 in Appendix 1). The hairpins were completely unzipped and the double stranded DNA was overstretched at about 65 pN [76]. The black dashed line shows a experimental force extension curve fitted well with a worm like chain model, which describes the polymer's semi flexibility. The simulation [137, 138] matched the unzipping pattern. Together, the SSLBs allowed us to manipulate DNA force measurements thus minimizing non-specific interactions, while sustaining high loads up to 70 pN. All together, the SSLBs served very well as a platform for single molecule force measurements.

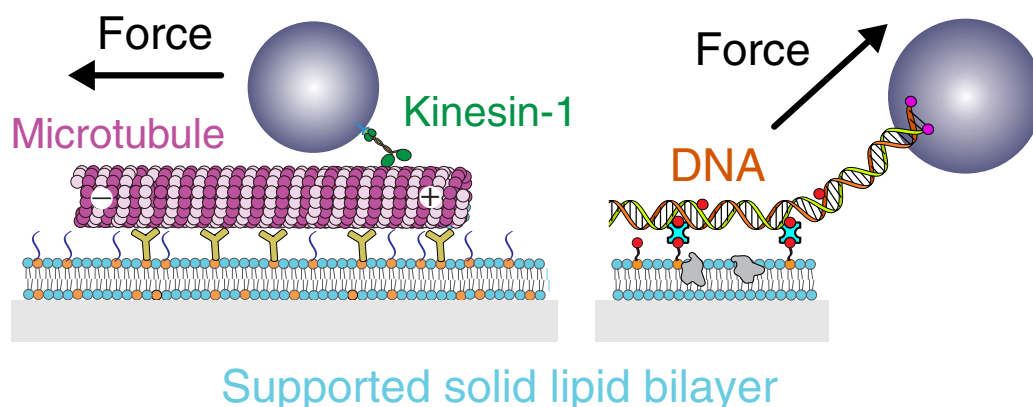


Figure 5.1: Supported solid lipid bilayer for a motor protein and DNA tethered microsphere assay.

5.2 Germanium nano- and microspheres

5.2.1 Size-controlled synthesis of water stable germanium nanospheres

The main goal of my PhD project was to explore the mechanistic substepping behavior of kinesin. To detect the substeps, we need a probe with high spatiotemporal resolution. The high refractive index nanoprobe, with high spatiotemporal resolution will serve as the ideal probe to resolve the motor's stepping mechanism. Semiconductor materials like silicon and germanium have a high refractive index. In my project as a first step, I have synthesized germanium nanospheres (GeNTOPs) using a wet chemical reduction method. GeNTOPs were synthesized similar as reported [139] with important modifications. In this process, germanium oxide (GeO_2) and sodium borohydride are used as a substrate and reducing agent, with quercetin as stabilizing agent. The reaction was carried out at 60°C . The size of the particles increased with an increase in the reaction time (Fig. 5.2 and Fig. 1a in Appendix 6) This is the first reported protocol to perform the synthesis of the water stable spherical GeNTOPs in sufficient amounts.

5.2.2 Characterization of germanium nanospheres using different techniques

As synthesized GeNTOPs were characterized using different techniques like transmission electron microscopy (TEM), dynamic light scattering (DLS) and optical tweezers. TEM measurements showed that the size of the GeNTOPs ranged from 29 nm to 200 nm, when the reaction time was increased from 3 h to 8 h (Fig. 5.2 and Fig. 1b in Appendix 6). To exclude a shrinking effect of particles while drying them for TEM, the results were

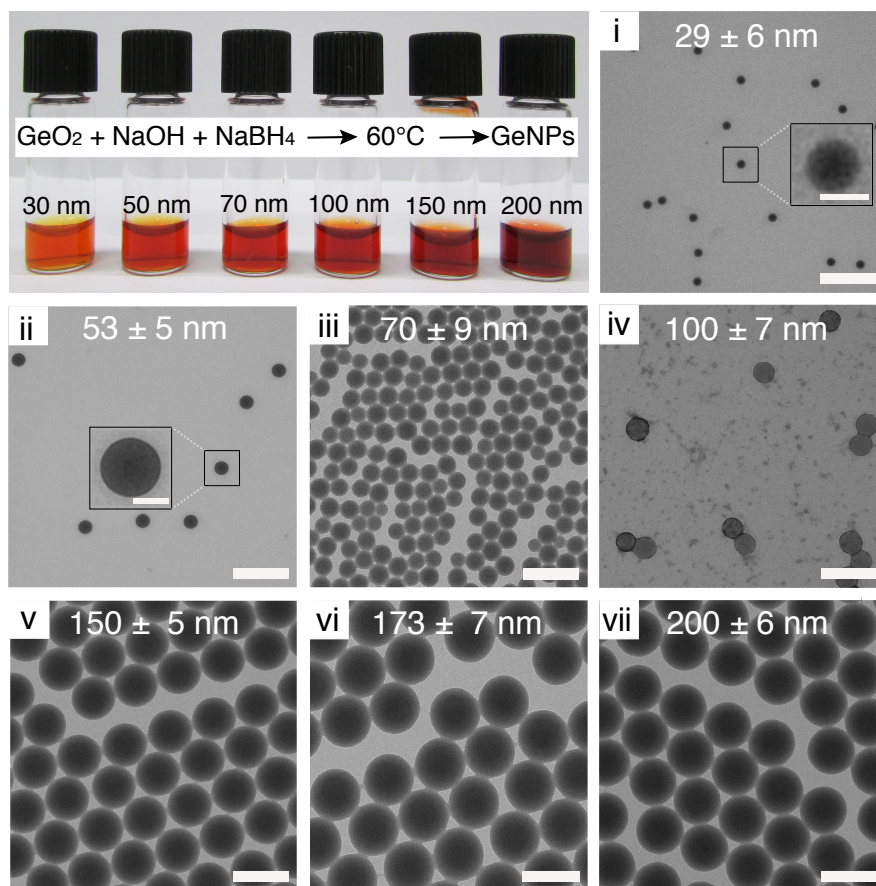


Figure 5.2: Water stable germanium nanospheres synthesized with different time intervals in solution and their TEM images correspond to 3-8 h reaction times with 1 h increments, respectively.

compared with size results from DLS and OT (Fig. 1c in Appendix 6). The size results from different techniques were consistent with each other. Next, to gain more information about the crystallinity of the particles, X-ray diffraction (XRD) studies were carried out.

5.2.3 X-ray diffraction shows cubic phase of germanium nanospheres

The lyophilized GeNTOPs of size 30 nm were used to characterize the crystalline nature of the nanoparticles. The XRD pattern for the GeNTOPs was compared with the reference pattern for a pure germanium crystal as reported before [140]. Germanium has a cubic crystal structure. Our lattice constant was in very good agreement with the

standard value of 5.6512 \AA (JCPDS card No. 03-065-0333) [141]. The calculated domain size also confirms the single cubic crystal phase of GeNTOPs (See Fig. 2 in Appendix 6).

5.2.4 Germanium nanospheres enable ultraprecise spatiotemporal measurements

Particles with a high refractive index enable a high trap stiffness. A Mie theory calculation was carried out to find the trap stiffness of different sized germanium nano spheres by using optical tweezers computational toolbox [90]. The lateral (axial) trap stiffness for the germanium nanospheres was experimentally measured at a laser power of 0.1 W in the trap and found to have a 6-fold and 10-fold high trap stiffness than polystyrene and silica nanospheres of the same size (Fig. 5.3 and Fig. 3 in Appendix 6). The experimental measurements agree well with the calculations showing that GeNTOPs have a high trapping efficiency.

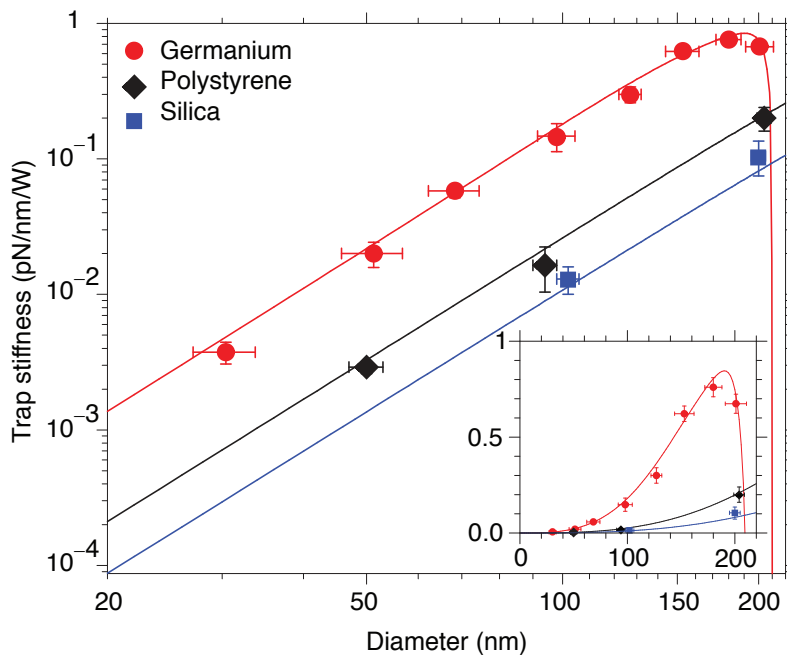


Figure 5.3: Trap stiffness plotted for germanium (red circle), polystyrene (black diamond) and silica (blue square) nanospheres on a log-log plot (Inset: lin-lin plot) with Mie theory calculations (black, red and blue lines).

Next, I measured the trap stiffness and the roll off frequency (f_c) of GeNTOPs at the laser power of 1 W , to check whether the particles produce heat and whether the

heat influences the trap stiffness. At maximum laser power (1 W), the power spectral density was recorded (Fig. 4 in Appendix 6). The analysis of the particle motion revealed an extremely high roll off frequency of $f_c = 68$ kHz with a trap stiffness of about 0.76 pN/nm/W. To measure the temporal resolution, the response time was calculated from the roll off frequency [35, 92]. The temporal resolution was around 2.8 μ s. These findings confirm that one could perform high spatiotemporal resolution measurements.

The other question is whether the GeNTOPs generate heat at high laser intensity. Heat generated by the probe can easily denature the biological sample. The temperature of the GeNTOPs was measured at different laser intensity as mentioned before [142]. The temperature of the particle increased from 29 °C, the sample temperature, to 42 °C when the laser intensity increased from 0.1 to 1 W which is, comparable with the behavior observed for polystyrene microspheres. Thus, there was no significant extra heating. As expected, a linear increase in the trap stiffness with laser power was also observed.

To resolve how kinesin steps and detaches, 72 nm sized GeNTOPs were used to enhance the spatiotemporal precision of optical tweezers by compensating the particle-volume-scaling of trapping forces in the Rayleigh regime. The smaller the size of the bead the greater the spatiotemporal precision. To determine whether the spatiotemporal trapping precision of GeNTOPs was improved compared to conventional microspheres, the GeNTOPs were optically trapped in a custom built ultrastable optical tweezers setup [136] (Fig. S1 in Appendix 6). The calibration [35, 92] results confirmed that we achieved the trap stiffness κ , required for kinesin picotensiometry [1, 2, 64, 70, 143]. I have observed that, the spatial precision was improved a lot with a trap response time of around 10 μ s (Fig. S2 in Appendix 2). The spatiotemporal resolution can be increased further by using smaller germanium nanospheres or a higher trap stiffness. Instead of smaller nanospheres, the response time can also be improved by a very high trap stiffness of photonically engineered germanium microspheres.

5.2.5 Antireflective germanium microparticles for high force measurements

Note that these are unpublished results not provided in the appendix.

Mie theory predicts nanonewton optical forces for antireflection coated germanium microspheres

To design an optimal antireflection coating of germanium microspheres with germanium oxide, T-matrix and Mie theory calculations were used[90] (Fig. 5.4). The core and shell size were optimized to achieve the highest trap stiffness for a laser wavelength of $\lambda = 1064$ nm. For the germanium oxide as a shell material with a refractive index $n_{coat} = 1.78$, the trap stiffness as a function of core and core-shell diameter is shown in Fig. 5.4. To achieve the high trap stiffness, a core size of $d_{coat} = 800$ nm with a coating thickness of $d_{coat} = 100$ -200 nm (light pink region in Fig. 5.4) need to be synthesized. Particles

with a smaller or larger shell than the optimal one cannot be trapped according to the calculation (white regions in Fig. 5.4).

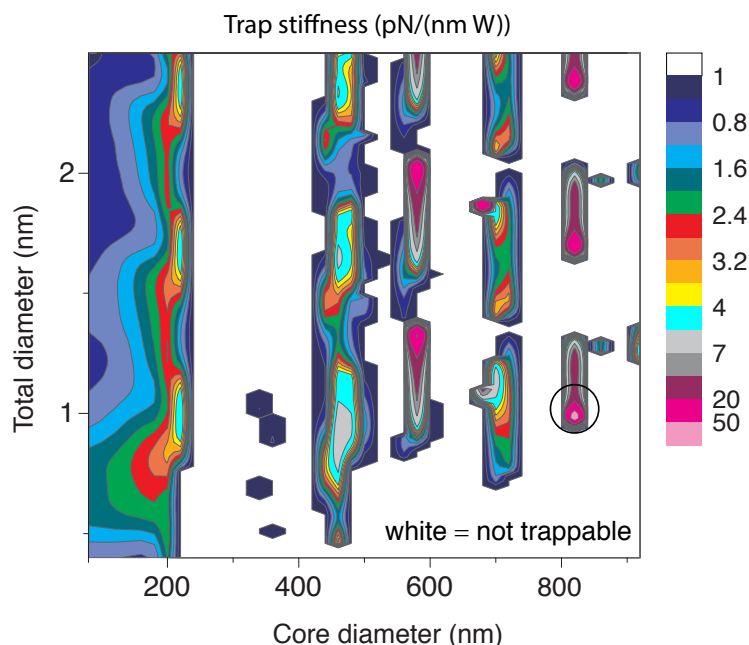


Figure 5.4: Mie theory predictions of lateral trap stiffness per power in the focus as a function of the core diameter and total core-shell diameter. White areas correspond to particles that cannot be trapped anymore. The circle marks the highest possible trap stiffness.

Synthesis and characterization of germanium core shell microspheres

To hit the maximum trap stiffness as described by theory, the germanium microparticles of different sizes were synthesized [119]. GeO_2 and PVP were dissolved in 0.5 M NaOH (Solution I) and the NaBH_4 was dissolved in chilled water (Solution II). When the synthesis was started by mixing solutions I and II, a colour change was observed. The former clear solutions first turned yellow and continued to become opaque brown. Depending on the reaction time, the solution turned further from a light brown tone to dark brown. Fig. 5.5 shows exemplary SEM images of the synthesized germanium microspheres at different reaction times. The synthesized microspheres are monodisperse and had a very smooth, spherical shape with a mean size with standard deviation of 504 ± 77 ($N = 102$), 740 ± 35 ($N = 202$) and 1085 ± 202 nm ($N = 105$) after 30, 60 and 90 min. Then, the 1085 nm diameter particles were oxidized by placing the sample in a thermal furnace at 550°C for about 8 h. After oxidation of the particles a core size of around 912 ± 15 nm and shell size of about 221 ± 11 nm observed. The particle size

increased about 50 nm during oxidation. TEM image of the germanium core shell particles is shown in Fig. 5.5. The crystalline core germanium with a germanium oxide shell layer can be visualized clearly. The core and shell diameter, yet, needs to be optimized to achieve the high trap stiffness. Nevertheless, one can synthesize germanium core shell particles to achieve a high trap stiffness and to utilize these particles for high force or high response time experiments.

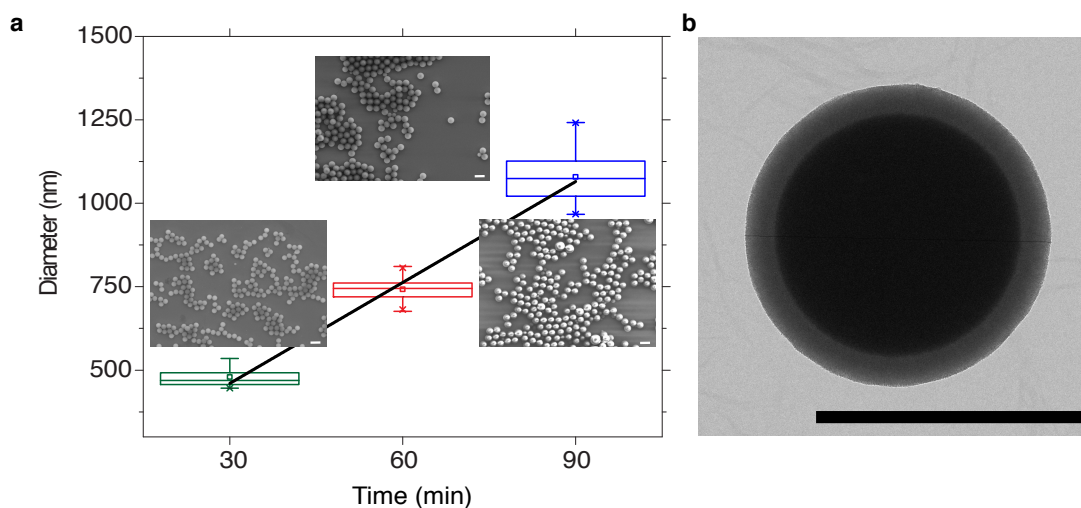


Figure 5.5: a) Germanium microspheres synthesized at different time intervals. The box plot denotes the diameter of the germanium microspheres at 30, 60 and 90 min. Insets: a) SEM images of the germanium microspheres b) TEM images of the germanium core shell microspheres after 8 h of oxidation. Scale bar: 1 μm .

5.3 Kinesin stepping

5.3.1 Membrane-coated germanium nanospheres for kinesin transport

To attach the kinesin to GeNTOPs, they were functionalized with a carboxylated lipid bilayer. This system mimics *in vivo* vesicles thus minimizing the nonspecific interactions. The lipid bilayer was PEGylated and functionalized with nanobodies which in turn bind to green-fluorescent-protein-(GFP)-tagged kinesin motors (Fig. 5.5 and Fig. S3 in Appendix 2). Due to the functionalization of the lipid bilayer, the diameter of the GeNTOPs increased to 93 ± 4 nm. This diameter corresponds to the average size of neuronal transport vesicles [144]. Thus, the assay geometry resembles native conditions inside cells. Single molecule conditions were achieved by manipulating the kinesin

motor-to-germanium nanosphere ratio. The speed and run length were quantified by interference reflection microscopy [145] and the results were in agreement with previous reports [65].

5.3.2 Kinesin takes 4-nm steps

GeNTOPs attached to single kinesins at physiological ATP concentrations were placed on microtubules, and their movement was recorded from the trap center (Fig. 1 in Appendix 2) using optical tweezers. In the kinesin stepping trace, with increasing hindering loads up to ≈ 5 pN, the motors were slowed down (Fig. 1 and Fig. S4 in Appendix 2). A step finding algorithm was used to determine step sizes and dwell times. Interestingly, instead of 8 nm steps, kinesin walked with 4 nm substeps that can support load [143]. (Table. S1, Fig. 1 and Fig. S5 in Appendix 2). For the higher forces, two dwell times were observed with a long (τ_1) and short dwell time (τ_2). I also found that τ_1 depended on force while τ_2 , hardly depended on force. Kinesin stepping traces recorded with low ATP concentrations (Fig. 5.6 and Fig. 2 in Appendix 2) confirmed that the first dwell time τ_1 increased and depends on both force and ATP while τ_2 hardly differed from the high-ATP values (Table. S2 in Appendix 2). Thus, I can conclude that kinesin motors walk with alternating 4 nm force and ATP-dependent steps.

5.3.3 Kinesin detachment and rescue

The next question that I addressed was how and from which substep do motors detach? From my result, I noted in about 50 % of the motility events, the last step was a short substep. When a motor detaches from the microtubule, we expected a relaxation time similar to the trap response time. But the time constant which we acquired was much larger than the trap response time. This discrepancy shows that kinesin still interacted with the microtubule and did not detach from it (Fig. 3a in Appendix 3).

As a control experiment, we pulled the kinesin sideways perpendicular to the axis of the microtubules. In this case, the kinesin did not interacted with the microtubule and as expected the relaxation time was consistent with the expected trap relaxation time and true motor detachment (Fig. S6 in Appendix 2). I used an unbiased change-point detection algorithm [146] to reveal 8-nm slip steps occurring on a microsecond time scale during this slipping motion (Fig. 5.6, Fig.S7 and S8 in Appendix 3)

Thus, I summarize, motors switched to a weakly bound slip state and interacted with the microtubule lattice while slipping back. The other question was, does kinesin truly detach from microtubules after a slip event or do motors switch back to a motility-competent state. To decode this mystery, the time between subsequent motility events was calculated and called restarting time (Fig. 3 in Appendix 2).

I found that restarting time distribution consisted of a sum of two exponentials with a time constant of 112 ± 1 ms and 4.1 ± 0.4 s, respectively. The short restarting time constant is in agreement with the one of a predicted weakly bound state prior to detachment [147]. Surprisingly, in $82 \pm 1\%$ of our events the motors did not detach and the motility was rescued after a slip event.

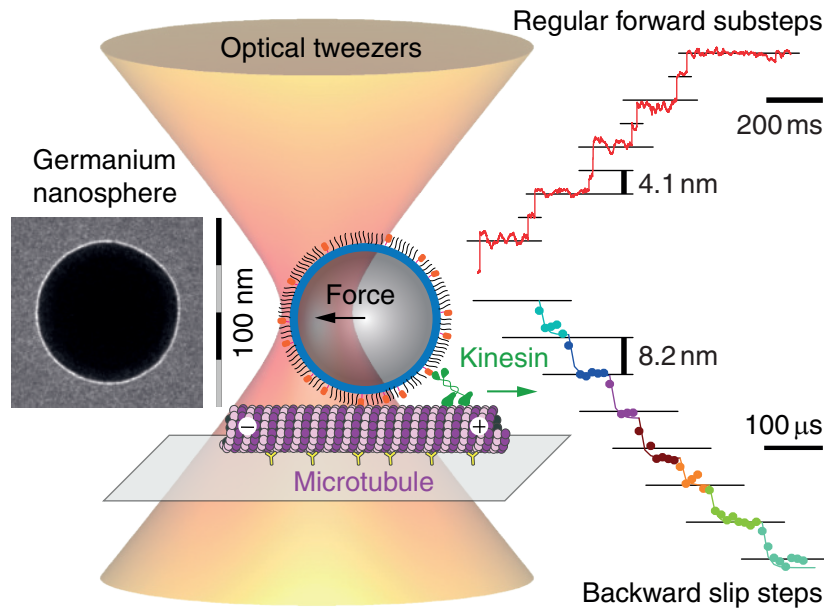


Figure 5.6: Ultraresolution kinesin traces with optically trapped germanium nanospheres. Membrane-coated germanium nanospheres (TEM micrograph, left; membrane resulted in a white contrast) allowed the measurement of substeps during the normal kinesin stepping cycle. Under load, kinesins did not detach but slipped backward along the microtubule in very fast 8 nm steps, which led to the discovery of rescues for vesicle transport.

6 Discussion

In this thesis, I have developed methods to resolve how kinesin steps and detaches with unprecedented spatiotemporal resolution. To perform all these single molecule assays, I have developed a solid supported lipid bilayer platform, to prevent the nonspecific interaction of the protein of interest to the surface. I have synthesized, high refractive germanium nanoprobe and showed that they have a 5-10 fold higher trap stiffness compared to conventional probe of similar size. I have shown that the molecular motor kinesin-1 takes alternative force dependent 4 nm substeps instead of 8 nm steps by using GeNTOPs. In addition to that, I have revealed that kinesin interacts with microtubules while motors are slipping back to the trap center with 8 nm fast slip steps. Only 20% of events showed true detachment after a step event while in 80% of the cases motor's motility was rescued. For kinesins, the slip and rescue state allows motors to slip back to their team during transport with direct reengagement in motility.

6.1 Supported solid lipid bilayers as an excellent platform for single molecule fluorescence and force measurements

I developed a supported solid lipid bilayer (SSLB) as an alternative platform to perform single-molecule fluorescence force measurements. Even though supported fluid lipid bilayers had been used previously for performing kinesin motility assays [26, 148, 149], we found that kinesin motors showed *transient* nonspecific binding on a sub-second time scale to such a lipid bilayer surface. Due to this nonspecific transient binding, we PEG-ylated the bilayer. PEGylation of the SSLB with 15:0 PC blocked the non-specific binding effectively. However, the PEGylation of supported fluid lipid bilayer, did not reduce transient binding of kinesin to the surface. One reason for the nonspecific binding apart from the diffusive nature of DOPC lipids could be the change in headgroup area being bigger in the fluid state in comparison to the solid state.

An advantage of the SSLB platform was that it was highly reproducible over a long period of time. The reason why silanized slides that are often used as a platform did not show a high reproducibility may be that the silanized surfaces have a particular shelf life and the stability of the silane depends on the humidity level in the lab environment. Hydrophobicity of the glass surface has to be monitored by the water contact angle, which was often either too low or high. If the hydrophobicity is not right, the adsorption

of antibodies to the surface may not work properly. In case of a low hydrophobic surface, less antibodies are absorbed leading to less specific binding. In other case, if the hydrophobicity is too high, it can easily denature the proteins. The denatured proteins on the surface in turn increase nonspecific binding. This kind of nonspecific binding was observed due to the denaturation of digoxigenin on the preparation of slides for our DNA assay. Negatively charged polyacrylic acid blocked the surface very well. But proteins interacting with the DNA, also may interact with the blocked surface as it is also negatively charged. Therefore, our SSLB is more suitable and better platform for the DNA and DNA binding protein assays compared to platforms based on hydrophobic slides. In addition, the chemicals utilized during the silanization process are more toxic and hazardous to the environment. Furthermore, the time necessary for blocking the silanized surfaces was longer by 60 min compared to the preparation of SSLB slides. Thus, we can say that the SSLB is efficient, less time consuming and more reliable platform for performing single molecule fluorescence and spectroscopy assays.

We can also switch the fluidity of the membrane from solid to fluid for doing single-molecule fluorescence and force measurements in analogue to cellular assays [23]. We could use a heating laser to heat a particular area [150] to melt the bilayer and manipulate the anchoring points with the help of the optical tweezers. If the desired pattern is attained it can be frozen by switching off the heating laser, thus again converting the fluid lipids back to the solid state. In combination with the excellent blocking performance, we expect that in the long term, our optimized SSLB will have many applications for single-molecule fluorescence and force measurements.

6.2 Germanium nano- and microspheres for optical tweezers measurement

6.2.1 Germanium nanosphere synthesis and functionalization

In general, I demonstrated the synthesis of GeNTOPs in the size range from 30 to 200 nm. Even though there are several reports on synthesizing germanium nanoparticles, they require toxic precursors or result in organic bi-products [116, 119] and most of the processes involve high temperatures [151, 152]. In solution-phase synthetic chemistry methods, there is a problem in achieving good crystallinity of the particles [114, 123, 126, 153]. Other problems associated with the wet chemical reduction method was the polydispersity of the nanoparticles, their tendency to form larger aggregates and that the particles were not spherical [125, 139, 154]. In my protocol, I produced GeNTOPs which are stable and monodisperse. The nanosphere stability was improved by functionalizing the nanospheres with a lipid bilayer as described previously [155]. Phospholipids are considered to be one of the best stabilizing agents. As the cell membrane is composed of various types of phospholipids and proteins, functionalization with such biomolecules will be a desirable route to improve the blood circulating time of nanoparticles and biocompatibility.

ity for *in vivo* applications. Moreover, the lipid stabilized germanium nanoparticles can be effectively conjugated with biomolecules of interest, drugs or antibodies for specific targeting.

After functionalization with lipids, the nanospheres tend to be in a dispersed form for several months. I have performed a quantitative analysis on the size of the nanospheres synthesized at different time intervals, measured the optical spring constants. We showed that GeNTOPs had a similar trapping efficiency than metallic nanospheres reported previously. Even though, the metallic nanospheres have a high trapping efficiency they have the disadvantage of quenching fluorescence and heating up. As the absorbance range of the GeNTOPs is far away from the NIR range, the absorption of the infrared trapping laser (1064 nm) was negligible and resulted in less heating of the particles. The GeNTOPs also had a high spatiotemporal resolution. This makes the GeNTOPs an ideal candidate to be used in biological applications such as force measurements in cells or of protein-protein interaction happening in microsecond time scales. In next step, I have coupled kinesin to GeNTOPs.

6.2.2 Antireflection coated germanium microspheres for high force measurements

Even though, the forces acquired with previously generated antireflective coated microspheres [129, 130] are larger than the conventional ones, still they are not enough for studying many mechanical events happening with high forces inside the cell. To attain a high force, I synthesized germanium microspheres.

The microparticle synthesis has been challenging. The particle size and spericity strongly depends on the pH and concentration of the precursors. A wrong concentration of the stabilizer (PVP) may lead to aggregation of the particles, if it is too low, it may stabilize unwanted shape of particles. Thus there are many reasons for the particles not turn to aggregate. One characteristic of nanoparticles is their huge surface in comparison to the volume. So, if there is an excess of surface stabilizing agent, this could lead to an extremely good stabilisation of the small particles and therefore lead to a slower growth of the particles, even after long reaction times.

To obtain the antireflective shell germanium cores were oxidized. After oxidation, the particles were expected to become a little larger due to the lower density of germanium-oxide in comparison to germanium itself. This effect could also not be seen for every reaction and every oxidation time. One reason could be the uneven distribution of heat inside the thermal oven. As expected from the measured particle sizes, all of the particles were trappable with different trap stiffness. Unfortunately, I was not able to match one of the regimes with the very high trap stiffness of 50 pN/(nm. W). Still I found some particles that had a trap stiffness of about 10 pN/(nm. W). This is to my knowledge, the highest trap efficiency measured to date [84] Due to the broad distribution of particle sizes for the same reaction duration and the same oxidation, the trap stiffness had a large

spread. The synthesis of germanium microparticles with different core size is possible by controlling the reaction time. The size of the particles grows linearly with time. This process is reproducible. Based on the theory, the oxidation time need to be optimized to get the correct core and shell size to hit the sweet spot of highest trap stiffness.

This antireflective high trap stiffness probes can be used to reduce radiation damage or to increase the number of particles being trapped while splitting the laser into multiple traps or to achieve very high optical forces [156]. Laser induced heating is another problem while performing high-force measurements [142]. Since germanium with a native oxide layer is used as a bio-compatible material and for destroying cancer cells, the anti-reflection coated germanium microspheres should be a good candidate for various biological applications [124].

I can conclude by noting that it was possible to produce trappable anti-reflective core shell germanium particles of different sizes in spherical forms. The trapping forces were in the expected range. Thus, high trap stiffness particles can be generated and can be used for high force measurement experiments.

6.3 Stepping mechanism of kinesin-1

The stepping mechanism of kinesin was studied with the help of GeNTOPs using optical tweezers. From the kinesin stepping trace, we have found that data was consistent with a model, where the kinesin hydrolysis cycle had split up into two mechanical substeps (Fig. 6.1). With P_i release from the rear and ATP binding to the front head, the rear neck linker is un- and the front one docked favoring the dissociation of ADP from the rear head [157, 158]. The P_i release from the rear head [159] causes neck linker undocking, or the neck linker to be in a flexible state [160]. Binding of ATP to the front head triggers the first half of the necklinker interact with the coverstrand thus forming the cover neck bundle. The second half of the neck linker interacts with the core motor domain for neck linker docking [161]. ATP binding followed by neck linker docking in the front head triggers a conformational change that accelerates the displacement of the trailing head by ≈ 4 nm [71, 162]. In the successive substep, the ATP was hydrolysed [66, 67, 163, 164] followed by P_i release, and un-docking of the neck linker. We think that the second ≈ 4 nm step happened after ATP hydrolysis.

From the literature [64] and our previous data, we speculate that both heads always remain bound to the microtubule lattice in a weakly bound state due to electrostatic interactions. If P_i is released after ATP hydrolysis from the front head before the ADP released from the rear one, both heads enter a weakly bound state branching off from the normal hydrolysis cycle (Fig. 6.1 and Fig. 4 in Appendix 2). Fast backward stepwise slipping motion opposed by hydrodynamic drag and protein friction [36] was observed. The step size while slipping back was around 8 nm which suggests that the heads interact with the canonic kinesin-microtubule binding site. Backward 8-nm steps were rarely observed with some short slip events (Fig. S8 in Appendix 2). The dwell time during

the fast slipping motion can be estimated by a model for protein friction. Based on the model the slip step dwell time was $\approx 70 \mu\text{s}$. This time constant is consistent with the dwell time measured experimentally during the fast backward sliding motion [147]. In the rescue state, ADP is released from one of the heads and ATP can bind to the empty nucleotide site in the front head. In the detachment state, kinesin detaches completely from the microtubules. The cycle and process repeats goes on with alternating rescue (80%) and detachment events (20%) from intermediate steps and states. It is also expected that motors switch to the slip state when there is no load suggesting that overall run lengths of motors are concatenations of processive runs interrupted by short diffusive periods [165, 166]. Thus, with the novel nanoprobe GeNTOPs, we could clarify the stepping mechanism and resolve a long standing controversy whether substeps exists or not.

Our data is also consistent with other kinesin stepping models. There could be two possible styles of how kinesin heads take 4 nm steps. Our favoured model (Fig. 6.1 and Fig. 4 in Appendix 2) suggests that the heads slide parallel to each other during the cycle. An alternative mechanism could be more consistent with Isojima et al.[71]. In this model, the heads do not slide parallel to each other but ATP binding triggers the trailing head to be rotated by 180° , while taking the first 4 nm substep. In the next step, ATP is hydrolyzed and with ADP and P_i release, the trailing head again rotates by 180° while taking the second 4 nm substep. Thus, in this model heads rotate around each other like cogwheels.

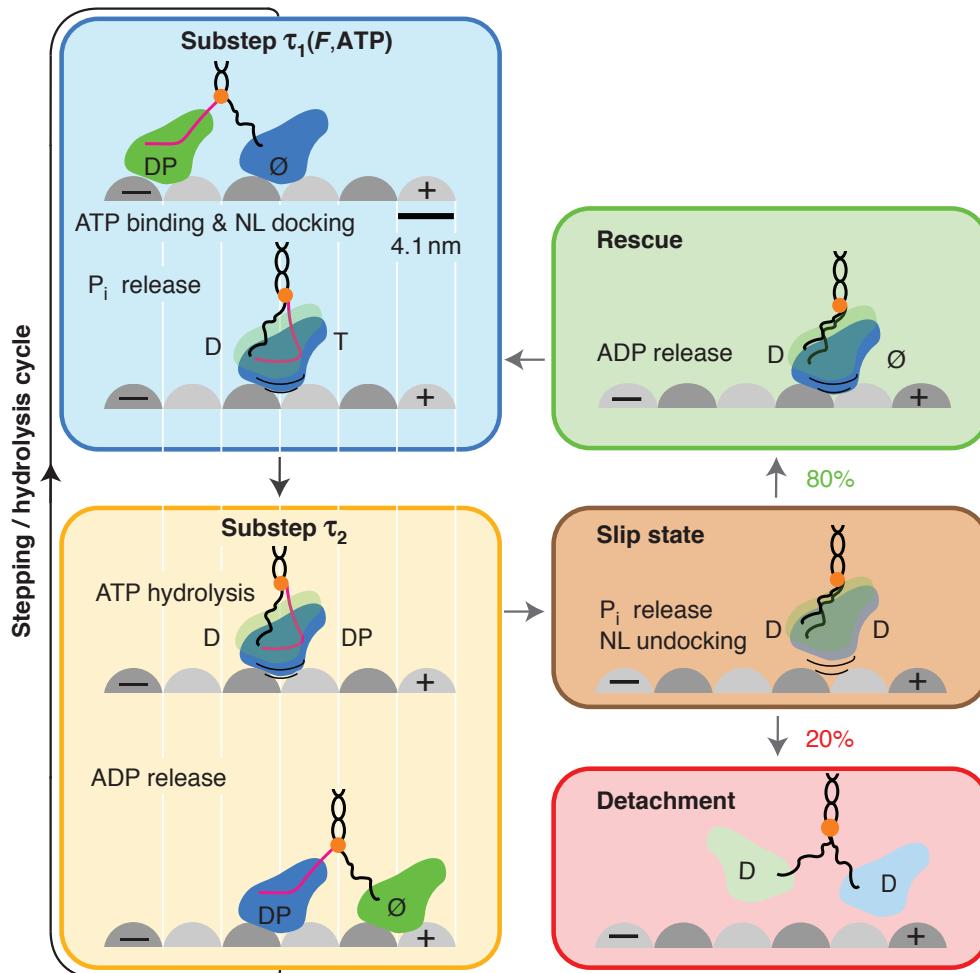


Figure 6.1: Hydrolysis cycle of kinesin-1. Side view of kinesin with two identical heads (blue and green) on a microtubule (grey spheres mark tubulin monomers). The hydrolysis cycle is divided into a force and ATP dependent (blue box) and hardly force and ATP dependent (orange box) substep. The motors may shift to a slip state (brown box) from which motors either detach (red box) or motility is rescued (green box). The centre of mass, a docked neck linker (NL) is indicated by an orange circle and magenta line, and nucleotide states by D: ADP, T: ATP, \emptyset : nucleotide free and P_i: inorganic phosphate.

7 Conclusion and outlook

Breakthroughs in scientific methods are steering the scientific community in a successful direction. The novel discoveries of features and techniques developed in this thesis enhanced the resolution/sensitivity of optical tweezers and single molecule assays. In summary, the performance of optical tweezers can be enhanced with the probe development allowing new experiments in biology and physics. In this chapter, I will provide a brief outlook of my project.

In my project, I have developed a supported lipid bilayer platform for performing single molecule fluorescence assays. They can be widely applied for force spectroscopy, single-molecule fluorescence microscopy and cellular assays in mechanobiology. I have developed novel germanium nanospheres that allow a high spatiotemporal resolution to resolve biological events happening on a microsecond time scale. I have applied these novel nanoprobes to address the long standing question of whether kinesin takes substeps. I have unravelled that kinesin's 8 nm step is broken into two 4 nm substeps resolving a controversy in the field. As a surprise to current models, I have found that kinesins subjected to hindering loads never detach from microtubules directly. Instead, motors slip on microtubules.

I have demonstrated the synthesis of GeNTOPs with a onetime wet chemical reduction method. The one-step synthesis yielded a large amount of nanospheres. The GeNTOPs showed a high trapping efficiency. Moreover, the synthesized GeNTOPs are biocompatible. Carboxylated lipid-bilayer coated nanospheres can be used for coupling any protein or biomolecule of interest.

The spatiotemporal resolution which I have achieved for the fast 8 nm steps on microsecond time scales, is an improvement by a factor of about $4.5\times$ and $20\times$ compared to the benchmark spatial and temporal resolution (Fig. 7.1 and Fig. S9 in Appendix 2) [167]. Thus, GeNTOPs allow us to study molecular motors without having to slow them down.

In addition, I have also developed antireflection coated germanium microspheres to achieve a very high trap efficiency. The correct shell formation of germanium oxide around the core germanium will enable us to reach nanonewton forces. The trap stiffness of antireflection coated germanium microspheres depends strongly on the size of the core and shell. The reproducibility and to get the germanium oxide shell around the core are the main problems, which will be solved in our lab in the near future.

Due to the high infrared refractive index, the germanium nanospheres and microspheres have wide applications in various fields. GeNTOPs being non toxic, could be a great alternative to compound semiconductor nanoparticles [139, 168]. Furthermore,

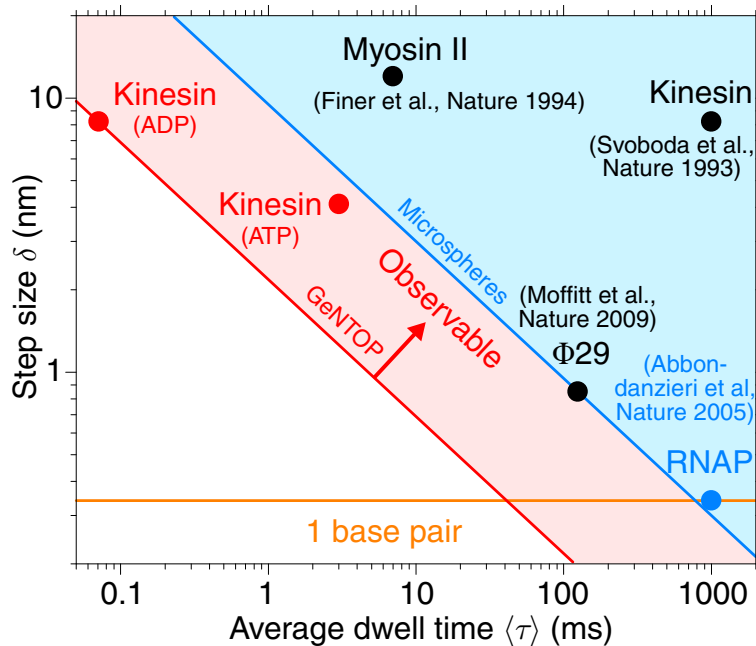


Figure 7.1: **Optical tweezers spatiotemporal resolution of molecular machines.** Red circles: 4-nm directed substeps (0–1 pN data point at 10 μ M ATP of table S2 in Appendix 2), fast 8-nm sliding steps in ADP state (Fig. 3A in Appendix 2).

GeNTOPs are suitable for biosensing and imaging at specific wavelength ranges where biological tissues are transparent [169], and promising for nano optoelectronic and photonics [110, 111]. These nanospheres can also be used to understand the nanoscale ferroelectric and photoswitching behavior, an area of interest for thermoelectric, non-volatile memory, and in solar applications. They are also used as anode materials in the lithium-ion batteries [110] and widely applied in spintronics, thermoelectrics, photocatalysis and photovoltaic applications [110, 111].

For optical tweezers, GeNTOPs can be used to study other molecular machines like myosins, dyneins or molecular motors like the RNA polymerase. This knowledge will broaden our understanding of how molecular machines work in our cells. With the ultra-resolution, GeNTOPs will enable the discovery of so far hidden conformational changes that were either too small or too fast to be detected. An example for a fast process is the measurement of transition states during the force-induced unfolding of proteins or RNA [170]. Transition states encode important information about the folding mechanisms in biomolecules [170]. Measuring transition states experimentally is technically challenging because of limits in spatiotemporal resolution. The problem can be solved by using GeNTOPs. Thus, GeNTOPs can open up new avenue for studying various single molecules and their fast conformational changes, folding and transition states providing insight into how proteins fold.

Abbreviation

β	displacement sensitivity	AFM	atomic force microscopy
Δx	relative displacement	ATP	adenosine triphosphate
δ	step size	BSA	bovine serum albumin
γ	drag coefficient	d_{coat}	thickness of the coating
$\gamma_{protein\,friction}$	drag coefficient during protein friction	d_{core}	core diameter
κ	trap stiffness	DLS	dynamic light scattering
λ	wavelength	DNA	deoxyribonucleic acids
τ	dwel time	f_c	roll off frequency
τ_{\parallel}	parallel relaxation time of nanosphere	$GeCl_4$	Germanium chloride
τ_{trap}	relaxation time of microsphere in a trap	GeNTOP	germanium nanosphere
D	diffusion coefficient	GeO_2	germanium oxide
d	diameter	GFP	green fluorescent protein
d	microsphere diameter	n_{coat}	refractive index of the coating
F_{grad}	gradient force	n_{core}	refractive index of the core
F_{scat}	scattering force	PC	15:0 Phosphatidyl-choline
k_B	Boltzmann constant	PEG	polyethylene-glycol
n	refractive index	Pi	phosphate
T	temperature	PS	polystyrene
t	time	PSD	position sensing device
ADP	adenosine diphosphate	PVP	polyvinylpyrrolidone
		QPD	quadrant photo diode
		SLB	supported lipid bilayer
		SSLB	solid supported lipid bilayer
		TEM	transmission electron microscope
		TIRF	total internal reflection fluorescence microscope

Acknowledgement

I am really thankful to many people who helped in different ways to finish my PhD. First and foremost, I would like to thank my advisor Prof. Dr. Erik Schäffer for giving me the opportunity to work in his lab in a challenging and exciting project. I am very grateful for his guidance, support and encouragement as well as his patience throughout the course of my PhD. I am really thankful for the freedom which motivated me a lot to chase my dream and helped me to think as a scientist. I am really amazed by his exquisite expertise in motor mechanics and data analysis. I would also like to thank him for always having an open door and ample time for discussing experiments, ideas and results with me.

I would also like to thank all lab members Christine Kiefer, Mohammad Kazem Abdosamadi, Maria Kharlamova, Mayank Chugh, Benedikt Fischer, Michael Bugiel, Tobias Jachowski, Anita Jannasch, Steve Simmert, Gero Hermsdorf, Viktoria Wedler, Shu Yao. Because of my lab members, a great working atmosphere was created which made my lab-life more enjoyable. I would like to especially thank Christine Kiefer and Mohammad Kazem Abdosamadi, who supported and encouraged me in all my downfalls and guided me in correct path to achieve my goals.

I would also like to thank my other committee members, Prof. Klaus Harter, Prof. Andreas Schnepf and Prof. Hans Yochim schöpe, for the time and encouragement. I would also like to thank Charly Rehm, a second mom for the international students for her kind and tremendous help. I would like to thank Carolina Carrasco Pulido, Anita Jannasch and Poornima Buddimae Santhosh to critically read and comment on my thesis.

I would also like to thank Thi Thu Trang, Nan Wang, Ezghi, for supporting me professionally and personally. I would like to express my heartfelt gratitude to Prabha Manishankar for being my excellent personal guide. I would like to thank Karthika, Kiran, Sruthi and Ganesh, who helped and supported me to overcome my struggles in my life. I would like to thank Pasupathi and Haemanth for listening to all my sorrows and for sharing unforgettable moments.

I would like to thank my soul mate Sathish Pandiyan and my best friend Sri Vani Uthra Ilangovan. Without their constant love and support, this thesis would not have been possible. Finally, I would like to thank all my family members who believe me and for their continuous support, encouragement, love and freedom.

I gratefully acknowledge the funding and support from “nanoBCP-Lab” funded by the Carl Zeiss Foundation and the PhD Network “Novel Nanoparticles” of the Universität Tübingen.

Bibliography

- [1] Masayoshi Nishiyama, Etsuko Muto, Yuichi Inoue, Toshio Yanagida, and Hideo Higuchi. Substeps within the 8-nm step of the ATPase cycle of single kinesin molecules. *Nat. Cell Biol.*, 3(4):425–428, 2001. ISSN 14657392. doi: 10.1038/35070116.
- [2] Chris M Coppin, Jeffrey T Finer, James A Spudich, and Ronald D Vale. Detection of sub-8-nm movements of kinesin by high-resolution optical-trap microscopy. *Proceedings of the National Academy of Sciences of the United States of America*, 93(5):1913–1917, 1996. ISSN 00278424. doi: 10.1073/pnas.93.5.1913.
- [3] Steven M. Block. Kinesin motor mechanics: Binding, stepping, tracking, gating, and limping. *Biophysical Journal*, 92(9):2986–2995, 2007. ISSN 00063495. doi: 10.1529/biophysj.106.100677.
- [4] Eva Bianconi, Allison Piovesan, Federica Facchin, Alina Beraudi, Raffaella Casadei, Flavia Frabetti, Lorenza Vitale, Maria Chiara Pelleri, Simone Tassani, Francesco Piva, Soledad Perez-Amodio, Pierluigi Strippoli, and Silvia Canaider. An estimation of the number of cells in the human body. *Annals of Human Biology*, 40(6):463–471, 2013. ISSN 03014460. doi: 10.3109/03014460.2013.807878.
- [5] Ignacio Tinoco and Ruben L Gonzalez. Biological mechanisms, one molecule at a time. *Genes and Development*, 25(12):1205–1231, 2011. ISSN 08909369. doi: 10.1101/gad.2050011.
- [6] Jordanka Zlatanova and Kensal van Holde. Single-Molecule Biology: What Is It and How Does It Work? *Molecular Cell*, 24(3):317–329, 2006. ISSN 10972765. doi: 10.1016/j.molcel.2006.10.017.
- [7] T. Ha. Single-molecule fluorescence methods for the study of nucleic acids. *Current Opinion in Structural Biology*, 11(3):287–292, 2001. ISSN 0959440X. doi: 10.1016/S0959-440X(00)00204-9.
- [8] D. Axelrod. Total Internal Reflection Fluorescence Microscopy. *Encyclopedia of Cell Biology*, 2(2):62–69, 2016. doi: 10.1016/B978-0-12-394447-4.20089-8.
- [9] Xavier Michalet, Achillefs N. Kapanidis, Ted Laurence, Fabien Pinaud, Soeren Doose, Malte Pflughoeft, and Shimon Weiss. The power and prospects of fluorescence microscopies and spectroscopies. *Annual Review of Biophysics and*

- Biomolecular Structure*, 32:161–182, 2003. ISSN 10568700. doi: 10.1146/annurev.biophys.32.110601.142525.
- [10] Erwin J.G. G Peterman, Hernando Sosa, and W. E. Moerner. Single-molecule fluorescence spectroscopy and microscopy of biomolecular motors. *Annual Review of Physical Chemistry*, 55(10):79–96, 2004. ISSN 0066426X. doi: 10.1146/annurev.physchem.55.091602.094340.
- [11] Carlos Bustamante, Jed C. Macosko, and Gijs J.L. L Wuite. Grabbing the cat by the tail: manipulating molecules one by one. *Nature Reviews Molecular Cell Biology*, 1(2):130–136, 2000. ISSN 14710072. doi: 10.1038/35040072.
- [12] G. Binnig, C. F. Quate, and Ch Gerber. Atomic force microscope. *Physical Review Letters*, 56(9):930–933, 1986. ISSN 00319007. doi: 10.1103/PhysRevLett.56.930.
- [13] Charles L. Asbury, Adrian N. Fehr, and Steven M. Block. Kinesin Moves by an Asymmetric Hand-Over-Hand Mechanism. *Science*, 302(5653):2130–2134, 2003. ISSN 00368075. doi: 10.1126/science.1092985.
- [14] A. Ashkin. Optical trapping and manipulation of small neutral particles using lasers. *Optics InfoBase Conference Papers*, 94(May):4853–4860, 2010. ISSN 21622701. doi: 10.1364/fio.2010.stu1.
- [15] T. R. Strick, J. F. Allemand, D. Bensimon, and V. Croquette. Behavior of supercoiled DNA. *Biophysical Journal*, 74(4):2016–2028, 1998. ISSN 00063495. doi: 10.1016/S0006-3495(98)77908-1.
- [16] Andrey Revyakin, Richard H. Ebright, and Terence R. Strick. Single-molecule DNA nanomanipulation: Improved resolution through use of shorter DNA fragments. *Nature Methods*, 2(2):127–138, 2005. ISSN 15487091. doi: 10.1038/nmeth0205-127.
- [17] E. Sackmann. Supported membranes: Scientific and practical applications. *Science*, 271(5245):43–48, 1996. ISSN 00368075. doi: 10.1126/science.271.5245.43.
- [18] Edward T Castellana and Paul S Cremer. Solid supported lipid bilayers : From biophysical studies to sensor design. *Surf Sci Rep.*, 61:429–444, 2006. doi: 10.1016/j.surfrep.2006.06.001.
- [19] Jay T Groves and Michael L Dustin. Supported planar bilayers in studies on immune cell adhesion and communication. *Journal of Immunological Methods*, 278(2003):19–32, 2003. doi: 10.1016/S0022-1759(03)00193-5.
- [20] Annette Granéli, Caitlyn C. Yeykal, Tekkatta Krishnamurthy Prasad, and Eric C. Greene. Organized arrays of individual DNA molecules tethered to supported lipid bilayers. *Langmuir*, 22(1):292–299, 2006. ISSN 07437463. doi: 10.1021/la051944a.

-
- [21] Mari Liis Visnapuu, Daniel Duzdevich, and Eric C. Greene. The importance of surfaces in single-molecule bioscience. *Molecular BioSystems*, 4(5):394–403, 2008. ISSN 17422051. doi: 10.1039/b800444g.
- [22] Serapion Pырpassopoulos, Henry Shuman, and Michael Ostap. Single-Molecule Adhesion Forces and Attachment Lifetimes of Myosin-I Phosphoinositide Interactions. *Biophys J.*, 99(12):3916–3922, 2010. ISSN 0006-3495. doi: 10.1016/j.bpj.2010.10.043.
- [23] Mirjam Andreasson-Ochsner, Gregory Romano, Maria Håkanson, Michael L. Smith, Deborah E. Leckband, Marcus Textor, and Erik Reimhult. Single cell 3-D platform to study ligand mobility in cell-cell contact. *Lab on a Chip*, 11(17):2876–2883, 2011. ISSN 14730189. doi: 10.1039/c1lc20067d.
- [24] Simon J Attwood, Youngjik Choi, and Zoya Leonenko. Preparation of DOPC and DPPC supported planar lipid bilayers for atomic force microscopy and atomic force spectroscopy. *International Journal of Molecular Sciences*, 14(2):3514–3539, 2013. ISSN 16616596. doi: 10.3390/ijms14023514.
- [25] Krishna K Sarangapani, Eris Duro, Yi Deng, Flavia de Lima Alves, Qiaozhen Ye, Kwaku N. Opoku, Steven Ceto, Adèle L. Marston, and Charles L. Asbury. Sister kinetochores are mechanically fused during meiosis I in yeast. *Science*, 346(6206):248–251, 2014. ISSN 15378276. doi: 10.1126/CIRCULATIONAHA.110.956839.
- [26] Rahul Grover, Janine Fischer, Friedrich W. Schwarz, Wilhelm J. Walter, Petra Schwille, and Stefan Diez. Transport efficiency of membrane-anchored kinesin-1 motors depends on motor density and diffusivity. *Proceedings of the National Academy of Sciences of the United States of America*, 1(46):7185–7193, 2016. ISSN 10916490. doi: 10.1073/pnas.1611398113.
- [27] Roxanne Glazier and Khalid Salaita. Supported lipid bilayer platforms to probe cell mechanobiology. *Biochimica et Biophysica Acta - Biomembranes*, 1859(9):1465–1482, 2017. ISSN 18792642. doi: 10.1016/j.bbamem.2017.05.005. URL <http://dx.doi.org/10.1016/j.bbamem.2017.05.005>.
- [28] Lu Ma, Yiyang Cai, Yanghui Li, Junyi Jiao, and Zhenyong Wu. Single-molecule force spectroscopy of protein-membrane interactions. *elife*, 6(11):1–21, 2017.
- [29] Colin D. Heyes, Jürgen Groll, Martin Möller, and G. Ulrich Nienhaus. Synthesis, patterning and applications of star-shaped poly(ethylene glycol) biofunctionalized surfaces. *Molecular BioSystems*, 3(6):419–430, 2007. ISSN 17422051. doi: 10.1039/b700055n.
- [30] Boyang Hua, Kyu Young Han, Ruobo Zhou, Hajin Kim, Xinghua Shi, Sanjaya C Abeysirigunawardena, Ankur Jain, Digvijay Singh, Vasudha Aggarwal, Sarah A

- Woodson, and Taekjip Ha. An improved surface passivation method for single-molecule studies. *Nat. Methods*, 11(12):1233–1236, 2014. ISSN 1548-7105. doi: 10.1038/nmeth.3143.
- [31] Yang Liu, Rebecca Medda, Zheng Liu, Kornelia Galior, Kevin Yehl, Joachim P. Spatz, Elisabetta Ada Cavalcanti-Adam, and Khalid Salaita. Nanoparticle tension probes patterned at the nanoscale: Impact of integrin clustering on force transmission. *Nano Letters*, 14(10):5539–5546, 2014. ISSN 15306992. doi: 10.1021/nl501912g.
- [32] Haogang Cai and Shalom Wind. Improved glass surface passivation for single molecule nanoarrays. *Langmuir*, 176(5):139–148, 2016. doi: 10.1016/j.physbeh.2017.03.040.
- [33] Yang Liu, Lori Blanchfield, Victor Pui-Yan Ma, Rakieb Andargachew, Kornelia Galior, Zheng Liu, Brian Evavold, and Khalid Salaita. DNA-based nanoparticle tension sensors reveal that T-cell receptors transmit defined pN forces to their antigens for enhanced fidelity. *Proceedings of the National Academy of Sciences of the United States of America*, 113(20):5610–5615, 2016. ISSN 10916490. doi: 10.1073/pnas.1600163113.
- [34] Jonne Helenius, Gary Brouhard, Yannis Kalaidzidis, Stefan Diez, and Jonathon Howard. The depolymerizing kinesin MCAK uses lattice diffusion to rapidly target microtubule ends. *Nature*, 441(1):115–119, 2006. ISSN 14764687. doi: 10.1038/nature04736.
- [35] Erik Schäffer, Simon F. Nørrelykke, and Jonathon Howard. Surface forces and drag coefficients of microspheres near a plane surface measured with optical tweezers. *Langmuir*, 23(7):3654–3665, 2007. ISSN 07437463. doi: 10.1021/la0622368.
- [36] V Bormuth, V Varga, J Howard, and E Schäffer. Protein friction limits diffusive and directed movements of kinesin motors on microtubules. *Science*, 325(1):870–874, 2009.
- [37] Christopher Gell, Volker Bormuth, Gary J. Brouhard, Daniel N. Cohen, Stefan Diez, Claire T. Friel, Jonne Helenius, Bert Nitzsche, Heike Petzold, Jan Ribbe, Erik Schäffer, Jeffrey H. Stear, Anastasiya Trushko, Vladimir Varga, Per O. Widlund, Marija Zanic, and Jonathon Howard. *Microtubule dynamics reconstituted in vitro and imaged by single-molecule fluorescence microscopy*, volume 95. Elsevier, first edit edition, 2010. ISBN 9780123748157. doi: 10.1016/S0091-679X(10)95013-9.
- [38] Karin Glasmästar, Charlotte Larsson, Fredrik Höök, and Bengt Kasemo. Protein adsorption on supported phospholipid bilayers. *Journal of Colloid and Interface Science*, 246(1):40–47, 2002. ISSN 00219797. doi: 10.1006/jcis.2001.8060.

-
- [39] Christina G. Siontorou, Georgia Paraskevi Nikoleli, Dimitrios P. Nikolelis, and Stefanos K. Karapetis. Artificial lipid membranes: Past, present, and future. *Membranes*, 7(3):1–24, 2017. ISSN 20770375. doi: 10.3390/membranes7030038.
- [40] Tania Kjellerup Lind, Marité Cárdenas, and Hanna Pauliina Wacklin. Formation of supported lipid bilayers by vesicle fusion: Effect of deposition temperature. *Langmuir*, 30(25):7259–7263, 2014. ISSN 15205827. doi: 10.1021/la500897x.
- [41] Vladimir P. Zhdanov. Ligand-receptor-mediated attachment of lipid vesicles to a supported lipid bilayer. *European Biophysics Journal*, 49(5):395–400, 2020. ISSN 14321017. doi: 10.1007/s00249-020-01441-0.
- [42] Philipp Kukura, Helge Ewers, Christian Müller, Alois Renn, Ari Helenius, and Vahid Sandoghdar. High-speed nanoscopic tracking of the position and orientation of a single virus. *Nature Methods*, 6(12):923–927, 2009. ISSN 15487091. doi: 10.1038/nmeth.1395.
- [43] Chiaki Yoshina-Ishii, Gregory P. Miller, Mary L. Kraft, Eric T. Kool, and Steven G. Boxer. General method for modification of liposomes for encoded assembly on supported bilayers. *Journal of the American Chemical Society*, 127(5):1356–1357, 2005. ISSN 00027863. doi: 10.1021/ja043299k.
- [44] Swathi Sudhakar, Tobias Jo, Michael Kittelberger, Ammara Maqbool, Gero Lutz Hermsdorf, Mohammad Kazem Abdosamadi, and Erik Schäffer. Supported Solid Lipid Bilayers as a Platform for Single-Molecule Force Measurements. *Nano Letters*, 19(12):8877–8886, 2019. ISSN 15306992. doi: 10.1021/acs.nanolett.9b03761.
- [45] Daniel a Fletcher and R Dyche Mullins. Cell mechanisms and cytoskeleton. *Nature*, 463(7280):485–492, 2010. doi: 10.1038/nature08908.Cell.
- [46] Harald Herrmann, Harald Bär, Laurent Kreplak, Sergei V. Strelkov, and Ueli Aebi. Intermediate filaments: From cell architecture to nanomechanics. *Nature Reviews Molecular Cell Biology*, 8(7):562–573, 2007. ISSN 14710072. doi: 10.1038/nrm2197.
- [47] Bill Wickstead and Keith Gull. The evolution of the cytoskeleton. *Journal of Cell Biology*, 194(4):513–525, 2011. ISSN 00219525. doi: 10.1083/jcb.201102065.
- [48] M. C. Ledbetter and K. R. Porter. A "microtubule" in plant cell fine structure. *Journal of Cell Biology*, 19(1):239–250, 1963. ISSN 15408140. doi: 10.1083/jcb.19.1.239.
- [49] Richard C. Weisenberg, William J. Deery, and Peter J. Dickinson. Tubulin-Nucleotide Interactions during the Polymerization and Depolymerization of Microtubules. *Biochemistry*, 15(19):4248–4254, 1976. ISSN 15204995. doi: 10.1021/bi00664a018.

- [50] Jonathon Howard and Anthony A. Hyman. Microtubule polymerases and depolymerases. *Current Opinion in Cell Biology*, 19(1):31–35, 2007. ISSN 09550674. doi: 10.1016/j.ceb.2006.12.009.
- [51] Tim Mitchison and Marc Kirschner. Dynamic instability of microtubule growth. *Nature*, 312(5991):237–242, 1984. ISSN 00280836. doi: 10.1038/312237a0.
- [52] P. T. Tran, R. A. Walker, and E. D. Salmon. A metastable intermediate state of microtubule dynamic instability that differs significantly between plus and minus ends. *Journal of Cell Biology*, 138(1):105–117, 1997. ISSN 00219525. doi: 10.1083/jcb.138.1.105.
- [53] Anna Akhmanova and Michel O. Steinmetz. Control of microtubule organization and dynamics: Two ends in the limelight. *Nature Reviews Molecular Cell Biology*, 16(12):711–726, 2015. ISSN 14710080. doi: 10.1038/nrm4084.
- [54] Arne Gennerich and Ronald D. Vale. Walking the walk: how kinesin and dynein coordinate their steps. *Current Opinion in Cell Biology*, 21(1):59–67, 2009. ISSN 09550674. doi: 10.1016/j.ceb.2008.12.002.
- [55] Arne Gennerich, Andrew P. Carter, Samara L. Reck-Peterson, and Ronald D. Vale. Force-Induced Bidirectional Stepping of Cytoplasmic Dynein. *Cell*, 131(5):952–965, 2007. ISSN 00928674. doi: 10.1016/j.cell.2007.10.016.
- [56] Steven M. Block, Lawrence S.B. Goldstein, and Bruce J. Schnapp. Bead movement by single kinesin molecules studied with optical tweezers. *Nature*, 348(6299):348–352, 1990. ISSN 00280836. doi: 10.1038/348348a0.
- [57] Nobutaka Hirokawa and Reiko Takemura. Molecular motors and mechanisms of directional transport in neurons. *Nature Reviews Neuroscience*, 6(3):201–214, 2005. ISSN 1471003X. doi: 10.1038/nrn1624.
- [58] Yusuke Kato, Takuya Miyakawa, and Masaru Tanokura. Overview of the mechanism of cytoskeletal motors based on structure. *Biophysical Reviews*, 10(2):571–581, 2018. ISSN 18672469. doi: 10.1007/s12551-017-0368-1.
- [59] Nobutaka Hirokawa, Yasuko Noda, Yosuke Tanaka, and Shinsuke Niwa. Kinesin superfamily motor proteins and intracellular transport, 2009. ISSN 14710072.
- [60] H Aizawa, Y Sekine, R Takemura, Z Zhang, M Nangaku, and N Hirokawa. Kinesin family in murine central nervous system. *Journal of Cell Biology*, 119(5):1287–1296, 1992. ISSN 00219525. doi: 10.1083/jcb.119.5.1287.
- [61] H. Miki, M. Setou, K. Kaneshiro, and N. Hirokawa. All kinesin superfamily protein, KIF, genes in mouse and human. *Proceedings of the National Academy of Sciences*

- of the United States of America*, 98(13):7004–7011, 2001. ISSN 00278424. doi: 10.1073/pnas.111145398.
- [62] Carolyn J Lawrence, R Kelly Dawe, Karen R Christie, Don W Cleveland, Scott C Dawson, Sharyn A Endow, Lawrence S B Goldstein, Holly V Goodson, Nobutaka Hirokawa, Jonathon Howard, Russell L Malmberg, J Richard McIntosh, Harukata Miki, Timothy J Mitchison, Yasushi Okada, Anireddy S N Reddy, William M Saxton, Manfred Schliwa, Jonathan M Scholey, Ronald D Vale, Claire E Walczak, and Linda Wordeman. A standardized kinesin nomenclature. *Journal of Cell Biology*, 167(1):19–22, 2004. ISSN 00219525. doi: 10.1083/jcb.200408113.
- [63] William O. Hancock and Jonathon Howard. Processivity of the motor protein kinesin requires two heads. *Journal of Cell Biology*, 140(6):1395–1405, 1998. ISSN 00219525. doi: 10.1083/jcb.140.6.1395.
- [64] Avin Ramaiya, Basudev Roy, Michael Bugiel, and Erik Schäffer. Kinesin rotates unidirectionally and generates torque while walking on microtubules. *Proceedings of the National Academy of Sciences of the United States of America*, 114(41):10894–10899, 2017. ISSN 0027-8424. doi: 10.1073/pnas.1706985114.
- [65] Michael Bugiel, Horatiu Fantana, Volker Bormuth, Anastasiya Trushko, Frederic Schiemann, Jonathon Howard, Erik Schäffer, and Anita Jannasch. Versatile microsphere attachment of GFP-labeled motors and other tagged proteins with preserved functionality. *Journal of Biological Methods*, 2(4):30, 2015. ISSN 2326-9901. doi: 10.14440/jbm.2015.79.
- [66] William O. Hancock. The Kinesin-1 Chemomechanical Cycle: Stepping Toward a Consensus. *Biophys. J.*, 110(6):1216–1225, 2016. ISSN 15420086. doi: 10.1016/j.bpj.2016.02.025.
- [67] Keith J. Mickolajczyk, Nathan C. Deffenbaugh, Jaime Ortega Arroyo, Joanna Andrecka, Philipp Kukura, and William O. Hancock. Kinetics of nucleotide-dependent structural transitions in the kinesin-1 hydrolysis cycle. *PNAS*, 112(52):E7186—E7193, 2015. ISSN 10916490. doi: 10.1073/pnas.1517638112.
- [68] Tepppei Mori, Ronald D. Vale, and Michio Tomishige. How kinesin waits between steps. *Nature*, 450(7170):750–754, 2007. ISSN 14764687. doi: 10.1038/nature06346.
- [69] Ana B. Asenjo and Hernando Sosa. A mobile kinesin-head intermediate during the ATP-waiting state. *PNAS*, 106(14):5657–5662, 2009. ISSN 00278424. doi: 10.1073/pnas.0808355106.
- [70] N. J. Carter and R. A. Cross. Mechanics of the kinesin step. *Nature*, 435(7040):308–312, 2005. ISSN 00280836. doi: 10.1038/nature03528.

- [71] Hiroshi Isojima, Ryota Iino, Yamato Niitani, Hiroyuki Noji, and Michio Tomishige. Direct observation of intermediate states during the stepping motion of kinesin-1. *Nature Chemical Biology*, 12(February):290–297, 2016. ISSN 1552-4450. doi: 10.1038/nchembio.2028.
- [72] Geoffrey M. Cooper and Robert E. Hausman. *The cell: a molecular approach*, volume 35. ASM press, Washington, 4 th editi edition, 1997. doi: 10.5860/choice.35-0264.
- [73] Francis Crick and James Watson. Molecular structure of nucleic acids. *Nature*, 171(23):737–738, 1953.
- [74] Robert G. Roeder. The complexities of eukaryotic transcription initiation:regulation of preinitiation complex assembly. *Science*, 1991(November):402–408, 1991.
- [75] James L. Keck. *Single-Stranded Dna Binding Proteins: Methods and Protocols*. Springer US, New York, 2012. ISBN 9781627030311.
- [76] Marcel Ander, Sivaraman Subramaniam, Karim Fahmy, A. Francis Stewart, and Erik Schäffer. A single-strand annealing protein clamps DNA to detect and secure homology. *PLoS Biology*, 13(8):1–23, 2015. ISSN 15457885. doi: 10.1371/journal.pbio.1002213.
- [77] A. Ashkin. Acceleration and Trapping of Particles by Radiation Pressure. *Physical Review Letters*, 24(4):156–159, 1970. ISSN 00319007. doi: 10.1103/PhysRevLett.24.156.
- [78] A. Ashkin, J. M. Dziedzic, J. E. Bjorkholm, and Steven Chu. Observation of a single-beam gradient force optical trap for dielectric particles. *Optical Angular Momentum*, 11(5):196–198, 2016. ISSN 0146-9592. doi: 10.1364/ol.11.000288.
- [79] J. M. Dziedzic & T. Yamane A. Ashkin. Optical trapping and manipulation of single cells using infrared laser beam. *Nature*, 327(24):524–526, 1987.
- [80] Karel Svoboda and Steven M Block. Biological applications of optical forces. *Annual Review of Biophysics and Biomolecular Structure*, 23:247–285, 1994. ISSN 10568700. doi: 10.1146/annurev.bb.23.060194.001335.
- [81] Y Harada and Toshimutu Asakura. Radiation forces on a dielectric sphere in the Rayleigh scattering regime. *Optics communications*, 124(March):529–541, 1996.
- [82] A. Ashkin. Forces of a single-beam gradient laser trap on a dielectric sphere in the ray optics regime. *Biophysical Journal*, 61(2):569–582, 1992. ISSN 00063495. doi: 10.1016/S0006-3495(92)81860-X.

-
- [83] J. D. Jackson and Ronald F. Fox. Classical Electrodynamics, 3rd ed . . *American Journal of Physics*, 67(9):841–842, 1999. ISSN 0002-9505. doi: 10.1119/1.19136.
- [84] Anita Jannasch. *High performance photonic probes and applications of optical tweezers to molecular motors*. PhD thesis, 2012.
- [85] A. Mazolli, P. A. Maia Neto, and H. M. Nussenzveig. Theory of trapping forces in optical tweezers. *Proceedings of the Royal Society A: Mathematical, Physical and Engineering Sciences*, 459(2040):3021–3041, 2003. ISSN 14712946. doi: 10.1098/rspa.2003.1164.
- [86] Craig F. Bohren. Absorption and scattering of light by small particles. *Absorption and scattering of light by small particles*, 1983. ISSN 0031-9112. doi: 10.1088/0031-9112/35/3/025.
- [87] Alexander Rohrbach and Ernst H. K. Stelzer. Optical trapping of dielectric particles in arbitrary fields. *Journal of the Optical Society of America A*, 18(4):839, 2001. ISSN 1084-7529. doi: 10.1364/josaa.18.000839.
- [88] Alexander Rohrbach. Stiffness of optical traps: Quantitative agreement between experiment and electromagnetic theory. *Physical Review Letters*, 95(16):1–4, 2005. ISSN 00319007. doi: 10.1103/PhysRevLett.95.168102.
- [89] T. A. Nieminen, H. Rubinsztein-Dunlop, and N. R. Heckenberg. Multipole expansion of strongly focussed laser beams. *Journal of Quantitative Spectroscopy and Radiative Transfer*, 79-80:1005–1017, 2003. ISSN 00224073. doi: 10.1016/S0022-4073(02)00335-7.
- [90] Timo A. Nieminen, Vincent L.Y. Y Loke, Alexander B. Stilgoe, Gregor Knöner, Agata M. Brańczyk, Norman R. Heckenberg, and Halina Rubinsztein-dunlop. Optical tweezers computational toolbox. *Journal of Optics A: Pure and Applied Optics*, 9(8):196–203, 2007. ISSN 14644258. doi: 10.1088/1464-4258/9/8/S12.
- [91] Matthias Grimm, Thomas Franosch, and Sylvia Jeney. High-resolution detection of Brownian motion for quantitative optical tweezers experiments. *Physical Review E*, 86(2):1–7, 2012. ISSN 15393755. doi: 10.1103/PhysRevE.86.021912.
- [92] Simon F. Tolić-Nørrelykke, Erik Schäffer, Jonathon Howard, Francesco S. Pavone, Frank Jülicher, and Henrik Flyvbjerg. Calibration of optical tweezers with positional detection in the back focal plane. *Review of Scientific Instruments*, 77(10), 2006. ISSN 00346748. doi: 10.1063/1.2356852.
- [93] A. Pralle, M. Prummer, E. L. Florin, E. H.K. K Stelzer, and J. K.H. H Hörber. Three-dimensional high-resolution particle tracking for optical tweezers by forward scattered light. *Microscopy Research and Technique*, 44(5):378–386, 1999. ISSN 1059910X.

- [94] Alexander Rohrbach, Holger Kress, and Ernst H.K. K Stelzer. Trapping force, force constant, and potential depths for dielectric spheres in the presence of spherical aberrations. *Applied Optics*, 43(9):1827–1829, 2004. ISSN 15394522. doi: 10.1364/AO.43.001827.
- [95] Anni Lehmuskero, Peter Johansson, Halina Rubinsztein-Dunlop, Lianming Tong, and Mikael Käll. Laser trapping of colloidal metal nanoparticles. *ACS Nano*, 9(4):3453–3469, 2015. ISSN 1936086X. doi: 10.1021/acs.nano.5b00286.
- [96] Maria Dienerowitz, Michael Mazilu, and Kishan Dholakia. Optical manipulation of nanoparticles: A review. *SPIE Reviews*, 1(1), 2010. ISSN 19463251. doi: 10.1117/1.2992045.
- [97] M. Ploschner, T. Čižmár, M. Mazilu, A. Di Falco, and K. Dholakia. Bidirectional optical sorting of gold nanoparticles. *Nano Letters*, 12(4):1923–1927, 2012. ISSN 15306984. doi: 10.1021/nl204378r.
- [98] Elena Messina, Emanuele Cavallaro, Adriano Cacciola, Maria Antonia Iatì, Pietro G. Gucciardi, Ferdinando Borghese, Paolo Denti, Rosalba Saija, Giuseppe Compagnini, Moreno Meneghetti, Vincenzo Amendola, and Onofrio M. Maragò. Plasmon-enhanced optical trapping of gold nanoaggregates with selected optical properties. *ACS Nano*, 5(2):905–913, 2011. ISSN 19360851. doi: 10.1021/nm102101a.
- [99] Yeonee Seol, Amanda E Carpenter, and Thomas T Perkins. Gold nanoparticles : enhanced optical trapping and. *Optics Letters*, 31(16):2429–2431, 2006.
- [100] Oto Brzobohatý, Martin Šiler, Jan Trojek, Lukáš Chvátal, Vítězslav Karásek, and Pavel Zemánek. Non-spherical gold nanoparticles trapped in optical tweezers: shape matters. *Optics Express*, 23(7):8179, 2015. ISSN 1094-4087. doi: 10.1364/oe.23.008179.
- [101] Poul Martin Hansen, Vikram Kjølner Bhatia, Niels Harrit, and Lene Oddershede. Expanding the optical trapping range of gold nanoparticles. *Nano Letters*, 5(10):1937–1942, 2005. ISSN 15306984. doi: 10.1021/nl051289r.
- [102] Karel Svoboda and Steven M. Block. Optical trapping of metallic Rayleigh particles. *Optics Letters*, 19(13):930, 1994. ISSN 0146-9592. doi: 10.1364/ol.19.000930.
- [103] Vincenzo Amendola, Stefano Polizzi, and Moreno Meneghetti. Laser ablation synthesis of gold nanoparticles in organic solvents. *Journal of Physical Chemistry B*, 110(14):7232–7237, 2006. ISSN 15206106. doi: 10.1021/jp0605092.
- [104] F. Moreno, P. Albella, and M. Nieto-Vesperinas. Analysis of the spectral behavior of localized plasmon resonances in the near- and far-field regimes. *Langmuir*, 29(22):6715–6721, 2013. ISSN 07437463. doi: 10.1021/la400703r.

-
- [105] Lana Bosanac, Thomas Aabo, Poul M. Bendix, and Lene B. Oddershede. Efficient optical trapping and visualization of silver nanoparticles. *Nano Letters*, 8(5):1486–1491, 2008. ISSN 15306984. doi: 10.1021/nl080490+.
- [106] E. Messina, M. G. Donato, M. Zimbone, R. Saija, M. A. Iatì, L. Calcagno, M. E. Fragalà, G. Compagnini, C D’Andrea, A. Foti, and P. G. Gucciardi. Optical trapping of silver nanoplatelets. *Optics Express*, 23(7):8720, 2015. ISSN 1094-4087. doi: 10.1364/oe.23.008720.
- [107] Frederick Gittes and Christoph F Schmidt. Brownian Motion of a Harmonically Bound Particle. *Signals and Noise in Micromechanical Measurements*, 55:129–156, 1998.
- [108] Jeffrey R. Moffitt, Yann R. Chemla, Steven B. Smith, and Carlos Bustamante. Recent advances in optical tweezers. *Annual Review of Biochemistry*, 77:205–228, 2008. ISSN 00664154. doi: 10.1146/annurev.biochem.77.043007.090225.
- [109] Jiahao Yan, Xinyue Liu, Churong Ma, Yingcong Huang, and Guowei Yang. All-dielectric materials and related nanophotonic applications. *Materials Science and Engineering R*, 141(February):100563, 2020. ISSN 0927796X. doi: 10.1016/j.mser.2020.100563.
- [110] Arseniy I. Kuznetsov, Andrey E. Miroshnichenko, Mark L. Brongersma, Yuri S. Kivshar, and Boris Luk’yanchuk. Optically resonant dielectric nanostructures. *Science*, 354(6314), 2016. ISSN 10959203. doi: 10.1126/science.aag2472.
- [111] Alex Krasnok, Martín Caldarola, Nicolas Bonod, and Andrea Alú. Spectroscopy and Biosensing with Optically Resonant Dielectric Nanostructures. *Advanced Optical Materials*, 6(5), 2018. ISSN 21951071. doi: 10.1002/adom.201701094.
- [112] Ana Andres-Arroyo, Bakul Gupta, Fan Wang, J. Justin Gooding, and Peter J. Reece. Optical Manipulation and Spectroscopy of Silicon Nanoparticles Exhibiting Dielectric Resonances. *Nano Letters*, 16(3):1903–1910, 2016. ISSN 15306992. doi: 10.1021/acs.nanolett.5b05057.
- [113] Wang, Huang, and Ren. Synthesis of Germanium Nanocubes by a Low-Temperature Inverse Micelle Solvothermal Technique. *Langmuir*, 21(2):751–754, 2005. ISSN 0743-7463. doi: 10.1021/la047953l.
- [114] Doh Lee, Jeffrey Pietryga, Istvan Robel, Donald Werder, Richard Schaller, and Victor Klimov. Colloidal synthesis of infrared-emitting Germanium nanocrystals. *Journal of the American Chemical Society*, 131(10):3436–3437, 2009. ISSN 00027863. doi: 10.1021/ja809218s.

- [115] Lance M. Wheeler, Laszlo M. Levij, and Uwe R. Kortshagen. Tunable band gap emission and surface passivation of germanium nanocrystals synthesized in the gas phase. *Journal of Physical Chemistry Letters*, 4(20):3392–3396, 2013. ISSN 19487185. doi: 10.1021/jz401576b.
- [116] Andreas Kornowski, Michael Giersig, Ralf Vogel, Ahdelkarim Chemseddine, and Hovsf Weller. Nanometer-Sized Colloidal Germanium Particles: Wet-Chemical Synthesis, Laser-Induced Crystallization and Particle Growth. *Advanced Materials*, 5(9):634–636, 1993.
- [117] Daniele Gerion, Natalia Zaitseva, Cheng Saw, Maria Francesca Casula, Sirine Fakra, Tony Van Buuren, and Giulia Galli. Solution synthesis of germanium nanocrystals: Success and open challenges. *Nano Letters*, 4(4):597–602, 2004. ISSN 15306984. doi: 10.1021/nl035231t.
- [118] Natalia Zaitseva, Zu Rong Dai, Christian D. Grant, Jennifer Harper, and Cheng Saw. Germanium nanocrystals synthesized in high-boiling-point organic solvents. *Chemistry of Materials*, 19(21):5174–5178, 2007. ISSN 08974756. doi: 10.1021/cm070062p.
- [119] H. P. Wu, M. Y. Ge, C. W. Yao, Y. W. Wang, Y. W. Zeng, L. N. Wang, G. Q. Zhang, and J. Z. Jiang. Blue emission of Ge nanocrystals prepared by thermal decomposition. *Nanotechnology*, 17(21):5339–5343, 2006. ISSN 09574484. doi: 10.1088/0957-4484/17/21/009.
- [120] Hua Bin Yin, Huai Hong Cai, Ji Ye Cai, Jiu Wei Teng, and Pei Hui Yang. Facile solution routes for the syntheses of water-dispersable germanium nanoparticles and their biological applications. *Materials Letters*, 109:108–111, 2013. ISSN 0167577X. doi: 10.1016/j.matlet.2013.07.041.
- [121] Alexandra Navrotsky Xuchu Ma, Fen Xu, Tonya M. Atkins, Andrea M. Goforth, Doinita Neiner, Susan M. Kauzlarich*, and Susan M Kauzlarich*. A Versatile Low Temperature Synthetic Route to Zintl Phase Precursors: Na₄Si₄, Na₄Ge₄ and K₄Ge₄ as Examples. *Dalton Trans*, 46(1):10250–10255, 2009. ISSN 15378276. doi: 10.1038/jid.2014.371.
- [122] Henry Gerung, Timothy J. Boyleb, Louis J. Tribby, Scott D. Bunge, C. Jeffrey Brinker, Sang M Han, Henry Gerung, Timothy J. Boyleb, Louis J. Tribby, Scott D. Bunge, C. Jeffrey Brinker, Sang M. Han, Henry Gerung, Timothy J. Boyleb, Louis J. Tribby, Scott D. Bunge, C. Jeffrey Brinker, and Sang M Han. Solution Synthesis of Germanium Nanowires Using a Ge+2 Alkoxide Precursor. *J Am Chem Soc*, 15(1):5244–5250, 2006. doi: 10.1038/jid.2014.371.

-
- [123] Xianmao Lu, Brian A. Korgel, and Keith P. Johnston. High yield of germanium nanocrystals synthesized from germanium diiodide in solution. *Chemistry of Materials*, 17(25):6479–6485, 2005. ISSN 08974756. doi: 10.1021/cm0515956.
- [124] Dimitri D. Vaughn, James F. Bondi, and Raymond E. Schaak. Colloidal synthesis of air-stable crystalline germanium nanoparticles with tunable sizes and shapes. *Chemistry of Materials*, 22(22):6103–6108, 2010. ISSN 08974756. doi: 10.1021/cm1015965.
- [125] Chengbin Jing, Xiaodan Zang, Wei Bai, Junhao Chu, and Aiyun Liu. Aqueous germanate ion solution promoted synthesis of worm-like crystallized Ge nanostructures under ambient conditions. *Nanotechnology*, 20(50):505607, 2009. ISSN 0957-4484. doi: 10.1088/0957-4484/20/50/505607.
- [126] Eric J. Henderson, Colin M. Hessel, and Jonathan G.C. C Veinot. Synthesis and photoluminescent properties of size-controlled germanium nanocrystals from phenyl trichlorogermane-derived polymers. *Journal of the American Chemical Society*, 130(11):3624–3632, 2008. ISSN 00027863. doi: 10.1021/ja710286a.
- [127] Matthew J. Lang Jijun Dong, Carlos E. Castro, Mary C. Boyce, Susan Lindquist, Jijun Dong, Carlos E. Castro, Mary C. Boyce, Matthew J. Lang, Susan Lindquist, Matthew J. Lang Jijun Dong, Carlos E. Castro, Mary C. Boyce, and Susan Lindquist. Optical Trapping with High Forces Reveals Unexpected Behaviors of Prion Fibrils. *Nat Struct Mol Biol.*, 17(2):1422–1430, 2010. ISSN 15378276. doi: 10.1038/jid.2014.371.
- [128] N. B. Simpson, D. McGloin, K. Dholakia, L. Allen, and M. J. Padgett. Optical tweezers with increased axial trapping efficiency. *Journal of Modern Optics*, 45(9):1943–1949, 1998. ISSN 13623044. doi: 10.1080/09500349808231712.
- [129] Anita Jannasch, Ahmet F. Demirörs, Peter D.J. J Van Oostrum, Alfons Van Blaaderen, and Erik Schäffer. Nanonewton optical force trap employing anti-reflection coated, high-refractive-index titania microspheres. *Nat. Photonics*, 6(7):469–476, 2012. ISSN 17494885. doi: 10.1038/nphoton.2012.140.
- [130] Anita Jannasch, Mohammad Abdosamadi, Avin Ramaiya, Suman De, Valentina Ferro, Aaron Sonnberger, and Erik Schäffer. Custom-Made Microspheres for Optical Tweezers Anita. In Arne Gennerich, editor, *Optical tweezers - methods and protocols*, chapter 6, pages 78–86. Springer US, Newyork, 2004. ISBN 9780123693952. doi: 10.1016/B0-12-369395-0/01244-6.
- [131] Jeffrey R Moffitt, Yann R Chemla, K Aathavan, Shelley Grimes, Paul J Jardine, Dwight L Anderson, and Carlos Bustamante. Intersubunit coordination in a homomeric ring ATPase. *Nature*, 457(January):446–451, 2009. ISSN 0028-0836. doi: 10.1038/nature07637.

- [132] A. A. Brian and H. M. McConnell. Allogeneic stimulation of cytotoxic T cells by supported planar membranes. *Proceedings of the National Academy of Sciences of the United States of America*, 81(19 I):6159–6163, 1984. ISSN 00278424. doi: 10.1073/pnas.81.19.6159.
- [133] Ralf P. Richter, Rémi Bérat, and Alain R. Brisson. Formation of solid-supported lipid bilayers: An integrated view. *Langmuir*, 22(8):3497–3505, 2006. ISSN 07437463. doi: 10.1021/la052687c.
- [134] Kenji Kawaguchi and Shin’Ichi Ishiwata. Temperature dependence of force, velocity, and processivity of single kinesin molecules. *Biochem. Biophys. Res. Commun.*, 272(3):895–899, 2000. ISSN 0006291X. doi: 10.1006/bbrc.2000.2856.
- [135] Ulrich Rothbauer, Kouros Zolghadr, Serge Muyldermans, Aloys Schepers, M. Cristina Cardoso, and Heinrich Leonhardt. A versatile nanotrap for biochemical and functional studies with fluorescent fusion proteins. *Mol. Cell Proteomics*, 7(2):282–289, 2008. ISSN 15359476. doi: 10.1074/mcp.M700342-MCP200.
- [136] Mohammed Mahamdeh and Erik Schäffer. Optical tweezers with millikelvin precision of temperature-controlled objectives and base-pair resolution. *Optics Express*, 17(19):17190, 2009. ISSN 1094-4087. doi: 10.1364/oe.17.017190.
- [137] Rafayel Petrosyan. Improved approximations for some polymer extension models. *Rheologica Acta*, 56(1):21–26, 2017. ISSN 00354511. doi: 10.1007/s00397-016-0977-9.
- [138] Smith Sb, Cui Y, and Bustamante C. Overstretching B-DNA: the elastic response of individual double-stranded and single-stranded DNA molecules. *Science*, 271(5250):795–798, 1996.
- [139] Yan Jie Guo, Fen Yang, Lu Zhang, Jiang Pi, Ji Ye Cai, and Pei Hui Yang. Facile synthesis of multifunctional germanium nanoparticles as a carrier of quercetin to achieve enhanced biological activity. *Chemistry - An Asian Journal*, 9(8):2272–2280, 2014. ISSN 1861471X. doi: 10.1002/asia.201402227.
- [140] Seongbeom Kim, Song Yi Park, Jaeki Jeong, Gi Hwan Kim, Parham Rohani, Dong Suk Kim, Mark T. Swihart, and Jin Young Kim. Production of pristine, sulfur-coated and silicon-alloyed germanium nanoparticles via laser pyrolysis. *Nanotechnology*, 26(30), 2015. ISSN 13616528. doi: 10.1088/0957-4484/26/30/305703.
- [141] Liangbiao Wang, Keyan Bao, Zhengsong Lou, Guobing Liang, and Quanfa Zhou. Chemical synthesis of germanium nanoparticles with uniform size as anode materials for lithium ion batteries. *Dalton Transactions*, 45(7):2814–2817, 2016. ISSN 14779234. doi: 10.1039/c5dt04749h.

-
- [142] Erwin J.G. G Peterman, Frederick Gittes, and Christoph F. Schmidt. Laser-induced heating in optical traps. *Biophysical Journal*, 84(2 I):1308–1316, 2003. ISSN 00063495. doi: 10.1016/S0006-3495(03)74946-7.
- [143] Karel Svoboda, Christoph F Schmidt, Bruce J Schnapp, and Be Steven M Block. Direct observation of kinesin stepping by optical trapping interferometry. *Nature*, 365(October):721–727, 1993.
- [144] Adam G. Hendricks, Eran Perlson, Jennifer L. Ross, Harry W. Schroeder, Mariko Tokito, and Erika L.F. F Holzbaaur. Motor Coordination via a Tug-of-War Mechanism Drives Bidirectional Vesicle Transport. *Current Biology*, 20(8):697–702, 2010. ISSN 09609822. doi: 10.1016/j.cub.2010.02.058.
- [145] S Simmert, M.K Abdosamadi, G Hermsdorf, and E Schäffer. LED-based interference-reflection microscopy combined with optical tweezers for quantitative three-dimensional microtubule imaging. *Opt. Express*, 26(11):1437–1448, 2018.
- [146] Paul A Wiggins. An Information-Based Approach to Change-Point Analysis with Applications to Biophysics and Cell Biology. *Biophys. J.*, 109(2):346–354, 2015. ISSN 0006-3495. doi: 10.1016/j.bpj.2015.05.038.
- [147] Hamid Khataee and Jonathon Howard. Force Generated by Two Kinesin Motors Depends on the Load Direction and Intermolecular Coupling. *PRL*, 122(18):188101, 2019. ISSN 10797114. doi: 10.1103/PhysRevLett.122.188101.
- [148] Janine Fischer. *Investigation of microtubule motility driven by Mmembrane-anchored motor proteins. Diploma Thesis.* PhD thesis, 2010. URL https://www.entorb.net/docs/Janine_Fischer-Diplomarbeit.pdf.
- [149] Qiaochu Li, Kuo Fu Tseng, Stephen J. King, Weihong Qiu, and Jing Xu. A fluid membrane enhances the velocity of cargo transport by small teams of kinesin-1. *Journal of Chemical Physics*, 148(12), 2018. ISSN 00219606. doi: 10.1063/1.5006806.
- [150] Erik D. Holmstrom, Nicholas F. Dupuis, and David J. Nesbitt. Pulsed IR heating studies of single-molecule DNA duplex dissociation kinetics and thermodynamics. *Biophysical Journal*, 106(1):220–231, 2014. ISSN 00063495. doi: 10.1016/j.bpj.2013.11.008.
- [151] Yoshiaki Nakamura, Kentaro Watanabe, Yo Fukuzawa, and Masakazu Ichikawa. Observation of the quantum-confinement effect in individual Ge nanocrystals on oxidized Si substrates using scanning tunneling spectroscopy. *Applied Physics Letters*, 87(13):1–3, 2005. ISSN 00036951. doi: 10.1063/1.2067711.

- [152] Yoshihito Maeda. Visible photoluminescence from nanocrystallite Ge embedded in a glassy SiO₂ matrix: Evidence in support of the quantum-confinement mechanism. *Physical Review B*, 51(3):1658–1670, 1995. ISSN 01631829. doi: 10.1103/PhysRevB.51.1658.
- [153] Daniel A. Ruddy, Justin C. Johnson, E. Ryan Smith, and Nathan R. Neale. Size and bandgap control in the solution-phase synthesis of near-infrared-emitting germanium nanocrystals. *ACS Nano*, 4(12):7459–7466, 2010. ISSN 19360851. doi: 10.1021/nn102728u.
- [154] Jianghong Wu, Yangang Sun, Rujia Zou, Guosheng Song, Zhigang Chen, Chunrui Wang, and Junqing Hu. One-step aqueous solution synthesis of Ge nanocrystals from GeO₂ powders. *CrystEngComm*, 13(11):3674–3677, 2011. ISSN 14668033. doi: 10.1039/c1ce05191a.
- [155] Poornima Budime Santhosh, Neethu Thomas, Swathi Sudhakar, Anju Chadha, and Ethayaraja Mani. Phospholipid stabilized gold nanorods: Towards improved colloidal stability and biocompatibility. *Physical Chemistry Chemical Physics*, 19(11):18494–18504, 2017. ISSN 14639076. doi: 10.1039/c7cp03403b.
- [156] Miles Padgett and Richard Bowman. Tweezers with a twist. *Nature Photonics*, 5(6):343–348, 2011. ISSN 17494885. doi: 10.1038/nphoton.2011.81.
- [157] Ahmet Yildiz, Michio Tomishige, Arne Gennerich, and Ronald D Vale. Intramolecular Strain Coordinates Kinesin Stepping Behavior along Microtubules. *Cell.*, 134(6):1030–1041, 2008. doi: 10.1016/j.cell.2008.07.018.
- [158] Ahmet Yildiz, Michio Tomishige, and Ronald D Vale. Kinesin Walks Hand-Over-Hand. *Science*, 303(January):676–679, 2004.
- [159] Nicholas R Guydosh and Steven M Block. Direct observation of the binding state of the kinesin head to the microtubule. *Nature*, 461(7260):125–128, 2009. ISSN 0028-0836. doi: 10.1038/nature08259.
- [160] Sarah Rice, Abel W Lin, Daniel Safer, Cynthia L Hart, Nariman Naber, Bridget O Carragher, Shane M Cain, Elena Pechatnikova, Elizabeth M Wilson-kubalek, Michael Whittaker, Edward Pate I, Roger Cooke, Edwin W Taylor, Ronald A Milligan, and Ronald D Vale. A structural change in the kinesin motor protein that drives motility. *Nature.*, 402(3):0–6, 1999.
- [161] Breane G. Budaitis, Shashank Jariwala, Dana N. Reinemann, Kristin I. Schimert, Guido Scarabelli, Barry J. Grant, David Sept, Matthew J. Lang, and Kristen J. Verhey. Neck linker docking is critical for kinesin-1 force generation in cells but at a cost to motor speed and processivity. *eLife*, 8:1–28, 2019. ISSN 2050084X. doi: 10.7554/eLife.44146.

-
- [162] Ryan B Case, Sarah Rice, Cynthia L Hart, Bernice Ly, and Ronald D Vale. Role of the kinesin neck linker and catalytic core in microtubule-based motility. *Curr Biol*, 10(3):157–160, 2000.
- [163] Bojan Milic, Johan O L Andreasson, William O. Hancock, and Steven M. Block. Kinesin processivity is gated by phosphate release. *PNAS*, 111(39):14136–14140, 2014. ISSN 10916490. doi: 10.1073/pnas.1410943111.
- [164] Johan O L Andreasson, Bojan Milic, Geng-yuan Chen, Nicholas R Guydosh, William O Hancock, and Steven M Block. Examining kinesin processivity within a general gating framework. *eLife*, 21(12):1–22, 2015. doi: 10.7554/eLife.07403.
- [165] Anita Jannasch, Volker Bormuth, Marko Storch, Jonathon Howard, and Erik Schäffer. Kinesin-8 is a low-force motor protein with a weakly bound slip state. *Biophysical Journal*, 104(11):2456–2464, 2013. ISSN 00063495. doi: 10.1016/j.bpj.2013.02.040.
- [166] Mayank Chugh, Maja Reißner, Michael Bugiel, Elisabeth Lipka, Arvid Herrmann, Basudev Roy, Sabine Müller, and Erik Schäffer. Phragmoplast Orienting Kinesin 2 Is a Weak Motor Switching between Processive and Diffusive Modes. *Biophysical Journal*, 115(2):375–385, 2018. ISSN 15420086. doi: 10.1016/j.bpj.2018.06.012.
- [167] Elio A Abbondanzieri, William J Greenleaf, Joshua W Shaevitz, Robert Landick, and Steven M Block. Direct observation of base-pair stepping by RNA polymerase. *Nature*, 438(11):460–465, 2005. doi: 10.1038/nature04268.
- [168] Jiyang Fan and Paul K. Chu. Group IV nanoparticles: Synthesis, properties, and biological applications. *Small*, 6(19):2080–2098, 2010. ISSN 16136810. doi: 10.1002/smll.201000543.
- [169] Dimitri D. Vaughn and Raymond E. Schaak. Synthesis, properties and applications of colloidal germanium and germanium-based nanomaterials. *Chemical Society Reviews*, 42(7):2861–2879, 2013. ISSN 14604744. doi: 10.1039/c2cs35364d.
- [170] Krishna Neupane, Feng Wang, and Michael T. Woodside. Direct measurement of sequence-dependent transition path times & conformational diffusion in DNA duplex formation. *Proceedings of the National Academy of Sciences of the United States of America*, 114(6):1329–1334, 2017. ISSN 10916490. doi: 10.1073/pnas.1611602114.

Appendix

Original published articles, submitted manuscripts and manuscript in preparation, which are included in this thesis.

Supported Solid Lipid Bilayers as a Platform for Single-Molecule Force Measurements

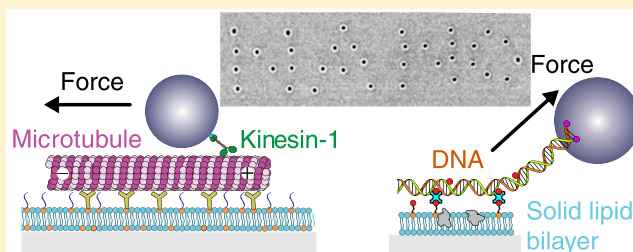
Swathi Sudhakar,[‡] Tobias Jörg Jachowski,[‡] Michael Kittelberger, Ammara Maqbool, Gero Lutz Hermsdorf, Mohammad Kazem Abdosamadi, and Erik Schäffer*[Ⓜ]

Eberhard Karls Universität Tübingen, ZMBP, Auf der Morgenstelle 32, 72076 Tübingen, Germany

Supporting Information

ABSTRACT: Biocompatible surfaces are important for basic and applied research in life science with experiments ranging from the organismal to the single-molecule level. For the latter, examples include the translocation of kinesin motor proteins along microtubule cytoskeletal filaments or the study of DNA–protein interactions. Such experiments often employ single-molecule fluorescence or force microscopy. In particular for force measurements, a key requirement is to prevent nonspecific interactions of biomolecules and force probes with the surface, while providing specific attachments that can sustain loads. Common approaches to reduce nonspecific interactions include supported lipid bilayers or PEGylated surfaces. However, fluid lipid bilayers do not support loads and PEGylation may require harsh chemical surface treatments and have limited reproducibility. Here, we developed and applied a supported *solid* lipid bilayer (SSLB) as a platform for specific, load bearing attachments with minimal nonspecific interactions. Apart from single-molecule fluorescence measurements, anchoring molecules to lipids in the solid phase enabled us to perform force measurements of molecular motors and overstretch DNA. Furthermore, using a heating laser, we could switch the SSLB to its fluid state allowing for manipulation of anchoring points. The assay had little nonspecific interactions, was robust, reproducible, and time-efficient, and required less hazardous and toxic chemicals for preparation. In the long term, we expect that SSLBs can be widely employed for single-molecule fluorescence microscopy, force spectroscopy, and cellular assays in mechanobiology.

KEYWORDS: DNA, kinesin, microtubules, supported lipid bilayer, PEGylation, optical tweezers



In vitro microscopy, particularly when performed on the single-molecule level, often requires samples to be attached to surfaces.^{1,2} Commonly, specific attachment of the molecules of interest is desired while nonspecific interactions of other molecules and probes are undesired. To achieve both specific and nonspecific interactions simultaneously and reproducibly may be one of the most time-consuming and critical steps in single-molecule assays. The simplest approach of using nonspecific blocking proteins like bovine serum albumin (BSA) or casein is often insufficient to meet the requirements of the experiment.

One common approach for specific immobilization of single molecules are silanized glass surfaces passivated with covalently attached poly(ethylene glycol) (PEG) molecules that reduce nonspecific interactions and fluorescent contaminations.^{2–10} As a simpler alternative in terms of preparation, passivation has been achieved using hydrophobic surfaces to which adapter molecules like antibodies or NeutrAvidin are adsorbed for specific attachment, while the remaining surface is blocked by amphiphilic molecules like the triblock copolymer Pluronic F127^{11–14} or Tween 20.¹⁵ However, all the above approaches typically involve chemicals with limited shelf life or sensitivity to humidity and harsh chemical surface treatments, which may be hazardous, potentially harmful, and ecotoxic. Also, since

protocols involve many steps and depend on surface heterogeneity¹⁰ and contamination, reproducibility of surface properties may be compromised. In addition, when using hydrophobic surfaces, proteins may denature.

As an alternative to PEGylation, supported lipid bilayers have been employed for a wide range of assays.^{2,16–26} The procedure to make supported lipid bilayers is simple, reproducible, and often only requires detergent cleaning of substrates. It is an effective approach compared to existing methods, as it mimics the cell membrane of living cells and prevents nonspecific surface adsorption of single biomolecules.²⁷ Apart from the Langmuir–Blodgett technique,¹⁷ supported lipid bilayers can be formed by fusing small unilamellar vesicles to the surface^{17,22,28,29} or by a continuous solvent exchange method without the need for vesicles.^{30,31} Bilayers in their fluid^{18–20,24} and solid-like gel state^{21–23,25} have been employed for various fluorescence microscopy experiments down to the single-molecule level. Mechanobiological experiments have been performed on supported solid lipid bilayers (SSLBs) on the cellular level^{21,25} but received

Received: September 11, 2019

Revised: November 19, 2019

Published: November 20, 2019

little attention for single-molecule force measurements. Here, we have optimized two SSLB systems for single-molecule force measurement. The first system is a kinesin motor-protein assay based on 15:0 phosphatidyl choline (PC) with covalent attachment of tubulin antibodies and PEG molecules to carboxylated lipids for specific binding of microtubules and additional blocking, respectively, supplemented with the blocking agent casein. The second system is a DNA-tethered-microsphere assay based on 1,2-distearoyl-*sn*-glycero-3-phosphocholine (DSPC) in combination with BSA and Tween 20 as additional blocking agents and biotinylated lipids for specific attachments. For both systems, single-molecule force measurements using optical tweezers could be performed. Specific attachments with minimal nonspecific interactions are shown through total internal reflection fluorescence (TIRF) and differential interference contrast (DIC) microscopy. Furthermore, the SSLB could be melted using a localized heating laser demonstrating the solid nature of the bilayer and allowing for repositioning of anchoring points in the membrane. The results show that SSLBs can be used as an alternative biological platform to existing surface passivation methods for various single-molecule force spectroscopy studies.

Results. In a typical single-molecule, kinesin stepping assay, microtubules are immobilized on a surface while imaging fluorescently tagged kinesin motors using TIRF microscopy.¹⁴ For the optimized SSLB kinesin assay (see [Materials and Methods](#)), we used a lipid mixture with a molar ratio of 4:1 of 15:0 PC and 1,2-distearoyl-*sn*-glycero-3-phosphoethanolamine-*N*-[carboxy[poly(ethylene glycol)]-2000] (DSPE-COOH) with a specified melting temperature (T_m) of 35 and 74 °C, respectively. To determine the melting temperature of the mixture, we used differential scanning calorimetry (DSC, [Figure 1a](#)). For the individual lipids, 15:0 PC and DSPE-COOH, we measured a T_m of 34 and 73 °C, respectively, consistent with the specifications. For the 4:1 molar ratio mixture, the melting temperature was 51 °C. Bilayers were formed by the vesicle fusion method at 65 °C allowing for defects to anneal above the melting temperature of the mixture.^{17,22,28,29} Subsequently, the supported lipid bilayers were used at room temperature, that is, below the melting temperatures of the mixture. After SSLB formation, we covalently coupled tubulin antibodies and 2 kDa amino-PEG molecules to the carboxyl groups of the membrane. In this manner, microtubules could be specifically and rigidly attached to the SSLB while preventing nonspecific interactions of the green fluorescent protein (GFP) tagged kinesin motors with the remaining surface ([Figure 1b](#)). To quantify the amount of blocking, we measured the average GFP fluorescence in the presence of a high motor concentration in small regions of interests (ROIs) that excluded microtubules ([Figure 1c](#)). For our optimized, PEGylated SSLB, the ROI intensity was 414 ± 2 gray values (mean \pm standard error of the mean if not stated otherwise, $N = 110$) comparable to the camera background value of 410 ± 1 but much larger compared to non-PEGylated SSLBs with 518 ± 5 ($N = 72$). In comparison to controls of a supported *fluid* lipid bilayer (SFLB), prepared in the same manner as the PEGylated SSLB but composed of a dioleoylphosphatidylcholine (DOPC, $T_m = -17$) and DSPE-COOH mixture, and a Pluronic F127 assay with average values of 580 ± 10 ($N = 60$) and 423 ± 2 ($N = 72$), respectively, the supported solid lipid bilayer had the least amount of nonspecific interactions. Specific interactions were present in

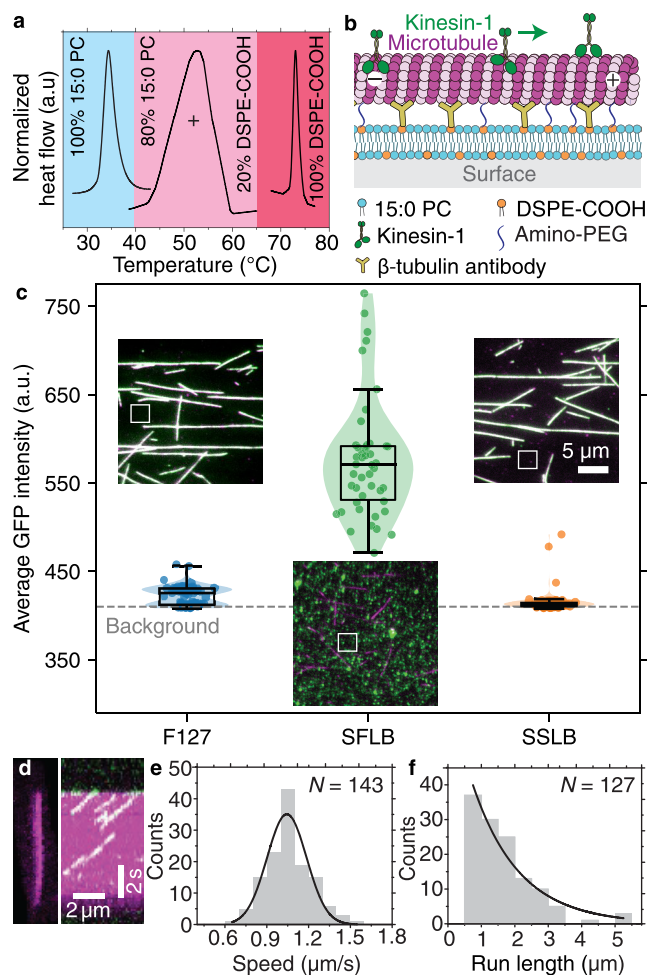


Figure 1. Surface passivation using a PEGylated supported solid lipid bilayer (SSLB) for a motor protein assay and quantification of specific and nonspecific kinesin interactions. (a) DSC curves for 15:0 PC, DSPE-COOH, and a 4:1 molar ratio mixture of the two lipids. (b) Schematic representation of kinesin motility on microtubules interacting with tubulin antibodies covalently attached to carboxylated lipids of the SSLB. Covalently attached PEG molecules further reduce nonspecific interactions. (c) Average ROI fluorescence intensity of GFP-labeled kinesin-1 bound nonspecifically to surface assays using Pluronic F127, SFLBs, and SSLBs with corresponding TIRF microscopy images (magenta, rhodamine-labeled microtubules; green, GFP-tagged kinesin; white, colocalization of motors on microtubules). Example ROIs are indicated by white squares. The dashed line indicates the average background intensity for all images. (d) (left) TIRF image of a microtubule. (right) Representative kymograph showing motile single kinesins on the microtubule depicted on the left. (e) Kinesin speed histogram with a Gaussian fit (line). (f) Run length histogram with an exponential fit (line).

all assays, as seen from the colocalization of the kinesin motors with microtubules. Note that due to the high amount of mostly transient nonspecific binding of the kinesin motors to the SFLB, detection of specific binding on the single-molecule level was difficult. To test whether the SSLB affected the functionality of the motor proteins, we used a low kinesin concentration to measure motility parameters of single motors ([Figure 1d–f](#)). Based on the kymographs ([Figure 1d](#)), we measured a mean motor speed and run length of 1.04 ± 0.02 m/s ($N = 143$) and 1.4 ± 0.2 m (best-fit value \pm fit error, $N = 127$), respectively, consistent with literature values.^{32–35} Thus,

SSLBs were a superior platform for single-molecule fluorescence microscopy assays.

To test whether SSLBs are indeed solid and sustain loads, we measured the force-dependent stepping behavior of kinesin-1 using optical tweezers (Figure 2). The GFP-tagged

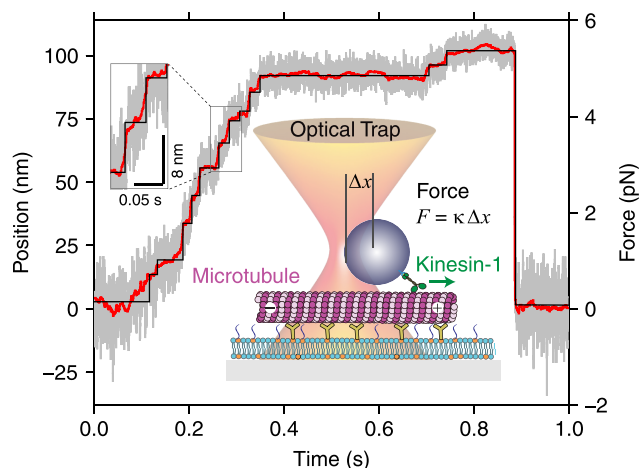


Figure 2. Representative trace depicting the displacement and force of an optically trapped microsphere driven by a single kinesin motor as a function of time (gray and red line, raw and filtered data, respectively; the black line corresponds to steps detected by a step detection algorithm³⁶). The zoomed in view shows 8 nm steps. Inset: Schematic of the PEGylated SSLB trapping assay. A single kinesin motor bound to an optically trapped microsphere walks on a microtubule displacing the microsphere from the trap center by Δx . For small displacements, the optical tweezers are a Hookean spring with a spring constant or trap stiffness κ . Thus, force is proportional to the displacement according to $F = \kappa\Delta x$.

kinesin motors were bound to PEGylated polystyrene microspheres via a covalently attached GFP nanobody.^{37,38} Under single-molecule conditions,³⁸ motor-coupled microspheres were trapped by the calibrated, high-precision optical tweezers^{12,39,40} and placed on microtubules in saturating ATP conditions. Single kinesin motors walked along the microtubule and displaced the microsphere in a stepwise fashion against the Hookean spring of the optical tweezers generating a maximum force of about 5.5 pN. This force is consistent with the literature^{38,41,42} and ensures functionality of the motor. In addition, we did not observe any nonspecific interactions of microspheres with the PEGylated SSLB platform. Furthermore, individual 8 nm steps could be discerned in the microsphere traces (zoomed in view of the trace in Figure 2). Both the resistance to piconewton loads and the resolution of individual nanometer-sized steps indicate a rigid attachment of the microtubule and the solid nature of the supported lipid bilayer. Thus, SSLBs were also an excellent platform for single-molecule force measurements.

Is the SSLB a good platform for other biomolecules like DNA and can it sustain higher loads? To address these questions, we unzipped and overstretched DNA tethered between the SSLB and optically trapped microspheres. For DNA experiments, we used a lipid mixture with a molar ratio of 2000:1 of 1,2-distearoyl-*sn*-glycero-3-phosphocholine (DSPC, $T_m = 55$ °C) and 1,2-distearoyl-*sn*-glycero-3-phosphoethanolamine-*N*-[biotinyl[poly(ethylene glycol)]-2000] (DSPE-biotin, $T_m = 74$ °C). The latter served as a specific binding site for one end of the DNA. Note that in

contrast to the kinesin assay, it was unnecessary to further PEGylate the bilayer. For specific attachment of the other DNA end and similar to microspheres for kinesin force experiments, we made PEGylated polystyrene microspheres with covalently attached NeutrAvidin or digoxigenin antibodies.³⁸ First, without DNA, we tested nonspecific binding of the microspheres to the SSLB with and without an additional treatment of protein blocking agents always in the presence of 0.1 vol % of the detergent Tween 20 (Figure 3a). Without any additional blocking, we found that a significant number of microspheres (17 ± 7 , mean microsphere count \pm standard deviation per field of view using LED-DIC⁴³) interacted

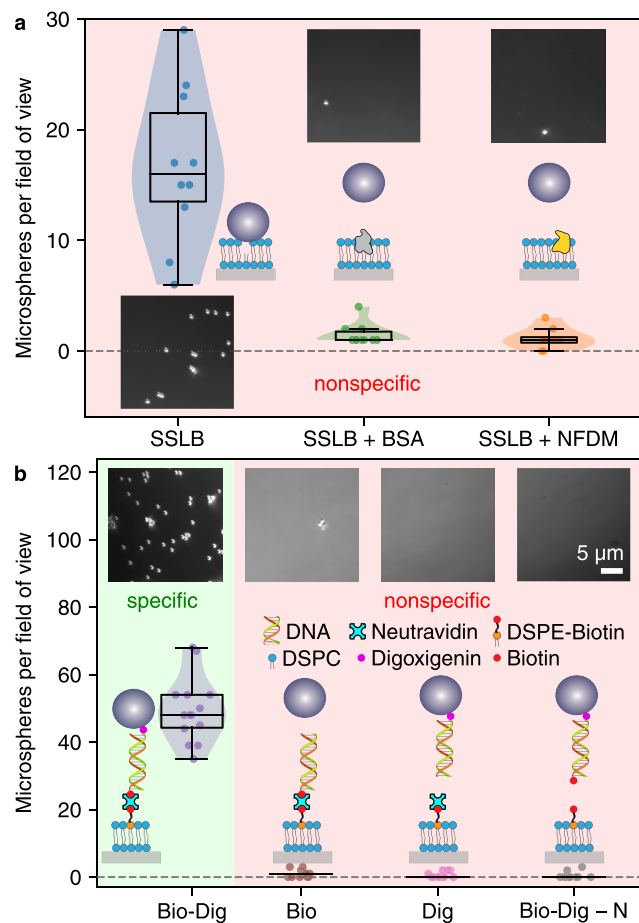


Figure 3. Surface passivation SSLBs for DNA tethered microsphere assays and quantification of specific and nonspecific interactions. (a) Number of nonspecifically bound PEGylated microspheres with covalently attached NeutrAvidin to SSLBs composed only of DSPC with and without additional blocking agents BSA and NFDm. (b) Number of specifically (green shaded) and nonspecifically (red shaded) bound PEGylated microspheres with covalently attached digoxigenin antibodies to SSLBs composed of a mixture of DSPC and DSPE-biotin. Specific binding was via DNA having biotin on one and digoxigenin on the other end (bio-dig, 50 ± 10 microspheres per field of view (FOV), mean \pm standard deviation). Controls used DNA having either only biotin (bio, 1 ± 1 microspheres/FOV) or digoxigenin (dig, 0.6 ± 1 microspheres/FOV) at one end, or DNA having both tags but the SSLB was not treated with NeutrAvidin (bio-dig - N, 0.5 ± 1 microspheres/FOV). Insets: Corresponding DIC images and schematics. The scale bar applies to all images. Note that the field of view used for quantification with an area of $905 \mu\text{m}^2$ was larger than the images shown.

nonspecifically with the SSLB, presumably at defects in the membrane.²² For SSLBs treated with BSA or nonfat dry milk (NFDm), nonspecific interactions were reduced more than 10-fold to a negligible level of 1.5 ± 1 and 1.1 ± 1 microspheres per field of view, respectively. Even though NFDm had a better blocking capacity, NFDm tended to form large clusters that compromised optical tweezer measurements. In addition, NFDm and casein led to nonspecific interactions with the DNA particularly when it was unzipped. Therefore, further SSLB experiments with DNA were performed in the presence of BSA.

To test specific binding, we tethered DNA having a biotin and digoxigenin tag at its respective ends between PEGylated, digoxigenin-antibody-coupled microspheres and SSLBs containing biotinylated lipids treated with NeutrAvidin (Figure 3b). In contrast to nonspecifically bound microspheres, all microspheres showed tethered particle motion indicative of specific attachment via the DNA. Controls showed again a negligible amount of nonspecific binding (Figure 3b). Based on the ratio of the number of nonspecifically to specifically bound microspheres, we expect that the number of false positives under specific binding conditions was less than 2%. Additional controls, using digoxigenin antibodies adsorbed to various hydrophobic surfaces,⁴⁴ and Pluronic F127¹⁵ or Tween20¹⁵ blocking treated with BSA or poly(acrylic acid), a negatively charged polymer mimicking nonspecific binding of DNA and blocking it, resulted in a large variation of false positives of at least 10% up to more than 50%. Thus, our method outperformed several other DNA attachment methods. Taken together, the SSLB with BSA blocking resulted in highly specific binding of DNA tethered microspheres with hardly any nonspecific interactions.

To test whether the SSLB could sustain higher loads, we unzipped and overstretched DNA with a closed hairpin (Figure 4). Loads were applied by trapping a tethered microsphere and moving a piezoelectric translation stage relative to the trapping laser.^{44,45} From the microsphere displacement and stage position, we calculated the DNA extension and force acting

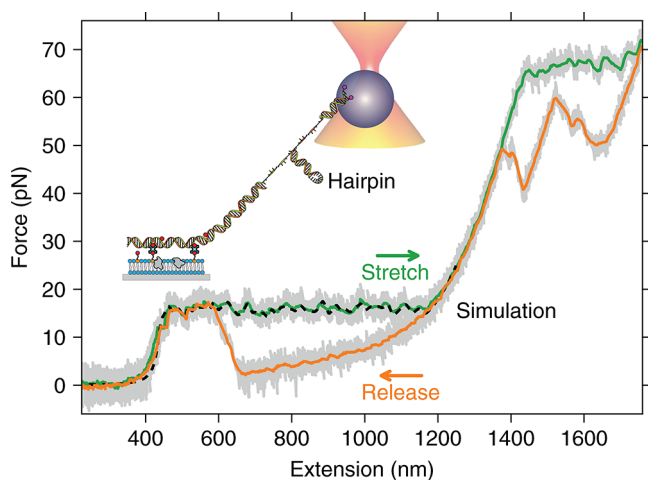


Figure 4. Force extension curve of a DNA hairpin with double stranded DNA (dsDNA) handles during a stretch–release cycle (green, stretching; orange, release; dashed black, simulation; gray, raw data). The SSLB and tethered microsphere attachment was the same as the specific condition in Figure 3b. Inset: Schematic of the DNA-tethered microsphere trapped and stretched by the optical tweezers with a partially unzipped DNA hairpin.

on the DNA. With increasing load, first the double stranded DNA (dsDNA) hairpin handles were stretched ($\lesssim 450$ nm extension) before the hairpin itself unzipped at about 15 pN (~ 450 – 1200 nm extension), exhibiting a sequence specific force–extension unzipping pattern.^{46,47} Once the hairpin was completely unzipped, the unzipped hairpin and the double stranded handles were further stretched (~ 1200 – 1400 nm extension) until the latter overstretched at about 65 pN eventually also separating the two strands of the double stranded handles ($\gtrsim 1400$ nm extension).⁴⁴ Upon force release, the overstretching of the DNA was reverted ($\gtrsim 1400$ nm extension) with a hysteretic re-zipping of the handles, followed by a reduction in extension of the handles and the opened hairpin (~ 1400 – 650 nm extension), and a re-zipping of the bases of the hairpin with a hysteresis (~ 650 – 450 nm extension). The black dashed line shows a simulation of the experimental force extension curve. The simulation accounts for the three-dimensional optical trap and is based on a combination of an improved worm-like chain model of Marko Siggia,⁴⁸ a freely jointed chain model for single stranded DNA,⁴⁹ and a thermodynamic theory.⁴⁷ The simulation fitted the force–extension data very well, especially the sequence specific unzipping pattern, allowing us to quantitatively determine the mechanical properties of the DNA. The SSLB DNA-tethered microsphere assay allowed for several hundred stretch–release cycles without degradation and nonspecific surface interactions. Together, the SSLB enabled quantitative DNA force measurements with long-term stability and minimal nonspecific interactions while sustaining loads up to 70 pN.

Controlling the phase transition of the SSLB provides an additional degree of freedom not available with any other surface passivation approach. In the fluid state of the membrane, lipids, including the anchoring points and tethered DNA, can be moved and organized by applying a hydrodynamic drag force through flow^{2,19} or potentially by using optical tweezers for individual manipulations. Here, we tested whether we could switch the SSLB to its fluid phase and reposition microspheres in a controlled fashion (Figure 5). We used an infrared heating laser with a wavelength of 1450 nm⁵⁰ to quickly heat the aqueous buffer above the melting point of the SSLB. Once the heating laser was turned on, individual fluorescent dye molecules within the lipid bilayer started to diffuse indicating that the membrane was fluid (Figure 5a). When we switched off the heating laser, within fractions of a second dye movement stopped consistent with the expected solid state of the SSLB. Thus, we could control the membrane phase on subsecond time scales allowing for a controlled, localized membrane organization. With the heating laser turned on, we could reposition microspheres within the heated region using the optical tweezers (Figure 5b,c and video S1). We demonstrate the repositioning of 35 microspheres by writing the word “NANO” (Figure 5d and videos S2 and S3).

Discussion. In general, our optimized SSLB platforms performed very well for single-molecule fluorescence and force measurements. Since supported fluid lipid bilayers had been used previously for kinesin assays,^{24,51,52} we were surprised that kinesin motors showed a significant amount of *transient* nonspecific binding on a subsecond time scale to phosphatidylcholine lipids. We attribute this transient binding to electrostatic interactions, most likely due to positively charged regions on kinesin motors⁵³ with the negative charges of the zwitterionic lipid headgroups or unreacted negatively charged, deprotonated carboxyl groups. Due to this transient binding,

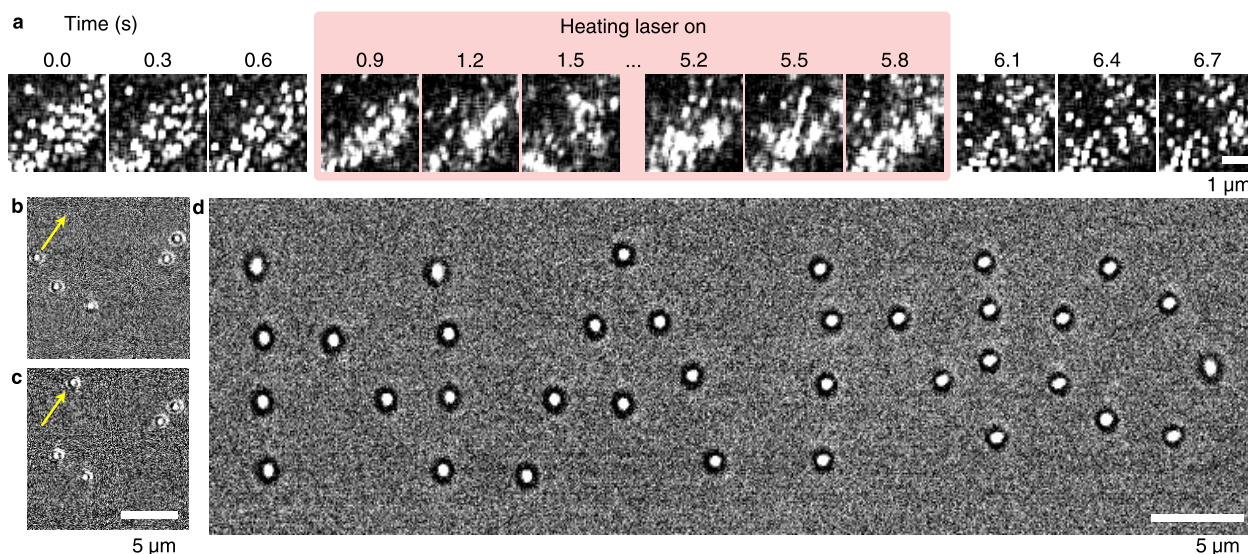


Figure 5. SSLB phase control. (a) Single dye molecules embedded in a SSLB and imaged by TIRF microscopy as a function of time. The heating laser was on from 0.9 to 5.8 s switching the SSLB into its fluid state. Note that some molecules bleach or blink. (b,c) Position of a microsphere attached to the SSLB via dsDNA (b) before and (c) after repositioning using the heating and trapping lasers (video S1). The yellow arrow indicates the repositioning process, while other microspheres serve as reference. Small differences of the reference microsphere positions between panels b and c are due to tethered particle motion. (d) The word “NANO” was produced by repositioning microspheres with the help of the heating and trapping lasers (videos S2 and S3).

we decided to PEGylate the bilayer. PEGylation of the SSLB composed mostly of 15:0 PC effectively blocked nonspecific binding (Figure 1c). However, PEGylation of the SFLB based on DOPC still showed a significant amount of transient binding. Apart from the mobility of the lipids, one reason for this transient, nonspecific binding in the case of the SFLB could be the difference in the headgroup area being larger in the fluid compared to the solid state. The fluidity and larger headgroup area might also reduce charge pairing of the zwitterionic headgroups⁵⁴ causing the negative charges of the headgroups to be more accessible. The accessibility of negative charges on non-PEGylated SSLBs might also explain why PEGylation was not necessary for the DNA experiments. Since DNA is negatively charged, there might be an effective electrostatic repulsion with the bilayer. In the presence of positively charged DNA binding proteins, PEGylation of the SSLB might become necessary.

Based on our results, the SSLB performed similarly to the Pluronic F127 assay. However, averaging over a long period and many different persons, reproducibility of the SSLB assay was higher. One reason for the variation of the Pluronic F127 assay on silanized surfaces might be the limited shelf life and sensitivity of silanes to humidity, which varies over the seasons. In cases where batches performed poorly, the hydrophobicity of the substrates quantified by the water contact angle, was often either too high or low. When the hydrophobicity is too low, not enough antibodies may adsorb that further specific binding is compromised. When the hydrophobicity is too high, proteins may denature on the surface. Denatured proteins may not be blocked sufficiently by the blocking agents increasing nonspecific binding. Such nonspecific binding we observed when we used the Pluronic F127 platform for our DNA assay employing digoxigenin antibodies on the hydrophobic surface. In this case, blocking with the negatively charged poly(acrylic acid) worked well. However, we expect that proteins that bind to DNA mainly through electrostatic interactions would also bind to the blocking polymer. Therefore, also for the DNA

assay, in particular when combined with DNA binding proteins, we expect our SSLB assay to outperform the Pluronic F127 assay. Moreover, the chemicals used during surface silanization are more hazardous and toxic to the environment. Furthermore, it took longer to block silanized slides with Pluronic F127 (~85 min) compared to prepare SSLB slides (~60 min), not accounting for the silanization process itself or lipid aliquotation. Taken together, the SSLBs were a more reliable, time efficient platform than the Pluronic F127 passivated surfaces.

In analogy to cellular assays,²¹ using a SSLB for single-molecule fluorescence and force measurements opens up the possibility to switch the fluidity of the membrane (Figure 5a). Using a heating laser allows switching on millisecond time scales.⁵⁰ After switching on the heating laser, we could observe single molecules diffusing in the membrane indicating its fluid nature. Since the laser can be used to heat a localized area, patterning of the anchoring points can in principle be achieved by the application of force through flow¹⁹ or optical tweezers. For example, heating only a stripe and applying a flow perpendicular to it, should move all anchoring points within the melted stripe to its boundary in analogy to DNA curtain experiments.^{2,19} Once a desired pattern is achieved it can be frozen in by switching off the heating laser. We tested this idea by repositioning individual microspheres (Figure 5b–d). Since heating may denature the involved proteins used for attachment and blocking, weaken noncovalent bonds, and melt the dsDNA (i.e., reduce the force for overstretching), we used the low-melting temperature 15:0 PC instead of DSPC that was used for the remaining DNA experiments. Thus, we could use less heating laser power. When we used a maximum trapping force well below the overstretching transition, we could only reposition about 50% of the microspheres. The remaining microspheres could not be moved. In these cases, the anchor point might be connected to defects in the membrane.²² Yet, these microspheres still showed tethered particle motion and their dsDNA tethers could be stretched

using the optical tweezers with and without the heating laser. Therefore, all other bonds for tether attachment were sufficiently strong even with the heating laser turned on. Furthermore, the low-force conditions ensured that the dsDNA tether was not melted and strands were not separated. Microspheres that could be moved were reattached to the membrane by pushing them down on the membrane surface using the trapping laser while the heating laser was still turned on. When repositioned particles were not pushed down on the membrane and the trap was turned off, microspheres were mostly not attached and diffused away. Thus, we infer for the microspheres that we could reposition that the DSPE-biotin lipid was pulled out of the fluid membrane. Based on the observations, we think that the lipid anchor was still connected to the DNA-tethered microsphere and that the lipid anchor was reinserted into the membrane after repositioning of the microspheres. To be able to reposition all microspheres for writing the word “NANO”, we increased the maximum trapping force above the DNA overstretching force. We think that for the microspheres that could not be repositioned with a lower force, the dsDNA strands were separated by the higher force and that upon repositioning, single-stranded-DNA-tethered microspheres bound nonspecifically to the surface. This nonspecific binding may explain the reduced tethered particle motion observed for a significant number of the “NANO” microspheres (video S3). Further optimization of the assay is necessary to improve the repositioning process. Nevertheless, the repositioning process is similar to the “cut-and-paste” surface assembly using atomic force microscopy⁵⁵ and opens up new possibilities for micromanipulation. In summary, we expect that in the long term, our optimized SSLB, allowing for the control of the membrane fluidity and microsphere repositioning combined with an excellent blocking performance, will have many applications for surface assembly, single-molecule fluorescence, and force measurements.

Materials and Methods. SSLB Preparation. Flow cells consisted of a glass coverslip sandwich separated by parafilm strips or double sided sticky tape that define a channel as described previously.⁵⁶ The cleaning procedure is briefly described. Coverslips were cleaned by sonication for 15 min in 5% mucosol, extensive rinsing in distilled water, sonication in 100% pure ethanol for 15 min, and again extensive rinsing in distilled water. This procedure was repeated at least once. Then coverslips were dried with filtered, dehydrated compressed air, and kept in a desiccator for about 1 h at 50 mbar. These precleaned coverslips can be stored in clean, parafilm-sealed containers for several weeks. All lipids were ordered from Avanti Polar Lipids, Inc. Individual lipids were dissolved in chloroform with stock concentrations of 10–25 mg/mL. Then, an amount of lipid solution that contained 1 mg of lipid was placed in a glass vial. To evaporate the solvent, the vial was placed in a desiccator overnight at 50 mbar. These aliquots were stored at $-20\text{ }^{\circ}\text{C}$. Lipids were hydrated in $65\text{ }^{\circ}\text{C}$ warm SSLB buffer (10 mM 4-(2-hydroxyethyl)-1-piperazineethanesulfonic acid (HEPES), 150 mM NaCl, pH 7.4) to concentrations of 1–10 mg/mL, mixed thoroughly by pipetting, and vortexed for 2 min to form multilamellar vesicles (MLVs). MLV solutions can be aliquoted and frozen. Subsequently, lipid mixtures were prepared by mixing the corresponding amounts of single-lipid MLV solutions to achieve the desired molar ratio between lipids. Alternatively, minor components (less than about 10 mol % of lipids) can be

added in their chloroform dissolved form to the aqueous lipid solutions. For differential scanning calorimetry measurements, a PerkinElmer 8000 DSC instrument and 10 mg of lipids from a desiccated 1 mg/mL MLV solution were used. Small unilamellar vesicles (SUVs) were formed by sonicating the MLV mixture for 20 min at $65\text{ }^{\circ}\text{C}$. Then, solutions were filled up with $65\text{ }^{\circ}\text{C}$ warm SSLB buffer to 1 mL resulting in a final total lipid concentration of about 0.5 mM. To induce fusion of SUVs to the glass surface, 5–6 μL of 0.5 M CaCl_2 was added to the SUV dispersion.⁵⁷ For SSLB formation, the flow cell channels were incubated for 10 min at $65\text{ }^{\circ}\text{C}$ with at least 50 μL of the CaCl_2 supplemented SUV dispersion on a hot plate. To remove excess CaCl_2 and unfused vesicles, the SSLB was washed with at least 100 μL of $65\text{ }^{\circ}\text{C}$ warm SSLB buffer. Incubation and washing can be repeated once. Subsequently, SSLB coated flow cells were cooled to room temperature for further use. If flow cell channels were closed, such flow cells could be stored for at least 1–2 weeks at $4\text{ }^{\circ}\text{C}$. For kinesin stepping assays, the SSLBs were prepared with 15:0 phosphatidyl choline (PC, 705 kDa) and 1,2-distearoyl-*sn*-glycero-3-phosphoethanolamine-*N*-[carboxy[poly(ethylene glycol)]-2000] (DSPE-COOH, 2779 kDa) in a 4:1 molar ratio. Based on a phosphoinositide strip (PIP) assay,⁵⁸ we found that PC and phosphatidylethanolamine (PE) groups interacted least with kinesin-1. For the negative control measurement, the SFLB was prepared with dioleoylphosphatidylcholine (DOPC, 786 kDa) and DSPE-COOH in a 4:1 molar ratio. For the DNA tether pulling assay and the SSLB phase transition experiment, 1,2-distearoyl-*sn*-glycero-3-phosphocholine (DSPC, 790 kDa) and 1,2-distearoyl-*sn*-glycero-3-phosphoethanolamine-*N*-[biotinyl[poly(ethylene glycol)]-2000] (DSPE-biotin, 3015 kDa) were used in a 2000:1 molar ratio. For the microsphere repositioning experiment, 15:0 PC and DSPE-biotin in a 2000:1 molar ratio were used.

SSLB PEGylation and Microtubule Attachment. Tubulin antibodies and PEG molecules were covalently bound to the SSLB via carbodiimide coupling using 1-(3-(dimethylamino)propyl)-3-ethylcarbodiimide hydrochloride (EDC, Sigma-Aldrich, Germany) and *N*-hydroxysulfosuccinimide sodium (NHS, Sigma-Aldrich, Germany). All steps were carried out at room temperature. To activate the carboxylic acid group of DSPE-COOH, a freshly prepared solution of 4.5 mg of NHS and 4.0 mg of EDC in 200 μL of coupling buffer (PolySciences, Germany) was added to the SSLB flow cell, incubated for 15 min, and washed out twice with 200 μL of coupling buffer. Then, 20 μL of monofunctional α -methoxy- ω -amino-PEG (mPEG, 2 kDa, catalogue number 122000-2, Rapp Polymere GmbH, Tübingen, Germany) at a concentration of 1 mg/mL in PEM buffer (80 mM PIPES, 1 mM EGTA, 1 mM MgCl_2 , adjusted with KOH to pH 6.9) was mixed with 20 μL of monoclonal β -tubulin antibodies (SAP.4G5; Sigma, Germany; specified concentration 3–6 mg/mL) diluted 100X in PEM buffer. With the antibody molecular weight of about 150 kDa and using the lower limit of the specified concentration, the antibody and mPEG concentrations were about 0.2 μM and 5 μM , respectively, resulting in a molar ratio of antibody to mPEG of about 1:25. The flow cell was incubated with this solution for 15 min and rinsed with 100 μL of PEM. Taxol stabilized, rhodamine-labeled microtubules were prepared as described previously,⁵⁶ and 20 μL of microtubules in PEM with 10 μM taxol (PEM-T) were incubated for about 10 min in the flow cell, which was subsequently rinsed with PEM-T. Note that when the antibody

concentration was decreased to 0.02 μM during the coupling reaction while keeping the molar concentration of mPEG constant, microtubules were not rigidly attached anymore. Microtubules were also not rigidly attached when the molar ratio of 15:0 PC to DSPE-COOH was increased to 9:1 (using 0.2 μM of antibody). Thus, more than 0.02 μM and 10 mol % antibody and DSPE-COOH, respectively, were required for proper fixation of microtubules to the SSLB surface.

Preparation Times for the SSLB and Pluronic F127 Assays. The Pluronic F127 assay was prepared as previously described.^{13,14,59} Without the precleaning procedures, lipid aliquotation, and silanization of the coverslips (the latter usually taking about 1 day for a batch of coverslips requiring harsh chemical cleaning steps), a rough estimate for the preparation time of the Pluronic F127 assay is about 85 min (15 min antibody incubation, 45 min Pluronic F127 blocking, 10 min microtubule binding, and about 15 min for preparation and time between steps). The SSLB preparation time is roughly 60 min (10 min SSLB preparation, 15 min COOH group activation, 10 min antibody coupling, 10 min microtubule binding, and about 15 min for preparation and time between steps).

TIRF Kinesin Stepping Assay. Truncated rk430 kinesin1-eGFP-6 \times His (here called kinesin-1) was purified as described previously.⁴² Kinesin-1 with a stock concentration of 12.1 mg/mL was diluted 1000 \times in motility buffer (PEM with 0.16 mg/mL casein, 1 mM ATP, and an antifade cocktail [20 mM D-glucose, 0.02 mg/mL glucose oxidase, 0.008 mg/mL catalase, and 10 mM dithiothreitol (DTT)]) for nonspecific binding TIRF measurements and 10⁶ \times for single-molecule TIRF measurements. Images were acquired in a custom-made TIRF microscope at 32 $^{\circ}\text{C}$.⁶⁰ To estimate the velocity and run length of kinesin-1 on microtubules, movies were recorded and imaged at a frame rate of 10 frames/s. The average intensity of GFP-tagged kinesin-1 nonspecifically bound to the differently treated surfaces was quantified using the software Fiji.⁶¹ Regions of interests were 28 \times 28 pixel large. Results were plotted in a combined Tukey box and violin plot. The box corresponds to quartiles, with the inside line being the second quartile (the median). The whiskers correspond to the lowest datum that is still within the 1.5 interquartile range (IQR) of the lower quartile, and the highest datum still within 1.5 IQR of the upper quartile. Data points beyond the whiskers are considered outliers. In addition, the probability density of the data smoothed by a kernel density estimator is shown using the function violinplot of the package Matplotlib.

Kinesin Optical Tweezers Assay. For force measurements, kinesin-1 was bound via a GFP nanobody³⁷ (gift of Ulrich Rothbauer, NMI, Reutlingen, Germany) (13 kDa) to carboxylated polystyrene microspheres (PS-COOH, Bangs Laboratories, order number PC03N/6487, diameter 590 nm, 10% solids, surface charge 28.5 $\mu\text{eq/g}$) using carbodiimide coupling as described previously³⁸ except that nanobodies were used instead of antibodies. GFP-nanobodies and mPEG were coupled directly to the microspheres in a molar ratio of 1:10 000. Kinesin-1 was bound to microspheres and used in motility buffer such that single-molecule conditions were met.³⁸ Measurements were performed at 29.4 $^{\circ}\text{C}$ in our high-precision optical tweezers setup.⁴⁰ The trap stiffness was about 0.053 pN/nm. Signals were recorded with 25 kHz in three dimensions with a position-sensitive photodiode imaging the back focal plane. Data was processed using a forward and backward filter.^{13,62} We developed and used a step-detection

Python package³⁶ based on the Chung–Kennedy filter.^{13,62} The filter works very efficiently in particular, for large data sets and was used here to detect steps in the kinesin traces. The filter time was set to 4.8 ms.

Preparation of Microspheres for DNA Experiments. Microspheres for DNA experiments were prepared similar to the ones for kinesin experiments except for larger carboxylated microspheres with a diameter of 820 (Bangs Laboratories, PC03N/11001) and the use of the Polylink Protein Coupling Kit (Bangslabs, PL01N, 13820) with either NeutrAvidin (Roche) or digoxigenin antibodies (Roche) carbodiimide coupled directly to the microspheres together with mPEG in a molar ratio of 1:40 000 and 1:75 000, respectively.

Specific and Unspecific DNA Constructs. Three different double stranded DNA (dsDNA) constructs with a length of 3057 bp were synthesized via a standard polymerase chain reaction (PCR) using λ -phage DNA as a template. Forward and backward primers (Table 1) contained either a 5'-biotin (bio), a 5'-digoxigenin and internal dT-digoxigenin (dig), or both modifications (bio-dig).

Table 1. Primers Used for Synthesis of the 3057 bp dsDNA Binding Construct^a

	forward primer	backward primer
(Bio)-	ATATCAACCCGGAGCTTGG	(Dig)-
		CTTTGCATCXTCCGCACTCT

^aX denotes dT-Dig.

DNA Unzipping Construct. The unzipping construct was built out of five dsDNA segments and three single stranded DNA (ssDNA) oligonucleotides. First, the dsDNA segments were synthesized via PCR with the primers given in Table 2.

Table 2. Primers used for Synthesis of the Unzipping Construct

primer ^a	sequence
at F	ATATCAACCCGGAGCTTGG
at B	P-
	TACCGTTTTGTGAAGAGCCAGCTCTGATGCCAATCCAC
ab F	P-CACTACAATTTGAAGAGCGAACTCAGCCAGAACGACAA
ab B	CTTTGCATCTTCCGCACTCT
A F	P-CAAAACGGTATGAAGAGCAAACCAAGCCAATCCCAA
A B	GCCATACGAACGAAGAGCCTGCTGCTTTTTCCGCTTTT
B F	GTGTCGATGTCATTGCCAGCACAAAAGCGGAAATC
B B	P-
	AATTGTAGTGTGAAGAGCCCGCGCCTTTGATTCTTTT
C F	TGTGCCAACACATTGCGACTATCGCACCATCAGCCA
C B	CAGTAGCTTGCACTGCGGCTTTGATTCCAC

^aF and B denote forward and backward primers.

Three of the segments (A, B, and C) were amplified with a standard nucleoside triphosphate mix (dATP, dTTP, dCTP, dGTP) and the Pfu DNA Polymerase (Invitrogen) resulting in two dsDNA spacer segments (A and B, 457 bp and 942 bp long, respectively) and a long dsDNA segment to be unzipped (C, 1399 bp). Two dsDNA segments were amplified with 10 of the dTTPs replaced with Dig-11-dUTPs and Bio-11-dUTPs and the Taq Polymerase resulting in the two attachment segments for the top (at, 249 bp) and the bottom (ab, 295 bp) of the unzipping construct. The dsDNA segments were purified, digested with the nicking enzymes Nt.BspQI and Nb.BsrDI (NEB) to produce 10 nt long ssDNA overhangs, and

Table 3. Oligonucleotides Used for the Assembly of the Unzipping Construct

oligo	sequence
linker A–C	P-TTCGTATGGCTTTTTGATACGTTCTTACCCATACTCCACCGTTGCTGTGCCAACA
linker B–C	P-GCAACGGTGGAGTATGGGTAAGAACGTATCTTTTTGTGTGCATGT
hairpin	P-CCGTCGTATTTTTTTTTTTTATACGACCGGCAGTAGCTTG

again purified. The dsDNA segments were ligated with the oligonucleotides listed in Table 3 and the T7 DNA Ligase (NEB). The unzipping construct was separated from by-products via gel purification. The resulting unzipping construct could be tethered between a microsphere and the surface with segment C being unzipped by pulling on the microsphere.

Unspecific Binding of Microspheres to SSLBs. Flow cells with preformed SSLBs were incubated for 10 min with 200 μL of three different blocking solutions containing buffer A only (see Table 4 for buffer composition), buffer A with BSA (10

Table 4. Buffer Components^a

buffer	NaCl (mM)	other components
A	10	
B	50	
C	10	10 mg/mL BSA
D	50	10 mg/mL BSA
E	50	20 mM ascorbic acid, 0.1 mg/mL BSA

^aAll buffers contain 0.1 vol % Tween 20 and 10 mM tris-(hydroxymethyl)aminomethane at pH 7.3.

mg/mL), and buffer A with NFDm (10 mg/mL, Blotting-Grade Blocker, Bio-Rad, Germany). Microspheres from the coupling reaction were washed twice with 100 μL of buffer A, resuspended in 10 μL of buffer A, and incubated for 15 min with 100 μL of buffer A, buffer A with BSA, and buffer A with NFDm. The microspheres were further spun down, resuspended in 20 μL of the corresponding buffer, flushed into the flow cell, and incubated for 15 min. Unbound microspheres were flushed out with the corresponding blocking buffer, and images of bound microspheres were recorded with a LED-DIC microscope⁴³ with a field of view of $34.8 \times 26.0 \mu\text{m}^2$ corresponding to an area of $905 \mu\text{m}^2$.

Specific Binding of dsDNA to SSLBs. Flow cells with preformed SSLBs were incubated with 200 μL of buffer C for 10 min and washed with 200 μL of buffer A without NeutrAvidin. Flow cells for positive controls were additionally incubated with 20 μL of NeutrAvidin (0.2 mg/mL) in buffer A for 5 min and washed with 200 μL of buffer A. Microspheres from the coupling reaction were blocked in buffer C overnight, washed three times with 200 μL of buffer A, and resuspended in 20 μL of buffer A. The dsDNA constructs (100 pM) were incubated for 10 min either in the flow cell (100 μL of bio-dig and bio) or with the microspheres (dig and bio-dig – N). Flow cells and microspheres were washed with 200 μL of buffer A, and microspheres were resuspended in 20 μL of buffer A. Microspheres were flushed in the corresponding flow cells and incubated for 15 min. Unbound microspheres were washed out with 200 μL of buffer A, and images of bound microspheres were recorded as for the nonspecific binding experiments.

Unzipping Experiment on SSLBs. Flow cells with preformed SSLBs were incubated with 200 μL of buffer D for 10 min, washed with 200 μL of buffer B, incubated with 20 μL of 0.2 mg/mL NeutrAvidin in buffer B for 5 min, and washed again with 200 μL of buffer B. Microspheres from the

coupling reaction were incubated in 100 μL of buffer D overnight, washed three times with 200 μL of buffer B, and resuspended in 10 μL of buffer B. Ten μL of 200 pM unzipping construct in buffer B was added and incubated for 20 min. Flow cells were incubated for 10 min with microspheres and the unzipping construct. All unbound microspheres and unzipping constructs were washed out by flushing the flow cell two times with 200 μL of buffer E. Unzipping was achieved by trapping a tethered microsphere ~ 160 nm above the surface with a lateral trap stiffness of about 0.7 pN/nm and moving the stage in horizontal direction with a triangular motion with an amplitude of 4.5 μm and a speed of 4.5 $\mu\text{m/s}$ in analogy to earlier experiments.⁴⁴ The experimental unzipping traces were simulated with the Python package “Unzipping Simulation”⁶³ using the ssDNA elastic modulus $S = 0.8$,⁴⁹ a ssDNA persistence length $L_p = 0.75$ nm,⁴⁹ and a ssDNA contour length per base of $z = 0.538$ nm/base. For the dsDNA, we used a contour length per bp of 0.338 and a persistence length of $L_{p,\text{dsDNA}} = 50$ nm. Base pairing energies used were “A” $1.2k_B T$, “T” $1.2k_B T$, “G” $3.4k_B T$, and “C” $3.4k_B T$. The resolution of the simulation was 1 nm.

Heating of SSLBs and Repositioning of Microspheres. The SSLB for the phase transition experiment was composed of DSPC supplemented with 0.0003 3,3'-dioctadecylxycarboxyanine perchlorate (DiO) (without DSPE-biotin). The microsphere repositioning experiment was done with 15:0 PC and DSPE-biotin in a 2000:1 molar ratio. The dsDNA was labeled with one biotin and two digoxigenins at the respective ends (see Table 1). Microspheres were attached to the surface with the protocol given in section “Specific Binding of dsDNA to SSLBs”. The trapping laser power was chosen in such a way that the maximum force of the trap was either well below or slightly above the dsDNA overstretching force for repositioning individual microspheres or writing the word “NANO”, respectively. Without the heating laser, the temperature was 28.2 °C. With the heating laser, the temperature was above the phase transition temperature of the corresponding lipid mixtures.

■ ASSOCIATED CONTENT

Supporting Information

The Supporting Information is available free of charge at <https://pubs.acs.org/doi/10.1021/acs.nanolett.9b03761>.

Video S1, Repositioning of one microsphere with the help of the heating and trapping laser: DNA-tethered microsphere attached to SSLB was repositioned using heating and trapping lasers. The video first shows tethered particle motion without heating or trapping. Then, the microsphere in the upper left-hand corner was trapped using the optical tweezers. Without the heating laser, the trapped particle could not be repositioned by moving the sample stage relative to the stationary trapping laser. Instead, the microsphere was pulled out of the optical trap (tested 3 \times). Once the heating laser was switched on, the lipid bilayer became fluid, and the microsphere could be repositioned. Tethered particle

motion resumed once the optical trap was turned off. Scale bar 5 μm . (MP4)

Video S2, Writing “NANO” by repositioning microspheres: 35 microspheres were used to write the word “NANO” by the same procedure as shown in Video S1; 45 \times real time; scale bar 5 μm . (MP4)

Video S3, Tethered particle motion of “NANO” microspheres: tethered particle motion of “NANO” microspheres; microspheres that show reduced or no tethered particle motion have nonspecific interactions with the SSLB after repositioning; scale bar 5 μm . (MP4)

AUTHOR INFORMATION

Corresponding Author

*E-mail: erik.schaeffer@uni-tuebingen.de.

ORCID

Erik Schäffer: 0000-0001-7876-085X

Author Contributions

[‡]S.S. and T.J.J. contributed equally to this work. E.S., S.S., and T.J.J. designed the research. S.S. and T.J.J. performed the kinesin and DNA/heating experiments, respectively. M.K. and A.M. helped to develop the supported lipid bilayer assay. G.L.H. developed and built the heating laser setup and helped with heating laser experiments. M.K.A. helped with the data analysis. S.S., T.J.J., and E.S. analyzed the data and wrote the manuscript. All authors commented on the manuscript.

Notes

The authors declare no competing financial interest.

ACKNOWLEDGMENTS

Authors thank Mayank Chugh for help in performing the PIP strip assays. We further thank him, Anita Jannasch, and Michael Bugiel for comments on the manuscript. Also, we thank Ulrich Rothbauer for the GFP nanobody and Begoña Ugarte-Urbe, Katia Cosentino, and Ana J. García-Sáez for a supported fluid lipid bilayer protocol. This work was supported by the International Max Planck Research Schools from Molecules to Organisms, Max Planck Institute for Developmental Biology, Tübingen, the Deutsche Forschungsgemeinschaft in terms of the Collaborative Research Center 1101, and the PhD Network: “Novel nanoparticles: from synthesis to biological applications” of the Eberhard Karls Universität Tübingen.

REFERENCES

- (1) Kim, H.; Ha, T. Single molecule nanometry for biological physics. *Rep. Prog. Phys.* **2013**, *76*, 016601.
- (2) Visnapuu, M. L.; Duzdevich, D.; Greene, E. C. The importance of surfaces in single molecule bioscience. *Mol. BioSyst.* **2008**, *4*, 394–403.
- (3) Ha, T.; Rasnik, I.; Cheng, W.; Babcock, H. P.; Gauss, G. H.; Lohman, T. M.; Chu, S. Initiation and re-initiation of DNA unwinding by the *Escherichia coli* Rep helicase. *Nature* **2002**, *419*, 638–641.
- (4) Heyes, C. D.; Groll, J.; Möller, M.; Nienhaus, G. U. Synthesis, patterning and applications of star-shaped poly(ethylene glycol) biofunctionalized surfaces. *Mol. BioSyst.* **2007**, *3*, 419–430.
- (5) Blümmel, J.; Perschmann, N.; Aydin, D.; Drinjakovic, J.; Surrey, T.; Lopez-Garcia, M.; Kessler, H.; Spatz, J. P. Protein repellent properties of covalently attached PEG coatings on nanostructured SiO₂-based interfaces. *Biomaterials* **2007**, *28*, 4739–4747.

(6) Zimmermann, J. L.; Nicolaus, T.; Neuert, G.; Blank, K. Thiol-based, site-specific and covalent immobilization of biomolecules for single-molecule experiments. *Nat. Protoc.* **2010**, *5*, 975–985.

(7) Schwartzman, M.; Palma, M.; Sable, J.; Abramson, J.; Hu, X.; Sheetz, M. P.; Wind, S. J. Nanolithographic control of the spatial organization of cellular adhesion receptors at the single-molecule level. *Nano Lett.* **2011**, *11*, 1306–12.

(8) Turner, D. K.; Wayman, A. E.; Rolando, C. N.; Dande, P.; Carter, P. W.; Remsen, E. E. Reduction of artifacts in fluorescence correlation spectroscopy due to sample desorption on optical glass surfaces. *Appl. Spectrosc.* **2013**, *67*, 692–698.

(9) Gust, A.; Zander, A.; Gietl, A.; Holzmeister, P.; Schulz, S.; Lalkens, B.; Tinnefeld, P.; Grohmann, D. A starting point for fluorescence-based single-molecule measurements in biomolecular research. *Molecules* **2014**, *19*, 15824–15865.

(10) Cai, H.; Wind, S. J. Improved glass surface passivation for single-molecule nanoarrays. *Langmuir* **2016**, *32*, 10034–10041.

(11) Helenius, J.; Brouhard, G.; Kalaidzidis, Y.; Diez, S.; Howard, J. The depolymerizing kinesin MCAK uses lattice diffusion to rapidly target microtubule ends. *Nature* **2006**, *441*, 115–119.

(12) Schäffer, E.; Nørrelykke, S. F.; Howard, J. Surface forces and drag coefficients of microspheres near a plane surface measured with optical tweezers. *Langmuir* **2007**, *23*, 3654–3665.

(13) Bormuth, V.; Varga, V.; Howard, J.; Schäffer, E. Protein friction limits diffusive and directed movements of kinesin motors on microtubules. *Science* **2009**, *325*, 870–873.

(14) Gell, C.; Bormuth, V.; Brouhard, G. J.; Cohen, D. N.; Diez, S.; Friel, C. T.; Helenius, J.; Nitzsche, B.; Petzold, H.; Ribbe, J.; Schäffer, E.; Stear, J. H.; Trushko, A.; Varga, V.; Widlund, P. O.; Zanic, M.; Howard, J. Microtubule dynamics reconstituted in vitro and imaged by single-molecule fluorescence microscopy. *Methods Cell Biol.* **2010**, *95*, 221–245.

(15) Hua, B.; Han, K. Y.; Zhou, R.; Kim, H.; Shi, X.; Abeyirigunawardena, S. C.; Jain, A.; Singh, D.; Aggarwal, V.; Woodson, S. A.; Ha, T. An improved surface passivation method for single-molecule studies. *Nat. Methods* **2014**, *11*, 1233–6.

(16) Sackmann, E. Supported membranes: scientific and practical applications. *Science* **1996**, *271*, 43–48.

(17) Castellana, E. T.; Cremer, P. S. Solid supported lipid bilayers: From biophysical studies to sensor design. *Surf. Sci. Rep.* **2006**, *61*, 429–444.

(18) Groves, J. T.; Dustin, M. L. Supported planar bilayers in studies on immune cell adhesion and communication. *J. Immunol. Methods* **2003**, *278*, 19–32.

(19) Granéli, A.; Yeykal, C. C.; Prasad, T. K.; Greene, E. C. Organized arrays of individual DNA molecules tethered to supported lipid bilayers. *Langmuir* **2006**, *22*, 292–299.

(20) Pyrpasopoulos, S.; Shuman, H.; Ostap, E. M. Single-molecule adhesion forces and attachment lifetimes of myosin-I phosphoinositide interactions. *Biophys. J.* **2010**, *99*, 3916–3922.

(21) Andreasson-Ochsner, M.; Romano, G.; Håkanson, M.; Smith, M. L.; Leckband, D. E.; Textor, M.; Reimhult, E. Single cell 3-D platform to study ligand mobility in cell–cell contact. *Lab Chip* **2011**, *11*, 2876–2883.

(22) Attwood, J. S.; Choi, Y.; Leonenko, Z. Preparation of DOPC and DPPC supported planar lipid bilayers for atomic force microscopy and atomic force spectroscopy. *Int. J. Mol. Sci.* **2013**, *14*, 3514.

(23) Sarangapani, K. K.; Duro, E.; Deng, Y.; Alves, F. d. L.; Ye, Q.; Opoku, K. N.; Ceto, S.; Rappsilber, J.; Corbett, K. D.; Biggins, S.; Marston, A. L.; Asbury, C. L. Sister kinetochores are mechanically fused during meiosis I in yeast. *Science* **2014**, *346*, 248–251.

(24) Grover, R.; Fischer, J.; Schwarz, F. W.; Walter, W. J.; Schwille, P.; Diez, S. Transport efficiency of membrane-anchored kinesin-I motors depends on motor density and diffusivity. *Proc. Natl. Acad. Sci. U. S. A.* **2016**, *113*, E7185–7193.

(25) Glazier, R.; Salaita, K. Supported lipid bilayer platforms to probe cell mechanobiology. *Biochim. Biophys. Acta, Biomembr.* **2017**, *1859*, 1465–1482.

- (26) Ma, L.; Cai, Y.; Li, Y.; Jiao, J.; Wu, Z.; et al. Single-molecule force spectroscopy of protein membrane interactions. *eLife* **2017**, *6*, e30493.
- (27) Glasmästar, K.; Larsson, C.; Höök, F.; Kasemo, B. Protein adsorption on supported phospholipid bilayers. *J. Colloid Interface Sci.* **2002**, *246*, 40–47.
- (28) Brian, A. A.; McConnell, H. M. Allogeneic stimulation of cytotoxic T cells by supported planar membranes. *Proc. Natl. Acad. Sci. U. S. A.* **1984**, *81*, 6159–6163.
- (29) Richter, R. P.; Bérat, R.; Brisson, A. R. Formation of solid-supported lipid bilayers: An integrated view. *Langmuir* **2006**, *22*, 3497–3505.
- (30) Hohner, A. O.; David, M. P. C.; Rädler, J. O. Controlled solvent-exchange deposition of phospholipid membranes onto solid surfaces. *Biointerphases* **2010**, *5*, 1–8.
- (31) Tabaei, S. R.; Choi, J.-H.; HawZan, G.; Zhdanov, V. P.; Cho, N.-J. Solvent-Assisted Lipid Bilayer Formation on Silicon Dioxide and Gold. *Langmuir* **2014**, *30*, 10363–10373.
- (32) Howard, J.; Hudspeth, A. J.; Vale, R. D. Movement of Microtubules by Single Kinesin Molecules. *Nature* **1989**, *342*, 154–158.
- (33) Block, S. M.; Goldstein, L. S. B.; Schnapp, B. J. Bead Movement by Single Kinesin Molecules Studied with Optical Tweezers. *Nature* **1990**, *348*, 348–352.
- (34) Kawaguchi, K.; Ishiwata, S. Temperature dependence of force, velocity, and processivity of single kinesin molecules. *Biochem. Biophys. Res. Commun.* **2000**, *272*, 895–899.
- (35) Ruhnaw, F.; Kloß, L.; Diez, S. Challenges in Estimating the Motility Parameters of Single Processive Motor Proteins. *Biophys. J.* **2017**, *113*, 2433–2443.
- (36) Jachowski, T. Stepfinder: A Python package to find steps in one dimensional data with low SNR. GitHub repository: <https://github.com/tobiasjj/stepfinder>, 2018–2019.
- (37) Rothbauer, U.; Zolghadr, K.; Muylderms, S.; Schepers, A.; Cardoso, M. C.; Leonhardt, H. A Versatile Nanotrapp for Biochemical and Functional Studies with Fluorescent Fusion Proteins. *Mol. Cell. Proteomics* **2008**, *7*, 282–289.
- (38) Bugiel, M.; Fantana, H.; Bormuth, V.; Trushko, A.; Schiemann, F.; Howard, J.; Schäffer, E.; Jannasch, A. Versatile microsphere attachment of GFP-labeled motors and other tagged proteins with preserved functionality. *J. Biol. Methods* **2015**, *2*, 30.
- (39) Tolić-Nørrelykke, S. F.; Schäffer, E.; Howard, J.; Pavone, F. S.; Jülicher, F.; Flyvbjerg, H. Calibration of optical tweezers with positional detection in the back focal plane. *Rev. Sci. Instrum.* **2006**, *77*, 103101.
- (40) Mahamdeh, M.; Schäffer, E. Optical tweezers with millikelvin precision of temperature-controlled objectives and base-pair resolution. *Opt. Express* **2009**, *17*, 17190–17199.
- (41) Svoboda, K.; Block, S. M. Force and velocity measured for single kinesin molecules. *Cell* **1994**, *77*, 773–784.
- (42) Ramaia, A.; Roy, B.; Bugiel, M.; Schäffer, E. Kinesin rotates unidirectionally and generates torque while walking on microtubules. *Proc. Natl. Acad. Sci. U. S. A.* **2017**, *114*, 10894–10899.
- (43) Bormuth, V.; Howard, J.; Schäffer, E. LED illumination for video-enhanced DIC imaging of single microtubules. *J. Microsc.* **2007**, *226*, 1–5.
- (44) Ander, M.; Subramaniam, S.; Fahmy, K.; Stewart, A. F.; Schäffer, E. A single strand annealing protein clamps DNA to detect and secure homology. *PLoS Biol.* **2015**, *13*, e1002213.
- (45) Wang, M. D.; Yin, H.; Landick, R.; Gelles, J.; Block, S. M. Stretching DNA with optical tweezers. *Biophys. J.* **1997**, *72*, 1335–1346.
- (46) Bockelmann, U.; Essevaz-Roulet, B.; Heslot, F. Molecular stick-slip motion revealed by opening DNA with piconewton forces. *Phys. Rev. Lett.* **1997**, *79*, 4489–4492.
- (47) Bockelmann, U.; Essevaz-Roulet, B.; Heslot, F. DNA strand separation studied by single molecule force measurements. *Phys. Rev. E: Stat. Phys., Plasmas, Fluids, Relat. Interdiscip. Top.* **1998**, *58*, 2386–2394.
- (48) Petrosyan, R. Improved approximations for some polymer extension models. *Rheol. Acta* **2017**, *56*, 21–26.
- (49) Smith, S. B.; Cui, Y.; Bustamante, C. Overstretching B-DNA: the elastic response of individual double-stranded and single-stranded DNA molecules. *Science* **1996**, *271*, 795–799.
- (50) Holmstrom, E.; Dupuis, N.; Nesbitt, D. Pulsed IR Heating Studies of Single-Molecule DNA Duplex Dissociation Kinetics and Thermodynamics. *Biophys. J.* **2014**, *106*, 220–231.
- (51) Fischer, J. Investigation of microtubule motility driven by Membrane-anchored motor proteins. Diploma Thesis, Technische Universität Dresden, May 12, 2010.
- (52) Li, Q.; Tseng, K.-F.; King, S. J.; Qiu, W.; Xu, J. A fluid membrane enhances the velocity of cargo transport by small teams of kinesin-1. *J. Chem. Phys.* **2018**, *148*, 123318.
- (53) Grant, B. J.; M. Gheorghe, D.; Zheng, W.; Alonso, M.; Huber, G.; Dlugosz, M.; McCammon, J. A.; Cross, R. A. Electrostatically Biased Binding of Kinesin to Microtubules. *PLoS Biol.* **2011**, *9*, e1001207.
- (54) Pasenkiewicz-Gierula, M.; Takaoka, Y.; Miyagawa, H.; Kitamura, K.; Kusumi, A. Charge Pairing of Headgroups in Phosphatidylcholine Membranes: A Molecular Dynamics Simulation Study. *Biophys. J.* **1999**, *76*, 1228–1240.
- (55) Kufer, S.; Puchner, E.; Gump, H.; Liedl, T.; Gaub, H. Single-molecule cut-and-paste surface assembly. *Science* **2008**, *319*, 594–596.
- (56) Jannasch, A.; Bormuth, V.; Storch, M.; Howard, J.; Schäffer, E. Kinesin-8/slow-force motor protein with a weakly bound slip state. *Biophys. J.* **2013**, *104*, 2456–2464.
- (57) Unsay, J. D.; Cosentino, K.; García-Sáez, A. J. Atomic force microscopy imaging and force spectroscopy of supported lipid bilayers. *J. Visualized Exp.* **2015**, e52867.
- (58) Urbanek, A. N.; Allwood, E. G.; Smith, A. P.; Booth, W. I.; Ayscough, K. R. Distinct actin and lipid binding sites in Ysc84 are required during early stages of yeast endocytosis. *PLoS One* **2015**, *10*, e0136732.
- (59) Simmert, S.; Abdosamadi, M. K.; Hermsdorf, G.; Schäffer, E. LED-based interference reflection microscopy combined with optical tweezers for quantitative three dimensional microtubule imaging. *Opt. Express* **2018**, *26*, 14499–14513.
- (60) Schellhaus, A. K.; Moreno-Andrés, D.; Chugh, M.; Yokoyama, H.; Moschopoulou, A.; De, S.; Bono, F.; Hipp, K.; Schäffer, E.; Antonin, W. Developmentally Regulated GTP binding protein 1 (DRG1) controls microtubule dynamics. *Sci. Rep.* **2017**, *7*, 9996.
- (61) Schindelin, J.; Arganda-Carreras, I.; Frise, E.; Kaynig, V.; Longair, M.; Pietzsch, T.; Preibisch, S.; Rueden, C.; Saalfeld, S.; Schmid, B.; Tinevez, J.-Y.; White, D. J.; Hartenstein, V.; Eliceiri, K.; Tomancak, P.; Cardona, A. Fiji: an open-source platform for biological-image analysis. *Nat. Methods* **2012**, *9*, 676–82.
- (62) Chung, S. H.; Kennedy, R. A. Forward-backward non-linear filtering technique for extracting small biological signals from noise. *J. Neurosci. Methods* **1991**, *40*, 71–86.
- (63) Jachowski, T. Unzipping Simulation: A Python package to simulate the unzipping of DNA double strands. GitHub repository: https://github.com/tobiasjj/unzipping_simulation, 2018–2019.

Germanium nanospheres for ultraresolution picotensiometry of kinesin motors

Swathi Sudhakar,¹ Mohammad Kazem Abdosamadi,¹ Tobias Jörg Jachowski,¹
Michael Bugiel,¹ Anita Jannasch,¹ Erik Schäffer^{1*}

¹Eberhard Karls Universität Tübingen, Cellular Nanoscience (ZMBP)
Auf der Morgenstelle 32, 72076 Tübingen, Germany

*To whom correspondence should be addressed; E-mail: erik.schaeffer@uni-tuebingen.de

INTRODUCTION

Cytoskeletal motors drive many essential mechanical processes inside cells. For example, kinesin motors are key for cell division or vesicle transport. Kinesin-1 transports cargo along microtubules by coupling ATP hydrolysis to perform mechanical work against piconewton loads. This force generation and overall transport distance are limited by motor detachment. However, how kinesins walk and detach is still unclear.

To simultaneously measure the nanoscale motion and forces of molecular machines, optical tweezers are often used. In the tight, mostly infrared laser focus of optical tweezers, small dielectric particles can be trapped and used as handles for sensitive position and force measurements. Because optical forces scale with the particle volume, piconewton force measurements with nanoparticles require a high laser power. This high power leads to excessive heating and precludes biological measurements. Therefore, for biological single-molecule measurements, micron-sized probes are used. However, such probes have a large hydrodynamic drag and, therefore, lack the spatiotemporal resolution to unravel important fast or small details in the

mechanochemistry of molecular machines. These details remain hidden in the storm of Brownian motion.

RATIONALE

To overcome this practical resolution limit of optical tweezers and resolve so far hidden conformational changes of proteins, we sought to compensate the volume scaling of optical trapping forces by the use of probe materials with a very high refractive index and low light absorption. This compensation should allow the use of nanometer-size probes and generation of piconewton optical forces without detrimental heating but with improved temporal response and spatial precision. Promising materials include silicon and germanium that become transparent in the near-infrared with very high refractive indices exceeding 4. However, efficient methods to fabricate such semiconductor nanospheres suitable for optical trapping do not exist.

RESULTS

We developed a solution-based method to synthesize germanium nanospheres. With a diameter of roughly 70 nm, they are about an order of magnitude smaller compared to commonly used microspheres and still allowed piconewton force measurements. To find out how kinesin works mechanically, we developed an *in vitro* reconstituted assay. To this end, we coated the nanospheres with a lipid bilayer (white rim in the transmission electron microscopy (TEM) image) mimicking vesicles and roughly their size inside cells. When we bound kinesin-1 to these “vesicles” and measured the interaction of single motors with microtubules under piconewton tension, we discovered that each hydrolysis cycle is broken up in two 4-nm center-of-mass substeps. The durations of these substeps alternated in their force and ATP dependence, with the duration of one of the substeps being nearly independent of both parameters. Furthermore, when subjected to hindering loads, motors never detached from the microtubule. Instead motors

slipped along the microtubule in 8-nm steps on microsecond time scales. These slip steps are consistent with a bond-rupture model that involves protein friction between the motor and its track. Surprisingly, motors usually did not detach after a slip event, but reengaged in motility that rescued cargo transport.

CONCLUSIONS

Germanium nanospheres are promising for bioimaging, sensing, optoelectronics, nanophotonics, and energy storage. For optical trapping, the nanospheres open a new temporal window to uncover hidden dynamics in molecular machines. The direct observation of load-bearing kinesin substeps resolves a long-standing controversy. Slipping and rescues should allow load distribution and synchronization when motors operate in teams. Understanding their mechanochemistry is important for a better understanding of cellular transport and other essential molecular functions of kinesins with implications, for example, for neurodegenerative diseases and cancer.

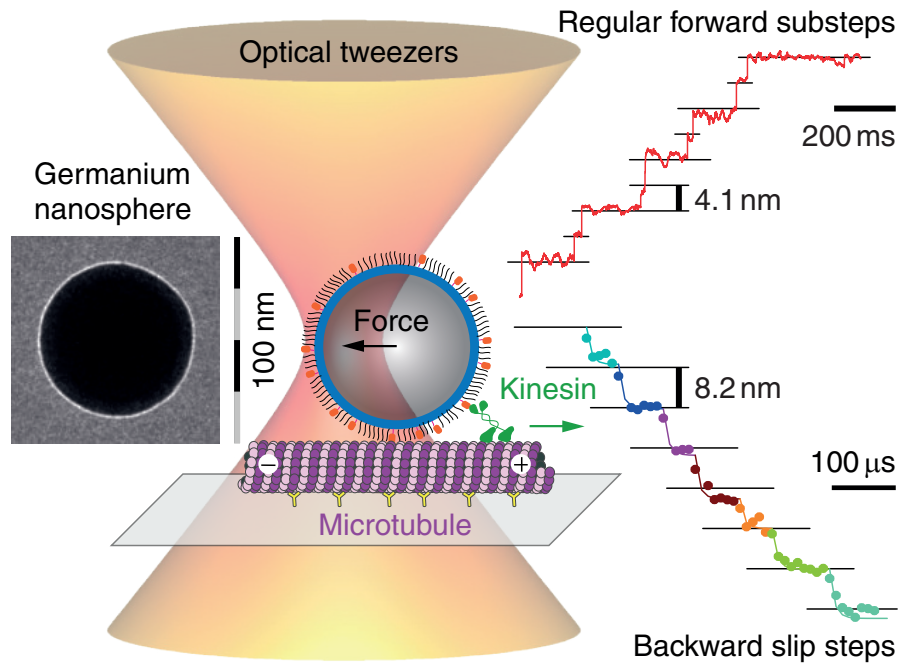


Fig. 1. Ultraresolution kinesin traces with optically trapped germanium nanospheres.

Kinesins are molecular machines that transport vesicles along microtubules inside cells. Membrane-coated germanium nanospheres (TEM micrograph, left) improved the spatiotemporal resolution of optical tweezers and allowed the measurement of substeps during the normal kinesin stepping cycle. Under load, kinesins did not detach but slipped along the microtubule, which led to the discovery of rescues for vesicle transport.

Germanium nanospheres for ultraresolution picotensiometry of kinesin motors

Swathi Sudhakar,¹ Mohammad Kazem Abdosamadi,¹ Tobias Jörg Jachowski,¹
Michael Bugiel,¹ Anita Jannasch,¹ Erik Schäffer^{1*}

¹Eberhard Karls Universität Tübingen, Cellular Nanoscience (ZMBP)
Auf der Morgenstelle 32, 72076 Tübingen, Germany

*To whom correspondence should be addressed; E-mail: erik.schaeffer@uni-tuebingen.de

Kinesin motors are essential for transport of cellular cargo along microtubules. How the motors step, detach, and cooperate with each other is still unclear. To dissect the molecular motion of kinesin-1, we developed germanium nanospheres as ultraresolution optical trapping probes. We found that single motors took 4-nm-center-of-mass steps. Furthermore, kinesin-1 never detached from microtubules under hindering load conditions. Instead, it slipped on microtubules in microsecond-long, 8-nm steps and remained in this slip state before detaching or reengaging in directed motion. Surprisingly, reengagement and, thus, rescue of directed motion was more frequent. Our observations broaden our knowledge on the mechanochemical cycle and slip state of kinesin. This state and rescues need to be accounted for to understand long-range transport by teams of motors.

One Sentence Summary: Optical trapping of high-refractive-index semiconductor nanoparticles shows how motors detach and walk in 4-nm steps.

Force spectroscopy on single molecular machines generating piconewton forces is often performed using optical tweezers (1–3). Since optical forces scale with the trapped particle volume, piconewton force measurements require micron-sized probes (1, 4). While smaller probes potentially improve the spatiotemporal resolution, laser induced heating so far limited biological measurements (1, 2, 4–6). Fundamental limits arise due to Brownian motion that both molecular motors and trapping probes are subjected to (5). By temporal averaging over this motion, discrete motor steps of size δ and the time between steps—the dwell time τ —can be resolved. Such single-molecule measurements have provided unprecedented insight into essential mechanochemical processes of life (1–3, 7). However, to resolve steps, such processes often have to be slowed down. For example, by using low nucleotide concentrations, the benchmark, 3.4-Å-DNA-base-pair-size steps of the RNA polymerase, naturally operating on a millisecond time scale, could only be resolved on a second time scale (7). Slowing down molecular machines may not only increase dwell times but alter other aspects of the mechanochemistry (8). The inherent trade-off between temporal and spatial precision and the resolution limit itself can be quantified by the product $\delta\sqrt{\tau}$ (2, 5). Its smallest possible value is a constant that determines the smallest detectable step size and/or shortest dwell time that can be resolved. Resolution is mainly limited by the probe’s drag coefficient and linker compliance between probe and molecular machine, but depends little on the machine itself. Thus, once instrumental noise is sufficiently reduced, this relation implies that detecting 8-nm steps of a kinesin motor on a millisecond time scale is as challenging as measuring Å-steps of a polymerase on a second time scale ($\tau_{\text{kinesin}}^{\text{min}}/\tau_{\text{RNAP}}^{\text{min}} = (\delta_{\text{RNAP}}/\delta_{\text{kinesin}})^2 = (0.34/8)^2 \approx 0.002$). Furthermore, apart from reducing linker compliance, spatiotemporal resolution can only be significantly improved relative to the benchmark by the use of nanometer-size optical trapping probes (2, 5). However, such probes for piconewton-force measurements do not exist.

Cytoskeletal motors like kinesins drive many essential cellular processes by coupling ATP

hydrolysis to perform mechanical work (9). During an ATP hydrolysis cycle, kinesin motors advance by 8 nm along microtubules against forces of several piconewton via a rotational hand-over-hand mechanism (8, 10). While consensus develops on how kinesin motors work (11, 12) important details remain unclear. For example, it is controversial whether intermediate mechanical steps in the hydrolysis cycle exist and can support load (13–18). In optical trapping assays (13–15), loads were applied via the motors coiled-coil, but intermediate-state measurements may have lacked sufficient resolution (16). In light scattering assays (17, 18), gold nanoparticles attached to one of the two motor heads provided sufficient resolution, but every other step cannot be detected, loads cannot be applied due to heating (6), and data interpretation may depend on the probe’s rotation and attachment point. Inside crowded cells, conditions are far more complex. To enhance cellular transport, kinesin motors work cooperatively in small teams (19–22). Yet, ultimately the transport distance and force generation are limited by motor detachment. However, how kinesins detach from microtubules is not known (20, 22).

Germanium nanospheres for ultraprecision spatiotemporal optical trapping measurements

To resolve how kinesin motors take steps and detach from microtubules, we sought to enhance the spatiotemporal precision of optical tweezers by compensating the particle-volume-scaling of trapping forces in the Rayleigh regime (where the probe is very small compared to the wavelength of the light) with the use of highest near-infrared refractive index **germanium nanospheres** as **trappable optical probes** (GeNTOPs). While various methods exist to make semiconductor nanoparticles (23–27), none provide water-stable, monodisperse, sufficiently large nanospheres for picotensiometry in adequate amounts. The synthesis that we developed derives from a solution-based method (25) and resulted in uniform GeNTOPs with a size of 72 ± 8 nm (mean \pm standard deviation, $N = 100$) measured by transmission electron microscopy

(TEM, Fig. 1A, see methods for details). To determine whether the spatiotemporal trapping precision of GeNTOPs was improved compared to commonly used microspheres, we trapped GeNTOPs in an ultrastable optical tweezers setup (28) (fig. S1, methods) and calibrated them by a combined power spectral density–drag force method (29, 30) (fig. S2). The GeNTOP calibration showed that we achieved the optical-trap spring constant, the trap stiffness κ , necessary for kinesin picotensiometry (8, 10, 13–15). Also, for the used laser power, the trap stiffness quantitatively agreed with a Mie theory calculation based on the dielectric properties of germanium at the infrared trapping laser wavelength (see methods). Thus, GeNTOPs had indeed the expected very high refractive index of 4.4. In summary, because of the GeNTOPs’ high refractive index and nanometric size, spatial precision is significantly improved and the trap response time reduced by about an order of magnitude to $\tau_{trap} = \gamma/\kappa \approx 10 \mu\text{s}$, where γ is the drag coefficient (fig. S2). By using a higher trap stiffness and/or smaller GeNTOPs—achieved through shorter reaction times—the response time can be reduced further.

Membrane-coated GeNTOPs for kinesin transport

To mimic *in vivo* vesicles, we coated GeNTOPs with a lipid bilayer (Fig. 1B, fig. S3, see methods). This bilayer, we functionalized further with nanobodies that bound truncated, recombinant green-fluorescent-protein-(GFP)-tagged kinesin-1 motors hereafter called kinesin. The use of a truncated kinesin and nanobodies minimized linker compliance. To minimize nonspecific interactions, we also PEGylated the bilayer. Overall, the functionalization increased the GeNTOP diameter to $93 \pm 4 \text{ nm}$ according to dynamic light scattering (mean \pm fit error). This diameter corresponds to the average size of neuronal transport vesicles (19). Forces that vesicles or our functionalized GeNTOPs experience during *in vivo* transport or in the optical trap, respectively, push the cargo in contact with the microtubule. This steric constraint defines the pulling geometry (Fig. 1B drawn to scale). Thus, dimensions and the force geometry when using GeNTOPs

are comparable to the situation inside cells. By using a low motor-to-GeNTOP ratio for further optical tweezers experiments, we ensured that only single kinesins transported GeNTOPs along microtubules with the expected speed and run length quantified by interference reflection microscopy (31) (fig. S3, see methods).

Kinesin takes 4-nm steps

To dissect the kinesin gait, we trapped single-kinesin-functionalized GeNTOPs at physiological ATP concentrations, placed them on microtubules, and recorded the kinesin-powered GeNTOP displacement from the trap center (Fig. 1B). Based on this displacement x within the linear response of the GeNTOPs (inset fig. S2), the Hookean spring load of the optical tweezers corresponds to a force $F = \kappa x$. In the exemplary trace of Fig. 1C (see more examples in fig. S4), motors slowed down with increasing hindering loads up to ≈ 5 pN. Also with increasing force, stepwise motion became more evident until GeNTOPs quickly returned to the trap center (in Fig. 1C at ≈ 2.1 s). To determine step sizes and dwell times, we used an efficient, automated filtering and step finding algorithm (see methods). Remarkably, instead of 8-nm steps (10), most forward-directed, center-of-mass steps were 4.14 ± 0.06 nm (center of Gaussian \pm fit error, including low ATP data). Because step size was consistent with the size of a tubulin monomer and hardly depended on force (inset Fig. 1D, fig. S5, table S1 and S2), the combined linker-motor stiffness was very high (at least 2 pN/nm, tenfold higher compared to previous reports (5), see methods) such that we could pool all steps together (Fig. 1D). There were only a few 8-nm forward and some 4-nm, but rarely any 8-nm, backward steps (table S1). Thus, our data directly shows that kinesin walks with 4-nm center-of-mass steps that can support load. Interestingly, for increasing forces, the step duration appeared to be alternating between a long and short dwell time that we denote by τ_1 and τ_2 , respectively (Fig. 1C). Quantitatively, dwell time survival functions pooled from different force intervals were consistent with a single exponential

for forces below 2 pN (Fig. 1E, fig. S5, table S1). For forces above 2 pN, survival functions were well-described by a sum of two exponentials with approximately equal amplitude. Equal amplitudes imply that both type of dwells occurred equally often consistent with alternating steps having different properties. While the first dwell time τ_1 depended on force, the second one, τ_2 , hardly depended on force (blue and orange lines in top right inset Fig. 1E, see methods). The sum of the two dwell times τ_{cycle} was consistent with a model based on the force-dependent speed of the motor (black circles and line in top right inset Fig. 1E, see methods) suggesting that each hydrolysis cycle is broken up into two mechanical substeps. Data recorded at low ATP concentrations (Fig. 2, see methods) show that only the first dwell time τ_1 that depended on force also depended on ATP while τ_2 -values at low ATP did not differ much from the high-ATP values (table S1 and S2). Furthermore, for forces larger than 3 pN and physiological ATP concentrations, for which we could clearly assign alternating steps, the step size of alternating steps, always measured after the dwell, did not differ significantly ($\delta_1 = 4.03 \pm 0.06$ nm, $N = 97$ and $\delta_2 = 3.94 \pm 0.06$ nm, $N = 88$ for τ_1 and τ_2 with fit error, respectively, bottom left inset Fig. 1E). However, we cannot rule out that the distributions consist of two closely spaced Gaussians with means that differ by the offset distance between neighboring protofilaments. Nevertheless, kinesin motors walked in on average 4-nm center-of-mass steps alternating in the force and ATP dependence of their dwell times.

Slipping, detachment, and motility rescue of kinesin

How and in which substep do motors detach? We noticed that in about 50 % of the motility events ($N = 149$), the last step before the GeNTOP quickly returned to the trap center was a short substep (Fig. 1C, fig. S4). For the subsequent fast backward motion, we expected an exponential relaxation with a time constant corresponding to the trap response time τ_{trap} in case of microtubule-motor detachment (9). However, while the backward motion directed along the

microtubule axis could be fitted by an exponential relaxation (black line in Fig. 3A), the average time constant $\tau_{\parallel} = 295 \pm 9 \mu\text{s}$ (standard error unless noted otherwise, $N = 149$)—and all individual ones without exception—was much larger than the trap response time. This discrepancy suggests that the kinesin still interacted with the microtubule and did not detach from it (Fig. 1C, Fig. 3A). To prevent microtubule interactions after the last step, we additionally pulled sideways on the kinesin-coated GeNTOP during motility events. With a load perpendicular to the microtubule axis, the relaxation time τ_{\perp} after the last step was only $30.7 \pm 0.8 \mu\text{s}$ ($N = 50$) consistent with the expected trap relaxation time in the proximity of the surface (30) and true motor detachment (fig. S6A,B). Also, when GeNTOPs without motors were pulled along microtubules, we observed the expected hydrodynamic drag, but otherwise no interactions (fig. S6C). Close inspection of the relaxation traces along the microtubule (without sideward loads, but with motors) revealed steps occurring on a microsecond time scale that were robustly detected by an unbiased change-point detection algorithm (32) (Fig. 3A and further examples in fig. S7 and S8, see methods). Individual steps were composed of an exponential relaxation with a time constant of $27 \pm 3 \mu\text{s}$ ($N = 20$) consistent with the trap relaxation time τ_{trap} and had a step size of $7.2 \pm 0.2 \text{ nm}$ ($N = 111$, inset Fig. 3A)—close to the 8 nm repeat of the microtubule lattice—with a slip step dwell time of $71 \pm 4 \mu\text{s}$ ($N = 124$) averaged over all forces. Values obtained at low ATP did not significantly differ (fig. S7). Thus, we conclude that motors switched to a slip state initiating fast backward motion. This motion consisted of individual slip steps in the direction of the applied load and did not depend on ATP. To determine whether motors truly detached from this slip state or whether motors could switch back to a motility-competent state, we analyzed the time between subsequent motility events that we call restarting time (inset Fig. 3B). Intriguingly, the restarting time survival function was also well described by a sum of two exponentials having a time constant of $112 \pm 1 \text{ ms}$ and $4.1 \pm 0.4 \text{ s}$, respectively (Fig. 3B). Two time constants imply that motility events started from two different states, possibly being

de novo binding and the slip state. The short restarting time constant that we measured is in very good agreement with the one of a proposed “weakly bound” state (22) prior to detachment of duration 131 ± 14 ms. Surprisingly, 82 ± 1 % of our events had this short restarting time constant suggesting that most motors did not detach but motility was rescued from the slip state.

Stepping and slip state model

Our data is consistent with a model for kinesin stepping that splits up the hydrolysis cycle into two mechanical substeps. In between the substeps, the motor can branch off from the normal stepping cycle that is tightly coupled to ATP hydrolysis and switch to an ATP independent slip state prior to detachment or rescue of motility (Fig. 4). Overall, our model builds on and expands previous models (8, 11, 12, 17, 33). Initially, motor heads are bound to the microtubule with ADP and inorganic phosphate (P_i) in the rear head and no nucleotide in the front one. With ATP binding to the front head and P_i release from the rear one, the rear neck linker is undocked and the front one docked. This process triggers the first 4-nm, ATP-dependent center-of-mass substep (Substep $\tau_1(F,ATP)$ in Fig. 4). Since load is acting on the front neck linker during docking, it may explain that the dwell time of this step also depends on force. This direct measurement of a combined load and ATP dependent substep supports an earlier finding that loads affect ATP binding (34). Upon ATP hydrolysis in the front head and ADP release from the rear one, the hydrolysis cycle is completed with a second 4-nm substep (Substep τ_2 in Fig. 4). Since ATP is already hydrolyzed, this substep does not depend on the ATP concentration. Also, load is mainly acting on the docked neck linker of the former front head (blue head in panel Substep τ_2 of Fig. 4). The other head has an undocked neck linker of sufficient reach to the next binding site. To reach the transition state before locking the front head into the next binding site, only a small amount of neck linker stretching associated with a small center-of-mass motion may be required. This small extension may correspond to the small distance to the transition

state that we measured (see SI Sect. 1.7) and explain why the dwell time of this step does not significantly depend on force (inset Fig. 1E and Fig. 2). The normal hydrolysis cycle is interrupted, if P_i is released from the front head directly after ATP hydrolysis and before ADP is released from the rear head. Then both heads have ADP bound and are thought to be in a “weakly bound” state (12, 35). We interpret this state as the ATP independent slip state (brown box in Fig. 4) that is characterized by fast backward motion in the direction of load. This motion was broken up in slip steps and is opposed by hydrodynamic drag and an ATP-independent microtubule interaction that we attribute to protein friction (36). The measured slip step size close to 8 nm suggests that the motor heads interact also in the slip state primarily with the canonical kinesin-microtubule binding site. While we rarely observed single 8-nm backward steps, we observed some short slip events (fig. S8). When using large microspheres with a large drag and higher inherent upward load due to the force geometry (Fig. 1B, fig. S3, see SI Sect. 2.2), such events may correspond to previously observed more frequent backward steps (15), recently interpreted as slips (35). Protein friction allows us to estimate the slip step dwell time. Based on the time constant for the fast movement back to the trap center $\tau_{\parallel} = \tau_{trap} + \gamma_{protein\,friction}/\kappa$, the force-averaged friction coefficient due to friction between the motor and its track is $\gamma_{protein\,friction} \approx 15$ nN s/m and the corresponding diffusion coefficient according to the Einstein relation is $D = k_B T / \gamma_{protein\,friction} \approx 0.3$ $\mu\text{m}^2/\text{s}$, where k_B is the Boltzmann constant and T the absolute temperature. Furthermore, if we model the backward movement in the slip state by a biased one-dimensional random walk, i.e. biased diffusion, with a step size of $\delta = 8$ nm, the expected average step time is $\tau \approx \delta^2 / (2D) \approx 70$ μs . This time constant is in excellent agreement with the directly measured slip step dwell time (Fig. 3A) and supports the notion of a weakly bound state prior to detachment (22) that we have biased by force. Unexpectedly, in only roughly 20 % of events, motors did truly detach (red box in Fig. 4), but in 80 % of the cases ADP must have dissociated from one of the heads rescuing directed motion (green box in

Fig. 4). We expect that motors also switch to the slip state when no load is applied. Without load, motors should diffuse on the microtubule in the ATP independent slip state and either detach or resume motility afterwards. Therefore, we suggest that overall run lengths of motors are concatenations of processive runs interrupted by short diffusive periods (see SI Sect. 2.3 and (37, 38)).

Conclusions

In general, widely available, size-controllable high-refractive index GeNTOPs will enable other applications due to having the highest near-infrared refractive index of common materials and being a semiconductor. Germanium nanospheres are a lower-toxicity alternative to compound semiconductor nanoparticles (23, 25), optimal for bioimaging and sensing at wavelengths biological tissues are transparent (24), promising for nanophotonics and optoelectronics (26, 27), and may enhance energy harvesting and storage (39). As for optical trapping and relative to the benchmark (7), the spatiotemporal resolution $\delta\sqrt{\tau}$ of the fast 8-nm steps on microsecond time scales, is an improvement by a factor of about $4.5\times$ and $20\times$ with respect to spatial and temporal resolution, respectively (fig. S9). Thus, GeNTOPs do allow to observe molecular machines without having to slow them down. In our case, the dwell time of the slip steps cannot be slowed down by reducing nucleotide concentrations because nucleotides likely did not exchange during slipping. For kinesins, the slip and rescue states allow motors to slip back to their team during transport with direct reengagement in motility. This process provides a route for load distribution and motor synchronization enhancing transport. Therefore, for a better understanding of long-range transport in crowded cells (20) and of other essential cellular functions of kinesins, the slipping and rescue processes need to be accounted for.

Materials and Methods

Synthesis of germanium nanospheres (GeNTOPs)

The germanium nanospheres were synthesized in an aqueous solution advancing a method of Guo *et al.* (25). As substrate, 17.0 mg of germanium oxide (GeO_2) and 96.0 mg of quercetin, acting as a stabilizing agent, were dissolved in 10 ml of a 0.15 M sodium hydroxide solution each and then mixed together while stirring for 10 min and adjusting the pH to 8.8 via titration with 37 % HCl (Solution A). Subsequently, 29.5 mg of sodium borohydride (NaBH_4 , reducing agent) was dissolved as quickly as possible in 3 ml of 4 °C-cold water and stored in a refrigerator at 4 °C (Solution B). Then, Solution A was stirred continuously in a preheated oil bath at 60 °C for 10 min and Solution B was added dropwise. The reaction was stopped after 5 h and GeNTOPs washed thrice thoroughly with water by centrifuging the sample at 13,000 rpm. All chemicals were purchased from Sigma Aldrich and used without further purification unless noted otherwise. Purified Type 1 water was used for all experiments (18.2 M Ω cm, Nanopure System MilliQ reference with Q-POD and Biopak filter). The size characterization analysis was done using a TEM-Jeol 1400 plus transmission electron microscope. About 10 μl of the GeNTOP solution was sonicated and subsequently 5 μl spotted on a TEM grid. Dynamic light scattering resulted in a diameter of 74 ± 3 nm (mean \pm fit error) consistent with the value obtained by TEM.

Lipid-bilayer functionalization of GeNTOPs

After the synthesis, GeNTOPs were coated with a lipid bilayer using established methods (40–42). Briefly, 1,2-dimyristoyl-sn-glycero-3-phosphocholine (DMPC) and 1,2-distearoyl-sn-glycero-3-phosphoethanolamine-N-[carboxy(polyethylene glycol)-2000] (DSPE-COOH, both from Avanti Polar Lipids, Inc.) were dissolved in chloroform (10 mg/ml). Aliquots of a 4:1 molar ratio mixture of these lipids were dried overnight in a desiccator at 50 mbar and stored

at -20°C . The dried lipid mixture was hydrated by adding 1 ml of 80°C warm buffer (10 mM 4-(2-hydroxyethyl)-1-piperazineethanesulfonic acid (HEPES), 150 mM NaCl, pH 7.4) resulting in a final total lipid concentration of about 0.5 mM. To form multilamellar vesicles (MLVs), the solution was mixed thoroughly by pipetting and vortexed for 2 min. Subsequently, small unilamellar vesicles (SUVs) were formed by sonicating the MLV mixture for 30 min at 80°C . The sonicated solution was centrifuged at 12,000 rpm for 15 min and SUVs collected from the supernatant. Then, equal volumes of GeNTOP and SUV solutions were mixed. To induce fusion of the liposomes onto the GeNTOPs, CaCl_2 was added to the mixture (3 mM final concentration) that was incubated for 45 min at 80°C in a thermomixer using a shaking speed of 600 rpm. The membrane-coated GeNTOPs were washed thrice in three different buffers, first with Buffer 1 (25 mM HEPES, 200 mM NaCl, 1 mM tris(2-carboxyethyl)phosphine (TCEP), pH 7.4, 5 mM EDTA) followed by washing them in Buffer 2 (25 mM HEPES, pH 7.4, 100 mM NaCl, 0.25 mM CaCl_2) and then in Buffer 3 (25 mM HEPES, pH 7.4, 25 mM NaCl, 1 mM TCEP, 0.25 mM CaCl_2). After each wash, GeNTOPs were collected by spinning the sample at 13,000 rpm for 15 min and gently resuspending them. After the last resuspension step, GeNTOPs were lyophilized and kept at 4°C for later use. For membrane visualization, $10\ \mu\text{l}$ of $2\ \mu\text{M}$ DiI lipophilic dye was added when hydrating the lipid mixture used to coat GeNTOPs. As a control, $100\ \mu\text{l}$ of uncoated GeNTOPs, was mixed with $10\ \mu\text{l}$ of $2\ \mu\text{M}$ DiI lipophilic dye and incubated for 45 min. After incubation, these GeNTOPs were washed thrice with water and suspended in $100\ \mu\text{l}$ water. Both the coated GeNTOPs with the membrane dye and control GeNTOPs were imaged by a Leica TCS SP8 confocal microscope with an excitation wavelength of 565 nm. No fluorescence was observed for the control.

GeNTOP PEGylation and nanobody coupling

For kinesin experiments, we PEGylated GeNTOPs and covalently bound GFP nanobodies to them as described previously (43) with some modifications. About 0.1 g of lyophilized GeNTOPs were dissolved in 1 ml water. From this stock, 25 μ l were washed twice with 975 μ l of 2-(N-morpholino)ethanesulfonic acid (MES) buffer (50 mM, pH = 6.0) by centrifuging GeNTOPs at 13,000 rpm for 15 min. Before each wash cycle, GeNTOPs were vortexed and sonicated in a bath sonicator for 15 s. Then, GeNTOPs were resuspended in 250 μ l MES buffer. After washing, GeNTOPs were vortexed and sonicated for 180 s. Then, 16.4 mg of 1-(3-(dimethylamino)propyl)-3-ethylcarbodiimide hydrochloride (EDC) and 8.3 mg of N-hydroxysulfosuccinimide sodium (NHS) were dissolved in 100 μ l of MES buffer. From the prepared solution, 9 μ l of NHS and 15.8 μ l of EDC were added to the resuspended GeNTOPs and the solution was mixed in a thermomixer for 15 min at 37 °C. Then, GeNTOPs were washed twice with 500 μ l of MES buffer, resuspended in 240 μ l of PBS-T (phosphate buffer saline supplemented with 0.1 % Tween 20), and vortexed and sonicated for 90 s. Subsequently, GFP-nanobodies (44) (13 kDa, gift of Ulrich Rothbauer, NMI, Reutlingen, Germany) and 2 kDa α -methoxy- ω -amino PEG (Rapp Polymere, Tübingen, Germany) in a molar ratio of 1:1000 were coupled covalently to the GeNTOPs by incubating them in a thermomixer for 1 h at 600 rpm and 37 °C. Afterwards, GeNTOPs were washed five times with PBS-T and stored at 4 °C.

Sample preparation and assay

Experiments were performed in flow cells that were constructed using silanized, hydrophobic glass cover slips and parafilm as described before (30, 36) but chlorotrimethylsilane (Merck Millipore, Burlington, MA) was used to render surfaces hydrophobic. Truncated rat kinesin1-eGFP-6xHis (rk430) was purified as described previously (8, 36). Microtubules stabilized with taxol added after polymerization and sometimes additionally 10 % rhodamine-labeled, were

prepared from porcine tubulin as described previously (45). Flow channels were washed with PEM buffer (80 mM 1,4-piperazinediethanesulfonic acid (PIPES), 1 mM EGTA, 1 mM MgCl₂, adjusted with KOH to pH 6.9), filled and incubated successively with anti β -tubulin I (monoclonal antibody SAP.4G5 from Sigma in PEM) for 15–20 min, Pluronic F-127 (1 % in PEM) for 20 min, and microtubules in PEM for 15 min. Kinesin with a stock concentration of 12.1 mg/ml was diluted 1000 \times in motility buffer (PEM with 0.16 mg/ml casein, 1 mM or 10 μ M ATP and an anti-fade cocktail [20 mM D-glucose, 0.02 mg/ml glucose oxidase, 0.008 mg/ml catalase and 10 mM dithiothreitol]). Then 4 μ l of the kinesin solution was mixed with 96 μ l of 10 \times diluted functionalized GeNTOPs and incubated for 10 min. About, 20 μ l of this GeNTOP-motility solution was flown into the channel for single-molecule force measurements. To rule out artifacts from angled motion in the optical trap (46), only microtubules aligned with the flow cell channel direction and perpendicular to the laser polarization (47) were chosen for experiments.

Single-molecule conditions

We measured the fraction of motile GeNTOPs $p_m \pm (p_m(1 - p_m)/N)^{1/2}$ (mean \pm error bar) by trapping GeNTOPs incubated with different concentrations of kinesin motors and placing them on microtubules to await motility (43, 48). The probability that a single motor transported the GeNTOP is $p_1 = (1 - p_m)(1 - \ln(1 - p_m))$ not accounting for that a motor, bound opposite to another one, may not be able to interact simultaneously. For single-molecule experiments, the pipetted kinesin-to-GeNTOP ratio was about 20 corresponding to a motile fraction of $p_m \lesssim 30\%$ implying single-molecule conditions with at least 95 % confidence. To measure speed and run length of single kinesin motors on microtubules in the absence of loads, we used a custom-built optical tweezers setup combined with interference reflection microscopy (IRM) (31). Motor-coated GeNTOPs were trapped and placed on a microtubule. If the GeNTOP showed motility, the trap was turned off and IRM images were acquired at a rate of 7 frames/s.

Based on kymographs, the mean motor speed and run length was $0.72 \pm 0.05 \mu\text{m/s}$ and $1.1 \pm 0.4 \mu\text{m}$ ($N = 12$), respectively, consistent with our own (8) and literature values (49–51).

Optical tweezers setup, instrument noise, and calibration

Optical trapping measurements were performed in our ultraprecision optical tweezers setup (28, 30). Briefly, the setup has near-Å resolution in surface-coupled assays (fig. S1) and is equipped with a millikelvin precision temperature control set to $29.500 \text{ }^\circ\text{C}$ (28). Signals of a 1064 nm trapping laser were recorded with a sampling rate of 100 kHz by back focal plane detection in three dimensions (52).

To assess the instrument noise, we tracked the position of a surface-immobilized fiducial marker as a function of time (fig. S1A). As a marker, we used a $0.59\text{-}\mu\text{m}$ diameter, polystyrene microsphere immobilized in a 0.1 M KCl solution on a bare glass surface. The displacement sensitivity was determined by scanning through the fiducial marker using a piezoelectric translation stage. Over 1000 s, overall drift and noise was less than 4 nm for all directions. To compare the instrument noise to previous measurements, we calculated the power spectral density (PSD) that provides a noise measure in the frequency domain (fig. S1B). Since the total noise relevant for the measurements is the PSD integral over the measurement bandwidth, we also calculated the Allan deviation (28) (fig. S1C) that directly provides a useful noise criterium in the time domain. In comparison to previous measurements done in our laboratory with the same setup (28, 53), the instrument noise was significantly reduced by a relocation of the setup to a room with excellent vibration and sound isolation and temperature stability (54). Previous power spectra from our laboratory of trapped high-refractive index, anti-reflection-coated titania microspheres (thick gray lines in fig. S1B) show a hydrodynamic resonance—the colored-noise nature of Brownian motion (53, 55)—and demonstrate that also for trapped probes noise levels were below $10 \text{ pm}^2/\text{Hz}$. Our previous data marked with a cyan line in fig. S1B was obtained

using a fiducial, surface-immobilized marker (28) and can be directly compared to our current measurements (red, orange, and brown lines). As pointed out above, the improvement is due to a better setup environment. Laser noise recorded without fiducial marker (thin dark gray line in fig. S1B) and converted to displacements using the same displacement sensitivity as for the x -direction indicate that laser pointing fluctuations were not limiting. The instrument noise was also significantly lower compared to other high-end setups that required helium to reduce pointing fluctuations of the laser (blue and magenta solid line in fig. S1B: trapped microspheres used in (7) with and without helium, respectively). The dashed blue line corresponds to the calculated power spectral density of the microspheres employed in (7) using their provided trap stiffness and size. The solid blue line should merge with this power spectrum when extrapolated to higher frequencies. Our colored-noise data of trapped titania microspheres (53) show that in particular at frequencies below 100 Hz, our data was not limited by instrument noise and was significantly below the data of (7). In our setup, helium was also not necessary and noise data was recorded directly at the surface—the noise relevant for a kinesin assay. At the surface, apart from laser fluctuations also mechanical noise is directly coupled into the system making low-noise surface-coupled assays equally demanding compared to the dumbbell assay employed in (7). Together, the instrument noise measurements show that the setup has sub-base-pair noise levels in a surface-coupled assay in three dimensions at least up to a measurement bandwidth of a second (fig. S1C). Thus, our spatiotemporal resolution was not limited by instrument noise but by fundamental thermal noise of the probe.

The optical trap was calibrated by a combined power spectral density–drag force method (29, 30). The average trap stiffness used for experiments was about 0.05 pN/nm. For the power spectra in fig. S2, the trap stiffness was 0.0552 ± 0.0005 pN/nm and 0.0561 ± 0.0005 pN/nm recorded at 2 μm and 5 μm distance from the surface using about 600 mW and 6.5 mW of laser power in the focus for the GeNTOP and polystyrene microsphere, respectively. Both trap stiff-

ness values quantitatively agreed with Mie theory calculations for our setup (47, 56, 57) using a refractive index of $4.4 + 0.11i$ (58) for the GeNTOPs. Due to absorption, we measured a temperature increase for the GeNTOPs at 600 mW trapping power of about 7 K above the flow cell temperature 500 nm away from the surface using our calibration method (53). This temperature increase is slightly more than what is expected for heating due to the trapping laser alone (59). Since the surface acts as a heat sink (59), we expect that during kinesin experiments heating was less. We did not notice any significant changes due to temperature, e.g. in motor speed or force generation, compared to when using polystyrene microspheres with the same trap stiffness.

Step detection and data processing

For step detection and filtering, data was processed using an optimized, automated step finding algorithm (60) based on a modified forward-and-backward filter from Chung & Kennedy that we implemented in Python (36, 60–62). The filter works very efficiently in particular, for large data sets consisting of millions of data points. For sufficiently large data sets, the algorithm automatically finds the optimal window length for filtering and step detection according to the following idea: if we smooth the signal with different window lengths, the standard deviation of the smoothed signal decreases with increasing window length as long as the window length is shorter than the dwell time of the steps. As soon as the window includes steps, i.e. is comparable to the dwell time of the steps, the standard deviation increases again. The window length with the lowest standard deviation is used as a proxy for the optimal window size that we empirically chose to be 4/5 of the latter window length. To filter the data while preserving steps, the optimal window size is used to calculate the variance-weighted mean of the forward and backward window corresponding to the filtered data point. For our data, we used a window size of 4.8 ms. For step detection during the fast backward motion, we used the unbiased “Steppi” algorithm (32). In selected traces (fig. S7), the algorithm detected steps corre-

sponding to single exponential relaxations with a time constant consistent with the trap response time. To robustly detect sliding steps in many traces, we fixed the relaxation time constant to the expected and exemplarily verified one. To account for the different trap response times in the different directions parallel and perpendicular to the microtubule axis and assuming that the hydrodynamic drag coefficient is the same in both directions (30), we chose a relaxation time of $\tau_{\perp}\kappa_{\perp}/\kappa_{\parallel} = 25 \mu\text{s}$, where κ_{\parallel} and κ_{\perp} are the trap stiffness in the direction of the microtubule axis and perpendicular to it, respectively, and τ_{\perp} is the experimentally measured value (Fig. 3A). The average trap stiffness of κ_{\parallel} and κ_{\perp} was $0.051 \pm 0.001 \text{ pN/nm}$ ($N = 149$) and $0.041 \pm 0.001 \text{ pN/nm}$ ($N = 50$). To apply sideward loads during a motility event, we manually displaced the sample 50 nm in a direction perpendicular to the microtubule axis and relative to the stationary optical trap using a piezo-translation stage resulting in sideward loads of about 2 pN. For the last short step, we measured a dwell time of $58 \pm 12 \text{ ms}$ ($N = 74$) longer than the average τ_2 value at that force indicating that the small increase of τ_2 with force promotes the switching to the diffusive state. Speeds as a function of force are based on linear fits to trace segments in the respective force intervals, where automatic threshold detection of force was based on the filtered data. The speed (table S1 and S2) was well described by a linear force-velocity relation with zero-load speed $v_0 = 0.64 \pm 0.02 \mu\text{m/s}$ and $0.22 \pm 0.02 \mu\text{m/s}$ and stall force $F_s = 4.92 \pm 0.03 \text{ pN}$ and $5.1 \pm 0.7 \text{ pN}$ for high and low ATP concentrations, respectively. Based on this relation and fitted parameters, the total dwell time for a hydrolysis cycle is $\tau_{\text{cycle}} = (2\delta)/(v_0(1 - F/F_s))$ (black line in top right inset Fig. 1E and inset Fig. 2), where we used $\delta = 4.1 \text{ nm}$. The force dependence of the substeps was modeled by $\tau(F) = \tau_0 \exp(Fx^{\ddagger}/(k_B T)) + \tau_{\text{const}}$, where for 1 mM ATP and the long dwell time τ_1 the zero-force dwell time τ_0 was $0.5 \pm 0.2 \text{ ms}$, the distance to the transition state x^{\ddagger} was $5.3 \pm 0.4 \text{ nm}$, and the constant τ_{const} was $7 \pm 2 \text{ ms}$ (blue line in top right inset Fig. 1E). For 1 mM ATP and the short dwell time τ_2 , the data was best modeled by a constant value of $6.0 \pm 1.6 \text{ ms}$ (orange line in top right inset Fig. 1E). Note that for $F < 2 \text{ pN}$,

a single exponential modeled the data best and we used the same value for τ_1 and τ_2 . For 10 μ M ATP, the zero-force dwell time τ_0 was 4 ± 2 ms and 2.1 ± 0.4 ms, the distance to the transition state x^\ddagger was 3.8 ± 0.6 nm and 1.2 ± 0.3 nm, and the offset τ_{const} was 24 ± 6 ms and zero for τ_1 and τ_2 , respectively (blue and orange line in inset Fig. 2).

References and Notes

1. K. Svoboda, S. M. Block, *Annu. Rev. Biophys. Biomol. Struct.* **23**, 247 (1994).
2. J. R. Moffitt, Y. R. Chemla, S. B. Smith, C. Bustamante, *Annu. Rev. Biochem.* **77**, 205 (2008).
3. A. Gennerich, *Optical Tweezers*, Methods Mol. Biol. (Springer, New York, 2017).
4. A. Ashkin, J. M. Dziedzic, J. E. Bjorkholm, S. Chu, *Opt. Lett.* **11**, 288 (1986).
5. F. Gittes, C. F. Schmidt, *Methods Cell Biol.*, M. P. Sheetz, ed. (Academic Press, 1997), vol. 55, pp. 129–156.
6. Y. Seol, A. E. Carpenter, T. T. Perkins, *Opt. Lett.* **31**, 2429 (2006).
7. E. A. Abbondanzieri, W. J. Greenleaf, J. W. Shaevitz, R. Landick, S. M. Block, *Nature* **438**, 460 (2005).
8. A. Ramaiya, B. Roy, M. Bugiel, E. Schäffer, *Proc. Natl. Acad. Sci. USA* **114**, 10894 (2017).
9. J. Howard, *Mechanics of motor proteins and the cytoskeleton* (Sinauer Associates, Sunderland, MA, 2001).
10. K. Svoboda, C. F. Schmidt, B. J. Schnapp, S. M. Block, *Nature* **365**, 721 (1993).
11. W. O. Hancock, *Biophys. J.* **110**, 1216 (2016).

12. R. A. Cross, *Biopolymers* **105**, 476 (2016).
13. C. M. Coppin, J. T. Finer, J. A. Spudich, R. D. Vale, *Proc. Natl. Acad. Sci. U. S. A.* **93**, 1913 (1996).
14. M. Nishiyama, E. Muto, Y. Inoue, T. Yanagida, H. Higuchi, *Nat. Cell Biol.* **3**, 425 (2001).
15. N. J. Carter, R. A. Cross, *Nature* **435**, 308 (2005).
16. S. M. Block, *Biophys. J.* **92**, 2986 (2007).
17. K. J. Mickolajczyk, *et al.*, *Proc. Natl. Acad. Sci. USA* **112**, E7186 (2015).
18. H. Isojima, R. Iino, Y. Niitani, H. Noji, M. Tomishige, *Nat. Chem. Biol.* **12**, 290 (2016).
19. A. G. Hendricks, *et al.*, *Curr. Biol.* **20**, 697 (2010).
20. Q. Feng, K. J. Mickolajczyk, G.-y. Chen, W. O. Hancock, *Biophys. J.* **114**, 400 (2018).
21. K. I. Schimert, B. G. Budaitis, D. N. Reinemann, M. J. Lang, K. J. Verhey, *Proc. Natl. Acad. Sci. USA* **116**, 6152 (2019).
22. H. Khataee, J. Howard, *Phys. Rev. Lett.* **122**, 188101 (2019).
23. J. Fan, P. K. Chu, *Small* **6**, 2080 (2010).
24. D. D. Vaughn II, R. E. Schaak, *Chem. Soc. Rev.* **42**, 2861 (2013).
25. Y. J. Guo, *et al.*, *Chem. Asian J.* **9**, 2272 (2014).
26. A. I. Kuznetsov, A. E. Miroshnichenko, M. L. Brongersma, Y. S. Kivshar, B. Luk'yanchuk, *Science* **354**, aag2472 (2016).
27. A. Krasnok, M. Caldarola, N. Bonod, A. Alú, *Adv. Opt. Mater.* **6**, 1701094 (2018).

28. M. Mahamdeh, E. Schäffer, *Opt. Express* **17**, 17190 (2009).
29. S. F. Tolic-Nørrelykke, E. Schäffer, J. Howard, F. S. Pavone, F. Jülicher, *Rev. Sci. Instrum.* **77**, 103101 (2006).
30. E. Schäffer, S. F. Nørrelykke, J. Howard, *Langmuir* **23**, 3654 (2007).
31. S. Simmert, M. Abdosamadi, G. Hermsdorf, E. Schäffer, *Opt. Express* **26**, 1437 (2018).
32. P. A. Wiggins, *Biophys. J.* **109**, 346 (2015).
33. J. O. L. Andreasson, *et al.*, *eLife* **21**, 1 (2015).
34. K. Visscher, M. J. Schnitzer, S. M. Block, *Nature* **400**, 184 (1999).
35. A. Toleikis, N. J. Carter, R. A. Cross, *Biophys. J.* (2020). DOI: 10.1016/j.bpj.2020.09.034.
36. V. Bormuth, V. Varga, J. Howard, E. Schäffer, *Science* **325**, 870 (2009).
37. A. Jannasch, V. Bormuth, M. Storch, J. Howard, E. Schäffer, *Biophys. J.* **104**, 2456 (2013).
38. M. Chugh, *et al.*, *Biophys. J.* **115**, 375 (2018).
39. T. H. Kim, H. K. Song, S. Kim, *Nanotechnology* **30**, 275603 (2019).
40. L. Ma, Y. Cai, Y. Li, J. Jiao, Z. Wu, *elife* **6**, 1 (2017).
41. P. B. Santhosh, N. Thomas, S. Sudhakar, A. Chadha, E. Mani, *Phys. Chem. Chem. Phys.* **19**, 18494 (2017).
42. I. Brouwer, *et al.*, *Nat. Commun.* **6**, 1 (2015).
43. M. Bugiel, *et al.*, *J. Biol. Methods* **2**, 30 (2015).
44. U. Rothbauer, *et al.*, *Mol. Cell Proteomics.* **7**, 282 (2008).

45. M. Bugiel, E. Böhl, E. Schäffer, *Biophys. J.* **108**, 2019 (2015).
46. M. Bugiel, A. Jannasch, E. Schäffer, *Optical Tweezers: Methods and Protocols*, A. Gennerich, ed. (Humana Press, 2016), chap. 5, pp. 109–136.
47. M. Mahamdeh, Campos, C.P, E. Schäffer, *Opt. Express* **19**, 11759 (2011).
48. K. Svoboda, S. M. Block, *Cell* **77**, 773 (1994).
49. S. Block, L. Goldstein, B. Schnapp, *Nature* **348**, 348 (1990).
50. D. L. Coy, M. Wagenbach, J. Howard, *J. Biol. Chem.* **274**, 3667 (1999).
51. D. Cai, K. J. Verhey, E. Meyhöfer, *Biophys. J.* **92**, 4137 (2007).
52. A. Pralle, M. Prummer, E. L. Florin, E. H. K. Stelzer, J. K. H. Hörber, *Microsc. Res. Tech.* **44**, 378 (1999).
53. A. Jannasch, M. Mahamdeh, E. Schäffer, *Phys. Rev. Lett.* **107**, 228301 (2011).
54. G. L. Hermsdorf, S. A. Szilagy, S. Rösch, E. Schäffer, *Rev. Sci. Instrum.* **90**, 015113 (2019).
55. A. Jannasch, A. F. Demirörs, P. D. Van Oostrum, A. Van Blaaderen, E. Schäffer, *Nat. Photonics* **6**, 469 (2012).
56. T. A. Nieminen, *et al.*, *J. Opt. A: Pure Appl. Opt.* **9**, 196 (2007).
57. V. Bormuth, *et al.*, *Opt. Express* **16**, 13831 (2008).
58. <https://www.filmetrics.com/refractive-index-database/Ge/Germanium>. Accessed 23.07.2020.
59. E. J. G. Peterman, F. Gittes, C. F. Schmidt, *Biophys. J.* **84**, 1308 (2003).

60. T. J. Jachowski, Stepfinder: A Python package to find steps in one dimensional data with low SNR., GitHub repository: <https://github.com/tobiasjj/stepfinder> (2019).
61. S. H. Chung, R. A. Kennedy, *J. Neurosci. Methods* **40**, 71 (1991).
62. D. A. Smith, *Philos. Trans. R. Soc. B* **353**, 1969 (1998).
63. E. H. Kellogg, *et al.*, *J. Mol. Biol.* **429**, 633 (2017).
64. S. Pyrpassopoulos, H. Shuman, E. M. Ostap, *Biophys. J.* **118**, 243 (2020).
65. J. T. Finer, R. M. Simmons, J. A. Spudich, *Nature* **368**, 113 (1994).
66. J. R. Moffitt, *et al.*, *Nature* **457**, 446 (2009).

Acknowledgments

We thank Ulrich Rothbauer (NMI, Reutlingen, Germany) for providing the anti-GFP nanobody, Andreas Schnepf for the use of the Zetasizer, and Mohammed Mahamdeh, Joe Howard, Martin Oettel, and Carolina Carrasco for comments on the manuscript. S.S. thanks Haemant Santhi Ponnusamy for help in Python scripting. **Funding:** This work was supported by the interdisciplinary “nanoBCP-Lab” funded by the Carl Zeiss Foundation (Forschungsstrukturprogramm 2017), the German Research Foundation (DFG, JA 2589/1-1, CRC1011, project A04), the Institutional Strategy of the University of Tübingen (Deutsche Forschungsgemeinschaft, ZUK 63), and the PhD Network “Novel Nanoparticles” of the Universität Tübingen. **Author contributions:** S.S., and E.S. designed research; S.S. performed all experiments; S.S., M.K.A., M.B., A.J. and E.S. analyzed data; M.K.A., M.B. and T.J.J. provided data analysis software and simulations; T.J.J. developed the Python package stepfinder; M.B. and A.J. performed preliminary experiments, developed protocols, controlled statistics, and provided advice; and S.S., and E.S. wrote the paper. All authors commented on the manuscript. **Competing interests:** Authors declare no competing interests. **Data and materials availability:** All data are available in the main text and the supplementary materials.

Supplementary materials

Materials and Methods

Figs. S1 to S9

Tables S1 to S2

References (40–66)

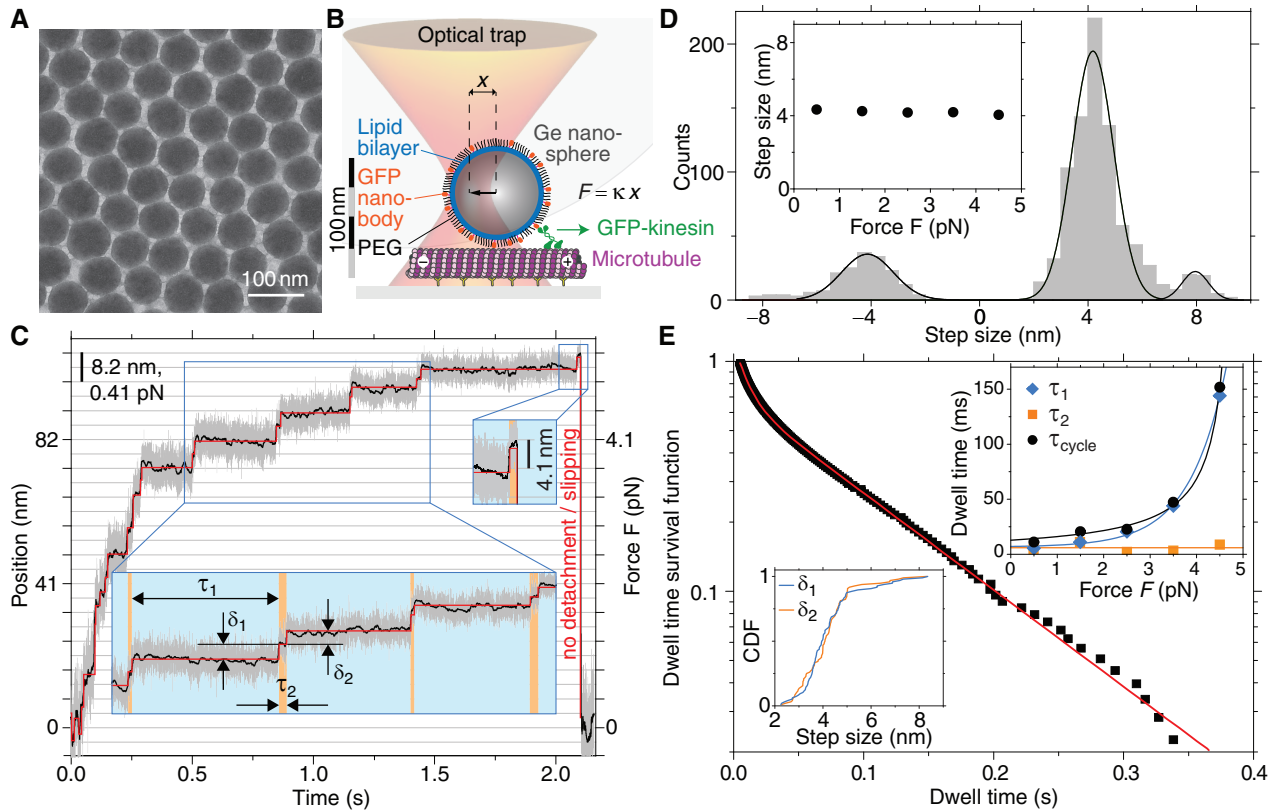


Fig. 1. Ultraresolution kinesin traces employing optically trapped germanium nanospheres. (A), TEM image of ≈ 70 nm germanium nanospheres (GeNTOPs). (B), Schematic of a kinesin motor transporting a functionalized GeNTOP along a microtubule roughly drawn to scale including a section of a gray-shaded $0.59 \mu\text{m}$ diameter microsphere for comparison (the optical trap is too small; see text and methods for details). (C), Time trace for a single-kinesin powered GeNTOP (100 kHz sampling rate, gray trace; filtered data, ≈ 100 Hz bandwidth, black trace; detected steps, red line; see methods). Insets: magnified views of substeps with definition of long and short dwell times τ_1 (blue shaded) and τ_2 (orange shaded) with corresponding step sizes δ_1 and δ_2 , respectively. (D), Step size histogram with a multi-Gaussian fit (line). Inset: Dominant step size versus force. (E), Dwell time distribution of steps for F between 2–3 pN with fit (red line). Inset: Dwell times (symbols) with models (lines) versus force (top right, see methods); and cumulative distribution function (CDF) of alternating step sizes (bottom left).

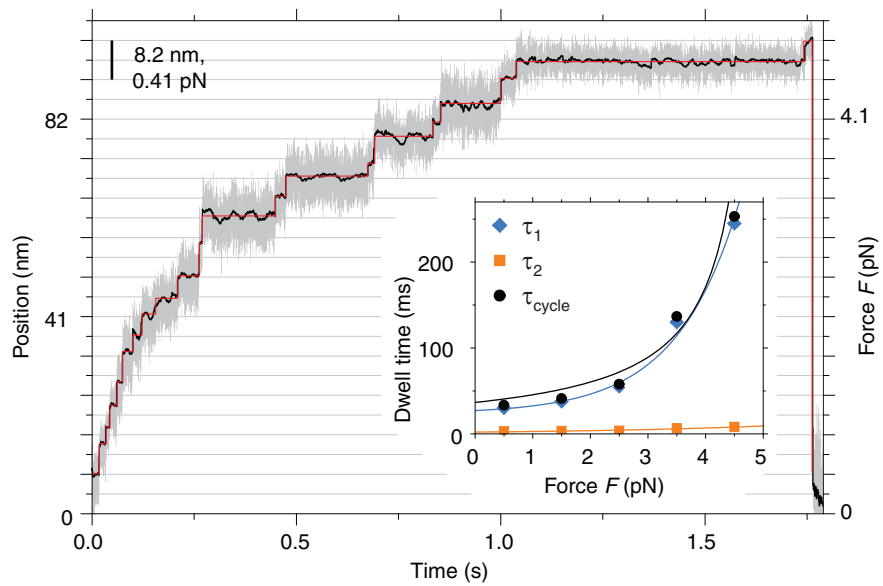


Fig. 2. Low-ATP-concentration kinesin trace. Time trace for a single-kinesin powered GeN-TOP at $10 \mu\text{M}$ ATP (100 kHz sampling rate, gray trace; filtered data, ≈ 100 Hz bandwidth, black trace; detected steps, red line; see methods). Inset: Dwell times (symbols) with models (lines) versus force (see methods).

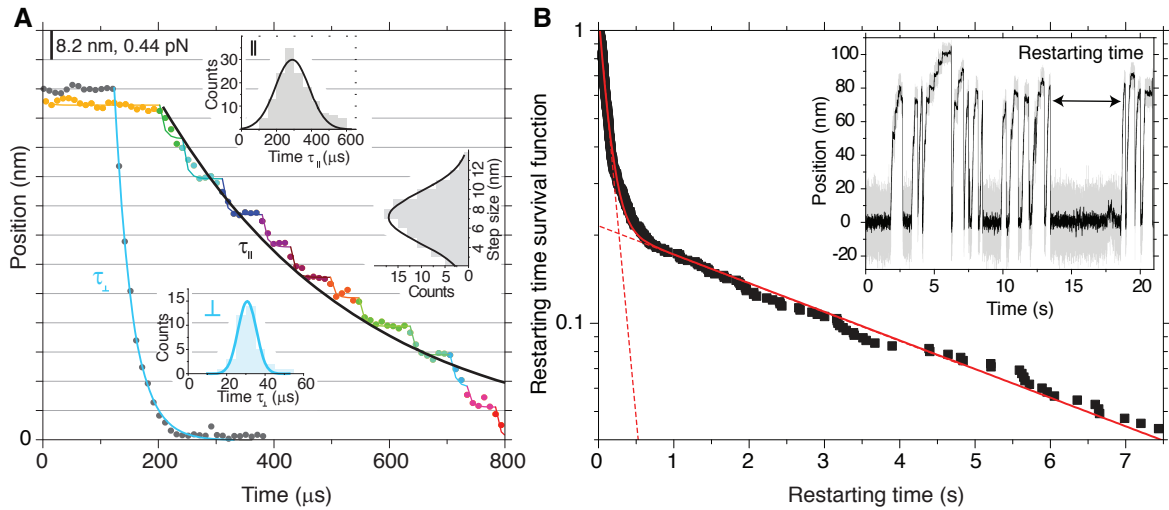


Fig. 3. Ultrafast slip steps and motility rescue. (A), Magnified time traces for a single-kinesin powered GeNTOP after the last step (gray and multicolored circles with or without sideward load, respectively, 100 kHz sampling rate) with single exponential fits (blue and black line for motion perpendicular (\perp) and parallel (\parallel) to the microtubule axis, respectively). Multicolored lines correspond to states detected by a change-point algorithm (32). Inset: histograms with Gaussian fits (solid lines) of relaxation time constants τ_{\parallel} and τ_{\perp} (same color code as single exponential fits) and slip step size for detected states. **(B)**, Restarting-time distribution (squares) fitted with a sum of two exponentials (line with dashed line extrapolation, $N = 550$). Inset: Illustration of the restarting time between consecutive kinesin motility events.

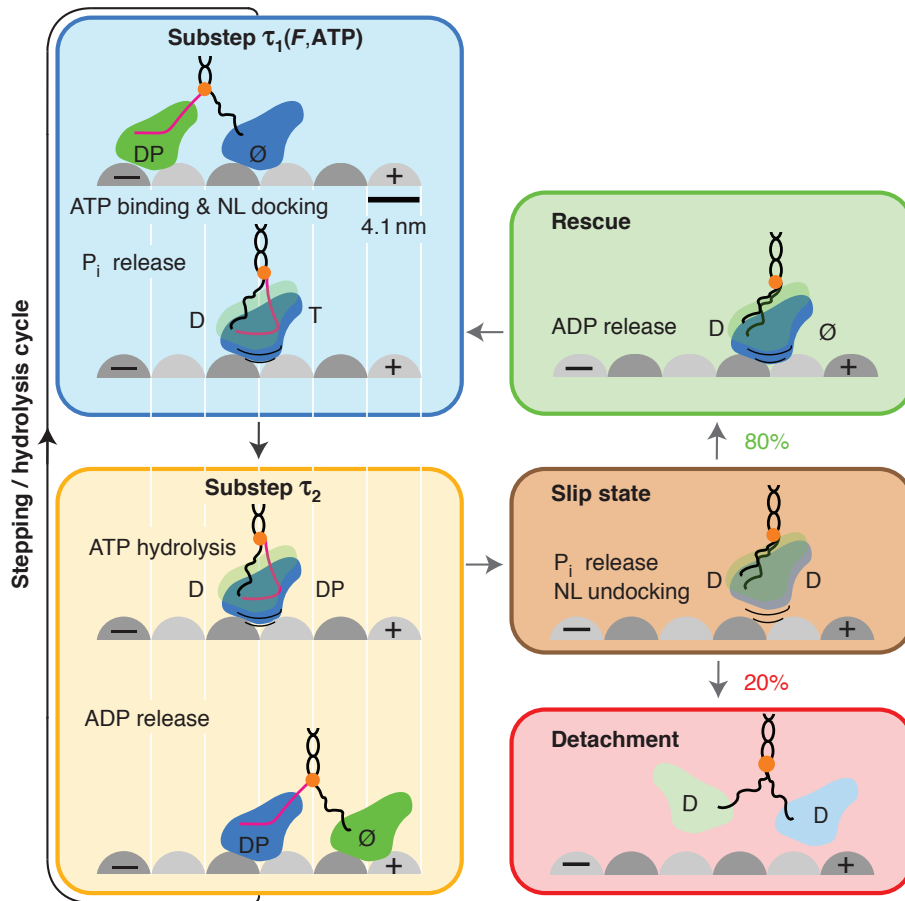


Fig. 4. Hydrolysis cycle with slip state, detachment and rescue. Side view of kinesin with two identical heads (blue and green) stepping along a microtubule (gray spheres mark tubulin monomers). The hydrolysis cycle is divided into a force and ATP dependent (blue box) and hardly force-dependent (orange box) substep with dwell times $\tau_1(F, ATP)$ and τ_2 , respectively. Between these substeps, motors may switch to a slip state (brown box) from which motors either detach (red box) or motility is rescued (green box). The center of mass is indicated by an orange circle, a docked neck linker (NL) marked by a magenta line, weak binding by lines underneath the heads, and nucleotide states by T: ATP, D: ADP, P_i : inorganic phosphate, and \emptyset : nucleotide free.



Supplementary Materials for
**Germanium nanospheres for ultraresolution
picotensiometry of kinesin motors**

Swathi Sudhakar, Mohammad Kazem Abdosamadi, Tobias Jörg Jachowski,
Michael Bugiel, Anita Jannasch, Erik Schäffer*

*Corresponding author. Email: erik.echaeffer@uni-tuebingen.de

This PDF file includes:

Supplementary Text
Figs. S1 to S9
Tables S1 to S2

Other Supporting Online Material for this manuscript includes the following:
(available at science.sciencemag.org/cgi/content/full/science.abd9944/DC1)

MDAR Reproducibility Checklist (.pdf)

Contents

1	Supplementary Text	3
1.1	Linker stiffness	3
1.2	Influence of vertical forces	3
1.3	Rescues and concatenation of runs	4

List of Figures

S1	Ultrastable optical tweezers	5
S2	Calibration of optically trapped germanium nanospheres (GeNTOPs)	6
S3	Single kinesins transported lipid-bilayer-coated GeNTOPs	7
S4	Exemplary kinesin traces at physiological ATP concentrations	8
S5	Step size, dwell time, and speed distributions versus force at physiological ATP concentrations	9
S6	Frictional drag coefficient based on fast backward motion	10
S7	Exemplary kinesin traces of fast backward motion in the slip state	11
S8	Exemplary kinesin trace with short slip events	12
S9	Optical tweezers spatiotemporal resolution of molecular machines	13

List of Tables

S1	Step size, dwell time and speed versus force at 1 mM ATP	14
S2	Step size, dwell time and speed versus force at 10 μM ATP	15

1. Supplementary Text

1.1. Linker stiffness

We estimated the linker stiffness based on the mean value of the step size, its error and load dependence combining results from both ATP concentrations (Fig. 1D inset, table S1 and S2). The linker is comprised of the lipid-bound nanobody and the truncated kinesin. Per substep, the force on the motor and linker increases by the product of the trap stiffness times the substep size $\Delta F_{step} = \kappa\delta \approx 0.2$ pN, where κ is the trap stiffness and δ the measured substep size. Assuming a linear spring, this force extends the linker by $\Delta x_L = \Delta F_{step} / \kappa_L$ per step, where κ_L is the linker stiffness. In general, the linker stiffness itself is thought to monotonically increase with force. The linker extension decreases the measured step size to $\delta = \delta_{motor} - \Delta x_L$, where δ_{motor} is the step size the motor takes. Based on these equations, the linker stiffness is $\kappa_L = \Delta F_{step} / (\delta_{motor} - \delta)$ (5, 10, 13).

The sum of the two motor substeps must correspond to the periodicity of the microtubule lattice, i.e. a tubulin dimer. For our measurements, the step size of the two substeps did not differ. Thus, on average the step size must correspond to the size of a tubulin monomer. The step size we measured did not significantly differ from the size of a tubulin monomer of 4.09 nm determined by electron microscopy for microtubules stabilized with taxol after polymerization (63). Also, when we fitted a line to our combined step size data as a function of load, the line did not have a significant slope, i.e. we could not measure a force dependence of the linker compliance. Thus, any effect on measured step size due to linker compliance must be within the error margin of measured mean step size. Based on the standard deviation of the means σ_{δ} , we determined a lower estimate of the linker stiffness $\kappa_L \gtrsim \Delta F_{step} / \sigma_{\delta}$. When we pooled all step sizes that were determined by the step finding algorithm from both ATP concentrations, the step size was 4.14 ± 0.06 nm (Gaussian center \pm fit error). Based on this error, the linker stiffness is at least 3 pN/nm. When we averaged the 10 mean step size values of table S1 and S2, the average mean step size was 4.18 ± 0.09 nm (mean \pm standard deviation). Based on this error the linker stiffness was at least 2 pN/nm—the value quoted in the main text. Thus, the linker stiffness was at least one order of magnitude larger than previously reported values (5, 10, 13) and contributed to our improved spatiotemporal resolution.

1.2. Influence of vertical forces

To initiate motility, we placed motor-coated GeNTOPs on microtubules by exerting a small downward force of about -0.1 pN. Since the trap position was not changed during an experiment, the *applied* vertical force was constant. However, this downward force normal to the microtubule axis was not the vertical force acting on the motor, but was counteracted by the surface and/or microtubule. The vertical force that the motor experienced was much higher, in the opposite upward direction, and caused by the contact of the probe with the surface during motility (22, 45, 64). Optical forces act through the center of the trapped probe. Thus, the lateral force that the motor generated during motility pushed the GeNTOP in contact with the microtubule. In this case, the vertical force on the motor was determined by the geometry of the experiment (Fig. 1B, magnified view in fig. S3) and was in magnitude comparable to the lateral force, i.e. in the piconewton range (64). Since the GeNTOPs were 5–10 \times smaller compared to probes of previous experiments, the pulling angle and inherent vertical force in our experiments was also much smaller compared to previous microsphere experiments, but likely larger compared to recent experiments in the so called “three-bead assay” (64). Since our GeNTOPs were comparable in size to vesicles that are transported *in vivo*, the force

geometry was similar. Therefore, we expect similar upward forces to act on the motor even in the significantly more complex *in vivo* situation.

Forces normal to the microtubule axis may affect the motility of motors in different ways. For example, vertical load may accelerate motor detachment (22, 64), and decrease stall durations (64), run length (22), and forward speed (45). In previous experiments, we showed that motors still slipped when upward forces were applied and that the occurrence of slips decreased with an applied upward load (Sect. 3 and Fig. S18 in supporting information of (8)). How the slip speed itself, i.e. the slip step dwell time, and the associated protein friction is affected by vertical force is not known. Motors also did not rotate during slips (8). Therefore, based on these previous measurements and our current data, we suggest that motor heads—both during regular stepping and slipping—always remain in contact with the microtubule lattice even under vertical loads. This contact could be mediated via electrostatic interactions, for example, with the negatively charged E-hooks of tubulin. Thus, we think that motors do not “lift their feet” during stepping but “shuffle” them along the microtubule.

1.3. Rescues and concatenation of runs

We discovered that directed motor motility can be rescued after a slip event. Rescues occurred after partial (fig. S8) or complete (Fig. 3) return to the trap center. In the latter case, no load was acting on the probe during rescue. In the absence of load, motors should also enter the slip state prior to detachment (Fig. 3, (22)). Thus, we expect that also runs of unloaded motors are concatenations of “mini runs” (37). The number of mini runs should follow a binomial distribution with the mean number of runs given by one over the detachment probability $\bar{n} = p_{detach}^{-1}$. The mini run length itself is the total run length divided by the mean number of runs, or simply the run length times the detachment probability. For our measured value of $p_{detach} = 0.2$ and a kinesin-1 run length of about 1 μm , the mini run length is 200 nm. We expect that an individual mini run has an exponential distribution. If the total run length would be a concatenation of always the *same number* of mini runs, we would expect that the total run length should have a gamma distribution. However, with a *binomially distributed number* of mini runs, the total run length is also exponentially distributed, which we verified by a simulation.

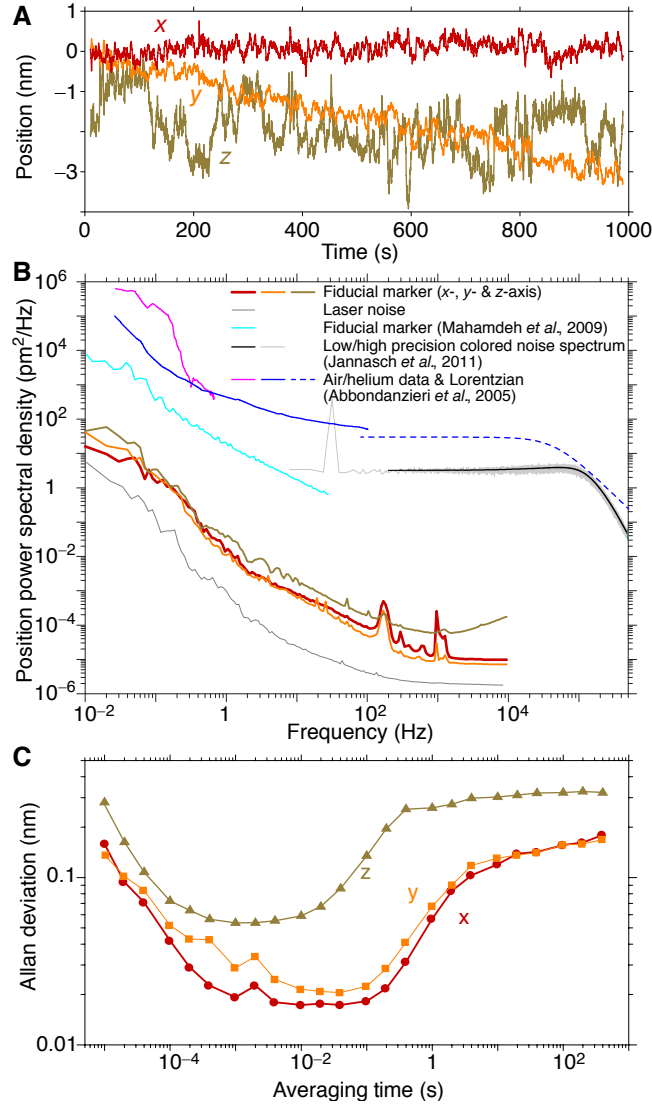


Fig. S1. Ultrastable optical tweezers. (A), Position of a fiducial marker as a function of time (100 kHz data blocked to 10 Hz bandwidth). (B), Position power spectral density recorded for a fiducial marker in comparison to the stability of the benchmark setup (Abbondanzieri *et al.*, 2005 (7)) and previously recorded data (Mahamdeh *et al.*, 2009 (28) and Jannasch *et al.*, 2011 (53); the latter features a calibration peak). (C), Allan deviation as a function of averaging time for the same data. Note that the setup was moved from a third-floor laboratory at the TU Dresden, Germany, where previous data (28, 53) was recorded, to a basement room at the University of Tübingen, Germany, with excellent vibration and sound isolation and temperature stability (54).

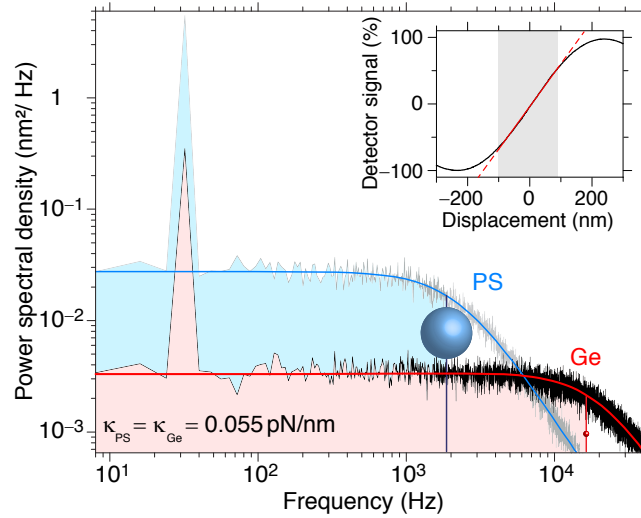


Fig. S2. Calibration of optically trapped germanium nanospheres (GeNTOPs). Power spectral density (average of 40 individual power spectra recorded with the same probe) of GeNTOP (70-nm diameter, germanium (Ge), black line) and microsphere motion (0.59- μm diameter, polystyrene (PS), gray line) trapped in water. Lorentzian-like spectra feature a calibration peak at 32 Hz (red and blue lines, fit to theory (29), see methods). Rolloff or corner frequencies f_c are indicated by vertical lines through schematic, proportionally scaled spheres. The corner frequency serves as a measure for the available measurement bandwidth (shaded areas) and is related to the trap response time $\tau_{trap} = (2\pi f_c)^{-1} = \gamma/\kappa$. Because of the fluctuation-dissipation theorem, the total area underneath the power spectra of the GeNTOP and microsphere motion is the same. However, power is distributed differently across the frequency space with a higher corner frequency and lower positional noise level at low frequencies for the GeNTOPs compared to the microsphere allowing for an improved spatiotemporal resolution. Inset: lateral detector response of a surface-immobilized GeNTOP as a function of displacement relative to the trap center (black line, linear fit red line).

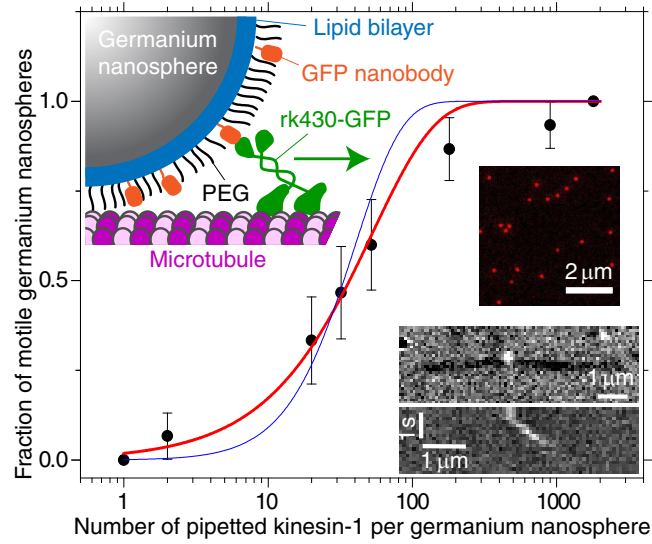


Fig. S3. Single kinesins transported lipid-bilayer-coated GeNTOPs. Fraction of motile GeNTOPs as a function of kinesin-to-GeNTOP ratio. Data (black circles, 40 tested nanospheres per condition) with Poisson statistics fit (transport by at least one (red line) or at least two (blue line) motors, see methods). Insets: Schematic of a kinesin motor (GFP tagged, truncated rat kinesin rk430-GFP) transporting a functionalized GeNTOP along a microtubule drawn roughly to scale (left). Confocal image of lipid bilayer-coated GeNTOPs with a membrane dye confirmed the presence of the lipid bilayer (top right). Interference reflection microscopy image and kymograph (bottom right) of a single kinesin-transported GeNTOP placed on a microtubule with the optical tweezers (bright and dark contrast, respectively).

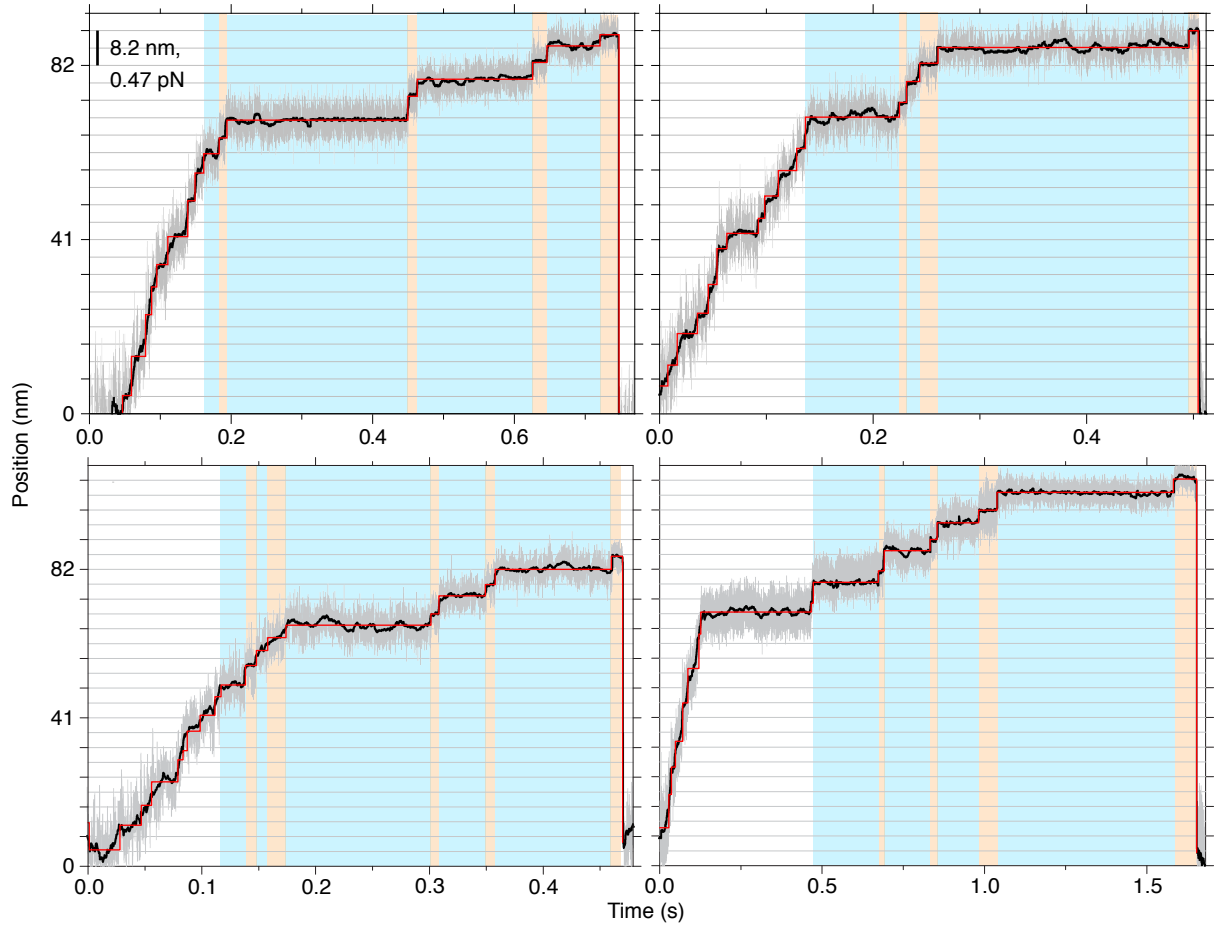


Fig. S4. Exemplary kinesin traces at physiological ATP concentrations. Time traces for a single-kinesin powered GeNTOP (100 kHz sampling rate, gray trace; filtered data, ≈ 100 Hz bandwidth, black trace; detected steps, red line; see methods). Long and short dwell times τ_1 and τ_2 are blue and orange shaded, respectively.

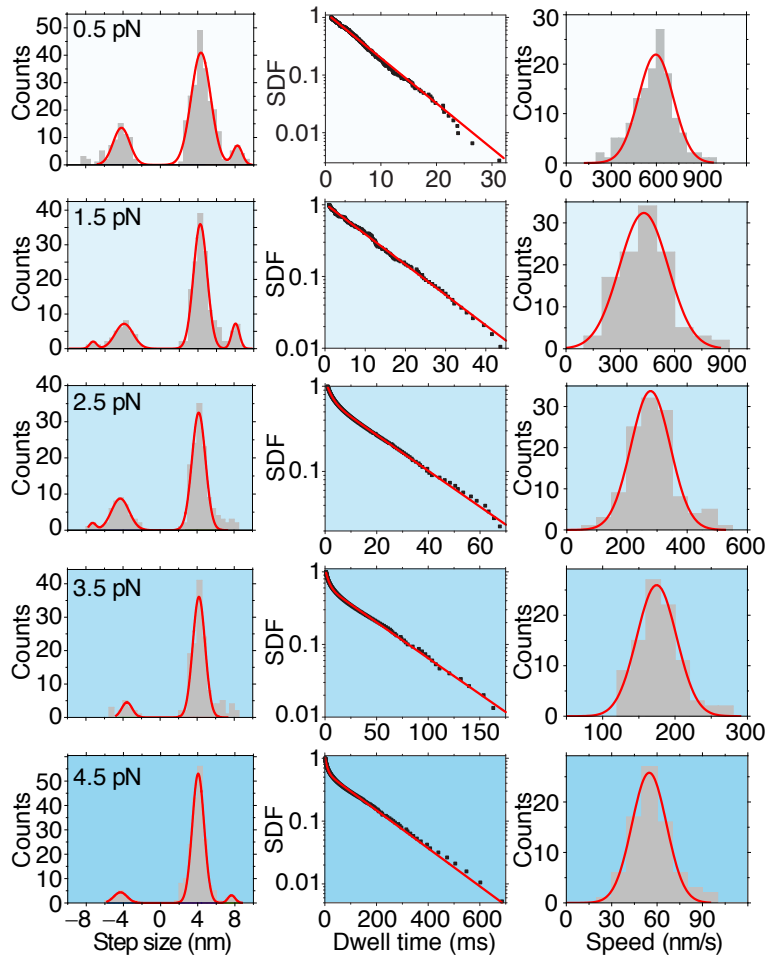


Fig. S5. Step size, dwell time, and speed distributions versus force at physiological ATP concentrations. Step size histograms with multi-Gaussian fit (left column), survival distribution functions (SDFs) of dwell times with fits of single or sum of two exponentials (middle column) and speed histograms with Gaussian fit (right column) for forces range with centers from 0.5 pN to 4.5 pN (top to bottom). See table S1 for fit results. Step sizes and dwell times resulted from the step finding algorithm that detected steps based on the raw data.

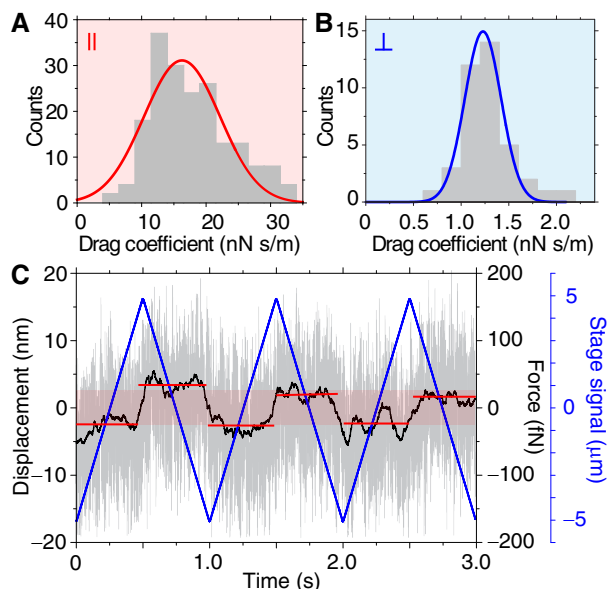


Fig. S6. Frictional drag coefficient based on fast backward motion. Histograms of the frictional drag coefficient measured **(A)**, parallel (γ_{\parallel} , left, red shaded) and **(B)**, perpendicular (γ_{\perp} , right, blue shaded) to the microtubule axis with Gaussian fits (red and blue lines). The frictional drag coefficient for the two directions was calculated according to $\gamma = \tau\kappa$ using the measured values for the relaxation time and trap stiffness (see Fig. 3 and methods). The resulting values for γ_{\parallel} and γ_{\perp} are 16.0 ± 0.8 nN s/m ($N = 149$) and 1.24 ± 0.07 nN s/m ($N = 50$), respectively. The latter frictional drag coefficient γ_{\perp} was larger than the hydrodynamic (viscous) drag coefficient expected from Stokes drag and the measured GeNTOP size. The ratio between the measured coefficient γ_{\perp} and the calculated Stokes drag coefficient is about 1.9. This increase is due to the surface proximity (30). Based on Faxén’s law, this ratio is consistent with the GeNTOP being 10 nm away from the surface. **(C)**, GeNTOP without motors dragged over a microtubule with a speed of $v = 20$ $\mu\text{m/s}$. The motorless GeNTOP was placed on top of a microtubule in the same manner as for motor-coated GeNTOPs that were used for all other experiments. Then, the stage (blue line) was moved relative to the stationary trapping laser in analogy to previous measurements (36). The lateral GeNTOP position and force F (black line) showed the expected hydrodynamic drag $F = \gamma v$ consistent with the drag coefficient measured perpendicular to the microtubule axis in (B) and a calibration directly on top of the microtubule of 1.21 ± 0.09 nN s/m (fit error). Red lines indicate average drag forces per pulling direction. The red shaded region is the overall average drag force of 24 ± 6 fN corresponding to a drag coefficient of 1.2 ± 0.3 nN s/m (mean \pm standard deviation, $N = 25$). We did not observe any interaction dragging 18 different GeNTOPs over 12 different microtubules. Note that all drag force measurements indicate that there was no severe laser heating, which would cause a reduction in viscosity and drag.

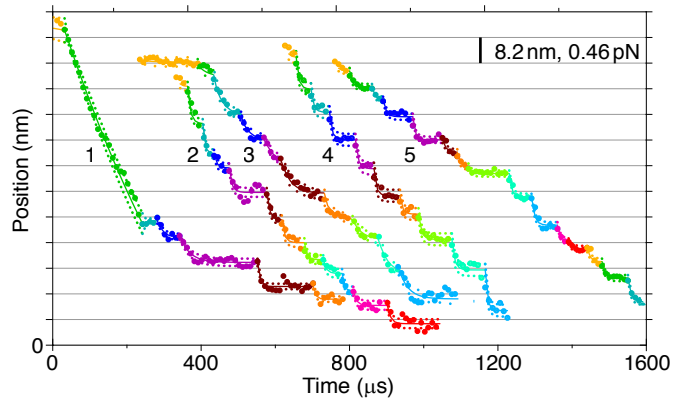


Fig. S7. Exemplary kinesin traces of fast backward motion in the slip state. Colored sections correspond to detected states fitted with a single exponential relaxation (solid lines) using the “Steppi” algorithm (32) (small dotted lines: 95% confidence interval; large dots: raw data). Traces 1 and 2 had no constraints (32) resulting in a step size of 7.7 ± 0.1 nm and exponential relaxation time of 27 ± 3 μ s ($N = 20$, excluding the first step of Trace 1). Trace 3 is an example recorded at low ATP. At low ATP, the average time constant of an exponential relaxation for the whole trace was $\tau_{||} = 292 \pm 8$ μ s ($N = 20$) consistent with the high ATP data (Fig. 3A). Based on the “Steppi” algorithm without constraints, slip steps at low ATP had a step size of 7.4 ± 0.3 nm ($N = 55$) with a corresponding dwell time of 73 ± 4 μ s ($N = 55$) again consistent with the high ATP data (see main text). For Traces 4 and 5, the relaxation time constant was fixed to 25 μ s (see methods). The force scale bar is based on the average trap stiffness for the traces.

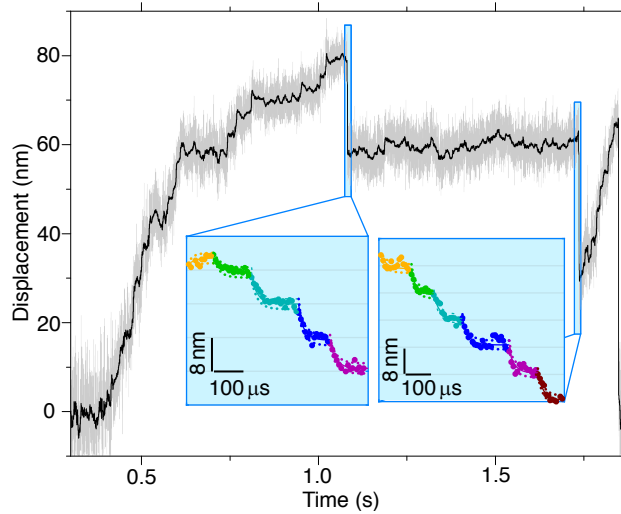


Fig. S8. Exemplary kinesin trace with short slip events. Time traces for a single-kinesin powered GeNTOP (100 kHz sampling rate, gray trace; filtered data, ≈ 100 Hz bandwidth, black trace; see methods). Insets: Magnified view of short backward slips. Colored sections correspond to detected single-exponential-relaxation states using the “Steppi” algorithm (32). Note that slip-step dwell times appear to be longer compared to Fig. 3A and fig. S7 potentially indicating that a second slip state may exist. In this state, one head may still be in the ADP·P_i state (37) with an undocked neck linker.

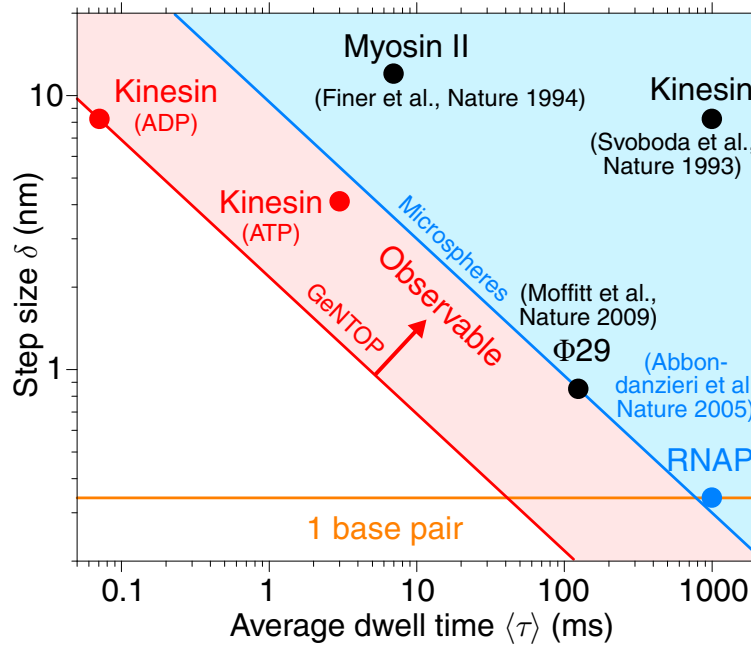


Fig. S9. Optical tweezers spatiotemporal resolution of molecular machines. Step size versus dwell time for various molecular machines (7, 10, 65, 66) in comparison to this work (red circles, 4-nm directed substeps (0–1 pN data point at 10 μ M ATP of table S2), fast 8-nm sliding steps (ADP state, Fig. 3A)). The blue line indicates the previous microsphere benchmark (7) and the red line the current GeNTOP spatiotemporal resolution (this work) according to the relation $\delta\sqrt{\langle\tau\rangle} \geq \frac{\sqrt{2k_B T N \gamma}}{\kappa_L} \text{SNR} = \text{const}$, where κ_L is the linker stiffness, N the number of data points per step, and SNR the signal-to-noise ratio (2). The half space above the lines is observable.

Table S1. Step size, dwell time and speed versus force at 1 mM ATP.

F	δ_+ (nm)	p	δ_- (nm)	p	τ_1 (ms)	p	τ_2 (ms)	p	v ($\mu\text{m/s}$)
0–1	4.34 ± 0.06 (217)	72	4.2 ± 0.2 (65)	22	5.5 ± 0.2 (306)	120	–	–	0.60 ± 0.01 (134)
	8.2 ± 0.6 (19)	6							
1–2	4.25 ± 0.04 (140)	72	4.0 ± 0.2 (34)	18	10.3 ± 0.8 (193)	103	–	–	0.43 ± 0.01 (110)
	7.8 ± 0.2 (15)	8	8.2 ± 0.6 (4)	2					
2–3	4.19 ± 0.04 (127)	71	4.1 ± 0.2 (42)	25	20.6 ± 0.1 (100)	71	2.1 ± 0.7 (78)	50	0.28 ± 0.01 (117)
	7.3 ± 0.5 (4)	2	7.3 ± 0.5 (5)	2					
3–4	4.18 ± 0.05 (127)	85	3.9 ± 0.4 (16)	10	44.7 ± 0.4 (84)	63	3.3 ± 0.7 (66)	49	0.18 ± 0.01 (112)
	7.8 ± 0.2 (7)	5							
≥ 4	4.06 ± 0.03 (168)	89	4.3 ± 0.4 (16)	8	144 ± 2 (104)	60	8.8 ± 0.2 (86)	47	0.055 ± 0.001 (92)
	7.6 ± 0.4 (6)	3							

F (pN): force, $\delta_{+/-}$: forward/backward step size—Gaussian center \pm fit error (N based on area underneath Gaussian normalized by total number of steps), p (%): relative percentage, τ : dwell time based on survival function fit (N according to relative amount), and v : speed—mean \pm standard error (N : number of trace segments fitted). All fits to data of fig. S5. Note that only few data points correspond to forces larger than 5 pN. Also note that p -values for dwell times directly reflect the fitted amplitude that may add up to more than 100 % indicating that some of the expected very short steps were missed. Errors on all percentages are less than 1 %.

Table S2. Step size, dwell time and speed versus force at 10 μ M ATP.

F	δ_+ (nm)	p	δ_- (nm)	p	τ_1 (ms)	p	τ_2 (ms)	p	v (μ m/s)
0–1	4.13 \pm 0.06 (53)	67	4.2 \pm 0.2 (15)	20	30.2 \pm 0.6 (44)	65	3.1 \pm 0.2 (34)	47	0.23 \pm 0.01 (12)
	7.2 \pm 0.2 (10)	13							
1–2	4.15 \pm 0.03 (53)	69	4.5 \pm 0.4 (9)	11	37.8 \pm 0.7 (42)	61	3.3 \pm 0.1 (34)	49	0.16 \pm 0.01 (17)
	7.6 \pm 0.36 (15)	20							
2–3	4.05 \pm 0.03 (59)	78	4.5 \pm 0.5 (7)	9	54.3 \pm 0.1 (40)	58	3.8 \pm 0.1 (37)	52	0.110 \pm 0.007 (13)
	7.5 \pm 0.17 (10)	13							
3–4	4.17 \pm 0.05 (42)	70	4.3 \pm 0.2 (6)	10	131 \pm 3 (33)	57	6.8 \pm 0.3 (27)	45	0.056 \pm 0.005 (15)
	7.84 \pm 0.36 (12)	20							
≥ 4	4.12 \pm 0.04 (77)	85	3.9 \pm 0.2 (6)	7	245 \pm 5 (41)	56	8.0 \pm 0.3 (40)	45	0.032 \pm 0.004 (15)
	8.12 \pm 0.13 (7)	8							

F (pN): force, $\delta_{+/-}$: forward/backward step size—Gaussian center \pm fit error (N based on area underneath Gaussian normalized by total number of steps), p (%): relative percentage, τ : dwell time based on survival function fit (N according to relative amount), and v : speed—mean \pm standard error (N : number of trace segments fitted). Note that only few data points correspond to forces larger than 5 pN. Also note that p -values for dwell times directly reflect the fitted amplitude that may add up to more than 100% indicating that some of the expected very short steps were missed.

Errors on all percentages are less than 1%.

Cite this: *Nanoscale Adv.*, 2020, 2, 4003


Received 20th May 2020

Accepted 12th July 2020

DOI: 10.1039/d0na00406e

rsc.li/nanoscale-advances

Polycationic gold nanorods as multipurpose *in vitro* microtubule markers

Viktoria Wedler, Fabian Strauß, Swathi Sudhakar, Gero Lutz Hermsdorf, York-Dieter Stierhof and Erik Schäffer *

Gold nanoparticles are intriguing because of their unique size- and shape-dependent chemical, electronic and optical properties. Gold nanorods (AuNRs) are particularly promising for various sensor applications due to their tip-enhanced plasmonic fields. For biomolecule attachment, AuNRs are often functionalized with proteins. However, by their intrinsic size such molecules block the most sensitive near-field region of the AuNRs. Here, we used short cationic thiols to functionalize AuNRs. We show that the functionalization layer is thin and that these polycationic AuNRs bind *in vitro* to negatively charged microtubules. Furthermore, we can plasmonically stimulate light emission from single AuNRs in the absence of any fluorophores and, therefore, use them as bleach- and blinkfree microtubule markers. We expect that polycationic AuNRs may be applicable to *in vivo* systems and other negatively charged molecules like DNA. In the long-term, microtubule-bound AuNRs can be used as ultrasensitive single-molecule sensors for molecular machines that interact with microtubules.

Introduction

The plasmon-enhanced scattering and absorption of gold nanoparticles enable many different applications.^{1,2} Of particular interest is the rod shape of AuNRs because the plasmon resonance can be tuned over a wide range from visible to near-infrared wavelengths.^{2,3} Beyond roughly 600 nm, gold has little interband transitions resulting in low plasmonic damping and large field enhancements at the AuNR tips. Therefore, the plasmonic resonance can be exploited for the enhancement of fluorescent dye signals or sensory fields.^{4,5} Importantly, plasmonically excited photoluminescence—without the use of fluorophores—enables AuNRs to be used as non-blinking and non-bleaching luminescent probes.³ Furthermore, the AuNR shape provides a transverse and longitudinal geometrical axis with different optical properties that enable angular measurements with polarized light.^{6,7} When the strong plasmonic field enhancement around the AuNR tips is combined with other resonators such as whispering gallery modes, it can further boost single-molecule measurements. In this manner, AuNRs may serve as ultrasensitive nanoantennas that even enable the detection of single-ion binding events on nanosecond time scales.^{5,8,9} The binding and turnover of single ions and molecules, for example during adenosine triphosphate (ATP) hydrolysis, are key to the conformational changes of molecular machines that drive essential cellular processes such as cell

division and transport.^{10–12} Yet, while consensus is developing on how motor proteins like kinesin operate^{13,14} important molecular details on how nucleotide states are related to conformational changes remain unclear. One reason is that tools are lacking to simultaneously detect molecular binding events and related conformational changes with sufficient spatiotemporal resolution.

During a hydrolysis cycle, kinesin transport-motors advance by 8 nm along a microtubule filament *via* a rotational hand-over-hand mechanism.¹⁵ Conformational changes of individual motors are often deduced from stepping or gliding assays, in which motors step on individual surface-attached cytoskeletal filaments, here microtubules, or surface-attached motors power filaments to glide over surfaces, respectively. Label-free microtubules can be visualized using dark field microscopy¹⁶ or interference-based microscopy methods such as differential interference contrast (DIC),^{17,18} interference reflection microscopy (IRM),^{19–21} or interferometric scattering microscopy (iSCAT).²² For fluorescence microscopy, microtubules can be polymerized from fluorescently labeled tubulin²³ or be visualized by immunofluorescence, *i.e.* using fluorescently labeled tubulin antibodies.²⁴ Since antibodies are large, fluorescently labeled tubulin nanobodies have been developed more recently.²⁵ For better photophysical properties and reduced photobleaching, not avoiding blinking though, quantum dots can be used for microtubule labeling.²⁶ Various microscopy techniques, often combined with optical tweezers, are used to gain molecular information from motor-microtubule assays.^{20,21,27–33} In gliding assays, AuNRs attached to microtubules were used to track translational or rotational

Eberhard Karls Universität Tübingen, Cellular Nanoscience (ZMBP), Auf der Morgenstelle 32, 72076 Tübingen, Germany. E-mail: erik.schaeffer@uni-tuebingen.de; Fax: +49 7071 295042; Tel: +49 7071 2978831



motion using DIC.^{27–29} Based on resonance-enhanced scattering, gold nanoparticles attached to kinesin motors themselves provided sufficient contrast to resolve intermediate steps and conformational changes during the stepping cycle.^{31,32} Still, the above-mentioned techniques are limited to resolve trajectories of motor motion and conformational changes that can only indirectly be correlated with chemical changes. AuNR-antenna-related techniques with the sensitivity to detect single ions on a nanosecond timescale open up the vision to directly and simultaneously measure conformational and chemical states of motor proteins during a hydrolysis cycle. As a first step towards this challenging goal, here we developed a method to bind AuNR nanoantennas close enough to microtubules such that motor proteins can walk through the most sensitive, tip-enhanced antenna volume of the AuNRs. Gold-nanoparticle-microtubule attachments are so far based on direct synthesis of irregularly shaped gold particles onto microtubule templates, or antibody or biotin-binding-protein functionalized gold nanoparticles.^{27–29,34–36} Such attachments may compromise nanoantenna-based motor sensing: NeutrAvidin and antibody coatings with a size of about 5 nm (ref. 37) and 10 nm,³⁸ respectively, block the most sensitive region of the plasmonic near-field below 10 nm (ref. 4 and 39–41) that is also important for whispering-gallery-mode-amplified sensing. Moreover, in the presence of proteins, gold nanoparticles may aggregate or denature proteins in contact with the gold surface.⁴² To prevent aggregation of AuNRs, standard stabilization detergents such as cetyltrimethylammonium bromide (CTAB) are used resulting also in several nanometer-thick AuNR coatings.^{8,40,43} Even though often used, CTAB-coated AuNRs are disadvantageous because they are cytotoxic and require a high CTAB concentration to prevent the colloidal suspension from aggregation.^{44–46} Alternatively, for usage in biological systems and reduced cytotoxicity, AuNRs have been charge-stabilized with (11-mercaptoundecyl)-*N,N,N*-trimethylammonium bromide (MUTAB).⁴⁷ Here, we followed the latter approach and used the thin, covalently bound, cationic MUTAB monolayer to attach the AuNRs *via* electrostatic interactions to the negatively-charged, unstructured E-hooks located on the outer surface of the hollow microtubule cylinder.⁴⁸ To verify the coating thickness and binding orientation of the MUTAB AuNRs relative to microtubules, we used transmission electron microscopy (TEM). Combined total internal reflection fluorescence (TIRF) and interference reflection microscopy (IRM) confirmed colocalization of MUTAB AuNRs with microtubules by detecting rhodamine-labeled MUTAB AuNRs or directly the photoluminescence of MUTAB AuNRs without any fluorescent labels for long-term, bleach- and blinkfree imaging. Furthermore, we optimized the glass surface itself for specific microtubule binding as close as possible to the surface to allow—in the future—for highest whispering gallery mode contrast while minimizing non-specific interactions of AuNRs.

Results

For MUTAB coupling of AuNRs, we synthesized AuNRs *via* a two-step wet chemical method using CTAB as a stabilizing agent⁴⁹

(molecule 1 in Fig. 1A top left, see Methods). Analyzing TEM images of AuNRs showed that they were 43 ± 4 nm long and 17 ± 1 nm wide with an aspect ratio of 2.6 ± 0.3 (means with standard deviations, $N = 34$, Fig. 1B). We measured a corresponding longitudinal surface plasmon resonance at about 675 nm using a spectrofluorometer. The negative staining also showed an irregular, about 4 nm thick coating around the AuNRs that we attribute to CTAB. We did not observe a regular coating theoretically expected for a bilayer. In agreement with the literature,⁴⁷ CTAB AuNRs were not stable under physiological buffer conditions. Because of the coating thickness and aggregation, we exchanged CTAB with MUTAB (molecule 2, Fig. 1A top row).⁴⁷ MUTAB functionalization successfully charge-stabilized the AuNRs for usage in physiological buffer and created a polycationic surface. We verified the positive charge and electrostatic repulsion between AuNRs by measuring their zeta potential of 31 ± 2 mV (mean with standard deviation, $N = 3$). In the TEM images, the MUTAB monolayers appeared as a smooth, about 1–2 nm-thick coating (Fig. 1C), much thinner compared to the irregular CTAB layer (Fig. 1B). Based on the chemical structure, the expected thickness is even below 1 nm. As an independent size measurement, we performed dynamic light scattering experiments. MUTAB AuNRs had an effective size of 43 ± 1 nm (mean with standard deviation, $N = 36$) consistent with the TEM measurements. In contrast, CTAB AuNRs had a size of 51 ± 8 nm (mean with standard deviation, $N = 36$). The difference in the mean values between CTAB and MUTAB AuNRs and the larger CTAB AuNR standard deviation are consistent with the irregular, 4 nm thick

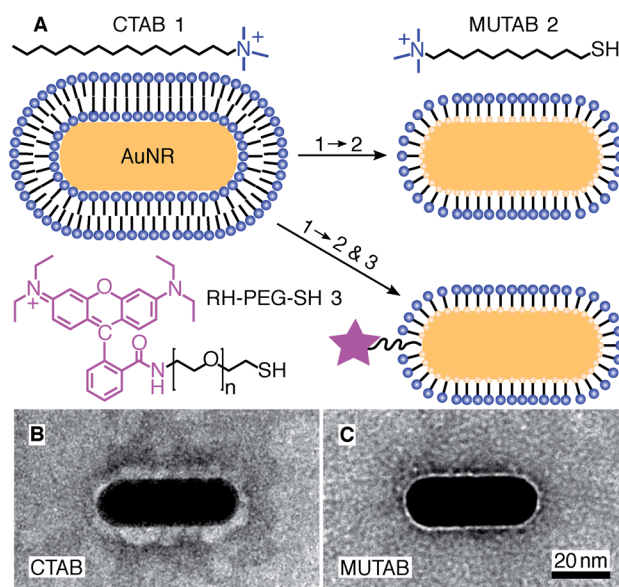


Fig. 1 (A) A gold nanorod (AuNR) coated with an adsorbed CTAB (molecule 1) bilayer is functionalized with MUTAB (molecule 2) to create a monolayer of cationic ligands covalently bound to the nanorod surface *via* gold–thiol bonds (top row). Alternatively, MUTAB was complemented with a rhodamine–PEG–thiol derivative (RH–PEG–SH, $n = 77$, molecule 3) as a fluorescent label. Negative-stained TEM images of (B) CTAB-coated and (C) MUTAB-functionalized AuNRs.



CTAB coating observed in the TEM images. Together, the data suggests that MUTAB functionalized AuNRs have a stable, homogeneous, and thin polycationic coating.

To test whether the polycationic MUTAB AuNRs interacted with the negatively charged microtubules (Fig. 2A), we incubated microtubules with AuNRs in physiological buffer and prepared them for TEM imaging (Fig. 2B–G). Most MUTAB AuNRs were bound to microtubules (Fig. 2B). We expected AuNRs to bind with their long axis parallel to the microtubules axis as this orientation would maximize the area of interaction (Fig. 2A). However, most AuNRs were tip bound (42% out of $N = 154$ AuNR-microtubule colocalizations distributed over five batches, Fig. 2E). Only, 12% were parallel and another 12% somewhat tilted relative to the microtubule axis (Fig. 2C and D). Furthermore, 25% of the colocalizations contained clusters of more than one AuNR (Fig. 2F) and 41% of these clusters bridged two or more microtubules similar to the AuNR cluster in the middle of Fig. 2G. Single AuNRs that bridged microtubules amounted to 9% (Fig. 2G). Overall, AuNRs were bound to microtubules in various orientations.

To colocalize AuNRs with microtubules *in vitro* under physiological buffer conditions and rule out TEM preparation and fixation artifacts, we imaged AuNRs and microtubules using IRM and TIRF microscopy²⁰ (Fig. 3–5). To visualize AuNRs *via* fluorescence, we first coupled a rhodamine B derivative (molecule 3 in Fig. 1A) in addition to MUTAB to AuNRs (Fig. 1A). To prevent quenching of the fluorophore by the AuNR,¹ we chose a dye that had a 3.4 kDa polyethylene glycol (PEG) linker with a contour length of about 21 nm. Since the dye is also cationic, the rhodamine–MUTAB AuNRs' measured zeta potential of 30 ± 5 mV (mean with standard deviation, $N = 3$) was not

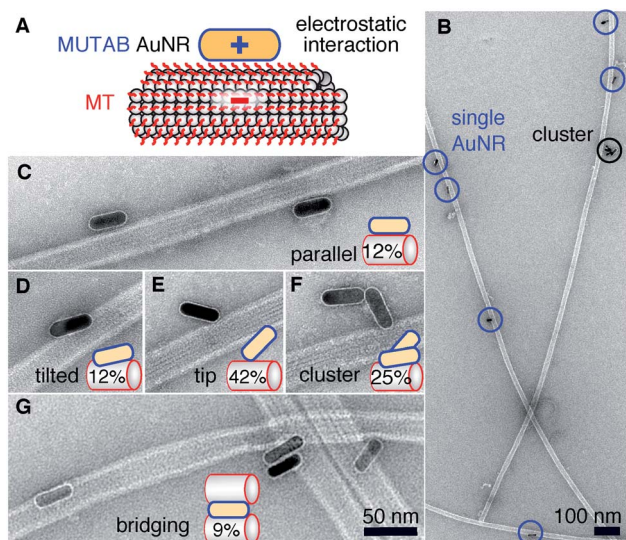


Fig. 2 (A) Proposed electrostatic interaction between a cationic MUTAB (blue) functionalized AuNR and the negatively charged E-hooks (red) of the microtubule (MT). (B) Overview TEM image of AuNR-decorated microtubules. Close-up view of AuNRs bound in a parallel (C) or tilted (D) fashion, bound with their tips (E), as a cluster (F), or bridging microtubules (G). Case percentages of microtubule–AuNR colocalizations are indicated in the schematic insets.

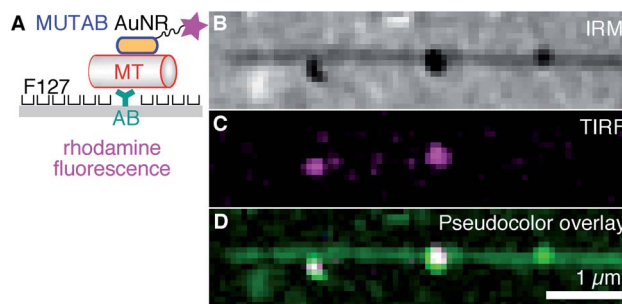


Fig. 3 (A) For fluorescence microscopy, AuNRs coated with MUTAB (blue, positively charged) and rhodamine (magenta star) were attached to a microtubule (MT, red, negatively charged) bound *via* an antibody (AB, dark cyan) to a surface (gray) that was PEGylated with the poloxamer Pluronic F127. (B) IRM, (C) TIRF, and (D) IRM–pseudocolor–TIRF overlay image of single rhodamine–MUTAB AuNRs bound to a single microtubule (see Methods for details on the pseudocolor overlay).

significantly different from the MUTAB AuNRs without the dye. The size of 49 ± 3 nm (mean with standard deviation, $N = 36$) determined by dynamic light scattering indicates a small increase in size most likely due to the PEG linker. For *in vitro* assays using the fluorophore-labeled AuNRs, we tested different methods how microtubules were bound to surfaces to minimize nonspecific interactions and the microtubule distance to the surface.

First, we tested a common microtubule immobilization assay for single molecule measurements based on hydrophobic surfaces.^{33,50,51} In this assay, antibodies are adsorbed for specific attachment of microtubules, while the remaining surface is blocked by PEGylation by means of adsorption of the triblock copolymer Pluronic F127 (Fig. 3A). As opposed to the TEM

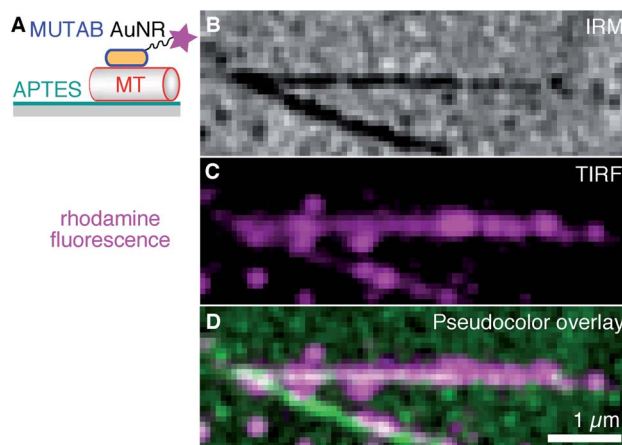


Fig. 4 (A) AuNRs coated with MUTAB (blue, positively charged) and rhodamine (magenta star) bound to a microtubule (MT, red, negatively charged) attached to an APTES (dark cyan, positively charged) coated surface (gray). (B) IRM, (C) TIRF, and (D) IRM–pseudocolor–TIRF overlay image of a high density of rhodamine–MUTAB AuNRs bound to two intersecting microtubules (see Methods for details on the pseudocolor overlay). Bright spots in (C) and (D) may be due to AuNR clusters.



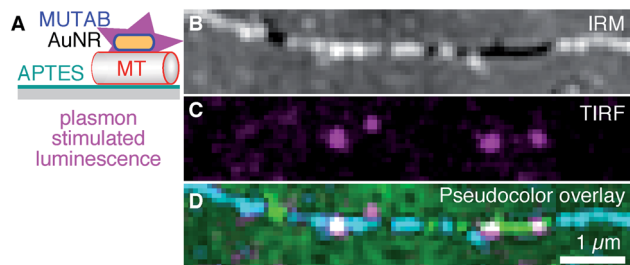


Fig. 5 (A) AuNRs for plasmonic excitation and photoluminescence emission without fluorophores (magenta). AuNRs were only coated with MUTAB (blue, positively charged) interacting with a microtubule (MT, red, negatively charged) attached to an APTES (dark cyan, positively charged) coated surface (gray). (B) IRM, (C) TIRF, and (D) IRM–pseudocolor–TIRF overlay image of AuNRs bound to a single microtubule (green/cyan indicating different microtubule–surface distances, see Methods for details on the pseudocolor overlay). Note that no fluorophores were present and that AuNR markers did not blink or bleach.

assays, microtubules were first attached to the surface and subsequently incubated with a low concentration of rhodamine–MUTAB AuNRs. In the IRM image, microtubules close to the surface and a few AuNRs appear dark due to destructive interference²⁰ (Fig. 3B). Since small fragments of microtubules also generate dark, point-like IRM signals comparable to the ones from AuNRs, we imaged the rhodamine–MUTAB AuNRs simultaneously using TIRF microscopy (Fig. 3C). Two of the dark IRM spots also showed up in the TIRF image and colocalized with the microtubule (Fig. 3D). Taken together, AuNRs were bound to microtubules in *in vitro* assays under physiological buffer conditions, showed little interaction with the remaining surface, and could be reliably identified by combined IRM and fluorescence microscopy.

Next, we tried to minimize the microtubule distance to the surface and increased the AuNR decoration density such that the whole contour of the microtubule becomes marked by the AuNRs (Fig. 4). Antibodies, having a size of about 10 nm, act as spacers keeping microtubules away from the surface, and, therefore, reduce the near-field sensitivity of whispering gallery mode resonators if such resonators were to be used for detecting microtubule-associated molecular machines. To reduce the microtubule distance to the surface, we coated surfaces with 3-aminopropyltriethoxysilane (APTES, Fig. 4A). Ideally, for a monolayer, we expect the coating to be about 1 nm thick,⁵² positively charged under the used buffer conditions, and to bind the negatively charged microtubules.⁵³ As with the PEGylated surface, we first bound microtubules to the surface and then incubated them with a 10-fold higher concentration of rhodamine–MUTAB AuNRs compared to Fig. 3. The IRM image (Fig. 4B) showed a mostly homogeneous dark contrast for the microtubules as expected for objects in surface proximity.²⁰ Qualitatively, already undecorated microtubules appeared darker on APTES surfaces compared to the PEGylated antibody surfaces indicating a smaller microtubule–surface distance for the APTES surface.²⁰ The decoration with the AuNRs increased the dark contrast further. Based on the TIRF and overlay images

(Fig. 4C and D, respectively), microtubules were fully decorated with rhodamine–MUTAB AuNRs. Additional, bright spots indicate the presence of AuNR clusters also seen in the TEM images (Fig. 2B and F). Furthermore, AuNRs next to the two long microtubules are possibly bound to smaller microtubule fragments and/or tubulin oligomers that were also present in the sample. Summarizing, microtubules were bound very close to the surface and highly decorated with polycationic AuNRs.

To be independent of fluorescent dyes and have probes that do not blink or bleach, we excited the intrinsic one-photon luminescence of AuNRs without any fluorophores (Fig. 5 using MUTAB AuNRs schematically illustrated in the top right of Fig. 1A). To this end, we used shorter and thicker AuNRs with a longitudinal localized surface plasmon resonance of 570 nm that we could image in the red channel of our TIRF microscope. We also stabilized these AuNRs with a size of $40 \times 25 \text{ nm}^2$ by MUTAB and incubated them with microtubules bound to APTES coated surfaces (Fig. 5A). The exemplary IRM image (Fig. 5B) shows a microtubule that had some parts of it elevated several tens of nanometers above the surface (white sections). The TIRF image shows the photoluminescence of a few MUTAB AuNRs with a brightness comparable to the one of rhodamine–MUTAB AuNRs under the same imaging conditions (Fig. 5C). Also under these conditions, most AuNRs colocalized with microtubules (Fig. 5D). The intensity of the individual spots in the TIRF image did not fluctuate beyond photon shot noise and did not show any signs of bleaching over the imaging period. We could image AuNRs for at least 10 min using 50 mW of output power for excitation—10× more compared to the excitation power used for Fig. 5C—without any signs of signal loss. Thus, the plasmon resonance could be used to stimulate photoluminescence of the AuNRs without any fluorophores.

Discussion & conclusions

We synthesized charge-stabilized, polycationic AuNRs that bind directly, free of protein coatings, with hardly any separation to microtubules in *in vitro* assays under physiological buffer conditions. Most likely, the specificity is mediated through electrostatic interactions. These interactions are also consistent with the notion that the MUTAB AuNRs were electrostatically repelled from the positively charged APTES surface attaching selectively to microtubules without any antibodies or further surface blocking (Fig. 4). Interestingly, the TEM images showed that many AuNRs were not bound parallel to the microtubule axis but *via* their tips (Fig. 2). This binding orientation may indicate that the tip-enhanced fields augment the electrostatic interaction causing tip binding to dominate over lateral contacts. Charge-stabilization allowed us to work with high AuNR concentrations, enabling high decoration densities of AuNRs that make the whole microtubule visible *via* the AuNR marker (Fig. 4). Since AuNRs have the capability to bridge microtubules and potentially bundle them, the order of reagents, concentrations, and incubation times have to be optimized if bundling is undesired. In analogy to microtubule bridging, AuNR clusters might be due to remnant tubulin or tubulin oligomers cross-linking AuNRs. In pure buffer without



proteins, we observed little clustering. We do not know whether the TEM sample preparation influenced the binding orientation. But since AuNRs resisted washing cycles with a large hydrodynamic drag during sample preparation, we conclude that AuNRs were strongly bound to microtubules. Also, we did not observe any visual movement of the AuNRs during image acquisition. In the TEM images, the microtubule lattice structure appeared to be intact and not influenced by the bound AuNRs. Occasionally, small lattice defects were visible near bound AuNRs. However, it remains unclear whether defects were due to the AuNR, already present before the AuNR bound,⁵⁴ or due to the sample preparation. Fully decorated microtubules observed by optical microscopy (Fig. 4) indicate that no major damage was inflicted by the AuNRs. Some variations in plasmon stimulated luminescence between individual AuNRs might indicate that AuNRs were tip-bound and due to polarization effects were not well excited.^{55,56} Nevertheless, because of the strong binding of MUTAB AuNRs to microtubules, we speculate that MUTAB AuNRs should also bind to and mark—in *vitro* and potentially also *in vivo*—other negatively charged molecules or organelles like DNA or mitochondria, respectively. While *in vitro*, there is usually a controlled number of negatively charged molecules present allowing for AuNRs to be used as a specific marker, *in vivo* there are more non-specific interactions. Nevertheless, due to the law of mass action, we expect the AuNRs to preferential bind the most negatively charged molecules and organelles.

For photoluminescence, we first functionalized the MUTAB AuNRs with rhodamine *via* a PEG linker for fluorescence microscopy. One contribution to the bright fluorescence, we observed for single AuNRs (Fig. 3), could be the electrostatic repulsion between the cationic dye and the cationic MUTAB surface. This repulsion could increase the extension of the 21 nm long PEG linker and thereby further decrease quenching that is often observed for fluorophores in close proximity to gold nanoparticles.¹ More importantly, without fluorophores, we could plasmonically stimulate the intrinsic luminescence of MUTAB AuNRs with comparable brightness to rhodamine-labeled MUTAB AuNRs. Using either photoluminescence or scattering, we successfully showed colocalization of single or multiple AuNRs with microtubules using a combination of IRM and TIRF microscopy. In particular, the plasmonic microtubule markers enable longtime observation of microtubules by TIRF microscopy without blinking and bleaching effects.

Finally, the MUTAB AuNRs' attachment *via* the thin cationic monolayer to microtubules leaves the plasmonically tip-enhanced areas accessible. Such AuNRs could be used as roadblocks to understand how kinesin and other microtubule-based motors bypass obstacles.^{57–60} If motors have a fluorescent tag, bypassing of motors in the proximity of the AuNR tips might show up as a transient increase in fluorescence.⁴ A direct encounter may lead to a pause in translocation. In the long term, to correlate translocation with conformational and chemical states of molecular machines that interact with microtubules, MUTAB AuNRs could be used as nanoantenna sensors in combination with whispering gallery modes allowing for a detailed molecular insight into how such machines work.

Methods

All chemicals were purchased from Sigma Aldrich and used without further purification unless noted otherwise. Purified Type 1 water was used for all experiments (18.2 M Ω cm, Nanopure System Milli-Q reference with Q-POD and Biopak filter).

Gold nanorod synthesis

Gold nanorods were prepared by a common seeding-growth method.⁴⁹ First, gold seeds were generated and second, these seeds were further grown to a rod shape by the structure directing aid of silver nitrate. Gold seeds were prepared by adding subsequently 125 μ L of 0.01 M HAuCl₄ and 300 μ L NaBH₄ to 3.75 mL 0.1 M CTAB solution while stirring vigorously for 2 min. Afterwards, the seed solution was left undisturbed in the dark for 2 h at room temperature of about 25 °C. The growth solution was prepared in 42.75 mL of a 0.1 M CTAB solution by consecutively adding the following substances: first, 1.8 mL of 0.01 M HAuCl₄ was added and gently stirred for 1 min and, second, 270 μ L of an aqueous 0.01 M AgNO₃ solution and 288 μ L of an aqueous 0.1 M ascorbic acid solution were added and stirred for 20 s. After this step, the yellowish color of the HAuCl₄ solution should turn colorless indicating its reduction. Immediately after the reduction, 189 μ L of the seed solution were mixed into the growth solution and stirred for 60 s. This solution turned purple after 30 min and was allowed to rest undisturbed and in the dark over night at room temperature.

For luminescence measurements, AuNRs (0.38 nM, A12-25-550-CTAB-DIH-1-25) with a length and width of 40 nm and 25 nm, respectively (aspect ratio 1.6) were purchased from Nanopartz Inc. (Loveland CO, USA). The plasmon resonances were specified as 525 nm and 570 nm.

Gold nanorod functionalization

Synthesized AuNRs were washed, concentrated by 30 min ultracentrifugation at 30 000g, and redispersed in 4 mL of water. An upper estimate for the AuNR concentration based on a theoretical yield of 100% is about 12 nM for the redispersed samples. Additionally, two 15 min washing steps at 11 000g ensured a clean product ready for functionalization. In the last washing step, AuNRs were concentrated to 1 mL. 80 mg of MUTAB were weighed and stored under nitrogen. Under vigorous stirring, MUTAB was dispersed in 3.7 mL of pure water plus optionally 0.3 mL of 14.7 mM rhodamine-3.4k PEG-thiol was added (Biochempeg Scientific Inc., Watertown, USA). After vigorous stirring, AuNRs were added and left for incubation at room temperature and in the dark for 2 days. The MUTAB or MUTAB-rhodamine functionalized AuNRs were washed 5 \times for 15 min by centrifugation at 11 000g as described previously, by removing the supernatant and redispersing the sample in pure water.

For purchased AuNRs, 250 μ L of 0.38 nM A12-25-550-CTAB-DIH-1-25 solution was added to 20 mg MUTAB dissolved in 250 μ L pure water and processed as described before. These MUTAB-550-AuNRs were concentrated by centrifugation and removal of supernatant to 0.7 nM.



Gold nanorod characterization

To determine the longitudinal plasmonic resonance, size, and surface potential of AuNRs, we used a Peqlab (Erlangen, Germany) Nanodrop ND-1000 spectrofluorometer (UV/Vis function) and a Malvern (Worcestershire, United Kingdom) Zetasizer Nano ZS for dynamic light scattering and zeta potential measurements. For both measurements, we used the following parameters for the dispersant (water) with a viscosity of 0.8872 cP, a Henry's function of 1.5, a dielectric constant of 78.5 and a refractive index of 1.33. The temperature was kept constant at 25 °C. For zeta potential measurements, the samples were transferred to a zeta cell (DTS1070, Malvern Instruments) and measured at an applied voltage of ± 150 V. For dynamic light scattering measurements, the samples were transferred into Sarstedt Disposable Cuvettes DTS0012 and measured with the integrated 633 nm He-Ne laser operating at an angle of 173°. For each sample, three automated runs of 70 s duration were performed for each sample. The intensity size distributions were obtained from the autocorrelation function using the "multiple narrow mode".

Microtubule preparation

Porcine tubulin (2 μ M) was polymerized in PEM buffer (80 mM PIPES, 1 mM EGTA, 1 mM MgCl₂, pH = 6.9) supplemented with 4 mM MgCl₂ and 1 mM GMPCPP for 4 h at 37 °C as described previously.³³ Afterwards, the microtubule solution was diluted in PEM (1 : 3 ratio), centrifuged (Airfuge Beckman Coulter, Brea, CA), and resuspended in 150 μ L PEM. Microtubules were visualized with interference reflection microscopy.^{20,21}

Transmission electron microscopy (TEM)

For TEM imaging, 5 μ L of microtubules in PEM were incubated for 10 min with a AuNRs solution (1 nM based on the concentration estimate above in 9 μ L water). Afterwards, AuNR-microtubule droplets (5 μ L) were incubated for 3 min on pioloform and carbon-coated copper TEM grids. After a 1 min washing step using a 20 μ L PEM droplet on the grid, the sample containing TEM grid was fixed with 2.5% glutaraldehyde for 5 min. Then, TEM grids were washed 5 \times with 20 μ L droplets of nanopure water and stained for 30 s with 1% aqueous uranyl acetate. Excess uranyl acetate was carefully removed with a dry filter paper and the sample was left to dry. Images were recorded with a JEOL 120 kV 1400plus transmission electron microscope with a Tietz TemCam F-416 CMOS camera. Out of 330 imaged single AuNRs or clusters, 154 were directly bound to microtubules (47%). From the rest, 76 were associated with broken microtubule filaments, tubulin oligomers or unidentifiable electron density. The remaining 100 AuNRs and clusters corresponding to 30% did not appear to be bound to anything. Whether some of the unbound AuNRs were initially bound to microtubules that were dissociated during the preparation or tubulin oligomers were masked by the high electron density of the AuNRs is unclear.

Flow cell preparation

For hydrophobic surfaces, we used methyltrichlorosilane functionalized glass surfaces. Coverslips (# 1.5 Corning 22 \times 22

mm² and # 0 Menzel 18 \times 18 mm² for the bottom and top of the flow cell, respectively) were cleaned *via* three sequences of Mucosal and ethanol sonication for 15 min each. After washing with deionized water, coverslips were additionally cleaned and activated for 10 min in 0.6 mbar oxygen plasma at 300 W (TePla 100 E plasma cleaner). Coverslips were rendered hydrophobic by methyltrichlorosilane vacuum silanization, processed into flow cells, and attached to the hydrophobic surface as described previously³³ except that residual microtubules were washed with a 1 : 9 PEM : water mixture to decrease the overall salt concentration. Then, MUTAB-rhodamine-AuNRs, plasmonically inactive at an excitation wavelength of 561 nm, were mixed with PEM and flowed in for measurements. Finally, residual AuNRs were removed by flowing in an anti-fading mix (glucose oxidase, D-glucose, and catalase with final concentrations of 0.02 mg mL⁻¹, 20 mM, and 0.008 mg mL⁻¹, respectively) in to increase the lifetime of the fluorescent dyes.

For direct microtubule-surface attachment, we used (3-aminopropyl)triethoxysilane (APTES) functionalized glass surfaces. Coverslips (# 1.5 Menzel 22 \times 22 mm² and # 1.0 Menzel 18 \times 18 mm² for the bottom and top of the flow cell, respectively) were cleaned with a 60 °C mixture of 0.9 M KOH and 1.3 M H₂O₂. Plasma cleaning and activation was performed as described in the previous paragraph. Silanization was performed by exposing coverslips to APTES vapor generated by applying 25 mbar vacuum for 2 min at room temperature to a desiccator containing 500 μ L APTES, followed by a 2 min incubation. Finally, remnant water was removed from the substrates by drying for 20 min at 120 °C. Flow cells were constructed using APTES coverslips and parafilm as described previously⁵³ but in a clean room environment. Flow cells were washed with pure water and then directly incubated with microtubules for 5 min before washing residual microtubules out with a 1 : 9 PEM : water mixture. Subsequently, MUTAB AuNRs without rhodamine but plasmonically active at an excitation wavelength of 561 nm were mixed with PEM and flowed in for measurements.

Note that for the red channel it was difficult to obtain near fluorescent-background-free surfaces. Clean room facilities, the use of the plasma cleaner, vacuum storage, and clean buffers based on double-distilled water were essential. Storage in our laboratory resulted in a significant background already after one day.

IRM and TIRF setup

Merged IRM and TIRF images were measured on a temperature-stabilized (29.000 °C) setup similar to a previously published setup²⁰ with millikelvin precision⁶¹ combining IRM and TIRF. Excitation wavelengths were 488 nm (100 mW LuxX 488-100 Omicron Laserage, Rodgau, Germany) for the green channel and 561 nm (100 mW OBIS 561CS-100, Coherent, Santa Clara, CA, USA) for the red channel. A HC-Beamsplitter BS 560 separated the signal into the two distinct channels using a custom-made color splitter.²⁰ The green channel was defined by an ET Bandpass 520/40 and the red channel by an ET Bandpass 605/70. For excitation of rhodamine and the AuNRs intrinsic luminescence, 5 mW output power of the 561 nm laser was used. The



image acquisition time was 200 ms using an Orca Flash 4.0 V2 camera (Hamamatsu Photonics, Hamamatsu City, Japan).

Image analysis

Images were further processed in Fiji⁶² and GIMP. For Fig. 4, the uneven parabolic background of the TIRF image was removed by using the image software Gwyddion's feature "remove polynomial background" with the horizontal and vertical polynomial degree of two. IRM contrast depends on microtubule distance to the surface. Black intensity gray levels of microtubules in IRM images correspond to microtubules that are directly on the surface while intermediate gray levels correspond to ≈ 40 nm and white intensity levels to ≈ 80 nm microtubule distance from the surface, respectively.²⁰ For AuNR-microtubule colocalizations and overlays of IRM/TIRF image, we used the following pseudocolor scale. We first inverted the 256 gray scale values of the IRM images and changed the inverted values to brightness values of green. Thus, a zero gray scale value of the original image (black—corresponding to microtubules in direct contact with the surface) is converted to bright green. For inverted gray values below a threshold chosen as the mean value, the mean image gray value was added and subsequently pixels were converted to brightness values of cyan. Thus, cyan regions indicated parts of microtubules that are not in direct contact with the surface. For the color conversion, we used Jython scripting in Fiji. Overall, AuNR—magenta in TIRF—ideally appear white if colocalized with microtubules that have the same intensity of pseudocolor green.

Author contributions

V. W. performed measurements and analyzed the data. F. S. helped with experiments. S. S. introduced gold nanorods to the laboratory. G. H. built the IRM/TIRF setup. Y.-D. S. performed TEM imaging. V. W. and E. S. designed the research and wrote the manuscript.

Conflicts of interest

There are no conflicts to declare.

Acknowledgements

The authors thank Anita Jannasch, Michael Bugiel, Carolina Carrasco, and Sebastian Kenzler for comments on the manuscript, Andreas Schnepf for the use of the Zetasizer, Rebecca Stahl for introduction to TEM sample preparation, the LISA+ Center of the University of Tübingen for usage of devices and the clean room, and Markus Turad and Ronny Löffler for advice and introduction to the LISA+ facility. We thank Narima Eerqing and Frank Vollmer for discussions on how to optimize AuNRs for whispering gallery mode sensing. G. L. H. acknowledges financial support from the International Max Planck Research Schools from Molecules to Organisms, Max Planck Institute for Developmental Biology, Tübingen. This work was

supported by the interdisciplinary "nanoBCP-Lab" funded by the Carl Zeiss Foundation, the European Research Council (ERC-POC Project No. 755161, PRIMASKOTI), and the PhD Network "Novel Nanoparticles" of the Universität Tübingen.

References

- 1 R. A. Sperling, P. Rivera Gil, F. Zhang, M. Zanella and W. J. Parak, *Chem. Soc. Rev.*, 2008, **37**, 1896–1908.
- 2 H. Chen, L. Shao, Q. Li and J. Wang, *Chem. Soc. Rev.*, 2013, **42**, 2679–2724.
- 3 M. B. Mohamed, V. Volkov, S. Link and M. A. El-Sayed, *Chem. Phys. Lett.*, 2000, **317**, 517–523.
- 4 S. Khatua, P. M. Paulo, H. Yuan, A. Gupta, P. Zijlstra and M. Orrit, *ACS Nano*, 2014, **8**, 4440–4449.
- 5 P. Zijlstra, P. M. Paulo and M. Orrit, *Nat. Nanotechnol.*, 2012, **7**, 379.
- 6 S. Link and M. A. El-Sayed, *J. Phys. Chem. B*, 1999, **103**, 8410–8426.
- 7 C. Sönnichsen and A. P. Alivisatos, *Nano Lett.*, 2005, **5**, 301–304.
- 8 M. D. Baaske and F. Vollmer, *Nat. Photonics*, 2016, **10**, 733.
- 9 S. Rosenblum, Y. Lovsky, L. Arazi, F. Vollmer and B. Dayan, *Nat. Commun.*, 2015, **6**, 6788.
- 10 K. E. Sawin and J. M. Scholey, *Trends Cell Biol.*, 1991, **1**, 122–129.
- 11 R. D. Vale and R. A. Milligan, *Science*, 2000, **288**, 88–95.
- 12 N. Hirokawa, Y. Noda, Y. Tanaka and S. Niwa, *Nat. Rev. Mol. Cell Biol.*, 2009, **10**, 682.
- 13 W. O. Hancock, *Biophys. J.*, 2016, **110**, 1216–1225.
- 14 R. A. Cross, *Biopolymers*, 2016, **105**, 476–482.
- 15 A. Ramaiya, B. Roy, M. Bugiele and E. Schäffer, *Proc. Natl. Acad. Sci. U. S. A.*, 2017, **114**, 10894–10899.
- 16 R. Kuriyama and T. Miki-Noumura, *J. Cell Sci.*, 1975, **19**, 607.
- 17 R. D. Allen, N. S. Allen and J. L. Travis, *Cell Motil.*, 1981, **1**, 291–302.
- 18 V. Bormuth, J. Howard and E. Schäffer, *J. Microsc.*, 2007, **226**, 1–5.
- 19 A. S. G. Curtis, *J. Cell Biol.*, 1964, **20**, 199–215.
- 20 S. Simmert, M. K. Abdosamadi, G. Hermsdorf and E. Schäffer, *Opt. Express*, 2018, **26**, 14499–14513.
- 21 M. Mahamdeh, S. Simmert, A. Luchniak, E. Schäffer and J. Howard, *J. Microsc.*, 2018, **272**, 60–66.
- 22 J. Andrecka, J. O. Arroyo, K. Lewis, R. A. Cross and P. Kukura, *Biophys. J.*, 2016, **110**, 214–217.
- 23 C. H. Keith, J. R. Feramisco and M. Shelanski, *J. Cell Biol.*, 1981, **88**, 234–240.
- 24 G. H. Bourne, J. F. Danielli and K. W. Jeon, in *Microtubules in Cultured Cells; Indirect Immunofluorescent Staining with Tubulin Antibody*, ed. G. H. Bourne, J. F. Danielli and K. W. Jeon, Academic Press, 1980, vol. 63, pp. 59–95.
- 25 M. Mikhaylova, B. M. C. Cloin, K. Finan, R. van den Berg, J. Teeuw, M. M. Kijanka, M. Sokolowski, E. A. Katrukha, M. Maidorn, F. Opazo, S. Moutel, M. Vantard, F. Perez, P. M. P. van Bergen en Henegouwen, C. C. Hoogenraad, H. Ewers and L. C. Kapitein, *Nat. Commun.*, 2015, **6**, 7933.



- 26 I. L. Medintz, H. T. Uyeda, E. R. Goldman and H. Mattoussi, *Nat. Mater.*, 2005, **4**, 435–446.
- 27 V. Jacobsen, P. Stoller, C. Brunner, V. Vogel and V. Sandoghdar, *Opt. Express*, 2006, **14**, 405–414.
- 28 G. Wang, W. Sun, Y. Luo and N. Fang, *J. Am. Chem. Soc.*, 2010, **132**, 16417–16422.
- 29 J. Won Ha, W. Sun, G. Wang and N. Fang, *Chem. Commun.*, 2011, **47**, 7743–7745.
- 30 A. Jannasch, V. Bormuth, M. Storch, J. Howard and E. Schäffer, *Biophys. J.*, 2013, **104**, 2456–2464.
- 31 K. J. Mickolajczyk, N. C. Deffenbaugh, J. Ortega Arroyo, J. Andrecka, P. Kukura and W. O. Hancock, *Proc. Natl. Acad. Sci. U. S. A.*, 2015, **112**, E7186–E7193.
- 32 H. Isojima, R. Iino, Y. Niitani, H. Noji and M. Tomishige, *Nat. Chem. Biol.*, 2016, **12**, 290–297.
- 33 M. Chugh, M. Reißner, M. Bugiel, E. Lipka, A. Herrmann, B. Roy, S. Müller and E. Schäffer, *Biophys. J.*, 2018, **115**, 375–385.
- 34 S. Behrens, W. Habicht, J. Wu and E. Unger, *Surf. Interface Anal.*, 2006, **38**, 1014–1018.
- 35 J. C. Zhou, Y. Gao, A. A. Martinez-Molares, X. Jing, D. Yan, J. Lau, T. Hamasaki, C. S. Ozkan, M. Ozkan, E. Hu, *et al.*, *Small*, 2008, **4**, 1507–1515.
- 36 J. C. Zhou, X. Wang, M. Xue, Z. Xu, T. Hamasaki, Y. Yang, K. Wang and B. Dunn, *Mater. Sci. Eng., C*, 2010, **30**, 20–26.
- 37 C. Rosano, P. Arosio and M. Bolognesi, *Biomol. Eng.*, 1999, **16**, 5–12.
- 38 M. Reth, *Nat. Immunol.*, 2013, **14**, 765.
- 39 M. N'Gom, S. Li, G. Schatz, R. Erni, A. Agarwal, N. Kotov and T. B. Norris, *Phys. Rev. B: Condens. Matter Mater. Phys.*, 2009, **80**, 113411.
- 40 X. Wang, Y. Li, H. Wang, Q. Fu, J. Peng, Y. Wang, J. Du, Y. Zhou and L. Zhan, *Biosens. Bioelectron.*, 2010, **26**, 404–410.
- 41 M. D. Baaske, M. R. Foreman and F. Vollmer, *Nat. Nanotechnol.*, 2014, **9**, 933–939.
- 42 D. Zhang, O. Neumann, H. Wang, V. M. Yuwono, A. Barhoumi, M. Perham, J. D. Hartgerink, P. Wittung-Stafshede and N. J. Halas, *Nano Lett.*, 2009, **9**, 666–671.
- 43 J. Gigault, T. J. Cho, R. I. MacCuspie and V. A. Hackley, *Anal. Bioanal. Chem.*, 2013, **405**, 1191–1202.
- 44 R. Cortesi, E. Esposito, E. Menegatti, R. Gambari and C. Nastruzzi, *Int. J. Pharm.*, 1996, **139**, 69–78.
- 45 H. Takahashi, Y. Niidome, T. Niidome, K. Kaneko, H. Kawasaki and S. Yamada, *Langmuir*, 2006, **22**, 2–5.
- 46 S. Lee, L. J. Anderson, C. M. Payne and J. H. Hafner, *Langmuir*, 2011, **27**, 14748–14756.
- 47 L. Vigderman, P. Manna and E. R. Zubarev, *Angew. Chem., Int. Ed.*, 2012, **51**, 636–641.
- 48 Y. Okada and N. Hirokawa, *Proc. Natl. Acad. Sci. U. S. A.*, 2000, **97**, 640–645.
- 49 B. Nikoobakht and M. A. El-Sayed, *Chem. Mater.*, 2003, **15**, 1957–1962.
- 50 E. Schäffer, S. F. Nørrelykke and J. Howard, *Langmuir*, 2007, **23**, 3654–3665.
- 51 S. Sudhakar, T. J. Jachowski, M. Kittelberger, A. Maqbool, G. L. Hermsdorf, M. K. Abdosamadi and E. Schäffer, *Nano Lett.*, 2019, **19**, 8877–8886.
- 52 D. F. Siqueira Petri, G. Wenz, P. Schunk and T. Schimmel, *Langmuir*, 1999, **15**, 4520–4523.
- 53 M. P. Nicholas, L. Rao and A. Gennerich, *Mitosis*, Springer, 2014, pp. 137–169.
- 54 M. Bugiel, A. Mitra, S. Girardo, S. Diez and E. Schäffer, *Nano Lett.*, 2018, **18**, 1290–1295.
- 55 W.-S. Chang, J. W. Ha, L. S. Slaughter and S. Link, *Proc. Natl. Acad. Sci. U. S. A.*, 2010, **107**, 2781.
- 56 H. Chen, L. Shao, T. Ming, K. C. Woo, Y. C. Man, J. Wang and H.-Q. Lin, *ACS Nano*, 2011, **5**, 6754–6763.
- 57 T. Korten and S. Diez, *Lab Chip*, 2008, **8**, 1441–1447.
- 58 I. A. Telley, P. Bieling and T. Surrey, *Biophys. J.*, 2009, **96**, 3341–3353.
- 59 M. Bugiel, E. Böhl and E. Schäffer, *Biophys. J.*, 2015, **108**, 2019–2027.
- 60 M. Bugiel and E. Schäffer, *Biophys. J.*, 2018, **115**, 1993–2002.
- 61 M. Mahamdeh and E. Schäffer, *Opt. Express*, 2009, **17**, 17190.
- 62 J. Schindelin, I. Arganda-Carreras, E. Frise, V. Kaynig, M. Longair, T. Pietzsch, S. Preibisch, C. Rueden, S. Saalfeld, B. Schmid, J.-Y. Tinevez, D. J. White, V. Hartenstein, K. Eliceiri, P. Tomancak and A. Cardona, *Nat. Methods*, 2012, **9**, 676–682.



Letters

Single depolymerizing and transport kinesins stabilize microtubule ends

Alexandra Ciorîță^{1,2,†}, Michael Bugiel^{1,†}, Swathi Sudhakar¹, Erik Schäffer¹, and Anita Jannasch^{1,*}

¹Cellular Nanoscience, Center for Plant Molecular Biology (ZMBP), University of Tübingen, Auf der Morgenstelle 32, 72076 Tübingen Germany

²Current address: National Institute for Research and Development of Isotopic and Molecular Technologies, Donat Str. 67-103, 400293 Cluj-Napoca, Romania

[†]These authors contributed equally to this work

*Correspondence: Anita.Jannasch@uni-tuebingen.de

ABSTRACT Microtubules are highly dynamic cellular filaments and many intracellular processes like cell division depend on an accurate control of their length. Among other factors, microtubule length is actively modulated by motors from the kinesin superfamily. For example, yeast kinesin-8, Kip3, depolymerizes microtubules in a collective manner by a force- and length-dependent mechanism. However, whether single motors depolymerize or stabilize microtubule ends is unclear. Here, using interference reflection microscopy, we measured the influence of single kinesin motors on the stability of microtubules in an *in vitro* assay. Surprisingly, using unlabeled, stabilized microtubules, we found that both single kinesin-8 and non-depolymerizing kinesin-1 transport motors stabilized microtubule ends further by reducing the spontaneous microtubule depolymerization rate. Since we observed this effect for two very different kinesins, it implies a more general stabilization mechanism. For Kip3, this behavior is contrary to the collective force-dependent depolymerization activity of multiple motors. The complex, concentration-dependent interaction with microtubule ends provides new insights into the molecular mechanism of kinesin-8 and its regulatory function of microtubule length.

Key words: Kinesin; microtubules; interference reflection microscopy (IRM); Monte-Carlo simulation

STATEMENT OF SIGNIFICANCE

Kinesin-8 motors are important for microtubule length regulation and are over-expressed in colorectal cancer. The budding yeast kinesin-8, Kip3, shortens microtubules collectively. Whether single motors can also depolymerize microtubules remains unclear. Here, we measured the shrinkage speed of microtubules in the presence of different kinesins using interference reflection microscopy. Surprisingly, we found that

single Kip3 motors stabilized microtubule ends. Furthermore, even conventional kinesin-1 that transports vesicles had a stabilizing effect implying the presence of a more general stabilization mechanism. A better understanding of kinesin-8 has implications for cell division and associated diseases.

Kinesin motors are involved in many different cellular processes like cell division or intracellular transport (1). They typically translocate along cytoskeletal microtubules and generate force and directed motion, driven by ATP hydrolysis (2, 3). Several kinesins affect the microtubule network itself also during mitosis, which makes them potential targets for cancer treatment (4, 5). For example, members of the kinesin-8 family are known to regulate microtubule dynamics (6–11). The budding yeast kinesin-8 *Kip3* has been shown to depolymerize microtubules in a collective, length- and force-dependent manner (7–9, 12). For depolymerization, it is essential that Kip3 reaches the microtubule end, which requires taking many steps before dissociating from the microtubule. Indeed, Kip3 has a very high run length (7). This high run length originates from a weakly-bound slip state (13) in addition to a second microtubule binding site located in the tail domain (14). This binding site also enhances Kip3's extraordinary long residence time at the microtubule end and enables Kip3 to crosslink and slide between different microtubules (14, 15). Furthermore, in contrast to its depolymerization activity at high concentrations, it has been suggested that Kip3 stabilizes microtubules at low concentrations (14). This suggestion is motivated by (i) longer microtubules in cells with kinesin-1 mutants that had been fused to Kip3's tail domain and (ii) *in vitro* assays with microtubules that showed lower shrinkage rates with added Kip3 tail domains. However, direct experimental evidence of microtubule stabilization by full-length Kip3 is missing so far. Moreover, without ATP, rigor-bound conventional kinesin-1 stabilized GDP microtubules (16). Whether this effect persists in the presence of ATP and with tubulin in the GTP state at microtubule ends is also unclear.

To test whether motile kinesin motors can stabilize microtubules, we measured the *in vitro* depolymerization speed of GMPCPP-stabilized microtubules (17) in the presence of different kinesins as a function of their concentration at physiological ATP conditions (Fig. 1, Supplementary Materials and Methods). We used the full-length budding yeast kinesin-8, Kip3, and a truncated rat kinesin-1, rK430, from here on referred to as kinesin-8 and kinesin-1, respectively (Supplementary Materials). Since depolymerization speeds were small, we performed microtubule length measurements over a long period (60 min) using interference reflection microscopy (IRM) (18). IRM enabled label-free microtubule imaging with no significant photodamage and little drift in our setup. In IRM images, surface-immobilized microtubules appear dark (Fig. 1A). We measured their depolymerization speed as the total length change—the difference between the microtubule length in the first and last recorded image—divided

Ciorîță et al.

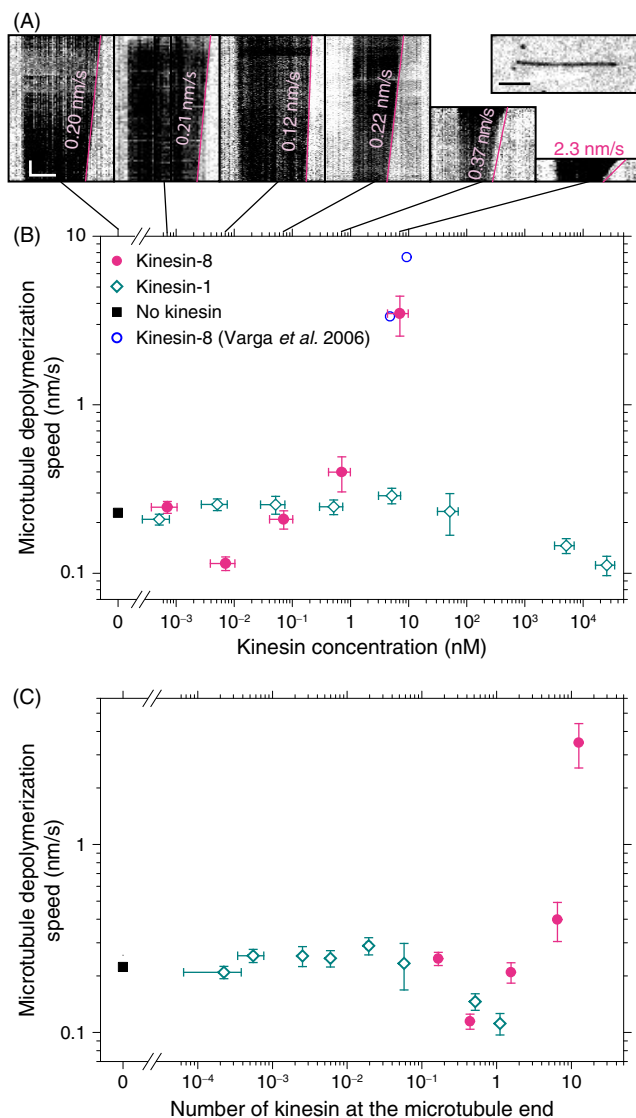


FIGURE 1 Kinesin stabilizes microtubules. (A) Kymographs of microtubules imaged with interference reflection microscopy (IRM) at different kinesin-8 concentrations. The vertical and horizontal scale bar are 10 min and $2\ \mu\text{m}$, respectively. *Magenta lines* illustrate the shrinkage of microtubules with respective plus-end depolymerization speeds. Upper right-hand corner: Exemplary IRM image of a microtubule (scale bar: $2\ \mu\text{m}$). (B) Total microtubule depolymerization speed as a function of motor concentration for kinesin-8 (full magenta circles), kinesin-1 (open green diamonds), and in the absence of kinesins (full black square). The open blue circle corresponds to literature data (7). (C) Depolymerization speed data as a function of average number of motors at the microtubule end (see Supporting Material for details).

by the total acquisition time. Representative kymographs are shown in Fig. 1A. For GMPCPP-stabilized microtubules and in the absence of any kinesin, we measured a spontaneous depolymerization speed of $0.236 \pm 0.009\ \text{nm/s}$ (mean \pm SEM, $N = 151$) corresponding to about $0.88\ \mu\text{m/h}$ (Fig. 1B). At very small kinesin-8 concentrations of $0.7\ \text{pM}$, the microtubule depolymerization speed did not significantly differ

from the value without kinesins. For intermediate kinesin-8 concentrations of around $7\ \text{pM}$, the depolymerization speed was reduced about two-fold to $0.11 \pm 0.01\ \text{nm/s}$. At higher kinesin-8 concentrations, depolymerization speeds increased again to values that are significantly higher than the one in the absence of kinesin-8. At the highest tested kinesin-8 concentration of $7\ \text{nM}$, we observed the expected length-dependent depolymerization (Fig. 1A, right kymograph showing a non-linear length change with time) in quantitative agreement with the literature (9). Thus, the significant reduction of depolymerization speed at an intermediate number of kinesin-8 motors relative to the spontaneous shrinkage speed, implies a stabilization of the microtubule ends.

Do other kinesins stabilize microtubule ends as well? To address this question, we measured the microtubule depolymerization speed at different concentrations of kinesin-1, which does not dwell at microtubule ends, but quickly falls off once the end had been reached. We observed no effect on the microtubule stability for kinesin-1 concentrations below $100\ \text{nM}$ (ANOVA, $F(5, 160) = 0.98$, $p = 0.43$). Importantly, for these concentrations, the overall weighted mean of $0.24 \pm 0.01\ \text{nm/s}$ was not different from the spontaneous microtubule depolymerization speed (t -test, $p = 0.7$). However, for very high motor concentrations of $5\ \mu\text{M}$ and $25\ \mu\text{M}$, we observed a significant decrease of the microtubule depolymerization speed (t -test between weighted mean for data below $100\ \text{nM}$ and the data point at $25\ \mu\text{M}$, $p = 1.8 \cdot 10^{-4}$). Thus, also a transport kinesin can stabilize microtubule ends at sufficiently high concentrations raising the question of how many kinesins need to be simultaneously at the microtubule end for stabilization.

To determine the average number of kinesins at the microtubule end, we programmed a simulation based on the known motility parameters of the motors (see Supporting Material). Directly measuring the number of kinesins at the microtubule end was not reliable because of insufficient localization precision at the end, photo bleaching during long measurements, or too many fluorophores at higher motor concentrations. Instead, we measured the landing rate as a function of motor concentration (Fig. S1) and used the known translocation speed, run length, and end residence time of the motors to determine for each concentration the average number of motors at the microtubule end. With the relation between the motor concentration and number at the end, we rescaled the concentration axis for both motors (Fig. 1C). Interestingly, for both motors, the stabilization effect occurred roughly at the same number of about one motor per microtubule end. Depolymerization by kinesin-8 occurred at higher numbers that result in traffic jams on individual protofilaments (Fig. S2) consistent with a collective depolymerization mechanism.

In summary, we have shown that if there is on average about one motile kinesin always present at a microtubule end, microtubules are stabilized. Due to kinesin-1's much smaller run length and end residence time, the concentration at which this condition is met is much higher in comparison to kinesin-8. Surprisingly, already one motor at the end seems

to be sufficient to stabilize all protofilaments narrowing down the previous estimate of less than six motors for strongly bound kinesin-1 on GDP-microtubules (16). Our kinesin-8 data directly confirms previous indirect measurements (14) that at low motor concentrations—corresponding to a single motor at the end according to our data—microtubules are stabilized. This finding widens the model of its biological role of microtubule length control. Cells may switch between microtubule stabilization and depolymerization modes by regulating the level of kinesin-8 expression during the cell cycle. Furthermore, since the number of motors at the end scales with microtubule length ((7, 9) and Supporting Material), short microtubules could be stabilized whereas long microtubules may be depolymerized at the same time.

What is the origin of microtubule stabilization by kinesin motors? Previous research suggested inter-protofilament crosslinking via the additional microtubule binding site in the tail domain of kinesin-8 (14). For kinesin-1, a similar electrostatic stabilization could be present through a weak interaction of the neck coiled-coil with the E-hooks of tubulin (19). Another contribution may be from the strongly bound state of kinesin motors at the microtubule end (16, 20), in case of kinesin-1 causing a conformational change of tubulin with an associated elongation and straightening of GDP-tubulin (16). We propose that in addition to these effects, the dimeric state of kinesin links the terminal two tubulin dimers together conferring stability. Recent experiments suggest that both kinesin heads always remain in direct contact with the microtubule lattice during stepping (2, 3). Thus, if a terminal tubulin dimer bound to a kinesin should dissociate from the microtubule lattice, it will still be tethered to the microtubule end via the kinesin dimer. In this manner, this terminal tubulin may quickly reattach with an effectively increased on-rate. This increase would lead to an overall stabilization of the microtubule end. Because of the three-start-helix structure of the microtubule (1) and assuming that the microtubule end is blunt (17), there is only one tubulin dimer at the very end of the helix that has only one lateral tubulin contact. Therefore, already one kinesin might be sufficient to stabilize this “weakest” spot of the microtubule. Further experiments with other kinesin dimers and possibly with truncated tail domains or modified neck coiled coils may be necessary to establish a general stabilization mechanism of kinesin dimers and a possible contribution from further microtubule interactions of their tails. While for kinesin-8 microtubule stabilization at low concentrations may be biologically relevant, we do not expect a relevant *in vivo* effect for kinesin-1 since unnaturally high motor concentrations were required. For kinesin-8, our observations support and widen the model on the dual-mode regulation of microtubule dynamics by this kinesin.

SUPPORTING MATERIAL

Supporting Methods and Material and two figures are available at <http://www.biophysj.org/biophysj/supplemental/XXX>.

AUTHOR CONTRIBUTIONS

A.J. and E.S. designed research; A.C., A.J., and S.S. performed measurements and analyzed the data. M.B. wrote the simulation and analyzed its results. M.B., A.J., and E.S. wrote the manuscript. All authors commented on the manuscript.

ACKNOWLEDGMENTS

This work was supported by the German Research Foundation (DFG, JA 2589/1-1), the interdisciplinary “nanoBCP-Lab” funded by the Carl Zeiss Foundation (Forschungsstrukturprogramm 2017), and the PhD Network “Novel Nanoparticles” of the Universität Tübingen. Alexandra Ciorîță was co-funded by the Erasmus+ programme of the European Union and by the Romanian Ministry of Research and Innovation (CCCDI – UEFISCDI, project number PN-III-P1-1.2-PCCDI-2017-0387 / 80PCCDI/2018, within PNCDI III). We would like to thank Andreas Neusch and Katrin Luginsland for preliminary experiments. We thank Viktoria Wedler and Carolina Carrasco-Pulido for comments on the manuscript.

SUPPORTING CITATIONS

References (21–39) appear in the Supporting Material.

REFERENCES

- Howard, J., 2001. Motor proteins and the cytoskeleton. Sinauer Associates, Sunderland, MA.
- Ramaiya, A., B. Roy, M. Bugiel, and E. Schäffer, 2017. Kinesin rotates unidirectionally and generates torque while walking on microtubules. *Proc. Natl. Acad. Sci. U. S. A.* 114:10894–10899.
- Sudhakar, S., M. K. Abdosamadi, T. J. Jachowski, M. Bugiel, A. Janasch, and E. Schäffer, 2020. Germanium nanospheres for ultraresolution picotensiometry of kinesin motors. *bioRxiv* 2020.06.18.159640.
- Braun, J., M. M. Möckel, T. Strittmatter, A. Marx, U. Groth, and T. U. Mayer, 2015. Synthesis and biological evaluation of optimized inhibitors of the mitotic kinesin Kif18A. *ACS Chem. Biol.* 10:554–560.
- Locke, J., A. P. Joseph, A. Peña, M. M. Möckel, T. U. Mayer, M. Topf, and C. A. Moores, 2017. Structural basis of human kinesin-8 function and inhibition. *Proc. Natl. Acad. Sci. U. S. A.* 114:E9539–E9548.
- Rischitor, P. E., S. Konzack, and R. Fischer, 2004. The Kip3-like kinesin KipB moves along microtubules and determines spindle position during synchronized mitoses in *Aspergillus nidulans* hyphae. *Eukaryot. Cell* 3:632–645.
- Varga, V., J. Helenius, K. Tanaka, A. A. Hyman, T. U. Tanaka, and J. Howard, 2006. Yeast kinesin-8 depolymerizes microtubules in a length-dependent manner. *Nat. Cell Biol.* 8:957–962.
- Gupta, M. L., P. Carvalho, D. M. Roof, and D. Pellman, 2006. Plus end-specific depolymerase activity of Kip3, a kinesin-8 protein, explains its role in positioning the yeast mitotic spindle. *Nat. Cell Biol.* 8:913–U33.
- Varga, V., C. Leduc, V. Bormuth, S. Diez, and J. Howard, 2009. Kinesin-8 motors act cooperatively to mediate length-dependent microtubule depolymerization. *Cell* 138:1174–1183.
- Du, Y., C. A. English, and R. Ohi, 2010. The kinesin-8 Kif18A dampens microtubule plus-end dynamics. *Curr. Biol.* 20:374–380.
- Glunčić, M., N. Maghelli, A. Krull, V. Krstić, D. Ramunno-Johnson, N. Pavin, and I. M. Tolić, 2015. Kinesin-8 motors improve nuclear centering by promoting microtubule catastrophe. *Phys. Rev. Lett.* 114:078103.

Ciorîță et al.

12. Bugiel, M., M. Chugh, T. J. Jachowski, E. Schäffer, and A. Jannasch, 2020. The kinesin-8 Kip3 depolymerizes microtubules with a collective force-dependent mechanism. *Biophys. J.* 118:1958–1967.
13. Jannasch, A., V. Bormuth, M. Storch, J. Howard, and E. Schäffer, 2013. Kinesin-8 is a low-force motor protein with a weakly bound slip state. *Biophys. J.* 104:2456–2464.
14. Su, X., W. Qiu, M. J. Gupta, J. Pereira-Leal, S. Reck-Peterson, and D. Pellman, 2011. Mechanisms underlying the dual-mode regulation of microtubule dynamics by Kip3/kinesin-8. *Mol. Cell* 43:751–763.
15. Su, X., H. Arellano-Santoyo, D. Portran, J. Gaillard, M. Vantard, M. Thery, and D. Pellman, 2013. Microtubule-sliding activity of a kinesin-8 promotes spindle assembly and spindle-length control. *Nat. Cell Biol.* 15:948–957.
16. Peet, D. R., N. J. Burroughs, and R. A. Cross, 2018. Kinesin expands and stabilizes the GDP-microtubule lattice. *Nat. Nanotechnol.* 13:386–391.
17. Hyman, A., S. Salsler, D. Drechsel, N. Unwin, and T. Mitchison, 1992. Role of GTP hydrolysis in microtubule dynamics: information from a slowly hydrolyzable analogue, GMPCPP. *Mol. Biol. Cell* 3:1155–1167.
18. Simmert, S., M. K. Abdosamadi, G. Hermsdorf, and E. Schäffer, 2018. LED-based interference-reflection microscopy combined with optical tweezers for quantitative three-dimensional microtubule imaging. *Opt. Express* 26:14499–14513.
19. Thorn, K. S., J. A. Ubersax, and R. D. Vale, 2000. Engineering the processive run length of the kinesin motor. *J. Cell Biol.* 151:1093–1100.
20. Arellano-Santoyo, H., E. A. Geyer, E. Stokasimov, G.-Y. Chen, X. Su, W. Hancock, L. M. Rice, and D. Pellman, 2017. A tubulin binding switch underlies Kip3/kinesin-8 depolymerase activity. *Dev. Cell* 42:37–51.
21. Chugh, M., M. Reißner, M. Bugiel, E. Lipka, A. Herrmann, B. Roy, S. Müller, and E. Schäffer, 2018. Phragmoplast orienting kinesin 2 Is a weak motor switching between processive and diffusive modes. *Biophys. J.* 115:375–385.
22. Bugiel, M., E. Böhl, and E. Schäffer, 2015. The kinesin-8, Kip3, switches microtubule protofilaments in a sideward random walk asymmetrically biased by force. *Biophys. J.* 108:2019–27.
23. Bugiel, M., H. Fantana, V. Bormuth, A. Trushko, F. Schiemann, J. Howard, E. Schäffer, and A. Jannasch, 2015. Versatile microsphere attachment of GFP-labeled motors and other tagged proteins with preserved functionality. *J. Biol. Methods* 2:e30.
24. Sudhakar, S., T. J. Jachowski, M. Kittelberger, A. Maqbool, G. L. Hermsdorf, M. K. Abdosamadi, and E. Schäffer, 2019. Supported solid lipid bilayers as a platform for single-molecule force measurements. *Nano Lett.* 19:8877–8886.
25. Mahamdeh, M., and J. Howard, 2019. Implementation of interference reflection microscopy for label-free, high-speed imaging of microtubules. *J. Vis. Exp.* 150:e59520.
26. Mahamdeh, M., and E. Schäffer, 2009. Optical tweezers with millikelvin precision of temperature-controlled objectives and base-pair resolution. *Opt. Express* 17:17190–17199.
27. Schindelin, J., I. Arganda-Carreras, E. Frise, V. Kaynig, M. Longair, T. Pietzsch, S. Preibisch, C. Rueden, S. Saalfeld, B. Schmid, J.-Y. Tinevez, D. J. White, V. Hartenstein, K. Eliceiri, P. Tomancak, and A. Cardona, 2012. Fiji: an open-source platform for biological-image analysis. *Nat. Methods* 9:676–82.
28. Thévenaz, P., U. Ruttimann, and M. Unser, 1998. A pyramid approach to subpixel registration based on intensity. *IEEE Transactions on Image Processing* 7:27–41.
29. Michálek, J. K., M. Čapek, and L. Kubínová, 2007. Fast algorithm for matching of image pairs for constant brightness applied to stacks of confocal microscope images. In *EUROGRAPHICS 2008*.
30. Norris, S. R., M. F. Núñez, and K. J. Verhey, 2015. Influence of fluorescent tag on the motility properties of kinesin-1 in single-molecule assays. *Biophys. J.* 108:1133–1143.
31. Bormuth, V., V. Varga, J. Howard, and E. Schäffer, 2010. Breaking of bonds between a kinesin motor and microtubules causes protein friction. In *Proceedings of SPIE*. volume 7762, 776208.
32. Guérin, T., J. Prost, and J.-F. Joanny, 2010. Dynamic instabilities in assemblies of molecular motors with finite stiffness. *Phys. Rev. Lett.* 104:248102.
33. Uppulury, K., A. K. Efremov, J. W. Driver, D. K. Jamison, M. R. Diehl, and A. B. Kolomeisky, 2013. Analysis of cooperative behavior in multiple kinesins motor protein transport by varying structural and chemical properties. *Cell Mol. Bioeng.* 6:38–47.
34. Khataee, H., and J. Howard, 2019. Force generated by two kinesin motors depends on the load direction and intermolecular coupling. *Phys. Rev. Lett.* 122:188101.
35. Chen, X., L. A. Widmer, M. M. Stangier, M. O. Steinmetz, J. Stelling, and Y. Barral, 2019. Remote control of microtubule plus-end dynamics and function from the minus-end. *eLIFE* 8:e48627.
36. Arpağ, G., S. Shastry, W. O. Hancock, and E. Tüzel, 2014. Transport by populations of fast and slow kinesins uncovers novel family-dependent motor characteristics important for *in vivo* function. *Biophys. J.* 107:1896–1904.
37. Bugiel, M., and E. Schäffer, 2018. Three-dimensional optical tweezers tracking resolves random sideward steps of the kinesin-8 Kip3. *Biophys. J.* 115:1993–2002.
38. Block, S. M., L. S. B. Goldstein, and B. J. Schnapp, 1990. Bead movement by single kinesin molecules studied with optical tweezers. *Nature* 348:348–352.
39. Svoboda, K., and S. M. Block, 1994. Force and velocity measured for single kinesin molecules. *Cell* 77:773–784.

Simultaneous Delivery of Curcumin and Quercetin with Anisotropic and Amphiphilic Mesoporous Core-Shell Silica Microparticles

Akanksha Dohare,^{#,a} Swathi Sudhakar,^{#,b} Björn Brodbeck,^{a,c} Ashutosh Mukherjee,^c Marc Brecht,^c Andreas Kandelbauer,^c Erik Schäffer,^b and Hermann A. Mayer^{*,a}

Authors contributed to the work equally

^aInstitute of Inorganic Chemistry, University of Tuebingen, Auf der Morgenstelle 18, Germany

^bZMBP, Cellular Nanoscience, University of Tuebingen, Auf der Morgenstelle 32, Germany

^cProcess Analysis and Technology (PA&T), Reutlingen Research Institute, Reutlingen University, Alteburgstrasse 150, 72762 Reutlingen, Germany

*Corresponding author: hermann.mayer@uni-tuebingen.de

Abstract

Spherical micrometer core-shell silica particles (**CS**) and anisotropic and amphiphilic dumbbell core-shell silica particles (**DCS1**) and (**DCS2**) were prepared by a simple etching process. The dumbbells **DSC1** and **DCS2** are constructed of large dense lobes and smaller hollow hemispheres. The properly adjusted stirring speed and the application of ammonium fluoride and ammonium carbonate as etching agents decided upon the formation of the shape and the surface anisotropy of the particles. Analysis of the particles with SEM and STEM revealed that the surface of the anisotropic particles **DCS1** and **DCS2** are covered with shells of mesoporous channels. In the case of amphiphilic **DCS1** the surface area around the dense lobe and the surface area of the small hemisphere differ in their zeta potentials. This was confirmed by drug loading experiments. As shown by confocal Raman microscopy and spectroscopy the two polyphenols curcumin (Cur) and quercetin (QT) accumulate in different compartments of the **DCS1** particles. The overall drug loading efficiency of Cur plus QT is high but differs widely between Cur and QT among the **CS**, **DCS1** and **DCS2** particles. Up to 98 % drug loading and 100 % releasing efficiency after 6 h at pH 5.5 was found. Cur and QT loaded **CS**, **DCS1** and **DCS2** showed different cancer cell inhibitory activities. The highest activity was detected for the dual drug loaded **DCS1** (IC₅₀ 13.5 nM).

Introduction

Transportation of drugs into cell membranes for medical diagnostic and treatment is of fundamental importance. Many of the present drugs are suffering from stability problems in biological environment and/or poor water solubility making the drugs less effective.^[1] Thus drug delivery strategies based on different materials have been developed.^[1-6] So far, several types of drug vehicles have been reported which includes liposomes,^[7] peptides,^[8] polymers,^[9-11] inorganic nano- and microparticles^[12-17] and organic/inorganic hybrid materials.^[18,19] A drawback of many materials is their low drug loading capabilities. To improve their therapeutic efficacy large amounts of carrier have to be applied. Unfortunately most of the carriers are accompanied by drawbacks such as poor biocompatibility, the application of large amounts of surfactants, the requirement for chemical modifications and complex preparation protocols which restricts their access.

The natural polyphenols curcumin (Cur) and quercetin (QT) affect numerous cellular targets and demonstrate activities on the cellular level.^[20-25] Both compounds suffer from poor bioavailability due to their low solubility in aqueous solutions and low stability in biological environment. Consequently, several approaches to deliver both natural polyphenols with different types of drug carriers have been suggested.^[26-33]

Mesoporous silica nano- and microparticles provide networks of pores, which result in large surface areas and high pore volumes.^[34-37] The opportunity to tailor particle size and shape as well as to tune the pore sizes in the nanometer scale have made these materials attractive for many applications in different fields.^[38-40] Moreover their intrinsic biocompatibility and biodegradability promise mesoporous silica particles as ideal platforms for drug delivery systems.^[15,39,41,42] By trapping the drug in the mesoporous network mesoporous silica prevents the degradation of the drugs and can act as solubility enhancer generating higher solution concentrations compared to the corresponding solid form.^[14] Thus this has led to a dramatic increase in the interest of mesoporous silica-based formulations in the last decade.^[1,43]

Although several studies have highlighted the controlled release of various therapeutic agents with mesoporous silica particles,^[44-46] in most of the reported examples only one kind of drug is entrapped into the mesoporous silica materials.^[47] Up to date, the co-delivery of multiple drugs with different molecular properties remains difficult.^[48] However, the possibility to load and release different drugs on the same systems allows to combine therapies and increases the opportunities for treating diseases. This requires materials with the ability to load and release drugs with different properties and function.

Mesoporous materials with multilevel morphology and hierarchical pore structures have been developed.^[49-53] Such particles provide different compartments and phase separated domains

and are thus interesting candidates for multi drug delivery purposes.^[54–56] Moreover the amphiphilic character, which is often accompanied by such multifunctional particles, increases the interfacial activity which improves the particle cell interaction.^[57]

We recently reported on anisotropic dumbbell core-shell silica microparticles, which are composed of two different hemispheres (Chart 1).^[58] The two lobes differ in size so that the particles are shaped like dumbbells, snowmen or acorns.^[59] The shells of both lobes are constructed of mesoporous MCM-41 type of channels and differ in their thickness. On the surface of the large lobe many SiOH functions are replaced by Si-F groups. Consequently, the surface charge of the smaller hemisphere is more negative than that of the larger hemisphere which gives the particles an amphiphilic character. While the core of the large lobe is dense, the interior of the small hemisphere is hollow. Thus, three compartments can be identified: (i) the shell of the large lobe with a weak surface charge, (ii) the shell of the small lobe that is negatively charged and (iii) the hollow cage, which is covered by the small hemisphere. The diversely functionalized hemispheres (SiF vs SiO-) as well as the different compartments make these particles attractive materials for the co-delivery of multiple drugs with different properties and function.

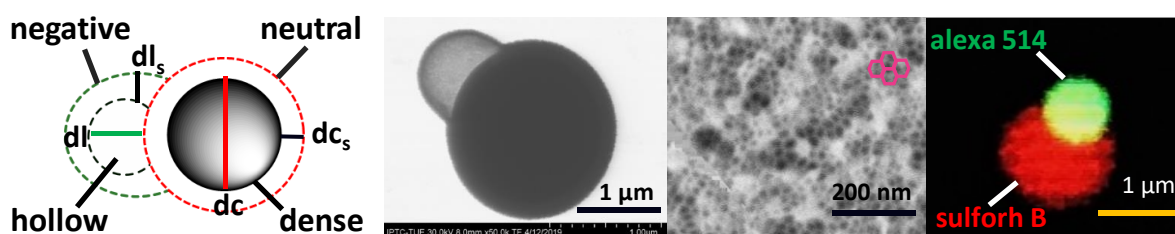


Chart 1 a) Cartoon of the anisotropic, amphiphilic core-shell dumbbell particle (d_l , d_{l_s} , d_c , d_{c_s} diameter of the hollow cavity, its shell, of the dense core and its shell), b) STEM micrograph of a representative particle, c) surface morphology of the shell displaying the hexagonally ordered mesoporous channels, d) particle coloured with negatively charged sulforhodamine B (red) and positively charged alexa 514 (green)

Here we demonstrate that due to the shape, surface anisotropy and their amphiphilic character these particles show distinctly different drug loading and releasing behaviour than comparable spherical core-shell silica particles. Moreover, we demonstrate that Cur and QT, when loaded on the amphiphilic anisotropic core shell particles accumulate in different compartments and lead to an enhanced cell toxicity.

Experimental Part

Cetyltrimethylammonium bromide (CTAB), *n*-tridecane (99 %), ammonium fluoride (98 %) and SiO₂ particles (1.5 μm) were purchased from ABCR. Ammonium carbonate (ACS reagent ≥ 30 % NH₃), curcumin, quercetin, dialysis bag (MWCO 10 KDa), dimethyl sulfoxide (DMSO), 3-[4,5-dimethylthiazole-2-yl]-2,5-diphenyltetrazolium bromide and ammonium hydroxide (28 %) were obtained from Sigma Aldrich. Deionised water and ethanol we used of technical grade.

Synthesis of the spherical core–shell (CS) and the anisotropic dumbbell core-shell silica particles (DCS1 and DCS2)

The anisotropic dumbbell core-shell (**DCS1**) silica particles were synthesized by following a procedure reported earlier^[58] with minor variations. Concisely, 2.1 g CTAB as surfactant, 2.1 g silica particles of 1.5 μm size were dissolved in 210 mL of water and sonicated for an hour. Then 11.6 mL *n*-tridecane was added and sonicated for another hour. To this suspension 12 mL of an ammonia and ammonium fluoride (1.35 mmol) solution was added and kept stirring at 210-240 rpm at 90 °C for 24 h. The anisotropic dumbbell silica-core shell particles (**DCS1**) were collected after centrifugation (2500 rpm for 1 min) and washed once with deionised water, twice with ethanol, once with diethyl ether and then calcined at 600 °C for 15 h.

The spherical core-shell silica particles (**CS**) were prepared by following the same procedure with the exception that the stirring speed was kept below 190 rpm.

For the preparation of the **DCS2** particles, the ammonium fluoride was replaced by an equimolar amount of ammonium carbonate by otherwise identical reaction conditions than for the **DCS1** particles.

Characterization of the CS, DCS1 and DCS2 particles

Scanning electron microscopy (SEM) and scanning transmission microscopy (STEM) images were acquired on a Hitachi SU8030 machine equipped with a triple detector. The particles were suspended in ethanol and kept in an ultrasonic bath for homogenization for 10 minutes. The samples were spin-coated onto silicon wafers for SEM and spotted on copper grids for STEM analysis.

The zeta potential in ethanol was measured at room temperature with a Zetasizer Nano ZS by Malvern. The samples were suspended in ethanol and transferred to a cuvette. Suspension in the measuring cell was almost clear. The concentration compared optically with a well measured

sample.

For Raman measurements, a WITec alpha300 RA&S confocal Raman microscope was used. This system is equipped with a lens-based UHTS 300 spectrometer connected via a 100 μm (NA=0.12) multi-mode optical fibre and thermoelectric cooled CCD and EMCCD (DU970N-BV). All Raman experiments were carried out using a laser of 532 nm with a nominal output power of 60 mW and a grating of 600 lines/mm. For illumination and collection the laser was focused on the sample through a Zeiss Epiplan-Neofluar objective of magnification 100x (NA = 0.9). Data procession was done using Control 5.0 software provided by WITec and all experiments were carried out at ambient conditions. We chose sapphire as a substrate due to its low background signal which does not overshadow the signal intensity from the region of interest. The peak positions of sapphire also do not interfere with the potential peak positions of QT and Cur, thus making sapphire an ideal substrate for Raman analysis of these drug loaded particles. The samples were prepared in the same way as described in the drug loading experiments.

Drug loading of curcumin (Cur) and quercetin (QT) in CS, DCS1 and DCS2 particles

For loading the microparticles **CS**, **DCS1** and **DCS2** with drugs, 0.5 mg/mL of an equimolar solution of Cur and QT, respectively, in ethanol was mixed with 1 mg/mL of the corresponding **CS**, **DCS1** and **DCS2** microparticles. The suspensions were shortly ultrasonicated and gently stirred for 4 h. Then, the Cur and QT loaded microparticles were centrifuged at 13,000 rpm for 3 min. The drug loading efficiency was detected by measuring UV-absorbance (Nanodrop, ND 1000 spectrometer) of Cur and QT at 450 and 270 nm, respectively, in the supernatants of the centrifuged sample and the initial 0.5 mg/mL solution. The following equation was used to determine the drug loading content of both drugs in **CS** and dumbbell microparticles **DCS1** and **DCS2**.

$$\text{Drug loading efficiency} = \frac{\text{Theoretical amount of drug loaded} - \text{Free drug}}{\text{Theoretical amount of drug loaded}} \times 100$$

***In vitro* drug release study**

In vitro drug release studies of Cur and QT from **CS**, **DCS1** and **DCS2** were investigated at pH 5.5 (environmental pH for tumors) and at pH 7.4 (physiological pH). The drug loaded **CS**, **DCS1** and **DCS2** particles were suspended in 2 mL of phosphate-buffered saline (PBS) and transferred to a dialysis bag (molecular weight cut-off 10 kDa, Sigma). Then they were placed in 25 mL of PBS, incubated at 37 °C and kept under stirring (100 rpm).^[60,61] The released drugs were

determined spectrophotometrically by measuring the absorbance at 450 and 270 nm. The concentration of released drug was then calculated using the standard curve of drugs as mentioned.^[60,61] The percentage of drug released was determined from the following equation as described earlier.^[62,63]

$$\text{Cumulative drug release (\%)} = \frac{\text{Cumulative amount released}}{\text{Total mass loaded}} \times 100$$

Cell viability studies

The cytotoxicity of the cells was studied by performing the 3-(4,5-dimethylthiazol-2-yl)-2,5-diphenyltetrazoliumbromide (MTT) assay as described.^[64] Briefly, the human bone osteosarcoma epithelial cancer cell lines (U2OS; 6x10³ cells) were seeded in a 96 well culture plate. After 12 h, the cells were treated with different concentrations of the drug loaded particles **CS**, **DCS1** and **DCS2** for 24 h. Control cells were treated with 0.1% DMSO in a culture medium. After treatment, the cells were incubated with the MTT solution (5 mg/mL in PBS) at 37°C for 4 h and then DMSO was added during shaking at room temperature. The spectrophotometric absorbance was measured at 570 nm on a microplate reader (Biotek, Multiplate reader, USA). Cell viability was expressed as the relative formazan formation in the treated samples compared with control cells after correction for background absorbance. The cytotoxicity (IC₅₀) was calculated based on the color yield of the treated cells which are proportional to the number of metabolically active cells and indirectly approximated cell viability. IC₅₀ is defined as the drug concentration required to inhibit growth of cells by 50 % relative to control (IC₅₀). A graph was drawn using Cell viability (%) with respect to the concentration of the sample. Results were plotted as the mean ± SD of three separate experiments. Percentage of cell viability was determined using the below formula.^[64]

$$\text{Cell Viability (\%)} = \frac{\text{Absorbance of the treated sample}}{\text{Absorbance of the untreated sample}} \times 100$$

Results and Discussion

Synthesis of **CS**, **DCS1** and **DCS2** microparticles

The protocol of the recently reported one-pot synthesis of monodisperse dumbbell silica core-shell particles was applied to prepare the **DCS1** particles.^[58] Thus a homogeneous suspension of nonporous dense spherical silica particles (d = 1.5 μm), CTAB and *n*-tridecane was treated under

stirring with a water solution of ammonia/ammonium fluoride at 90°C. Stirring below 190 rpm generates the spherical core-shell particles **CS** (Figure 1A,D), while stirring between 240 and 280 rpm produced the amphiphilic dumbbell particles **DCS1** (Figure 1B,E). If the ammonium fluoride is replaced by ammonium carbonate the particles **DCS2** (Figure 2C,F) are obtained. In this etching process,^[65–68] silica species are gradually dissolved from the surface of the dense silica particles and re-condensed close to the side of dissolution.^[38] In cooperation with the CTAB micelles, which are located on the surface of the silica particles, these silica species generate MCM 41 type of mesoporous shells around the silica particles.^[69] Due to the addition of the swelling agent *n*-tridecane additional droplets are formed which adsorb on the surface and serve as templates for the formation of the second hemispheres in **DCS1** and **DCS2** (Figure 1).

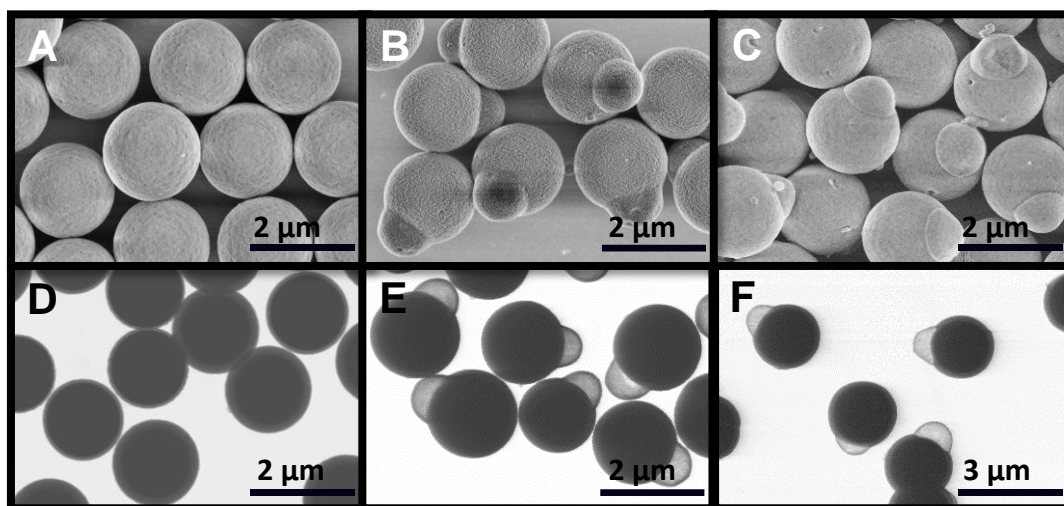


Figure 1. SEM (A-C) and STEM (D-F) images of **CS** (A,D), **DCS1** (B,E) and **DCS2** (C,F) silica particles

According to the SEM and STEM micrographs, the protocol produces monodisperse spherical **CS** (Figure 1 A,D) and dumbbell like anisotropic particles **DCS1** and **DCS2** (Figure 1 B,E, C,F and Figure 1S supporting information). The core and the shell as well as the hollow cavity of the small hemispheres in **DCS1** and **DSC2** can be distinguished from the STEM micrographs (Figure 1 E,F and Table 1). The shells which cover all particles consist of highly hexagonally ordered tunnels with uniform pore sizes of approximately 4.3-5.9 nm (Chart 1). The diameter of the mesoporous shell of the spherical **CS** is 176 nm and can be adjusted with the reaction time.^[65] During the same reaction time a shell as thick as 118 and 124 nm around the dense cores in **DCS1** and **DCS2** are

formed. The shells of the small hemispheres which cover the hollow cavity are found to be 63 and 47 nm thick, respectively (Table 1).

Table 1. Pore size distribution and specific surface area obtained by nitrogen physisorption of **CS**, **DCS1** and **DCS2**. Geometrical parameters d_c , d_{c_s} , d_l and d_{l_s} (for definition see Chart 1)

	Specific surface area (m ² /g)	Total pore volume (cm ³ /g)	Average pore size (nm)	d_c (nm)	d_{c_s} (nm)	d_l (nm)	d_{l_s} (nm)
CS	239.01	0.32	4.3; 5.7	1230	176		
DCS1	120.77	0.17	5.5	1332	118	410	63
DCS2	201.04	0.30	4.5; 5.9	1220	124	340	47

Reversible nitrogen adsorption and desorption isotherms are found for the core-shell materials **CS**, **DCS1** and **DCS2**, which display a typical Langmuir IV hysteresis (Figure 2S supporting information). The H1 loop is characteristic for narrow uniform mesopores as found in template MCM-41 silica.^[70] Average pore size distributions calculated from the adsorption branch of the nitrogen isotherms by the BJH method (Table 1) ranges from 4.3 to 5.9 nm. Interestingly, for **CS** and **DCS2** bimodal pore distributions within this range are observed.^[65] All physicochemical data of the anisotropic core-shell particles compare well with those reported for dumbbells of this type.^[58]

Dyeing experiments with positively and negatively charged dyes of the rhodamine family demonstrated the amphiphilic character of the anisotropic particles **DCS1** (Chart 1 and Figure 3S supporting information).^[58] The different zeta potentials on the smaller and larger lobe were traced back to the exchange of surface SiOH groups with SiF functions on the larger hemisphere.^[58] This is a consequence of the application of NH₄F as etching agent. Thus introducing ammonium carbonate as etching agent generates the anisotropic dumbbell particles **DCS2** with a uniform charge distribution across the particle surface. This agrees with an overall smaller Zeta potential for **DCS2** (-47.4 ± 0.9 mV) than for **DCS1** (-25.5 ± 0.6 mV). Compared to the spherical **CS** and anisotropic **DCS2** particles, the amphiphilic dumbbells **DCS1** have smaller specific surface areas and smaller pore volumes.

Drug loading efficiency

In general, the amount of drug that can be loaded onto mesoporous silica depends on the surface area, the pore volume, the pore geometry and on the number of silanol groups on the surface, which when deprotonated are responsible for the negative surface charge of the silica material.^[1] This is nicely reflected in the drug loading efficiency of the spherical **CS**, the anisotropic and amphiphilic **DCS1** as well as the anisotropic and non-amphiphilic **DCS2** particles when treated with ethanolic solutions of equimolar amounts of both drugs Cur and QT. As summarized in Table 2, the overall loading behaviour of Cur plus QT is similarly high but varies widely between Cur and QT among these three types of particles.

Table 2. Drug loading efficiency of **CS**, **DCS1** and **DCS2**

	Cur loading efficiency (%)	QT loading efficiency (%)	Total drug loading (%)
CS	45 ± 5	43 ± 6	88 ± 11
DCS1	58 ± 6	40 ± 7	98 ± 13
DCS2	85 ± 6	10 ± 5	95 ± 11

While comparable loading contents were found for Cur (45 ± 5%) and QT (43 ± 6 %) in mesoporous **CS**, the anisotropic and amphiphilic **DCS1** loads larger amounts of Cur (58 ± 6%) than QT (40 ± 7%) (Table 2). There is even a more profound difference of Cur and QT loading in the anisotropic and non-amphiphilic particle **DCS2**. Thus 85 ± 6 % loading efficiency of Cur and only 10 ± 5 % for QT are observed for **DCS2**. This is remarkable since **CS** and **DCS2** provide comparable specific surface areas and total pore volumes (Table 1). Contrary to this, although the total pore volume of the dumbbell particle **DCS1** is much less compared to that of the **CS** particle (Table 1), the overall loading efficiency of Cur plus QT in **DCS1** is even higher than in **CS** (Table 2).

From the molecular point of view, these results can be explained in terms of the interaction of Cur and QT with the surface Si-OH and Si-F functions, respectively. Both polyphenols are able to interact with Si-OH groups on silica surfaces. The keto-enol tautomerism of Cur supports donating as well as accepting hydrogen bonds.^[21,71] However, under the present reaction conditions it is assumed that Cur interacts with its enolic form with the nucleophilic Si-OH groups on the silica surface of the particles.^[72] Consequently, Cur prefers to accumulate in those areas of the particles with negative zeta potentials. In contrary to this QT selects a more lipophilic environment when forming adducts with surface Si-OH groups.^[73] Thus QT is stored in those areas with non-polar

Si-F functions. Because the spherical core-shell particles **CS** contain Si-OH and Si-F functions, which are equally distributed all over the surface both drugs are loaded in comparable amounts into the mesoporous shell (Table 2). In **DSC2** only Si-OH groups are uniformly spread across the anisotropic particle which makes it more attractive for Cur than for QT to be loaded.

Most interestingly the amphiphilic character of **DSC1** allows QT to be loaded into the porous shell of the large lobe and most of Cur into the porous shell of the small hemisphere. Moreover, the hollow cavity of the small hemisphere in **DCS1** serves as compartment for Cur as well. This is deduced from the large amount of Cur loaded in **DCS1** compared to the small shell of the small lobe (Table 2). Thus, the mesoporous channels in the shell of the small lobe allow the diffusion of Cur into the cavity.^[74] The permeability for small molecules of the shell covering the cavity has been demonstrated earlier.^[58] This indicates that if both Cur and QT are loaded at the same time to **DCS1** they encapsulate into different areas of the silica particle. This is supported by confocal Raman microscopy (Figure 2).

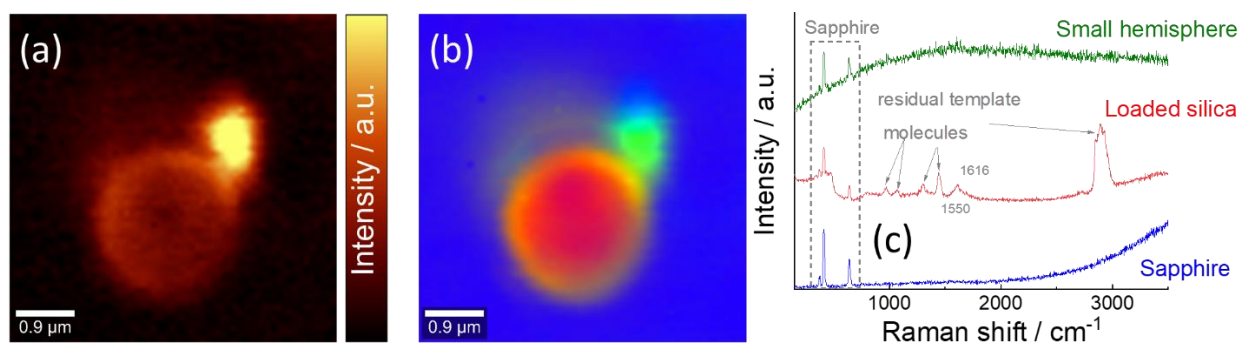


Figure 2 a) Raman intensity distribution image of Cur-Qt-**DCS1** in the spectral range 150 cm^{-1} to 3500 cm^{-1} ; b) Intensity distribution of the Cur-Qt-**DCS1** of three components based on a Principle Component Analysis (PCA); c) the corresponding spectra for each component (see also supporting informations).

Figure 2a shows the Raman peak intensity distribution across a silica particle of **DCS1** loaded with Cur and QT in the spectral range from 150 cm^{-1} to 3500 cm^{-1} . The particle is clearly distinguishable from the background; it shows a medium intensity in the area that can be associated with the core-particle and a much higher intensity in the region of its small hemisphere. A principle component analysis (PCA) of all Raman spectra yields three principle components explaining 93% of the total data. Based on this number of responsible components the data were analysed with Control 5.0 data processing software provided by WITec using an inbuilt PCA. The components were assigned to colours (blue, red, green) for better visualisation. The result of the

decomposition is shown in Figure 2b. The blue component can be associated with the substrate (sapphire), the red with the core-particle and the green with the lobe of the small hemisphere. The shell of the large lobe is yellow indicating a coexistence of the two components (green, red). The corresponding spectra are shown in Figure 2c.

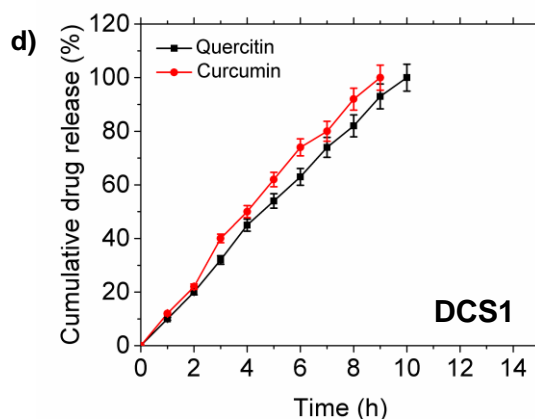
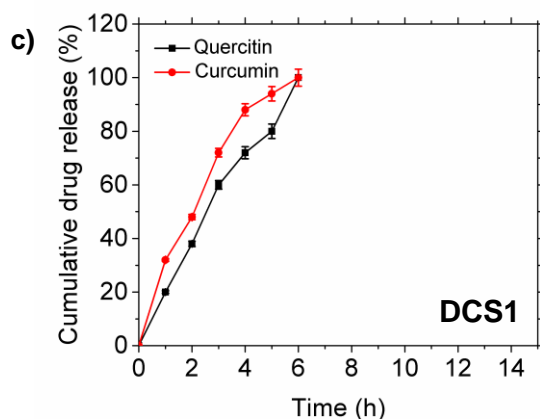
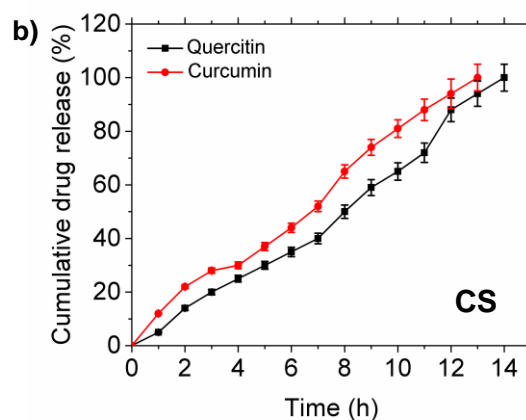
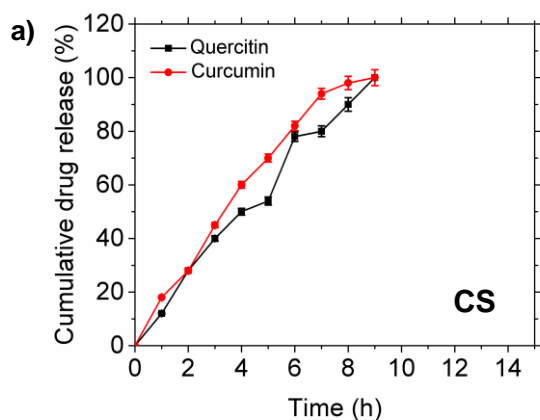
The spectrum of the blue component is dominated by the signals from sapphire with prominent peaks at 412 cm^{-1} , 645 cm^{-1} , and 312 cm^{-1} ; the increasing background from 2500 cm^{-1} is also typical for sapphire.^[75]

The spectrum of the red component shows a number of peaks. Besides the prominent peaks of sapphire also typical signals from silica and residual template molecules are present at 969 cm^{-1} , 1073 cm^{-1} , 1305 cm^{-1} , 1444 cm^{-1} and a broad peak at 2893 cm^{-1} in the red spectrum. This can be assigned to residual template molecules in the pores of **DCS1** since a spectrum was measured with and without drugs loaded (Figure 4S supporting information). The remaining peaks at 1550 cm^{-1} , 1616 cm^{-1} can be assigned to the drugs loaded. The assignment is not straight forward due to the strong overlapping of the signals in this region. The peak at 1616 cm^{-1} and 1550 cm^{-1} are close to C=O stretch and O-H bend of QT respectively.^[76] Nevertheless, certain peaks of Cur also appear in the same range e.g. C=O stretch at 1626 cm^{-1} and C=C aromatic stretch at 1601 cm^{-1} .^[77–80] However, Cur should show a certain luminescence which is not observed in this contribution also its prominent peak at 1626 cm^{-1} is missing. The green component is dominated by luminescence without additional Raman peaks. This luminescence peak can be attributed to Cur since the fitting results shows a maximum at approx. 1500 cm^{-1} , that corresponds to 578 nm which is close to fluorescence emission of Cur.^[81,82] In conclusion, QT prefers to load into the shell of the large lobe while Cur stores in the shell and in the cavity of the small hemisphere. Although the accumulation of minor amounts of Cur on the large lobe cannot be excluded.

***In vitro* drug release study**

The drug release behaviour for Cur and QT loaded **CS**, **DCS1** and **DCS2** particles were evaluated at pH 5.5 and 7.4 (Figure 3). As the Cur loading content is higher in **DCS1** and **DCS2**, the percentage of drug release is also higher than that of QT in the dumbbell particles. All particles showed quicker drug release in acidic pH. Both drugs get released faster from the dumbbell particles **DCS1** (6 h) and **DCS2** (7 h) than from the spherical **CS** (9 h) mesoporous particles in acidic environment. At the physiological pH, Cur gets released faster than QT from all particles (Figure 3).

The crucial requirement on formulating the poorly water-soluble drug is dissolution enhancement with an immediate drug release from the microcarrier particles. However, on formulating the drug as a molecular dispersion adsorbed into a silica matrix, a rapid release from the **DCS1** and **DCS2** was observed. There are reports that it took 30 h to complete the release of the catophril drug from mesoporous silica particles and that it took 19 h for the complete release of 5- fluorouracil from their mesoporous silica particles.^[83] Even though there are drug release studies on mesoporous silica particles, the time taken for releasing the loaded drug is larger than the time period for 100 % drug release, here.



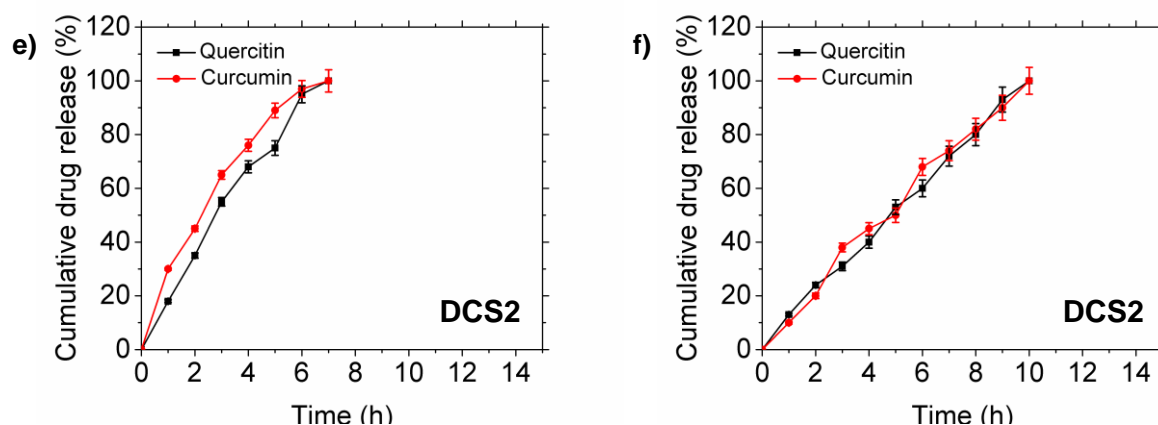
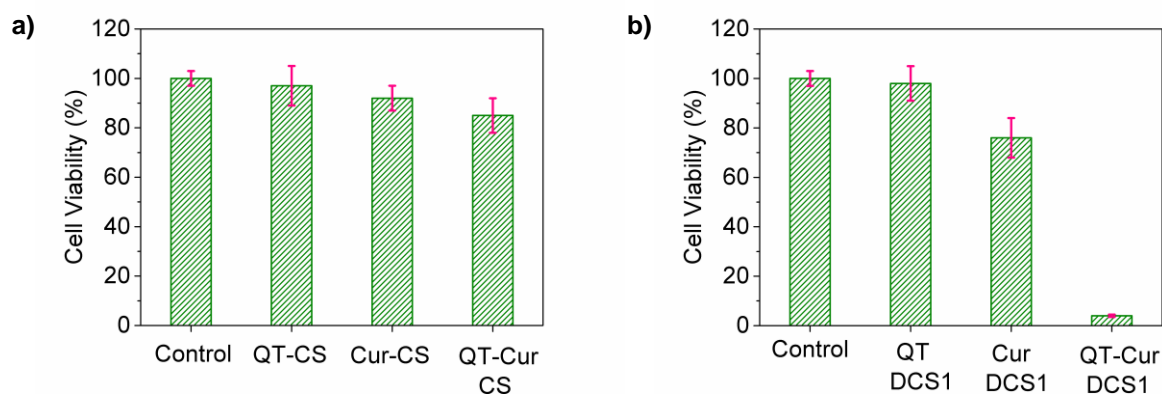


Figure 3: Cumulative percentage of Cur and QT released from **CS** (a, b) **DCS1** (c, d) **DCS2** (e, f) at pH 5.5 (left column) and pH 7.4 (right column).

Cell Viability assay

The typical characterization of cancer cells is the uncontrolled proliferation of the cells. The non-toxicity of quercetin, curcumin and mesoporous silica particles on normal cells were reported elsewhere.^[43,84,85] The cytotoxicity of Cur and QT loaded on **CS**, **DCS1** and **DCS2** individually and as a combinatorial approach were examined by performing the 3-(4,5-dimethylthiazol-2-yl)-2,5-diphenyltetrazolium bromide (MTT) assay against U2OS (human bone osteosarcoma epithelial cell lines).^[64] The results indicate that Cur and QT loaded particles have significant toxicity towards the U2OS cancer cells and that the activity strongly depends on the amounts of drugs loaded and the shape of the silica particle (Figure 4).



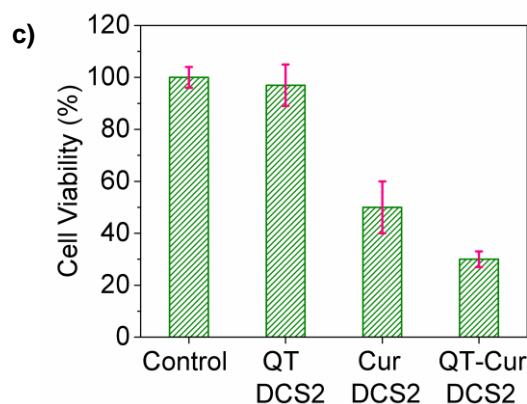


Figure 4: Cell viability assays after 24 h incubation of U2OS cancer cells with a) **CS** alone, QT-**CS**, Cur-**CS** and QT-Cur- **CS**; b) **DCS1** alone, QT-**DCS1**, Cur-**DCS1** and QT-Cur-**DCS1**; c) **DCS2** alone, QT-**DCS2**, Cur-**DCS2** and QT-Cur-**DCS2** at 25 nM. The data represent the average of at least three independent measurements.

The IC_{50} concentration of QT-**CS**, Cur-**CS** and Cur-QT-**CS** were 200, 150 and 100 nM for the respective drug loaded **CS** particles. Figure 4 displays the results of the cytotoxicity for QT loaded, Cur loaded and both drugs loaded silica particles **CS**, **DCS1** and **DCS2**. The QT-**CS**, Cur-**CS** and Cur-QT-**CS** particles showed 97%, 95% and 92%, cell viability, respectively, at 25 nM concentration after 24 h (Figure 4a). The respective epi-fluorescence and phase contrast images (Figure 5) for the QT-**CS**, Cur-**CS** and Cur-QT-**CS** also show that the cells do not undergo any morphological changes or cell death after 24 h.

For the QT-**DCS2**, Cur-**DCS2** and Cur-QT-**DCS2** particles, about 97%, 50% and 30% of cell viability was observed at 25 nM of drug concentration as shown in the Figure 5c. The higher cell toxicity of Cur-**DCS2** compared to Cur-**CS** is a result to the higher concentration of Cur delivered by **DCS2** (Table 2).

The viability of the cells at 25 nM concentration for QT-**DCS1**, Cur-**DCS1** and Cur-QT-**DCS1** was around 85%, 79% and 4% at the end of the 24h (Figure 4b). In the same order the IC_{50} was found to be 105, 57 and 13.5 nM after 24 h. Note that IC_{50} for Cur and QT alone is 21.6 μ M and 100 μ M, respectively.^[86,87] Thus the drug loaded **DCS1** particles showed an enhanced effect even in nanomolar concentrations when compared to drug loaded **CS** and drugs alone.

The corresponding cell images of **DCS1** at the end of 24 h are shown in Figure 6. The Figure 6a-c shows the phase contrast, epi-fluorescence and overlay imaging of the cells when treated with **DCS1** without drugs. All the cells are viable and no cytotoxicity was observed from **DCS1**, which

agrees with reports that silica particles are nontoxic to the cells.^[15] When the cells are treated with drug loaded Cur-QT-**DCS1** at 25 nM, changes in the morphological structure of the cells are observed. The cells died either because of necrosis or apoptosis as shown in the Figure 6d-f. Figure 6g-i and 6j-l corresponds to the cells treated with Cur-**DCS1** and QT-**DCS1** at 25 nM concentration. Changes in the morphological structure of the cells are observed at 25 nM concentration. Thus, one can conclude that the Cur-QT-**DCS1** particles showed greater cytotoxicity effect than Cur-QT-**CS** and Cur-QT-**DCS2** particles.

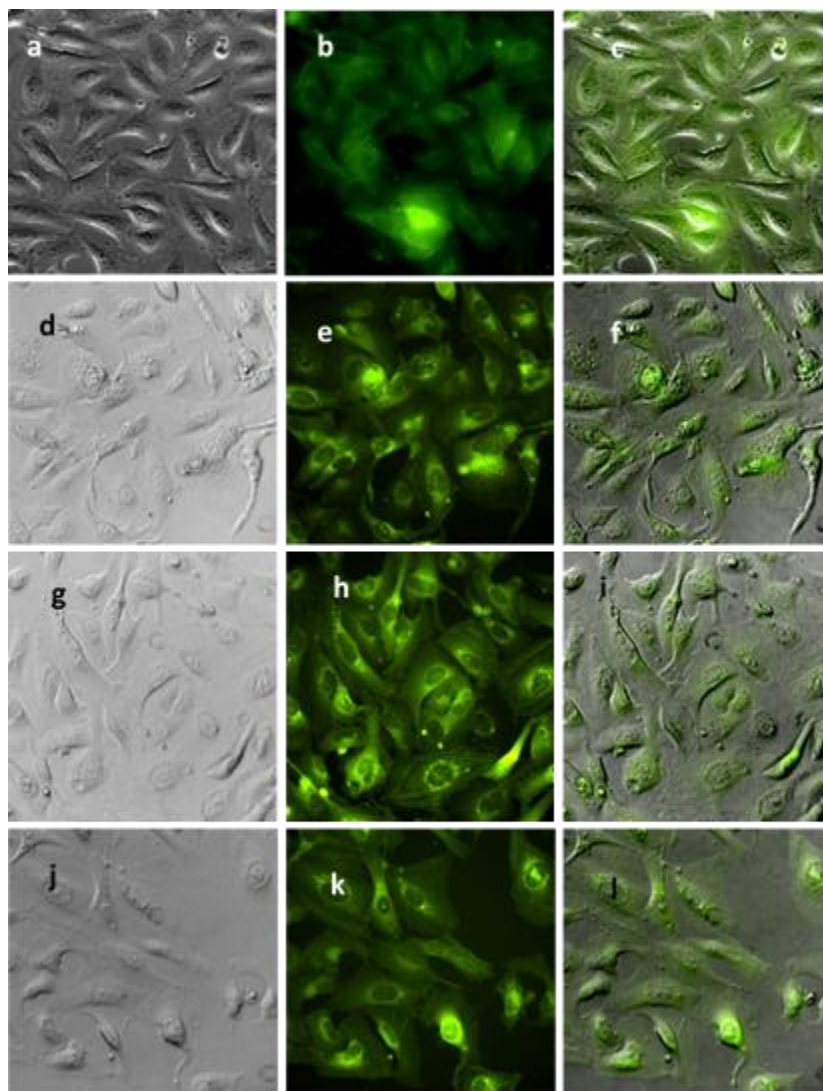


Figure 5: Phase contrast (first panel), epifluorescence (second panel) and overlaid (third panel) images of the U2Os cell lines. (a-c) U2OS cells treated with **CS** alone; (d-f) Cells treated with Cur-QT-**CS**; (g-i) Cells treated with Cur-**CS**; (j-l) Cells treated with QT-**CS** at 25 nM concentration for 24 h.

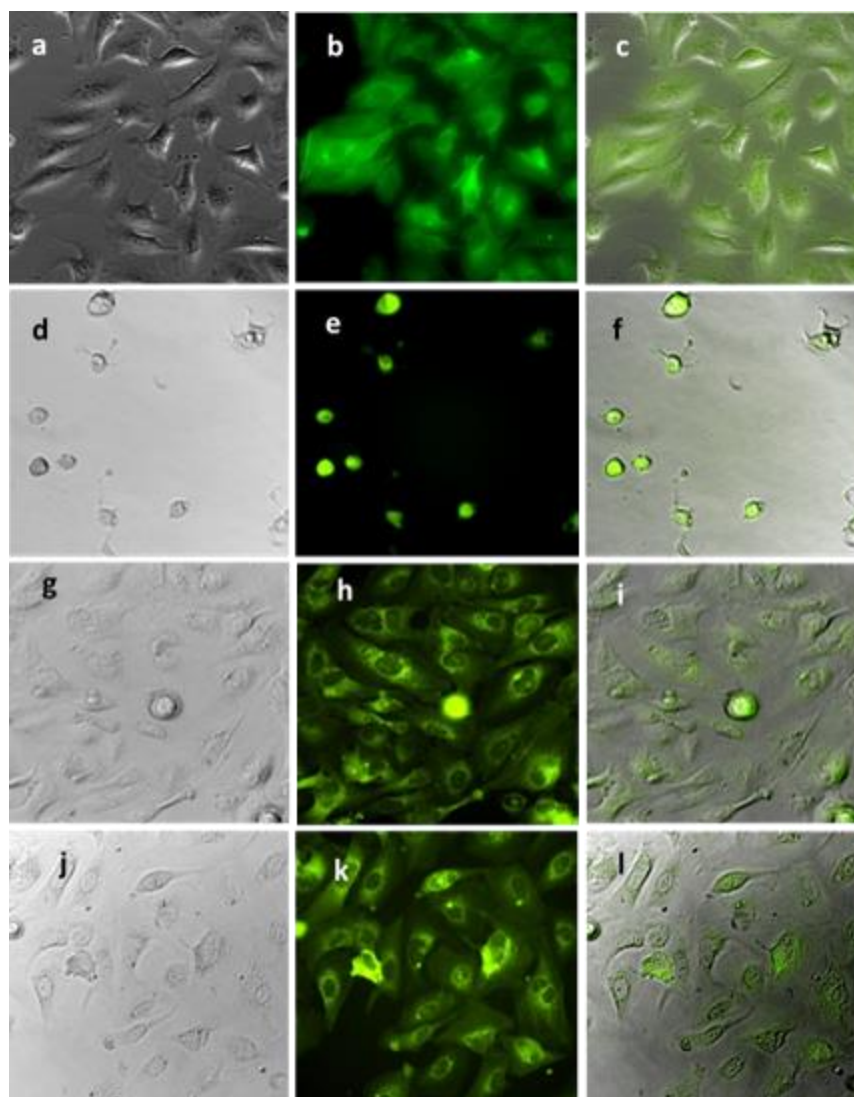


Figure 6: Phase contrast (first panel), epifluorescence (second panel) and overlaid (third panel) images of the U2Os cell lines. (a-c) U2OS cells treated with **DCS1** alone; (d-f) Cells treated with Cur-QT-**DCS1**; (g-i) Cells treated with Cur-**DCS1**; (j-l) Cells treated with QT-**DCS1** at 25 nM concentration for 24 h.

Conclusion

Varying the stirring speed and the added salts in a simple etching process of μm sized silica particles allows to access spherical core-shell **CS**, anisotropic core-shell **DCS2** and anisotropic and amphiphilic core-shell **DCS1** silica particles. The three particles differ in their architecture and provide mesoporous channels, hollow cavities and different surface charge distributions. The

porous shells and the cavity allows to accumulate different molecules. This was demonstrated by loading the polyphenols Cur and QT into the mesopores and cavities of the three particles. The loading behavior of these two drugs vary significantly among the three particles. Moreover, the anisotropic and amphiphilic core-shell **DCS1** particle is able to discriminate between Cur and QT by accumulating them in different areas of the particle.

Cell viability studies also show strong variations among the three drug loaded particles. While the effect of drug loaded **CS** on cells is moderate, the cell toxicity increases from drug loaded **DCS2** to drug loaded **DCS1**. Most interestingly although **CS** and **DCS1** deliver comparable amounts of both drugs, the cell toxicity of Cur-QT-**DCS1** is dramatically higher compared to Cur-QT-**CS**. Obviously, the anisotropic character in shape and surface charge of **DCS1** allows for a much better interaction of the drug loaded particle with the cells.^[57]

Acknowledgement

Prof. Dr. Tilman E. Schaeffer for providing the U2OS cells. We are grateful to Elke Nadler (University of Tübingen) for SEM and STEM measurements. Lorenz Bock is acknowledged for measuring N₂ adsorption and desorption isotherms. AD was supported by a National Overseas Scholarship and is thankful to the Government of India for financial support. BB was financially supported by a HAW Prom grant within the „Programm zur Stärkung der Hochschulen für Angewandte Wissenschaften in Promotionsverfahren durch Förderung kooperativer (Einzel-) Promotionen“ We thank the Ministerium für Wissenschaft, Forschung und Kunst Baden-Württemberg for financial support. AM would like to acknowledge the financial support within the framework “IngenieurNachwuchs 2016” (project: Compe TERS) by the German federal ministry of education and research (BMBF).

Authors contribution

M.B., A.K., E.S., and H.A.M. designed research; A.D., S.S., B.B. and A.M. performed research and analysed the data. H.A.M. wrote the manuscript and all authors reviewed the manuscript.

References

- [1] F. Ditzinger, D. J. Price, A.-R. Ilie, N. J. Köhl, S. Jankovic, G. Tsakiridou, S. Aleandri, L. Kalantzi, R. Holm, A. Nair, C. Saal, B. Griffin, M. Kuentz, *Journal of Pharmacy and Pharmacology* **2019**, *71*, 464.
- [2] C. Barbé, J. Bartlett, L. Kong, K. Finnie, H. Q. Lin, M. Larkin, S. Calleja, A. Bush, G. Calleja, *Advanced Materials* **2004**, *16*, 1959.
- [3] A. Biswas, A. Shukla, P. Maiti, *Langmuir* **2019**, *35*, 12285.
- [4] A. S. Hoffman, *Journal of Controlled Release* **2008**, *132*, 153.
- [5] J. Folkman, *Biomaterials* **1990**, *11*, 615.
- [6] K. Park, *Journal of Controlled Release* **2014**, *190*, 3.
- [7] T. M. Allen, P. R. Cullis, *Advanced Drug Delivery Reviews* **2013**, *65*, 36.
- [8] D. Böhme, A. G. Beck-Sickingler, *J. Pept. Sci.* **2015**, *21*, 186.
- [9] J. Logie, S. C. Owen, C. K. McLaughlin, M. S. Shoichet, *Chem. Mater.* **2014**, *26*, 2847.
- [10] E. V. Skorb, H. Möhwald, *Adv. Mater. Interfaces* **2014**, *1*, n/a.
- [11] M.-Q. Gong, J.-L. Wu, B. Chen, R.-X. Zhuo, S.-X. Cheng, *Langmuir* **2015**, *31*, 5115.
- [12] V. Morales, M. N. Idso, M. Balabasquer, B. Chmelka, R. A. García-Muñoz, *J. Phys. Chem. C* **2016**, *120*, 16887.
- [13] H. Geng, Y. Zhao, J. Liu, Y. Cui, Y. Wang, Q. Zhao, S. Wang, *International Journal of Pharmaceutics* **2016**, *510*, 184.
- [14] A.-L. Lainé, D. Price, J. Davis, D. Roberts, R. Hudson, K. Back, P. Bungay, N. Flanagan, *International Journal of Pharmaceutics* **2016**, *512*, 118.
- [15] D. Tarn, C. E. Ashley, M. Xue, E. C. Carnes, J. I. Zink, C. J. Brinker, *Acc. Chem. Res.* **2013**, *46*, 792.
- [16] R. Joshi, V. Feldmann, W. Koestner, C. Detje, S. Gottschalk, H. A. Mayer, M. G. Sauer, J. Engelmann, *Biological Chemistry* **2013**, *394*, 125.
- [17] T. Heikkilä, J. Salonen, J. Tuura, N. Kumar, T. Salmi, D. Y. Murzin, M. S. Hamdy, G. Mul, L. Laitinen, A. M. Kaukonen, J. Hirvonen, V.-P. Lehto, *Drug Delivery* **2007**, *14*, 337.
- [18] Y.-Y. Yang, X. Wang, Y. Hu, H. Hu, D.-C. Wu, F.-J. Xu, *ACS Appl. Mater. Interfaces* **2014**, *6*, 1044.
- [19] Y. Yang, K. Achazi, Y. Jia, Q. Wei, R. Haag, J. Li, *Langmuir* **2016**, *32*, 12453.
- [20] S. J. Hewlings, D. S. Kalman, *Foods* **2017**, *6*, 92.
- [21] K. M. Nelson, J. L. Dahlin, J. Bisson, J. Graham, G. F. Pauli, M. A. Walters, *J. Med. Chem.* **2017**, *60*, 1620.
- [22] Z. Stanić, *Plant Foods Hum Nutr* **2017**, *72*, 1.
- [23] K. Pallauf, G. Rimbach, *Ageing Research Reviews* **2013**, *12*, 237.
- [24] N. Hasima, B. Ozpolat, *Cell Death Dis* **2014**, *5*, e1509.
- [25] J. Adiwidjaja, A. J. McLachlan, A. V. Boddy, *Expert Opinion on Drug Metabolism & Toxicology* **2017**, *13*, 953.
- [26] G. Zhao, X. Dong, Y. Sun, *Langmuir* **2019**, *35*, 1846.
- [27] Z. Li, L. Zhang, X. Wei, J. Liu, Z. Wang, *Langmuir* **2019**, *35*, 453.
- [28] N. A. Nasab, H. H. Kumleh, M. Beygzadeh, S. Teimourian, M. Kazemzad, *Artificial Cells, Nanomedicine, and Biotechnology* **2018**, *46*, 75.
- [29] M. Agrawal, S. Saraf, S. Saraf, S. G. Antimisiaris, M. B. Chougule, S. A. Shoyele, A. Alexander, *Journal of Controlled Release* **2018**, *281*, 139.
- [30] K. Shahani, J. Panyam, *Journal of Pharmaceutical Sciences* **2011**, *100*, 2599.
- [31] K. Radhakrishnan, J. Tripathy, A. Datey, D. Chakravorty, A. M. Raichur, *New J. Chem.* **2015**, *39*, 1754.
- [32] A. Aras, A. R. Khokhar, M. Z. Qureshi, M. F. Silva, A. Sobczak-Kupiec, E. A. G. Pineda, A. A. W. Hechenleitner, A. A. Farooqi, *Asian Pacific Journal of Cancer Prevention* **2014**, *15*, 3865.
- [33] S. Sunoqrot, T. Al-Debsi, E. Al-Shalabi, L. Hasan Ibrahim, F. N. Faruqu, A. Walters, R. Palgrave, K. T. Al-Jamal, *ACS Biomater. Sci. Eng.* **2019**, *5*, 6036.
- [34] C. T. Kresge, M. E. Leonowicz, W. J. Roth, J. C. Vartuli, J. S. Beck, *Nature* **1992**, *359*, 710.

- [35] C. J. Brinker, Y. Lu, A. Sellinger, H. Fan, *Advanced Materials* **1999**, *11*, 579.
- [36] D. Zhao, J. Feng, Q. Huo, N. Melosh, G. H. Fredrickson, B. F. Chmelka, G. D. Stucky, *Science* **1998**, *279*, 548.
- [37] Y. Wan, Zhao, *Chem. Rev.* **2007**, *107*, 2821.
- [38] A. Galarneau, J. Iapichella, K. Bonhomme, F. Di Renzo, P. Kooyman, O. Terasaki, F. Fajula, *Advanced Functional Materials* **2006**, *16*, 1657.
- [39] S. Huh, J. W. Wiench, B. G. Trewyn, S. Song, M. Pruski, V. S.-Y. Lin, *Chem. Commun.* **2003**, *0*, 2364.
- [40] L. Travaglini, L. De Cola, *Chem. Mater.* **2018**, *30*, 4168.
- [41] L. Luo, Y. Liang, T. Chassé, R. Anwender, *Particle & Particle Systems Characterization* **2018**, *35*, 1800312.
- [42] F. Torney, B. G. Trewyn, V. S.-Y. Lin, K. Wang, *Nature Nanotech* **2007**, *2*, 295.
- [43] I. I. Slowing, J. L. Vivero-Escoto, C.-W. Wu, V. S.-Y. Lin, *Advanced Drug Delivery Reviews* **2008**, *60*, 1278.
- [44] G. V. Deodhar, M. L. Adams, B. G. Trewyn, *Biotechnology Journal* **2017**, *12*, 1600408.
- [45] M. Yu, Z. Gu, T. Ottewell, C. Yu, *J. Mater. Chem. B* **2017**, *5*, 3241.
- [46] L. Dai, J. Li, B. Zhang, J. Liu, Z. Luo, K. Cai, *Langmuir* **2014**, *30*, 7867.
- [47] R. Li, Y. Xie, *Journal of Controlled Release* **2017**, *251*, 49.
- [48] Y. Zhao, B. G. Trewyn, I. I. Slowing, V. S.-Y. Lin, *J. Am. Chem. Soc.* **2009**, *131*, 8398.
- [49] A. Motahari, N. Hu, A. Vahid, A. Omrani, A. A. Rostami, D. W. Schaefer, *Langmuir* **2018**, *34*, 6719.
- [50] J. Du, R. K. O'Reilly, *Chem. Soc. Rev.* **2011**, *40*, 2402.
- [51] A. Zhang, L. Gu, K. Hou, C. Dai, C. Song, X. Guo, *RSC Adv.* **2015**, *5*, 58355.
- [52] K. Möller, T. Bein, *Chem. Mater.* **2017**, *29*, 371.
- [53] V. Cauda, A. Schlossbauer, J. Kecht, A. Zürner, T. Bein, *J. Am. Chem. Soc.* **2009**, *131*, 11361.
- [54] L.-T.-C. Tran, S. Lesieur, V. Faivre, *Expert Opinion on Drug Delivery* **2014**, *11*, 1061.
- [55] L. Luo, Y. Liang, E. S. Erichsen, R. Anwender, *Chemistry – A European Journal* **2018**, *24*, 7200.
- [56] G. Tuncelli, A. N. Ay, B. Zümreoglu-Karan, *Materials Science and Engineering: C* **2015**, *55*, 562.
- [57] G. Agrawal, R. Agrawal, *ACS Appl. Nano Mater.* **2019**, *2*, 1738.
- [58] J. Maisch, F. Jafarli, T. Chassé, F. Blendinger, A. Konrad, M. Metzger, A. J. Meixner, M. Brecht, L. Dähne, H. A. Mayer, *Chem. Commun.* **2016**, *52*, 14392.
- [59] A. Perro, S. Reculosa, S. Ravaine, E. Bourgeat-Lami, E. Duguet, *J. Mater. Chem.* **2005**, *15*, 3745.
- [60] N. S. Elbially, S. F. Aboushoushah, B. F. Sofi, A. Noorwali, *Microporous and Mesoporous Materials* **2020**, *291*, 109540.
- [61] P. Yang, S. Gai, J. Lin, *Chem. Soc. Rev.* **2012**, *41*, 3679.
- [62] F. Islami, A. G. Sauer, K. D. Miller, R. L. Siegel, S. A. Fedewa, E. J. Jacobs, M. L. McCullough, A. V. Patel, J. Ma, I. Soerjomataram, W. D. Flanders, O. W. Brawley, S. M. Gapstur, A. Jemal, *CA: A Cancer Journal for Clinicians* **2018**, *68*, 31.
- [63] Y. Gao, S. Ding, X. Huang, Z. Fan, J. Sun, Y. Hai, K. Li, *Drug Development and Industrial Pharmacy* **2019**, *45*, 273.
- [64] P. B. Santhosh, N. Thomas, S. Sudhakar, A. Chadha, E. Mani, *Phys. Chem. Chem. Phys.* **2017**, *19*, 18494.
- [65] H. Dong, J. D. Brennan, *J. Mater. Chem.* **2012**, *22*, 13197.
- [66] X. Fang, C. Chen, Z. Liu, P. Liu, N. Zheng, *Nanoscale* **2011**, *3*, 1632.
- [67] T. Zhang, J. Ge, Y. Hu, Q. Zhang, S. Aloni, Y. Yin, *Angewandte Chemie International Edition* **2008**, *47*, 5806.
- [68] Y. Chen, H. Chen, L. Guo, Q. He, F. Chen, J. Zhou, J. Feng, J. Shi, *ACS Nano* **2010**, *4*, 529.
- [69] A. Monnier, F. Schüth, Q. Huo, D. Kumar, D. Margolese, R. S. Maxwell, G. D. Stucky, M. Krishnamurty, P. Petroff, A. Firouzi, M. Janicke, B. F. Chmelka, *Science* **1993**, *261*, 1299.
- [70] M. Thommes, K. Kaneko, A. V. Neimark, J. P. Olivier, F. Rodriguez-Reinoso, J. Rouquerol, K. S. W. Sing, *Pure and Applied Chemistry* **2015**, *87*, 1051.
- [71] B. Jain, *Journal of Molecular Structure* **2017**, *1130*, 194.

- [72] R. K. Gangwar, G. B. Tomar, V. A. Dhumale, S. Zinjarde, R. B. Sharma, S. Datar, *J. Agric. Food Chem.* **2013**, *61*, 9632.
- [73] G. Berlier, L. Gastaldi, E. Ugazio, I. Miletto, P. Iliade, S. Sapino, *Journal of Colloid and Interface Science* **2013**, *393*, 109.
- [74] D. Jin, K.-W. Park, J. H. Lee, K. Song, J.-G. Kim, M. L. Seo, J. H. Jung, *J. Mater. Chem.* **2011**, *21*, 3641.
- [75] X. Du, M. Zhang, Q. Meng, Y. Song, X. He, Y. Yang, J. Han, *Opt. Express, OE* **2010**, *18*, 22937.
- [76] Y. Numata, H. Tanaka, *Food Chemistry* **2011**, *126*, 751.
- [77] T. M. Kolev, E. A. Velcheva, B. A. Stamboliyska, M. Spiteller, *International Journal of Quantum Chemistry* **2005**, *102*, 1069.
- [78] P. R. K. Mohan, G. Sreelakshmi, C. V. Muraleedharan, R. Joseph, *Vibrational Spectroscopy* **2012**, *62*, 77.
- [79] P. Sanphui, N. R. Goud, U. B. R. Khandavilli, S. Bhanoth, A. Nangia, *Chem. Commun.* **2011**, *47*, 5013.
- [80] H. Van Nong, L. X. Hung, P. N. Thang, V. D. Chinh, L. V. Vu, P. T. Dung, T. Van Trung, P. T. Nga, *Springerplus* **2016**, *5*, 1147.
- [81] M. H. M. Leung, D.-T. Pham, S. F. Lincoln, T. W. Kee, *Phys. Chem. Chem. Phys.* **2012**, *14*, 13580.
- [82] P. K. Singh, K. Wani, R. Kaul-Ghanekar, A. Prabhune, S. Ogale, *RSC Adv.* **2014**, *4*, 60334.
- [83] X. She, L. Chen, Z. Yi, C. Li, C. He, C. Feng, T. Wang, S. Shigdar, W. D. and L. Kong*, Tailored Mesoporous Silica Nanoparticles for Controlled Drug Delivery: Platform Fabrication, Targeted Delivery, and Computational Design and Analysis. *Mini-Reviews in Medicinal Chemistry* **2018**, *18*, 976–989.
- [84] M. Ebrahimifar, M. H. Roudsari, S. M. Kazemi, H. E. Shahmabadi, L. Kanaani, S. Alavi, M. I. Vasfi, *Asian Pac J Cancer Prev* **2017**, *18*, 65.
- [85] M. Hashemzaei, A. Delarami Far, A. Yari, R. E. Heravi, K. Tabrizian, S. M. Taghdisi, S. E. Sadegh, K. Tsarouhas, D. Kouretas, G. Tzanakakis, D. Nikitovic, N. Y. Anisimov, D. A. Spandidos, A. M. Tsatsakis, R. Rezaee, *Oncology Reports* **2017**, *38*, 819.
- [86] D. K. Walters, R. Muff, B. Langsam, W. Born, B. Fuchs, *Invest New Drugs* **2007**, *26*, 289.
- [87] D. Catanzaro, E. Ragazzi, C. Vianello, L. Caparrotta, M. Montopoli, *Natural Product Communications* **2015**, *10*, 1934578X1501000813.

Germanium nanosphere as high precision optical tweezer probe

Swathi Sudhakar, Mohammad Kazem Abdosamadi, Viktoria Welder,
Pasupathi Rajendran, and Erik Schäffer*

*Eberhard Karls Universität Tübingen, ZMBP, Auf der Morgenstelle 32, 72076 Tübingen,
Germany*

E-mail: erik.schaeffer@uni-tuebingen.de

Abstract

Optical tweezers are often used to study about the mechanism of single molecular machines. However, the use of common microspheres like silica and polystyrene to research about the kinesin stepping mechanism have certain limitations in their maximum force, measurement precision, or the degrees of freedom that can be measured. For example, the ultimate precision of the experiment is limited by the drag coefficient, i.e. the size of the microsphere. Thus, ideally, microspheres should be as small as possible. But for the polystyrene microspheres, if they are too small, then the maximum trapping forces are smaller than the motor-generated forces creating a lower practical size limit of about 200 nm. To overcome this problem, we have developed germanium nanoparticles with diameters ranging from 30-200 nm. With a high refractive index of 4.4, their trapping efficiency is more than 10-fold higher than silica. Using 70-nm-diameter of germanium nanoparticles, we measured the stepping behavior of kinesin-1. In the long-term, the development of novel probes enables novel applications.

Introduction

Optical tweezers acts as a highly precise and sensitive handle for measuring forces and distances in the sub-piconewton and in nanometer regime, respectively.¹⁻³ For the study of biomolecules like motor proteins or DNA, it is crucial to attach a tool, for example, a silica or polystyrene to the biomolecule of interest, thus the nanometer-scale motion and the forces acting on the microspheres can be computed using optical tweezers.⁴⁻⁷

But , the ultimate precision of the experiment is limited by the drag coefficient, i.e. the size of the microsphere. Thus, ideally, microspheres should be as small as possible. However, if microspheres are too small, maximum trapping forces are smaller than motor-generated forces creating a lower size limit of about 200 nm for polystyrene. Note that for Rayleigh scatters trapping forces scale with the volume of the particles, but the problem faced by these beads are they do not produce clear signals on the detector and so their signal-to-noise ratio for nanometry is low. On the other hand there are also studies associated with optical trapping of metallic nanoparticles like gold⁸⁻¹¹ and silver nanospheres^{12,13} in size range from 20 to 300 nm. But the main problem over trapping of metallic nanoparticles was the significant heating of the particles caused by absorption of light. The heating of the metallic probes¹⁴⁻¹⁶ can potentially denature the biological samples.

To overcome these problems, we used germanium nanoparticles as trappable optical probes (GENTOPs) which are several times smaller than those conventionally used polystyrene microspheres. Germanium nanospheres have excited scientists because of their size-dependent optical properties and their potential applications in biological imaging, optoelectronics, and therapeutics.^{17,18} As the germanium particle have a high refractive index,¹⁹ their trapping stiffness is larger than a similar-sized latex particle. Moreover, GeNTOPs have negligible absorption of the light in near infra red, leading to the less heat up unlike metallic nanoparticles, thus allows us to perform force measurements with biological samples.

For studying the biomolecule of interests using GeNTOPs, it is crucial to know the range of forces that can be exerted on different sized GeNTOPs. Thus, we synthesized GeNTOPs of different sizes ranging from 30 to 200 nm, using wet chemical reduction method and performed stable optical trapping of individual GeNTOPs of different sizes. This is the first study to report on optical trapping of GeNTOPs in the above said size range. We also found that synthesized GeNTOPs has six and ten fold high trap stiffness than commercially used polystyrene and silica particles of same size. Thus all these properties makes the GeNTOPs, ideal candidate for optical tweezer-based micromanipulation to probe biological nanomachines like motor proteins

Results and discussion

Size controlled synthesis of water stable GeNTOPs

Germanium nanospheres were synthesized using wet chemical reduction method as reported²⁰ with slight modification (see Experimental section). In this process, Germanium oxide (GeO_2) and sodium borohydride (NaBH_4) is used as a substrate and reducing agent. Quercetin is used as an stabilizing agent. GeNTOPs were visualized with the help of Transmission electron Microscopy(TEM) and size was observed to increased from 29 nm to 200 nm, when the reaction time was increased from 3 h to 8 h. At corresponding time interval of 3,4,5,6,7 and 8 h, the particle size of about 29 ± 6 ($N = 100$), 53 ± 5 ($N = 80$), 70 ± 9 ($N = 90$), 100 ± 7 ($N = 120$), 150 ± 5 ($N = 112$), 150 ± 5 ($N = 112$), 173 ± 7 ($N = 132$), 200 ± 6 ($N = 148$) was measured. Next, we compared the size of the particles using different techniques like TEM, Dyanamic Light Scattering (DLS) and with optical tweezer (OT) in order to exclude the shrinking effect of particles while drying in TEM preparation. The size of the particles from each measurements are found to be similar and the results are in correlation with each other. Next we tested the crystallinity, of the particles. Because, the more particles are crystalline, higher the trap stiffness.

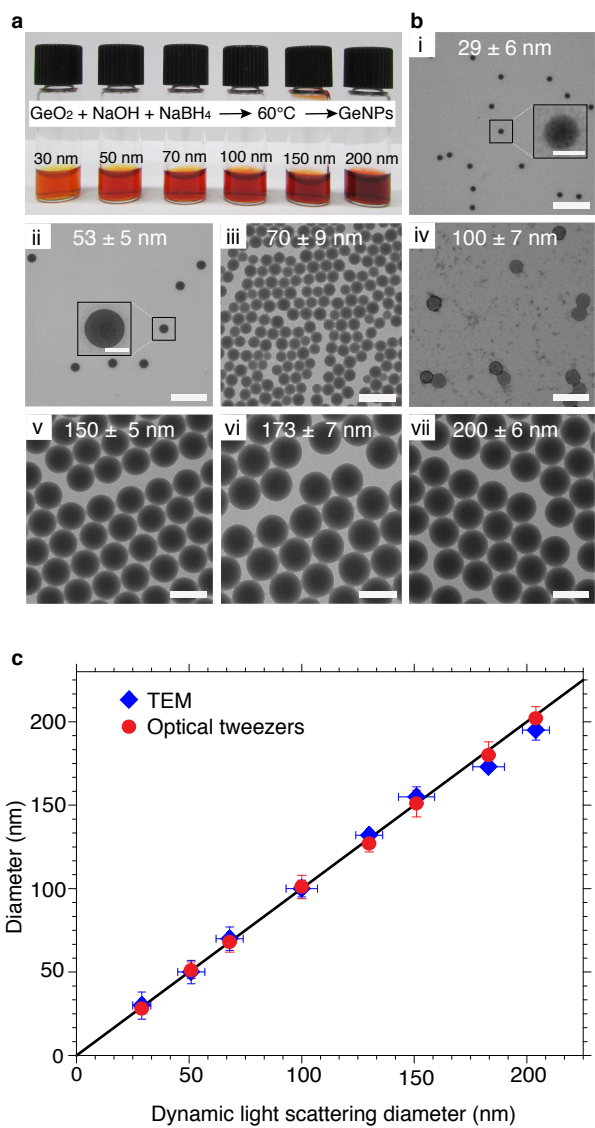


Figure 1: (a) Germanium nanospheres of different diameter from 30 nm to 200 nm in solution (b) Transmission electron microscopic images of GeNPs i) 29 ± 6 ($N = 100$), ii) 53 ± 5 ($N = 80$), iii) 70 ± 9 ($N = 90$), iv) 100 ± 7 ($N = 120$), v) 150 ± 5 ($N = 112$), vi) 150 ± 5 ($N = 112$), vii) 173 ± 7 ($N = 132$), viii) 200 ± 6 ($N = 148$) (mean \pm standard deviation of the mean) at different time intervals (c) Diameter of different sized GeNPs measured with different techniques like TEM, Optical tweezers and dynamic light scattering

X-Ray diffraction studies shows cubic crystal phase of GeNTOPs

The GeNTOPs were lyophilized and the X-Ray powder diffraction (XRD) studies were carried out for the GeNTOPs sized 30 nm. XRD analysis were used to determine the phase of the sample. Fig. 2 shows the XRD pattern of the GeNTOPs. Diffraction peaks with 2 theta values at 27.22, 45.17, 53.65, 65.9, 72.6 and 90.2 deg corresponding to 111, 220, 311, 400, 331 and 511 lattice was observed. The clear peaks had an exact match with the reference pattern for pure germanium crystal as reported before.²¹ All of the peaks in fig 2 represents the germanium cubic crystal structure with lattice constant value of 5.662 ± 0.06 Å, which is in excellent agreement with the standard value with $a = 5.6512$ Å (JCPDS card No. 03-065-0333).²² The domain size calculated was around 22.8 ± 0.2 nm which confirms that the nanospheres are made of single crystal. Thus X-Ray diffraction studies shows single diamond cubic crystal phase of GeNTOPs.

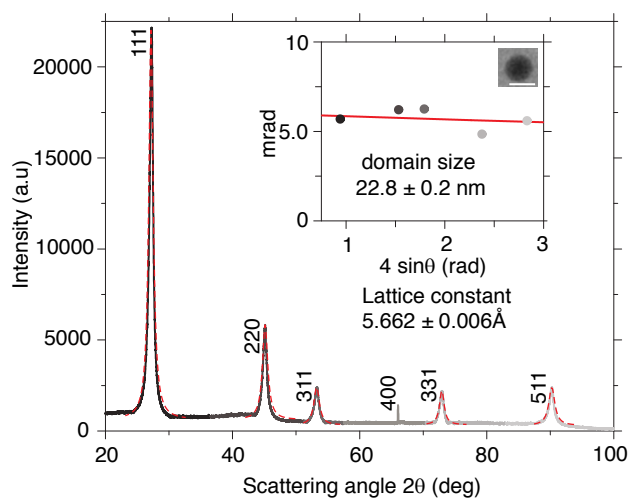


Figure 2: Xray diffraction(XRD) spectrum of GeNTOPs. Inset(Left): The Schematic diagram showing lattice constant value calculated with 5.662 ± 0.06 Å Inset (Right): Williamson hall plot with calculated domain size of 22.8 ± 0.2 nm

GeNTOPs have high trap efficiency with high corner frequency

Now, we know that the GeNTOPs are crystalline in nature. Usually the particles with high crystallinity, exhibits high trap stiffness while trapping. The trap stiffness for these high refractive germanium nanoprobe at different size was calculated by mie theoretical simulations studies based on the optical tweezers computational toolbox with refractive index value of $4.4 \pm 0.11 i$ by Nieminen et al.²³ The size and drag coefficient of the GeNTOPs were calculated by computing the power spectrum resulting from the thermal motion of the microspheres with the response to a sinusoidal movement of the stage²⁴ at a frequency of 32 Hz. The lateral (axial) trap stiffness for the germanium nanospheres was experimentally calculated at the laser power of 0.1 W (10% laser intensity) and found to have 6-fold and 10-fold high trap stiffness than polystyrene and silica nanospheres of same size. The size of the particles were plotted against the trap stiffness as log-log plot in Figure 4.a and lin-lin plot as inset. The measurements (black, red and blue solid symbols) agree well with the predictions (black, red and blue solid line) showing that we achieved the maximum possible trapping efficiency.

Next we want to check the trap stiffness and corner frequency (f_c) for GeNTOPs at maximum laser power of 1 W, to ensure that heat produced by the particle doesn't have any effect in the trap stiffness at high laser power. Both the factors increased linearly with the increase in the laser power in the focus. At maximum laser power (1 W), a power spectral density spectrum was recorded (Fig.3) and analysis of the particle motion revealed extremely high corner frequency. For example, in Fig. 3 the corner frequency for 180 nm particles was $f_c = 68$ kHz, implying a large trap stiffness of about 0.76 pN/nm/W, which is in consistent with the mie theoretically calculated values. The temporal resolution of the experimental system is largely determined by the response time of the nanospheres upon the generation of force. To measure the time resolution, the response time can be calculated from the corner frequency (f_c) as described before.^{24,36} The temporal resolution, acquired was around 2.8 μ s, which enable one to perform high spatio temporal resolution

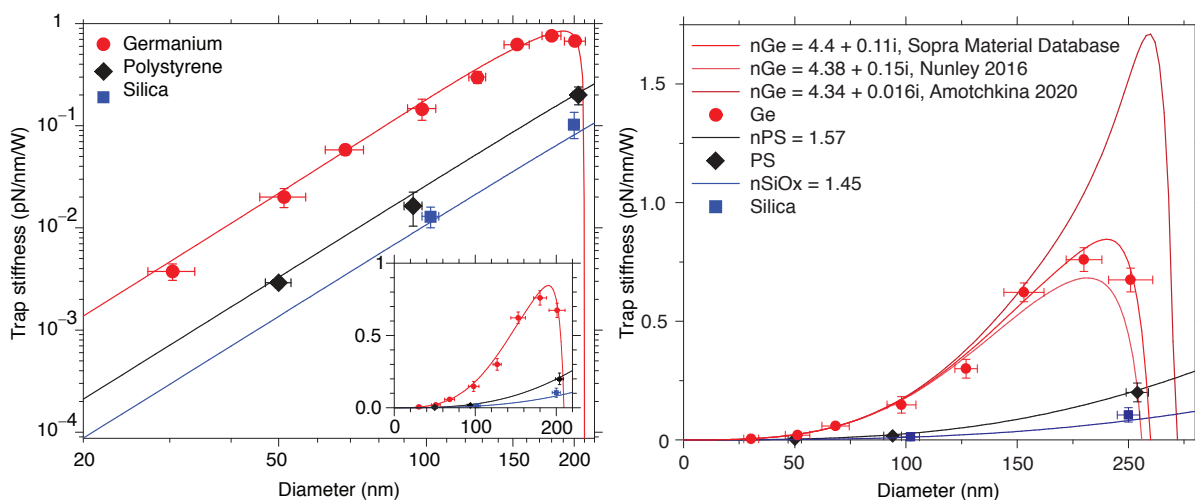


Figure 3: Trap stiffness per power for germanium nanospheres (black square), polystyrene (red diamonds), and silica (blue hexagons) as a function of different sized GeNTOPs diameter. The plots show mean and standard deviation. The solid lines (black, red and blue) correspond to the Mie theory calculations in log-log plot. Inset: Trap stiffness vs nanosphere diameter in lin-lin plot.)

measurements with this 180 nm GeNTOPs. Will the GeNTOPs generate heat at high laser intensity? Because, thermal damage caused by the probes at the high laser intensities to biological samples has been a matter of concern and investigation. In-order to check whether GeNTOPs generate heat, we measured the temperature of the particle at different laser intensity as mentioned before.²⁵ The temperature of the particle increased from 29 °C to 42 °C which is in consistent with the polystyrene microsphere. The trap stiffness also increased linearly with increase in the laser intensity.

Discussion

In general, we synthesised and demonstrated the stable optical trapping of germanium nanospheres with diameters from 30 to 200 nm. There are many reports on synthesizing germanium nanoparticles but they required toxic precursors and most of the process involves high temperatures and organic byproducts.^{26,27} In solution-phase synthetic

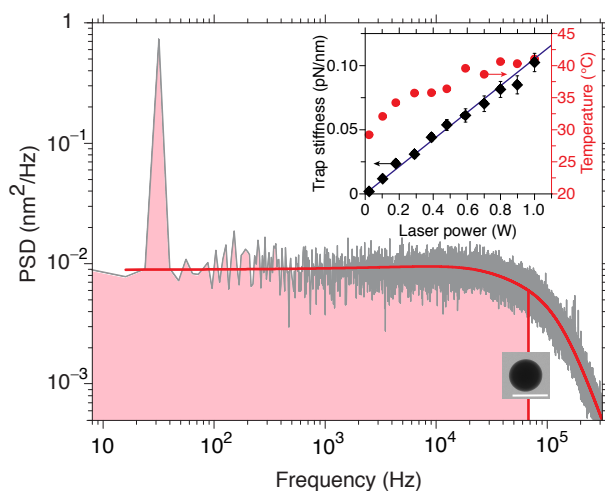


Figure 4: Power spectral density (PSD, average of 40 individual power spectra) for the GeNTOPs trapped at maximum laser power(1W) in water. The spectrum (grey line) features a calibration peak at 32 Hz (red line, fit to theory from,³⁶ see Methods). Inset-Trap stiffness k and Temperature (T) of the nanosphere as a function of laser power P in the focus (black, trap stiffness; red, temperature).(see Methods and ref. 13)

chemistry method, there is problem in achieving the good crystallinity of the particles as required.^{28–31} Jing , Guo and Wu et.al,^{20,32,33} reported the synthesis of germanium nanospheres from GeO_2 with different stabilizing agent but the nanospheres remained poly dispersed and tend to form aggregates. In our protocol, we produced germanium nano spheres which are stable and mono dispersed. The problem with as synthesized germanium nano spheres was they started to form aggregates after one week. In order to overcome this problem, the GeNTOPs were coated with lipid bilayer composed of Dimyristoylphosphatidyl- choline (DMPC) lipid as described previously(cite my paper).

The nano spheres tend to be in monodispersed form even after three months. We performed a quantitative analysis on the size of nanospheres synthesized at different time intervals, calculated the spring constants and characterized the optical trapping of semiconductor nanospheres. We showed that GeNTOPs has better trapping efficiency than the nanospheres reported previously. Eventhough, the metallic nanospheres have high trapping efficiency than commercially available polystyrene and silicon nano spheres, they have the disadvantage like quenching the fluorescence signal, heating up and weak

optical trapping of the smaller sized particles. As the absorbance range (280 nm) of the GeNTOPs are far away from the NIR range (1064 nm), the absorption of the light in NIR region is negligible and resulted in less heating up of the particles. The GeNTOPs also has high spatio temporal resolution. The temporal resolution achieved with the particles were around 2 μ s. This makes the GeNTOPs an ideal candidate to be used in biological application such as to perform force measurements in cells, study about protein interaction happening in microsecond level.

Experimental

Synthesis of Germanium nanospheres

The GeNTOPs were synthesized by following Guo et al²⁰ procedure with little modification. Briefly, 0.0150 g of germanium oxide, a substrate was mixed with 0.076 g of quercetin (stabilizing agent) and completely dissolved in 20 ml of 0.15 M solution (Solution A). In next step, 0.0295 g of sodium borohydride (NaBH_4 , reducing agent) was dissolved in 3 ml of distilled water and stored in a refrigerator at 4 °C (Solution B). The pH value of the resulting solution A was adjusted to pH 8.8 via titration with 37% HCL. Under continuous stirring the mixture was placed in a preheated oil bath at 60 °C with uninterrupted stirring. The reaction was stopped at different time points at 3, 4, 5, 6, 7 and 8 h, respectively. The sample was collected at different time intervals and washed thoroughly by centrifuging the sample at 13,000 rpm to remove remaining amounts of unreacted chemicals.

Characterization of Germanium nanospheres

The size characterization analysis were done using different techniques like Transmission electron microscopy (TEM- Jeol 1400 plus), Dynamic light scattering (Malvern, Zetasizer Nano ZSP) and with optical tweezer (Custom made). For, TEM about 10 μ L of the samples

were sonicated and 5 μL of the sample were spotted in copper grid. About 1 ml of the sample (sonicated for 5 min) was used for DLS measurement. For, trapping experiments with optical tweezers, the sample was diluted 100 times and 20 μL was filled in flow cells. Flow cells were constructed as described before.³⁴ About 10 mg of the lyophilized powder was used for X-ray powder diffraction (XRD) measurement (Philips X'pert X-ray diffractometer).

Optical tweezers set up

Measurements were performed in single-beam optical tweezers optimized for stability and performance. Briefly, for trapping, we used a laser with 1.0 W output power at 1,064 nm and a position-sensitive photodiode for back-focal-plane detection. The temperature of the objectives was stabilized with feedback to 29.4 $^{\circ}\text{C}$.³⁵

Power spectral density and temperature measurement

Calibration was based on a drag force method using a small sinusoidal stage movement combined with power spectral analysis.^{24,36} Using the calibration, we measured the drag coefficient and associated diameter of the nanosphere, and the trap stiffness k for all spatial directions. Calibration measurements were performed at 10% laser power (output power, 0.10 W) and trap stiffness was scaled up for 100% laser power (output power, 1 W, Figure 3). Control measurements confirmed the linearity between trap stiffness and laser power (Figure 4). For comparison, we used polystyrene microspheres with diameters of 0.590 ($n_{\text{PS}} \approx 1.57$, Bangs Laboratories). For the temperature measurement, the laser power was increased from 0 W to 1 W with step size of 0.1 W. For every laser power, time series were collected and PSD spectrum were acquired as mentioned before.

Acknowledgement

The author thanks Mats Dahlgren for version one of `achemso`, and Donald Arseneau for the code taken from `cite` to move citations after punctuation. Many users have provided feedback on the class, which is reflected in all of the different demonstrations shown in this document.

Supporting Information Available

This will usually read something like: “Experimental procedures and characterization data for all new compounds. The class will automatically add a sentence pointing to the information on-line:

References

- (1) Ashkin, A. Optical trapping and manipulation of small neutral particles using lasers. *Proc. Natl. Acad. Sci. USA* **1997**, *94*, 4853–4860.
- (2) Svoboda, K.; Block, S. M. Biological applications of optical forces. *Annual Review of Biophysics and Biomolecular Structure* **1994**, *23*, 247–285.
- (3) Ferro, V.; Sonnberger, A.; Abdosamadi, M. K.; McDonald, C.; Schäffer, E.; McGloin, D. Improved antireflection coated microspheres for biological applications of optical tweezers. *Optical Trapping and Optical Micromanipulation XIII* **2016**, 9922, 99222T.
- (4) Bugiel, M.; Fantana, H.; Bormuth, V.; Trushko, A.; Schiemann, F.; Howard, J.; Schäffer, E.; Jannasch, A. Versatile microsphere attachment of GFP-labeled motors and other tagged proteins with preserved functionality. *J. Biol. Methods* **2015**, *2*, 30.
- (5) Sudhakar, S.; Jo, T.; Kittelberger, M.; Maqbool, A.; Hermsdorf, G. L.; Ab-

- dosamadi, M. K.; Scha, E. Supported Solid Lipid Bilayers as a Platform for Single-Molecule Force Measurements. *Nano Lett.* **2019**, *19*, 8877–8886.
- (6) Bormuth, V.; Jannasch, A.; Ander, M.; van Kats, C. M.; van Blaaderen, A.; Howard, J.; Schäffer, E. Optical trapping of coated microspheres. *Optics Express* **2008**, *16*, 13831.
- (7) Keir C. Neuman and AttilaNagy, Single-molecule force spectroscopy: optical tweezers, magnetic tweezers and atomic force microscopy. *Nature methods* **2012**, *5*, 491–505.
- (8) Jauffred, L.; Taheri, S. M. R.; Schmitt, R.; Linke, H.; Oddershede, L. B. Optical Trapping of Gold Nanoparticles in Air. *Nano Letters* **2015**, *15*, 4713–4719.
- (9) Hansen, P. M.; Bhatia, V. K.; Harrit, N.; Oddershede, L. Expanding the optical trapping range of gold nanoparticles. *Nano Letters* **2005**, *5*, 1937–1942.
- (10) Brzobohatý, O.; Šiler, M.; Trojek, J.; Chvátal, L.; Karásek, V.; Paták, A.; Pokorná, Z.; Mika, F.; Zemánek, P. Three-dimensional optical trapping of a plasmonic nanoparticle using low numerical aperture optical tweezers. *Scientific Reports* **2015**, *5*, 8106.
- (11) Hajizadeh, F.; S.Reihani, S. Optimized optical trapping of gold nanoparticles. *Optics Express* **2010**, *18*, 551.
- (12) Bosanac, L.; Aabo, T.; Bendix, P. M.; Oddershede, L. B. Efficient optical trapping and visualization of silver nanoparticles. *Nano Letters* **2008**, *8*, 1486–1491.
- (13) Messina, E.; Donato, M. G.; Zimbone, M.; Saija, R.; Iatì, M. A.; Calcagno, L.; Fragalà, M. E.; Compagnini, G.; D'Andrea, C.; Foti, A.; Gucciardi, P. G.; Maragò, O. M. Optical trapping of silver nanoplatelets. *Optics Express* **2015**, *23*, 8720.
- (14) Seol, Y.; Carpenter, A. E.; Perkins, T. T. Gold nanoparticles: enhanced optical trapping and. *Optics Letters* **2006**, *31*, 2429–2431.
- (15) Jauffred, L.; Samadi, A.; Klingberg, H.; Bendix, P. M.; Oddershede, L. B. Plasmonic Heating of Nanostructures. *Chemical Reviews* **2019**, *119*, 8087–8130.

- (16) Chikazawa, J. I.; Uwada, T.; Furube, A.; Hashimoto, S. Flow-induced transport via optical heating of a single gold nanoparticle. *Journal of Physical Chemistry C* **2019**, *123*, 4512–4522.
- (17) Vaughn, D. D.; Schaak, R. E. Synthesis, properties and applications of colloidal germanium and germanium-based nanomaterials. *Chemical Society Reviews* **2013**, *42*, 2861–2879.
- (18) Fan, J.; Chu, P. K. Group IV nanoparticles: Synthesis, properties, and biological applications. *Small* **2010**, *6*, 2080–2098.
- (19) Ishii, S.; Chen, K.; Okuyama, H.; Nagao, T. Resonant Optical Absorption and Photothermal Process in High Refractive Index Germanium Nanoparticles. *Advanced Optical Materials* **2017**, *5*.
- (20) Guo, Y. J.; Yang, F.; Zhang, L.; Pi, J.; Cai, J. Y.; Yang, P. H. Facile synthesis of multifunctional germanium nanoparticles as a carrier of quercetin to achieve enhanced biological activity. *Chem. Asian J.* **2014**, *9*, 2272–2280.
- (21) Kim, S.; Park, S. Y.; Jeong, J.; Kim, G. H.; Rohani, P.; Kim, D. S.; Swihart, M. T.; Kim, J. Y. Production of pristine, sulfur-coated and silicon-alloyed germanium nanoparticles via laser pyrolysis. *Nanotechnology* **2015**, *26*.
- (22) Wang, L.; Bao, K.; Lou, Z.; Liang, G.; Zhou, Q. Chemical synthesis of germanium nanoparticles with uniform size as anode materials for lithium ion batteries. *Dalton Transactions* **2016**, *45*, 2814–2817.
- (23) Nieminen, T. A.; Loke, V. L.; Stilgoe, A. B.; Knöner, G.; Brańczyk, A. M.; Heckenberg, N. R.; Rubinsztein-Dunlop, H. Optical tweezers computational toolbox. *Journal of Optics A: Pure and Applied Optics* **2007**, *9*.

- (24) Tolić-Nørrelykke, S. F.; Schäffer, E.; Howard, J.; Pavone, F. S.; Jülicher, F.; Flyvbjerg, H. Calibration of optical tweezers with positional detection in the back focal plane. *Review of Scientific Instruments* **2006**, *77*.
- (25) Peterman, E. J.; Gittes, F.; Schmidt, C. F. Laser-induced heating in optical traps. *Biophysical Journal* **2003**, *84*, 1308–1316.
- (26) Nakamura, Y.; Watanabe, K.; Fukuzawa, Y.; Ichikawa, M. Observation of the quantum-confinement effect in individual Ge nanocrystals on oxidized Si substrates using scanning tunneling spectroscopy. *Applied Physics Letters* **2005**, *87*, 1–3.
- (27) Maeda, Y. Visible photoluminescence from nanocrystallite Ge embedded in a glassy SiO₂ matrix: Evidence in support of the quantum-confinement mechanism. *Physical Review B* **1995**, *51*, 1658–1670.
- (28) Lee, D. C.; Pietryga, J. M.; Robel, I.; Werder, D. J.; Schaller, R. D.; Klimov, V. I. Colloidal synthesis of infrared-emitting Germanium nanocrystals. *Journal of the American Chemical Society* **2009**, *131*, 3436–3437.
- (29) Ruddy, D. A.; Johnson, J. C.; Smith, E. R.; Neale, N. R. Size and bandgap control in the solution-phase synthesis of near-infrared-emitting germanium nanocrystals. *ACS Nano* **2010**, *4*, 7459–7466.
- (30) Lu, X.; Korgel, B. A.; Johnston, K. P. High yield of germanium nanocrystals synthesized from germanium diiodide in solution. *Chemistry of Materials* **2005**, *17*, 6479–6485.
- (31) Henderson, E. J.; Hessel, C. M.; Veinot, J. G. Synthesis and photoluminescent properties of size-controlled germanium nanocrystals from phenyl trichlorogermane-derived polymers. *Journal of the American Chemical Society* **2008**, *130*, 3624–3632.
- (32) Jing, C.; Zang, X.; Bai, W.; Chu, J.; Liu, A. Aqueous germanate ion solution promoted

synthesis of worm-like crystallized Ge nanostructures under ambient conditions. *Nanotechnology* **2009**, *20*, 505607.

- (33) Wu, J.; Sun, Y.; Zou, R.; Song, G.; Chen, Z.; Wang, C.; Hu, J. One-step aqueous solution synthesis of Ge nanocrystals from GeO₂ powders. *CrystEngComm* **2011**, *13*, 3674–3677.
- (34) Chugh, M.; Reißner, M.; Bugiel, M.; Lipka, E.; Herrmann, A.; Roy, B.; Müller, S.; Schäffer, E. Phragmoplast Orienting Kinesin 2 Is a Weak Motor Switching between Processive and Diffusive Modes. *Biophysical Journal* **2018**, *115*, 375–385.
- (35) Mahamdeh, M.; Schäffer, E. Optical tweezers with millikelvin precision of temperature-controlled objectives and base-pair resolution. *Optics Express* **2009**, *17*, 17190.
- (36) Schäffer, E.; Nørrelykke, S. F.; Howard, J. Surface forces and drag coefficients of microspheres near a plane surface measured with optical tweezers. *Langmuir* **2007**, *23*, 3654–3665.